UNIVERSITÀ
DEGLI STUDI
FIRENZE

DOTTORATO DI RICERCA IN
FISICA E ASTRONOMIA

CICLO XXVIII

COORDINATORE: Prof. Roberto Livi

Quantum Simulation with Ytterbium Atoms in Synthetic Dimensions

Settore Scientifico Disciplinare: FIS/03

Dottorando
Dott. Mancini Marco

Tutore
Prof. Fallani Leonardo

Coordinatore
Prof. Roberto Livi

Anni 2012/2013-2013/2014-2014/2015

Abstract

This thesis reports on the experimental investigation of ultracold fermionic Ytterbium atoms in optical lattices. Ytterbium is a two-electron atom and, due to its rich electronic structure, it allows the investigation of many different physical phenomena. In particular, it is characterized by a purely nuclear spin, which is completely decoupled from the electronic degrees of freedom. This property makes Ytterbium a valuable candidate in the context of quantum simulation. I will mainly focus on how we exploited the coherent Raman coupling between different nuclear spin states in order to engineer an artificial magnetic field for ultracold atoms. The nuclear spin degree of freedom acts as a synthetic dimension that, in addition to a real one-dimensional optical lattice, gives rise to a synthetic two dimensional lattice. Since the Raman coupling depends on the particular position of the atoms in the real one-dimensional lattice, when a particle hops around a closed loop in this synthetic system it acquires a non-zero phase, which is reminiscent of the Aharonov-Bohm phase acquired by a charged particle in a magnetic field. This technique allowed us to experimentally realize chiral edge states within this ribbon geometry and, for the first time, to observe skipping-type orbit dynamics, that is a hallmark of quantum Hall physics.

The optical detection and careful manipulation of the number of spin components allowed us to study also the behaviour of a one-dimensional liquid of interacting fermions with a tunable number of spin components, validating for the first time the prediction that a one-dimensional liquid of fermions with many spins exhibits properties of a bosonic spinless liquid.

Moreover, in addition to their nuclear spin, two-electron atoms possesses an excited metastable state that can be addressed with an ultranarrow clock laser. Coherent control of Ytterbium clock transition ${}^1S_0 \rightarrow {}^3P_0$ in three-dimensional optical lattices has led to the first observation of fast, coherent spin-exchange oscillations between two ^{173}Yb atoms in different electronic orbitals. These experiments show that Ytterbium, with its many powerful properties, is a perfect candidate for the realization of a novel quantum simulator of unique many-body phenomena.

Contents

Introduction

In the last two decades, thanks to the incredible advances in atomic manipulation through laser light, it has been possible to cool down atomic gases to the nanokelvin regime, enlighting their quantum nature and realizing degenerate samples, both bosonic [1, 2] and fermionic [3]. These achievements led to the emergence of the new branch of physics of ultracold atoms, which is characterized by an unprecedented control over the experimental parameters. In particular, ultracold atoms are perfect candidates to practically implement the famous idea of R. Feynman [4] regarding the possibility of engineering a quantum system to simulate, experimentally, a specific quantum physical phenomenon or theoretical model. Within this context, the unique development of a tuning knob of the interactions between the atoms [5] and the realization of optical lattices [6, 7], opened the door to the simulation of condensed-matter models [8] and led to the investigation of strongly-correlated many-body systems [9, 10]. Moreover, the realization of artificial magnetic fields for ultracold neutral atoms [11–15] and the engineering of spin-orbit coupling [16, 17] opened the door to the study of quantum Hall physics within a controllable experimental setup and to the investigation of topological properties of some paradigmatic condensed-matter models [18–20].

This PhD thesis fits into these last frontiers of quantum simulation, and it is mainly focused on the realization of a synthetic magnetic field for a gas of ultracold fermions loaded in an optical lattice. Unlike previous techniques, based on laser-assisted tunneling [12, 13, 21] or lattice shaking schemes [18, 20], we use a completely novel approach based upon the concept of *synthetic dimensions* [22, 23]. The atom we use in our lab, fermionic ^{173}Yb, possesses $N = 6$ spin components in its ground state, that can be coherently coupled by means of Raman transitions. Interestingly, the mathematical description for this coherent spin system is completely equivalent to the one describing a particle hopping between different sites of a one-dimensional lattice. Indeed, the spin components can be treated as *synthetic lattice sites*, coherently connected by the tunneling given by the Raman coupling. If the atoms are then loaded in a *real* one-dimensional lattice, the Raman coupling effectively gives rise to

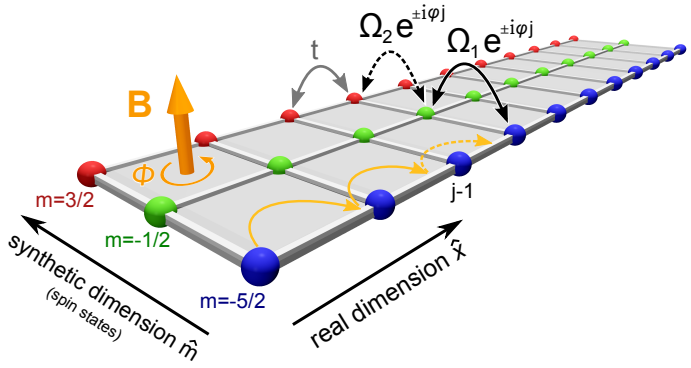

Figure 1: 1. A synthetic gauge field in a synthetic dimension. We confine the motion of fermionic ultracold atoms in a hybrid lattice, generated by an optical lattice along a real direction $\hat{x}$ with tunneling t, and by laser-induced hopping between spin states along a synthetic direction $\hat{m}$. By inducing a complex tunneling $\Omega_R e^{i\Phi j}$ along $\hat{m}$, the atom wave function acquires a phase Φ per plaquette, mimicking the effect of a transverse magnetic field **B** on effectively charged particles.

a synthetic two-dimensional lattice. In order to realize an effective magnetic field in this 2D hybrid lattice, it is sufficient that the phase of the Raman coupling depends on the particular lattice site in which an atom sits. In this way, atoms tunneling from different sites will acquire different phases giving an effective Aharonov-Bohm phase when the trajectory forms a closed loop, as it is depicted in Fig. 1. The generated effective magnetic field is of the order of one flux-quantum per plaquette, corresponding to unreachable magnetic field intensities of thousands of Tesla, for experiments in solid-state physics. The synthetic dimensions approach is straightforwardly implemented, without the need of complex superlattice potentials or non-trivial lattice driving schemes. Furthermore, the chosen Raman light, leads to heating effects that are completely negligible on the timescale of the experiments. Also, the possibility of optically detecting the single spin components (by means of optical Stern-Gerlach or spin-selective imaging) effectively realizes single-site detection along the synthetic direction. Another important feature of this hybrid 2D lattice is the presence of sharp edges, at the border of the spin direction. We have indeed investigated edge-physics properties and, for the first time, we have observed, in neutral matter, chiral edge-currents and skipping-orbit-like trajectories [24, 25], paving the way to the study of quantum-Hall physics within the highly controllable environment of ultracold quantum gases.

In this PhD thesis I will also describe how it is possible to exploit the properties of quantum degenerate Ytterbium (^{173}Yb) Fermi gases [26]

loaded in optical lattices to pursue the study of many other physical systems. Unlike alkalis, Ytterbium is a two-electron atom which does not possess an electronic angular momentum ($J = 0$) in its ground state and, in the case of the fermionic isotopes, only a nuclear spin exists, which is completely decoupled from the electronic degrees of freedom. These peculiar properties have two striking consequences: the first one, is the existence of a metastable excited state which is connected to the ground state via an optical clock transition [27–31], bringing Ytterbium in the spotlight for applications within quantum metrology [28, 32]. This state can also be used as an additional "orbital" degree of freedom for quantum simuation applications. This characteristic allowed us to study two-orbital physics, in particular observing for the first time coherent inter-orbital spin-exchange oscillations, whose nature is at the basis of some paradigmatic quantum magnetism lattice model [33–35]. Also, we have very recently observed a new kind of Feshbach resonance, called *orbital* Feshbach resonance [36] in which the scattering properties between atoms in different electronic states can be tuned by means of an external magnetic field. We studied the hydrodynamic time-of-flight expansion of a strongly interacting Fermi gas, and used the characteristic aspect-ratio inversion to identify the position of the Feshbach resonance [37, 38].

The second property, connected to the presence of a purely nuclear spin, is manifested in the physics of collisions. In particular, the interaction between ultracold ^{173}Yb atoms does not depend on the nuclear spin orientation, giving rise to a high degree of symmetry, called $SU(N)$ symmetry [34], where N is the number of nuclear spin components. This cancels any possible collision-induced spin relaxation mechanism making the spin component a good quantum number. This property allowed us to study the role of spin multiplicity in the context of one-dimensional physics, going beyond the standard solid-state, spin 1/2 case. In particular, we have investigated the correlations-induced broadening of the momentum distribution as a function of the number of spin components and also observed, for the first-time, the predicted [39] high-spin bosonization phenomena in a multicomponent one-dimensional liquid of fermions.

Thesis overview

This thesis is organized as follows:

- Chapter 1 describes the basic theoretical ingredients necessary to describe ultracold fermions in optical dipole potentials. Attention will be given to the description of optical lattices, state-dependent dipole potentials and the low-energy properties of scattering between ultracold atoms. The fundamental ingredient of the coherent coupling between internal degrees of freedom, will be introduced.

- Chapter 2 is devoted to the description of the experimental setup and of techniques developed to reach quantum degeneracy with the fermionic ^{173}Yb isotope. We will describe the all-optical procedures used to detect, manipulate and coherently couple the nuclear-spin components. Thanks to these, three main experiments have been performed which will be described in three independent chapters.

- Chapters 3, 4, 5 are at the heart of this PhD thesis and describe the engineering of an artificial magnetic field in a ribbon geometry in which one direction is constituted by the sites of a real one-dimensional optical lattice and the other direction is encoded in the coherently coupled nuclear spin components, which can be interpreted [22, 23] as an "extra-dimensional" lattice. With this novel technique it has been possible to observe, for the first time, paradigmatic phenomena of quantum Hall physics such as chiral edge states and skipping-orbit-like dynamics [24]. The theory at the basis of these observations will be reviewed in Chapter 4, where we give a basic description of quantum Hall physics from a lattice perspective.

  These results pave the way to the study of strongly interacting fermions in a "Hall-ribbon" geometry, allowing the investigation of fractional quantum Hall physics [40–42] and of exotic quantum phases in neutral matter [43].

- Chapter 6 describes the first experiment performed on the ytterbium setup, which constitutes the main topic of the PhD thesis of my colleague G. Pagano [44, 45]. We studied static and dynamic properties of a one-dimensional liquid of fermions with a tunable number of spin components. In one dimension the Landau-Fermi liquid model breaks down and a new description is needed, based on the famous Tomonaga-Luttinger liquid model [46, 47]. In particular, we studied the role of spin multiplicity, going beyond the standard two-components case typical of electrons in condensed-matter physics.

- Chapter 7 mostly regards the second experiment perfomed [48] on the ytterbium setup, in which we coherently addressed the excited metastable $^3P_0$ state using an ultra-narrow clock laser developed by my colleague G. Cappellini during his PhD [49]. We studied the role of interactions between atoms loaded in a three-dimensional optical lattice in different nuclear-spin and electronic states. Because of the symmetry of the two-particles wavefunction, two possibilities exist, symmetric and anti-symmetric electronic states, which are separated by an exchange energy. For the first time we observed inter-orbital spin-exchange oscillations, a fundamental ingredient in the field of quantum magnetism, in particular for the realization of the paradigmatic Kondo lattice model [34]. The final part of the Chapter is ded-

icated to the description of some very recent results [50] regarding the first observation of a novel kind of Feshbach resonance, called *orbital* Fesbach resonance, affecting atoms in different electronic orbitals. We identified the position of the resonance by studying the hydrodinamic expansion of a Fermi gas in the strongly interacting regime. We also verified the predicted [36] scaling law of the resonance position as Δm^{-1} in which $\Delta m = m - m'$ is the difference between two generic spin components out of the $F = 5/2$ manifold. This scaling law is a direct manifestation of the $SU(N)$ character of both the ${}^1S_0$ and ${}^3P_0$ states.

Publications

The following articles have been published in the context of this thesis:

- *"A one dimensional liquid of fermions with tunable spin"*
  G. Pagano, **M. Mancini**, G. Cappellini, P. Lombardi, F. Schäfer, H. Hui, X. J. Liu, J. Catani, C. Sias, M. Inguscio and L. Fallani, Nature Physics **10**, 198 (2014).

- *"Direct Observation of Coherent Inter-orbital Spin-Exchange Dynamics"*
  G. Cappellini, **M. Mancini**, G. Pagano, P. Lombardi, L. Livi, M. Siciliani de Cumis, P. Cancio, M. Pizzocaro, D. Calonico, F. Levi, C. Sias, J. Catani, M. Inguscio, and L. Fallani, Physical Review Letters **113**, 120402 (2014).

- *"Observation of chiral edge states with neutral fermions in synthetic Hall ribbons"*
  M. Mancini, G. Pagano, G. Cappellini, L. Livi, M. Rider, J. Catani, C. Sias, P. Zoller, M. Inguscio, M. Dalmonte, L. Fallani, Science **349**, 6255 (2015).

- *"A compact ultranarrow high-power laser system for experiments with 578 nm Ytterbium clock transition"*
  G. Cappellini, P. Lombardi, **M. Mancini**, G. Pagano, M. Pizzocaro, L. Fallani, J. Catani, Review of Scientific Instruments **86**, 073111 (2015).

- *"A strongly interacting gas of two-electron fermions at an orbital Feshbach resonance"*
  G. Pagano, **M. Mancini**, G. Cappellini, L. Livi, C. Sias, J. Catani, M. Inguscio, L. Fallani, Physical Review Letters **115**, 265301 (2015).

1 Trapped Fermi gases: basic tools

This chapter reviews some basic concepts that are common to many atomic physics experiments. We will start from Section 1.1 where a brief reminder of the theory of a non-interacting Fermi gas will be given. Next, in Section 1.2, we will discuss how to trap and manipulate the atoms in optical dipole traps. The fundamental tool of the optical lattice will be introduced, presenting the typical description in term of Bloch bands and Bloch wavefunctions. We will describe also a method to engineer state-dependent dipole potentials, allowing for the detection and manipulation of the spin degree of freedom (see Sec. 2.5). On the same line, in Section 1.3, we will illustrate how to coherently couple the internal degrees of freedom by means of Raman transitions. Finally, Section 1.4 describes briefly the low-energy scattering between ultracold fermions enlighting the emergence of $SU(N)$ symmetry which characterizes our particular atomic species.

1.1 Non interacting Fermi gases in harmonic potential

Non interacting fermionic atoms are characterized by the Fermi-Dirac distribution:

$$\mathcal{F}(\epsilon) = \frac{1}{e^{\frac{\epsilon-\mu}{k_B T}} + 1} \tag{1.0}$$

which represents the occupation probability of a single particle state with energy ϵ at temperature T. In Eq. (1.1) k_B is the Boltzmann constant and μ is the chemical potential which is fixed by the total number of particles N. At $T = 0$ the chemical potential coincides with the Fermi energy, $\mu(T = 0) = E_F$. It is useful to introduce also the Fermi wavevector $k_F = \sqrt{2mE_F}/\hbar$ and the Fermi temperature $k_B T_F = E_F$, in which m is the atomic mass and $\hbar$ is the reduced Planck constant. Another quantity of interest is the fugacity $z = \exp(\frac{\mu}{k_B T})$ which is a monotonic function useful to characterize the degree of quantum degeneracy of the

gas: for a thermal gas $T \gg T_F$, $z \simeq 0$ and the Fermi-Dirac distribution approaches the Boltzmann distribution, while for the deeply degenerate regime $T \ll T_F$, $z \to +\infty$ and $\mathcal{F}(\epsilon)$ tends to the Heaviside function $\Theta(E_F - \epsilon)$.

For a gas trapped in a three-dimensional harmonic potential

$$V(\mathbf{r}) = \frac{1}{2} m(\omega_x^2 x^2 + \omega_y^2 y^2 + \omega_z^2 z^2) \tag{1.0}$$

the density of states at energy ϵ is equal to

$$g(\epsilon) = \frac{\epsilon^2}{2(\hbar\bar{\omega})^3} \tag{1.0}$$

where we defined the geometric mean trap frequency $\bar{\omega} = (\omega_x\, \omega_y\, \omega_z)^{1/3}$. Integrating the density of states weighted by the Fermi-Dirac distribution at $T = 0$, we get the total number of atoms

$$N = \int_0^\infty g(\epsilon)\Theta(E_F - \epsilon)d\epsilon = \int_0^{E_F} g(\epsilon)d\epsilon \tag{1.0}$$

which defines the Fermi energy $E_F = \hbar\bar{\omega}(6N)^{1/3}$. The fugacity $z(N,T)$ can be obtained by inverting the following relation numerically:

$$N = \int_0^\infty g(\epsilon)\mathcal{F}(\epsilon)d\epsilon = -\left(\frac{k_B T}{\hbar\bar{\omega}}\right)^3 \mathrm{Li}_3(-z) \tag{1.0}$$

where $\mathrm{Li}_n(x)$ is the polylogarithmic function of the order n. Using the Sommerfeld expansion in the low-temperature limit we can write the chemical potential,

$$\mu(N,T) = k_B T \log(z(N,T)) \simeq E_F \left(1 - \frac{\pi^2}{3}\frac{T^2}{T_F^2}\right) \tag{1.0}$$

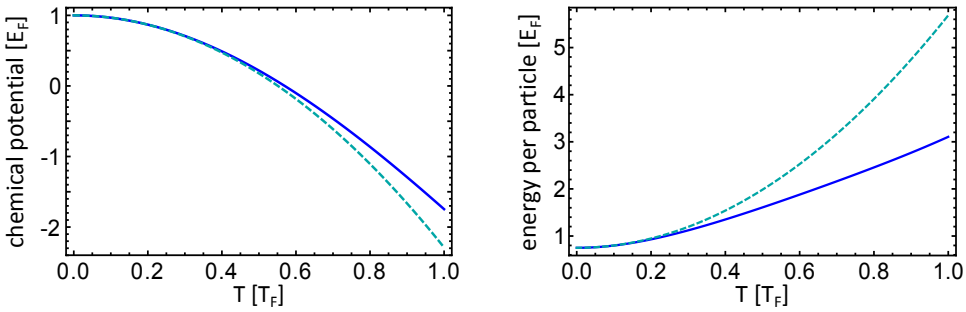

Figure 1.1: Chemical potential (left) and energy per particle (right) for a non-interacting trapped Fermi Gas. The dotted curves are the low-temperature approximations.

and the energy per particle,

$$\frac{E(N,T)}{N} = -\frac{3k_B^4 T^4 \mathrm{Li}_4(-z)}{N\hbar^3\bar{\omega}^3} \simeq \frac{3}{4}E_F\left(1+\frac{2\pi^2}{3}\frac{T^2}{T_F^2}\right) \tag{1.0}$$

which are plotted in Fig. 1.1.

1.1.1 Density and momentum distribution

In order to extract the real space and momentum distributions, a semi-classical approximation is typically used, which is quite accurate in the limit of large atoms number N where many single-particle states are occupied [51]. Within local-density approximation (LDA), the number density in phase space is

$$f(\mathbf{r},\mathbf{p}) = \frac{1}{(2\pi\hbar)^3}\frac{1}{e^{\beta\left(\frac{\mathbf{p}^2}{2m}+V(\mathbf{r})-\mu\right)}+1}. \tag{1.0}$$

where $\beta = 1/k_B T$ and from which we can obtain the density and momentum distributions by integration in momentum space and position space, respectively [52]:

$$\begin{aligned} n(\mathbf{r}) &= \int d\mathbf{p}\, f(\mathbf{r},\mathbf{p}) = -\frac{1}{\lambda_{dB}^3}\mathrm{Li}_{3/2}\left(-ze^{-\beta V(\mathbf{r})}\right) \\ n(\mathbf{p}) &= \int d\mathbf{r}\, f(\mathbf{r},\mathbf{p}) = -\frac{1}{m^3\bar{\omega}^3}\frac{1}{\lambda_{dB}^3}\mathrm{Li}_{3/2}\left(-ze^{-\beta\frac{\mathbf{p}^2}{2m}}\right) \end{aligned} \tag{1.0}$$

where $\lambda_{dB} = \sqrt{2\pi\hbar^2/mk_BT}$ is the de-Broglie wavelength. An important observation is that the momentum distribution for an ideal Fermi gas is isotropic, leading to a correspondingly isotropic expansion when the gas is released from a harmonic potential. As it is discussed in [45] the column-integrated 3D momentum distribution is used to fit the column density in time-of-flight absorption images, in order to extract the ratio T/T_F from the fugacity z through the relation: $T/T_F = (-6\mathrm{Li}_3(-z))^{-1/3}$.

1.2 Optical Dipole Potentials

It has become experimental routine to produce ensembles of neutral atoms in the microkelvin regime. It is thus possible to trap the atoms by means of optical dipole traps that rely on the electric dipole interaction with far-detuned laser light [7]. In this case the optical excitation is very low and the radiation force due to photon scattering is negligible as compared to the dipole force.

When a neutral particle is placed into laser light, the electric field $\mathbf{E}$ induces an atomic dipole moment $\mathbf{d}$ proportional to the complex dynamic

polarizability of the atom $\alpha(\omega)$, $\mathbf{d} = \alpha(\omega)\mathbf{E}$, where ω is the driving frequency. The interaction potential of the induced dipole moment $\mathbf{d}$ in the driving field $\mathbf{E}$ is given by:

$$U(\mathbf{r},\omega) = -\frac{1}{2\epsilon_0 c}\mathrm{Re}[\alpha(\omega)]I(\mathbf{r}), \tag{1.0}$$

where $I(\mathbf{r}) = 2\epsilon_0 c|E(\mathbf{r})|^2$ is the field intensity. The interaction potential is nothing else than the light shift experienced by the atom in the laser field and it is proportional to the real part of the polarizability, which describes the in-phase component of the dipole oscillation [53]. From the gradient of the interaction potential we can extract the dipole force:

$$F_{dip}(\mathbf{r},\omega) = -\nabla U(\mathbf{r},\omega) = \frac{1}{2\epsilon_0 c}\mathrm{Re}[\alpha(\omega)]\nabla I(\mathbf{r}) \tag{1.0}$$

which is thus a conservative force.

We have to consider also the dissipative processes associated with light absorption and spontaneous re-emission, which are connected to the imaginary part of the dynamic polarizability. The absorption can be interpreted in terms of number of photons which are scattered in cycles of absorption and spontaneous emission processes. The corresponding scattering rate is:

$$\Gamma_{sc}(\mathbf{r},\omega) = \frac{1}{\hbar\epsilon_0 c}\mathrm{Im}[\alpha(\omega)]I(\mathbf{r}). \tag{1.0}$$

In the case of a two-level atom and using the semiclassical approximation for the atomic polarizability [7] the following expressions are derived for the dipole potential and the scattering rate in the case of large detunings:

$$U(\mathbf{r},\omega) = -\frac{3\pi c^2}{2\omega_0^3}\left(\frac{\Gamma}{\omega_0-\omega}+\frac{\Gamma}{\omega_0+\omega}\right)I(\mathbf{r}) \tag{1.1}$$

$$\Gamma_{sc}(\mathbf{r},\omega) = \frac{3\pi c^2}{2\hbar\omega_0^3}\left(\frac{\omega}{\omega_0}\right)^3\left(\frac{\Gamma}{\omega_0-\omega}+\frac{\Gamma}{\omega_0+\omega}\right)^2 I(\mathbf{r}) \tag{1.2}$$

where ω_0 is the resonant frequency of the two-level atom and Γ is the spontaneous decay rate of the excited level.

These formulas can be easily generalized to the case of a multi-level atom interacting with a far-off resonant laser light[1]. The dipole potential and the scattering rate experienced by an atom in a particular electronic

[1]We are still considering the case in which each level does not possess a magnetic substructure.

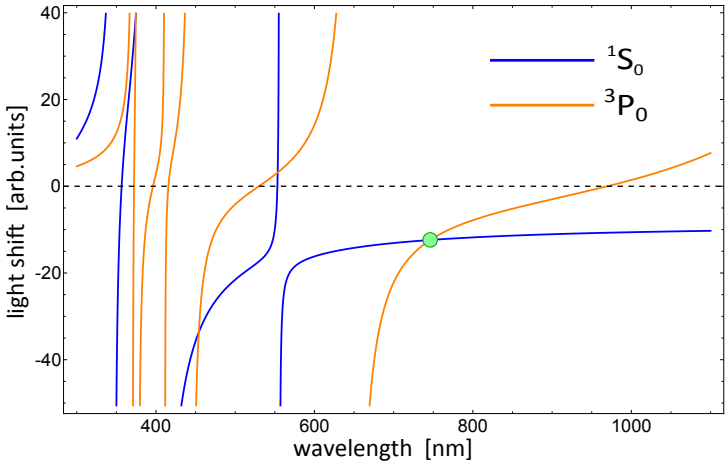

Figure 1.2: Calculation of the dipole potential experienced by the $^1S_0$ and $^3P_0$ Yb levels using equation (1.2). The green dot indicates the magic wavelength for which the two light shifts are equal. This will be important in Chapter 7, where the experiments with the clock transition are discussed.

state $|n\rangle$ are given by:

$$U_n(\boldsymbol{r},\omega) = -\sum_{m\neq n} \frac{3\pi c^2}{2\omega_{mn}^3}\left(\frac{\Gamma_{mn}}{\omega_{mn}-\omega}+\frac{\Gamma_{mn}}{\omega_{mn}+\omega}\right) I(\boldsymbol{r})$$

$$\Gamma_{sc}^{(n)}(\boldsymbol{r},\omega) = \sum_{m\neq n} \frac{3\pi c^2}{2\hbar\omega_{mn}^3}\left(\frac{\omega}{\omega_{mn}}\right)^3\left(\frac{\Gamma_{mn}}{\omega_{mn}-\omega}+\frac{\Gamma_{mn}}{\omega_{mn}+\omega}\right)^2 I(\boldsymbol{r})$$

where ω_{mn} identifies the transition frequency from level $|n\rangle$ to level $|m\rangle$ with its respective decay rate Γ_{mn}. In Fig. 1.2 we show the calculated dipole potential experienced by an Yb atom in the $^1S_0$ (blue line) and $^3P_0$ (orange line) energy states. The green dot indicates the "magic" wavelength (one of the many present) for which the two light shifts are equal. This will be important in Chapter 7, in which experiments involving the clock transition will be described.

1.2.1 Optical lattices

Optical lattices are a fundamental tool in the context of quantum simulation with ultracold atoms. They permit the realization of real crystals of light, which emulate the crystalline solid structure in which electrons move. Such optical structures are experimentally obtained by superimposing two counter-propagating gaussian laser beams, resulting in the dipole potential:

$$V_{1D}(r,z) = V_0 e^{-2\frac{r^2}{w^2(z)}}\cos^2(k_L z) \simeq V_0\cos^2(k_L z) + \frac{1}{2}m\omega_r^2 r^2 + \frac{1}{2}m\omega_z^2 z^2 \quad (1.2)$$

where V_0 is proportional to the intensity of the laser beams and to the polarizability of the atoms, k_L is the laser wavenumber and the quadratic terms generate an additional harmonic confinement which comes from the gaussian shape of the laser beams. The depth of an optical lattice is naturally expressed in terms of the recoil energy $E_R = \hbar^2 k_L^2/2m$ through the dimensionless parameter $s = V_0/E_R$. The radial and axial trapping frequencies of the additional harmonic terms are obtained by expanding the original dipole potential to second order around $r = 0$ and $z = 0$. We express these frequencies in terms of the lattice depth:

$$\begin{aligned} \omega_r &= \sqrt{\frac{4V_0}{mw_0^2}} = \sqrt{\frac{4E_R}{mw_0^2}}\sqrt{s}, \\ \omega_z &= \sqrt{\frac{2V_0}{mz_R^2}} = \sqrt{\frac{2E_R}{mz_R^2}}\sqrt{s} \end{aligned} \tag{1.2}$$

where w_0 is the beam waist of the gaussian beams and z_R the Rayleigh range defined as $z_R = \pi w_0^2/\lambda$. By expanding the co-sinusoidal term in Eq. (1.2.1) around $z = 0$, we obtain the harmonic frequency associated to the single lattice sites created by the interference pattern along the z-axis, namely:

$$\omega_\perp = \sqrt{\frac{2k_L^2}{m}V_0} = \frac{2E_R}{\hbar}\sqrt{s}. \tag{1.2}$$

Optical lattices are a versatile and manoeuvrable tool not only to build perfect periodic potentials but also to tune the dimensionality of the system. Indeed by superimposing many counterpropagating beams along orthogonal directions, it is possible to realize different geometric patterns, from one-dimensional tubes [44] to three-dimensional simple cubic lattice structures [54]. If the beams intersect at specific angles, more exotic patterns can be obtained such as triangular lattices [55] or graphene-like lattices [56]. By neglecting the weak harmonic confinement it is possible to analytically solve the hamiltonian of an atom in an optical lattice, finding the energy levels and the eigenfunctions in terms of Mathieu functions.

Bloch bands and Bloch functions

The problem of a single particle in a periodic potential has been extensively studied in the last century in solid state physics [57]. The hamiltonian we want to solve is:

$$H = \frac{p^2}{2m} + V_0 \cos^2(k_L z), \tag{1.2}$$

which gives rise to a second-order differential equation that takes the form of the famous Mathieu equation, $\psi'' + [a - 2q\cos(2x)]\psi = 0$ where $a =$

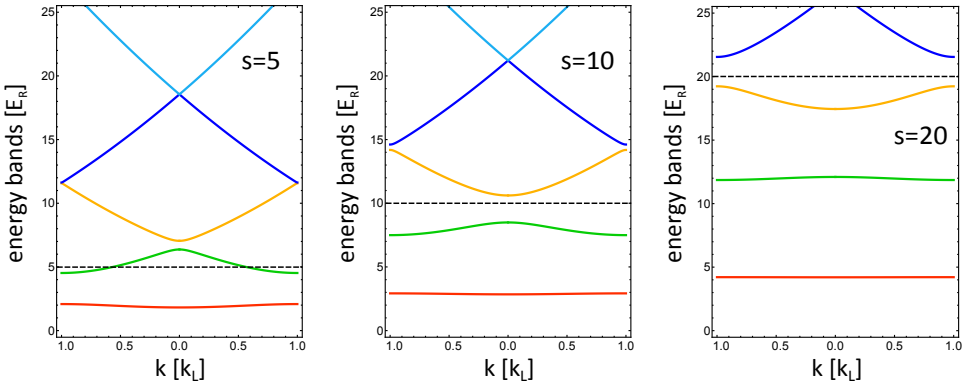

Figure 1.3: Energy band diagrams for various lattice depths. The dotted lines indicates the lattice depths in recoil energy unit. Note how the energy levels flatten out by increasing the lattice depth.

$E/E_R - s/2$, $q = s/4$ and $x = k_L z$. The solutions of this equation are called Mathieu functions, have the same periodicity of the lattice and form a complete orthogonal set. The Bloch wavefunctions are linear combinations of Mathieu functions and can be written as:

$$\psi_{n,k}(x) = \mathcal{C}\left(E^{(n)}(k) - \frac{s}{2}, -\frac{s}{4}, x\right) + i\,\mathrm{Sign}(k)\mathcal{S}\left(E^{(n)}(k) - \frac{s}{2}, -\frac{s}{4}, x\right), \tag{1.2}$$

where $\mathcal{C}$ and $\mathcal{S}$ denote the even and odd Mathieu functions respectively and the coordinate x is expressed in lattice spacing units $d_L = \lambda_L/2$. The energy levels in recoil energy units can be expressed in term of the Mathieu characteristic values $\mathcal{A}[k, -s/4]$:

$$E^{(n)}(k) \quad = \quad \mathcal{A}\left[k \pm 2\,\mathrm{Sign}\,(k)\left(\frac{n+1}{2} - 1\right), -\frac{s}{4}\right] + \frac{s}{2}, \tag{1.3}$$

where, in the reduced zone scheme, the $+$ sign refers to odd band index n and the $-$ sign refers to even band index n, whereas $k \in (-1, 1]$ in units of lattice wavenumber k_L. The energy bands for different values of s are plotted in Fig. 1.3 along with the lattice parameter s. Within this formalism, it is possible to define a tunneling energy J associated to the probability of a particle to hop from a site to the nearest-neighboring one. In a tight-binding approximation [9], this quantity is related to the kinetic energy of the particle in a given band of index n and it is proportional to the width of the band itself:

$$J^{(n)} = \frac{|E^{(n)}(1) - E^{(n)}(0)|}{4} \tag{1.3}$$

In the case of a 3D lattice, formed by three orthogonal retro-reflected beams, the hamiltonian is separable and the energy spectrum can be com-

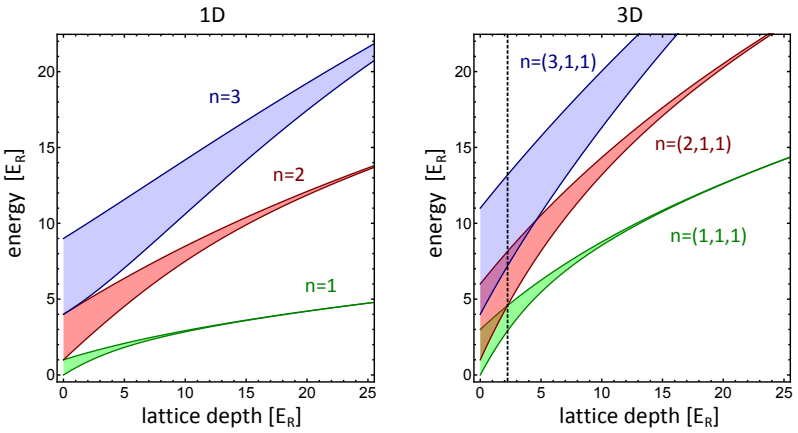

Figure 1.4: Band structure as a function of lattice depth. Shown are the first three energy bands for a 1D lattice (left) and the corresponding first three energy bands along the direction x for a 3D lattice (right). The vertical dashed line in the 3D case denotes a lattice depth of $V_0 \simeq 2.2E_R$, where the band gap opens.

puted simply by adding the energies along each direction:

$$E^{(n_x,n_y,n_z)}(\mathbf{k}) \quad = \quad E^{(n_x)}(k_x) + E^{(n_y)}(k_y) + E^{(n_z)}(k_z). \tag{1.4}$$

If the lattice depth is equal along the three directions, the first excited band is threefold degenerate and consists of the sum of two lowest energy 1D bands and one first-excited 1D band. While in 1D the energy gap between the fundamental and the first excited band opens as soon as $s > 0$, in 3D the band gap only opens for lattice depths larger than $V_0 \simeq 2.2E_R$. This is illustrated in Figure 1.4.

In the experiments we will describe in the following chapters, the atoms are loaded in the lowest band of the optical lattice. An equilibrium state is prepared by adiabatically ramping up the intensity of the lattice beams, using an exponential ramp, to avoid Landau-Zener tunneling processes towards the excited bands. A fundamental observable is the lattice momentum distribution (Fig. 1.5, see Chapter 5), directly related to the population in the various Bloch bands. The lattice beams are switched off adiabatically with respect to the inverse of the band gap, but faster than the external trap period (band mapping, [54, 58]). With this technique we map the lattice momentum onto the atomic velocity distribution, that is directly measured by standard time of flight absorbtion imaging. For example, in Fig. 1.5 we show the quasimomentum distribution of a Fermi gas occupying uniformly the first Brilluoin zone corresponding to the lowest energy Bloch band. The square shape reflects the simple cubic geometry of our 3D optical lattice.

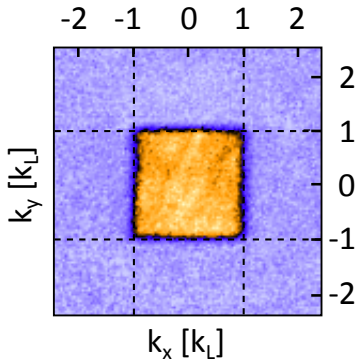

Figure 1.5: False-color time-of-flight image of the lattice momentum distribution of spin-polarized fermions in a 3D optical lattice at $s_x = s_y = s_z = 30$. With $N_{at} = 2 \cdot 10^4$ and $\bar{\omega} \simeq 2\pi \times 50$ Hz, only the lowest band is populated.

1.2.2 Tight-binding approximation

When the lattice depth s increases, the atomic wavefunction becomes more and more localized in a single lattice site so that the description in terms of delocalized Bloch waves is not convenient anymore. It is useful to introduce the Wannier states (see Fig. 1.6) which, in the one-dimensional case, can be written as Fourier transform of Bloch waves [9]:

$$w_n(z - ld_L) = A \int_{-k_L}^{k_L} e^{-i(kld_L + \theta_{n,k})} \psi_{n,k}(z) dk \tag{1.4}$$

in which A is a normalization constant, l is an integer number whereas $\theta_{n,k}$ comes from the fact that the Bloch waves are defined up to a phase factor. Because of this phase factor, the definition of the Wannier functions is not unique, but depends on the particular set $\theta_{n,k}$. The ambiguity can be solved by choosing the phase factors that give rise to the maximally localized Wannier functions [59] which minimize the variance

$$\Delta x^2 = \langle w_n(x)|x^2|w_n(x)\rangle - (\langle w_n(x)|x|w_n(x)\rangle)^2 \tag{1.4}$$

and form a complete set of localized states. Wannier functions referred to different bands and lattice sites respect the orthogonality relation $\langle w_n(x - ld_L)|w_{n'}(x - l'd_L)\rangle = \delta_{n,n'}\delta_{l,l'}$. For a separable potential, the extension to the 3D case is trivial:

$$w_{n_x,n_y,n_z}(x, y, z) = w_{n_x}(x) w_{n_y}(y) w_{n_z}(z) \tag{1.4}$$

which represents localized wavefunctions that collapse onto the harmonic oscillator eigenfunctions when the lattice depth tends to infinity. However, we note that the Wannier functions are not eigenfunctions of the lattice Hamiltonian (1.2.1), since they are linear combinations of Bloch wavefunctions.

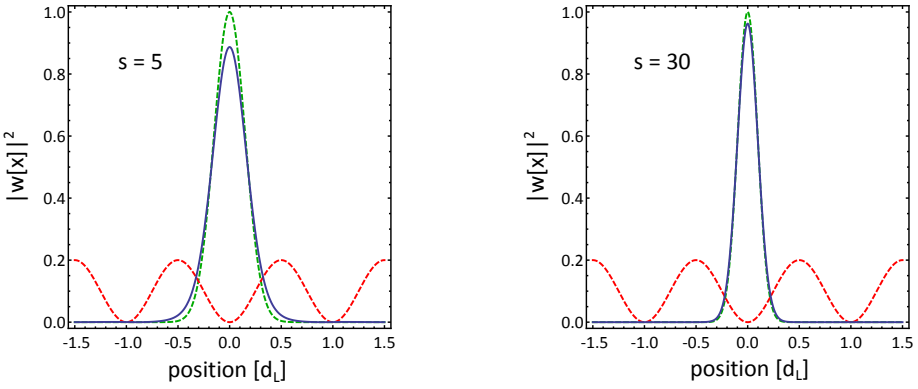

Figure 1.6: Wannier functions. **(a)** $s = 5$. **(b)** $s = 30$. Solid blue lines are the absolute squared values of the Wannier functions while the green dashed lines are the absolute square values of the harmonic oscillator eigenfunctions with $\hbar\omega = 2\sqrt{s}E_R$. The red dashed line represent the lattice potential.

The Wannier functions are very useful in the second-quantization formulation of the lattice Hamiltonian. Indeed, in the tight-binding approximation, it is convenient to expand the fermionic operators in terms of Wannier states:

$$\hat{\psi}_m^\dagger(\mathbf{r}) = \sum_j w(\mathbf{r} - \mathbf{r}_j)\hat{c}_{jm}^\dagger \tag{1.4}$$

where m is a spin index, $\hat{c}_{jm}^\dagger$ is the fermionic operator creating a particle at site $\mathbf{r}_j$ and the single band approximation has been assumed, for which $w_n = w_1 \equiv w(\mathbf{r} - \mathbf{r}_j)$. The Hamiltonian in second-quantization takes the form:

$$\begin{aligned}\hat{H} =& \sum_m \int d\mathbf{r}\, \hat{\psi}_m^\dagger(\mathbf{r}) \left[-\frac{\hbar^2}{2m}\nabla^2 + V_{ext}(\mathbf{r})\right] \hat{\psi}_m(\mathbf{r}) \\ &+ \frac{1}{2}\sum_{m,m'} \int d\mathbf{r} d\mathbf{r}'\, \hat{\psi}_{m'}^\dagger(\mathbf{r}')\hat{\psi}_m^\dagger(\mathbf{r})\mathcal{U}_{int}(\mathbf{r},\mathbf{r}')\hat{\psi}_m(\mathbf{r})\hat{\psi}_{m'}(\mathbf{r}')\end{aligned}$$

in which V_{ext} and $\mathcal{U}_{int}$ are the lattice and interaction potentials respectively. Using the expansion of Eq. (1.2.2), the above Hamiltonian becomes:

$$\hat{H} = -\sum_{i,j} t_{ij}\hat{c}_{im}^\dagger \hat{c}_{jm} + \mathcal{U}_{int} \sum_{j,m<m'} \hat{c}_{jm}^\dagger \hat{c}_{jm'}^\dagger \hat{c}_{jm'}\hat{c}_{jm} \tag{1.3}$$

where t_{ij} describes the hopping from site $\mathbf{r}_j$ to site $\mathbf{r}_i$. Since the Wannier wavefunctions are well localized in each lattice site, we can consider hopping between neighboring sites, $\mathbf{r}_j \to \mathbf{r}_j \pm \mathbf{u} \cdot d_L$ in which $\mathbf{u}$ is a unit vector.

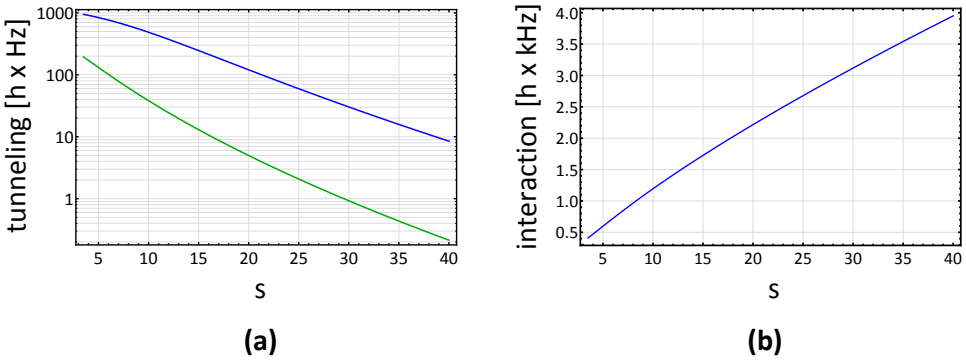

Figure 1.7: Tunneling and interaction energies. **(a)** Tunneling energy between nearest-neighbor sites as a function of the lattice depth. The green line refers to atoms occupying the fundamental lattice band whereas the blue lines refers to atoms occupying the first excited lattice band. **(b)** On-site interaction as a function of the lattice depth, for two ^{173}Yb atoms occupying the fundamental lattice band.

The tunneling energy then becomes:

$$t = \int d\mathbf{r}\, w^*(\mathbf{r}) \left[-\frac{\hbar^2}{2m}\nabla^2 + V_{ext}(\mathbf{r}) \right] w(\mathbf{r} + \mathbf{u} \cdot d_L) \tag{1.3}$$

which is plotted in Fig. 1.7a in case of a one-dimensional optical lattice at various lattice depths. Also, since we are in the ultracold regime, we can assume a two-body contact interaction (see Sec. 1.4) in order to obtain an on-site interaction energy[2] between fermions with different spins:

$$\mathcal{U}_{int} = \frac{4\pi\hbar^2 a}{m} \int d\mathbf{r} |w(\mathbf{r})|^4 \tag{1.3}$$

in which a is the $s-$wave scattering length. In Fig. 1.7b we plot the value of $\mathcal{U}_{int}$ as a function of the lattice depth in the case of two ^{173}Yb atoms interacting with a scattering length $a = 200\, a_0$.

1.2.3 State dependent dipole potentials

Everything we described so far assumes that the frequency of the laser used to generate the optical dipole potential is far-detuned from the ^{173}Yb atomic transitions. In particular, when this condition is satisfied, the light shift experienced by atoms in the ground state is indipendent of the particular spin component m_F (where $F = 5/2$ for ^{173}Yb in the $^1S_0$ state).

[2] This formula is valid for weak interactions, when $a \ll a_{ho}$ where a_{ho} is the harmonic oscillator length associated to a single lattice site. In the opposite limit, a new model must be introduced [60] taking into account the modification of the lattice wavefunctions due to the strong interactions.

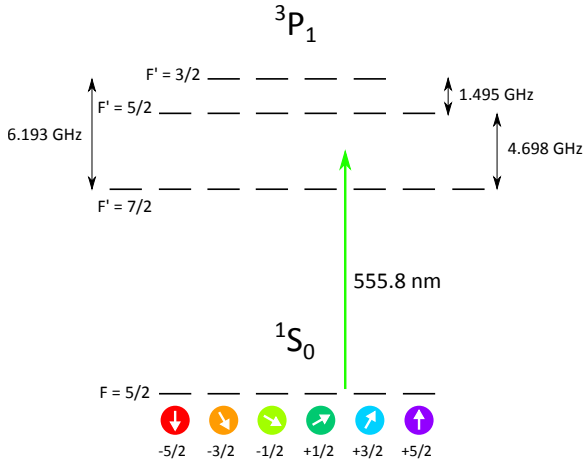

Figure 1.8: Hyperfine structure of the $^1S_0 \rightarrow {}^3P_1$ ^{173}Yb transition.

When instead the laser frequency detuning with respect to a particular transition is comparable or even smaller than the hyperfine splitting ($|\delta_L| \lesssim \Delta_{HFS}$), the proper excited energy level substructure must be considered. Equations (1.2),(1.2) are indeed approximate limits of the complete expressions[3]:

$$U_n(\mathbf{r},\omega,q) = -\sum_{n\neq m} \frac{3\pi c^2}{2\omega_{mn}^3} |\mathcal{C}_{mn}(q)|^2 \left(\frac{\alpha_{JJ'}\Gamma_{mn}}{\omega_{mn}-\omega} + \frac{\alpha_{JJ'}\Gamma_{mn}}{\omega_{mn}+\omega}\right) I(\mathbf{r})$$

$$\Gamma_{sc}^{(n)}(\boldsymbol{r},\omega,q) = \sum_{m\neq n} \frac{3\pi c^2}{2\hbar\omega_{mn}^3} \left(\frac{\omega}{\omega_{mn}}\right)^3 |\mathcal{C}_{mn}(q)|^2 \left(\frac{\alpha_{JJ'}\Gamma_{mn}}{\omega_{mn}-\omega} + \frac{\alpha_{JJ'}\Gamma_{mn}}{\omega_{mn}+\omega}\right)^2 I(\boldsymbol{r})$$

in which the transition strengths, defined as the absolute square of the Clebsch-Gordan coefficients $|\mathcal{C}_{mn}(q)|^2$, the dependence on the light polarization state $q = (1,0,-1)$ in spherical basis, and the multiplicity factor $\alpha_{JJ'} = (2J'+1)/(2J+1)$ appear [61].
The Clebsch-Gordan coefficients related to a particular transition $|n\rangle = |\gamma J F m_F\rangle \rightarrow |m\rangle = |\gamma J' F' m_F + q\rangle$, in which $|n\rangle$ and $|m\rangle$ are two states with well-defined electronic, hyperfine and spin-projection quantum numbers, are given by:

$$\begin{aligned} \mathcal{C}_{mn}(q) &= (-1)^{2F'+J+I+m_F} \\ &\times \sqrt{(2J+1)(2F+1)(2F'+1)} \\ &\times \begin{Bmatrix} J & J' & 1 \\ F' & F & I \end{Bmatrix} \begin{pmatrix} F' & 1 & F \\ (m_F+q) & q & -m_F \end{pmatrix} \end{aligned} \tag{1.3}$$

[3]The term $\Gamma_{mn} = \frac{\omega_{mn}^3}{3\pi\epsilon_0\hbar c^3}\frac{2J+1}{2J'+1}|\langle J||d||J'\rangle|^2$ gives the possibility of calculating the reduced dipole matrix element between two fine-structure states J, J'.

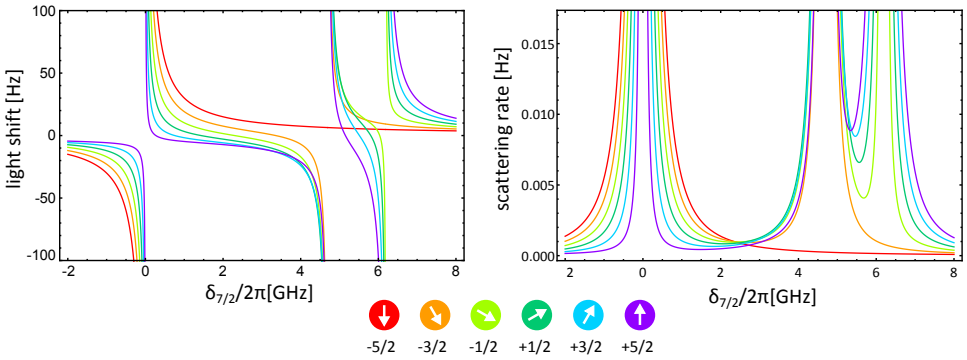

Figure 1.9: State-dependent potential (left) and scattering rate (right) experienced by the $^1S_0$ state in the presence of 556 nm light. The plot is made versus the detuning $\delta_{7/2} = \omega_{7/2} - \omega$ from $F = 5/2 \rightarrow F' = 7/2$ resonance. The peak intensity is $I = 1\,\mathrm{mW/cm^2}$ and the polarization is σ^-.

where the arrays enclosed in curly brackets and round brackets denote respectively the $6j$-symbol and the $3j$-symbol [61]. The dependence of $\mathcal{C}_{mn}(q)$ on m_F and q results in different line strengths characterising each of the transitions within the magnetic substructure of a dipole transition.

In this subsection we consider the specific case of a radiation whose frequency is close to the $^1S_0 \rightarrow {}^3P_1$ transition resonance. In Fig. 1.8 we report the hyperfine structure of the $^3P_1$ energy level which splits into three sublevels with total angular momentum $F' = 3/2, 5/2, 7/2$. Assuming no external magnetic field, we can calculate the light shift and the scattering rate experienced by each spin component m_F in the $^1S_0$ state, when exposed to 556 nm radiation. In Figure 1.9 we plot the calculated light shift and scattering rate as a function of the detuning from the $F = 5/2 \rightarrow F' = 7/2$ cycling transition. We used σ^- polarized light ($q = -1$) and an intensity $I = 1\,\mathrm{mW/cm^2}$. We can see that, by approaching $\delta_{7/2} = \omega_{7/2} - \omega = 0$ from the left, the dependence of the light shift on the particular spin state increases, in particular it is higher for the $m_F = -5/2$ state which experiences the strongest Clebsch-Gordan coefficient. In Section 2.5.2 we will describe how to use this radiation in order to implement an "optical Stern-Gerlach" detection technique.

1.3 Raman transitions

The simplest system in which a Raman transition may be driven is the three-level Λ-configuration system, illustrated in Fig. 1.10. Two long-lived ground states are coupled via a radiative upper state which, because the single photon detuning is sufficiently large, is never significantly populated [62]. We call $|e\rangle$ the excited state and $|g_1\rangle$, $|g_2\rangle$ the two ground states, corresponding to the atomic resonance frequencies ω_{01} and ω_{02} respec-

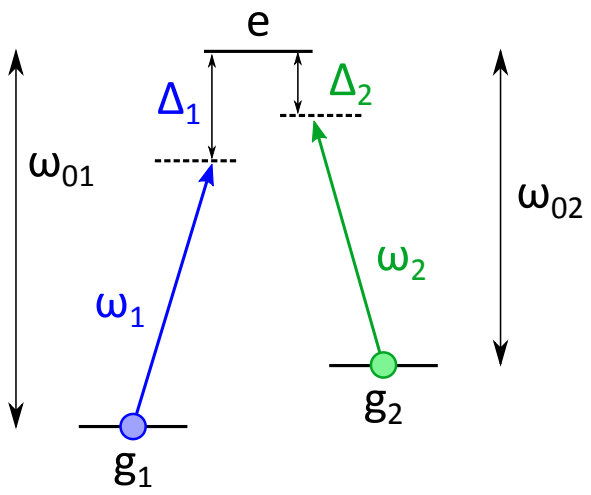

Figure 1.10: Three-level $\Lambda-$configuration scheme. $|g_1\rangle$ and $|g_2\rangle$ are coupled resonantly via a two-photon process.

tively [61]. Considering a total electric field:

$$\mathbf{E}(\mathbf{r},t) = \boldsymbol{\varepsilon}_1 E_{01}\cos(\mathbf{k}_1\cdot\mathbf{r}-\omega_1 t) + \boldsymbol{\varepsilon}_2 E_{02}\cos(\mathbf{k}_2\cdot\mathbf{r}-\omega_2 t), \tag{1.2}$$

we can write the free atomic Hamiltonian into the rotating frame of the laser field as:

$$\hat{H}_A = \frac{\hat{p}^2}{2m} + \Delta_1|g_1\rangle\langle g_1| + \Delta_2|g_2\rangle\langle g_2|, \tag{1.2}$$

where $\Delta_1 = \omega_1 - \omega_{01}$ and $\Delta_2 = \omega_2 - \omega_{02}$ are the detunings with respect to the corresponding transitions. Considering Eq. (1.3), we can write the Hamiltonian of the three-level atom interacting with the electric field in rotating-wave approximation (RWA) [61] as:

$$\hat{H}_I = \frac{\hbar}{2}\left[\Omega_1 e^{i\mathbf{k_1}\cdot\mathbf{r}}\hat{\sigma}_1^\dagger + \Omega_1^* e^{-i\mathbf{k_1}\cdot\mathbf{r}}\hat{\sigma}_1\right] + \frac{\hbar}{2}\left[\Omega_2 e^{i\mathbf{k_2}\cdot\mathbf{r}}\hat{\sigma}_2^\dagger + \Omega_2^* e^{-i\mathbf{k_2}\cdot\mathbf{r}}\hat{\sigma}_2\right], \tag{1.2}$$

where $\hat{\sigma}_i = |g_i\rangle\langle e|$ is a lowering operator and $\hbar\Omega_i = -\langle e|\mathbf{d}|g_i\rangle\cdot\mathbf{E}_{0i}(\mathbf{r})$ is the single-photon Rabi frequency. Choosing the ansatz $|\Psi\rangle = \psi_{g_1}|g_1\rangle + \psi_{g_2}|g_2\rangle + \psi_e|e\rangle$, we can impose $\partial\psi_e/\partial t = 0$ if the detunings Δ_1, Δ_2 are sufficiently large (adiabatic approximation), obtaining:

$$\psi_e(t) = \frac{\Omega_1}{2\Delta}\psi_{g_1}(t) + \frac{\Omega_2}{2\Delta}\psi_{g_2}(t), \tag{1.2}$$

where we defined $\Delta = (\Delta_1+\Delta_2)/2$ assuming $|\Delta_1 - \Delta_2| \ll \Delta$, namely that the two frequency detunings are nearly equal, and we supposed $p^2/2m \ll \hbar|\Delta|$. Plugging Eq. (1.3) in the Schrödinger equation $(H_A + H_I)|\Psi\rangle = i\hbar\frac{\partial|\Psi\rangle}{\partial t}$ leads to a two-level effective Hamiltonian with coherent couplings

between the ground states:

$$\hat{H}_R = \begin{pmatrix} \dfrac{\hat{p}^2}{2m} + U_1 & \dfrac{\hbar\Omega_R}{2} e^{i\mathbf{q}_R\cdot\mathbf{r}} \\ \dfrac{\hbar\Omega_R^*}{2} e^{-i\mathbf{q}_R\cdot\mathbf{r}} & \dfrac{\hat{p}^2}{2m} + U_2 - \delta_R \end{pmatrix}, \tag{1.2}$$

where $\mathbf{q}_R = 2\mathbf{k}_R \equiv \mathbf{k}_1 - \mathbf{k}_2$ is the momentum acquired by the atom that undergoes a "spin-flip" process from $|g_1\rangle$ to $|g_2\rangle$, $\delta_R = \Delta_1 - \Delta_2 = (\omega_1 - \omega_2) - (\omega_{01} - \omega_{02})$ is the detuning with respect to the two-photon resonance and

$$\Omega_R = \frac{\Omega_1\Omega_2^*}{2\Delta}, \qquad U_\alpha = \frac{|\Omega_\alpha|^2}{4\Delta}, \tag{1.2}$$

are respectively the effective two photon Rabi frequency and the light shift on $|g_\alpha\rangle$ with $\alpha = 1, 2$. Assuming Ω_R real and choosing a reference frame such that $\mathbf{k}_R \cdot \mathbf{r} = k_R x$, it is particularly useful to express the Raman Hamiltonian in terms of Pauli matrices:

$$\hat{H}_R = \frac{\hat{p}^2}{2m}\hat{\mathbb{1}} + \frac{\hbar\Omega_R}{2}\left[\hat{\sigma}_x \cos(2k_R x) - \hat{\sigma}_y \sin(2k_R x)\right] + \frac{\delta'}{2}\hat{\sigma}_z \tag{1.2}$$

where we inserted the differential light shift in $\delta' = \delta_R - (U_2 - U_1)$. it is worth noting that by applying the gauge transformation $\hat{U} = e^{ik_R\hat{x}\hat{\sigma}_z}$ we obtain:

$$\hat{H}'_R = \hat{U}\hat{H}_R\hat{U}^\dagger = \begin{pmatrix} \dfrac{(p - \hbar k_R)^2}{2m} + \dfrac{\delta'}{2} & \dfrac{\hbar\Omega_R}{2} \\ \dfrac{\hbar\Omega_R^*}{2} & \dfrac{(p + \hbar k_R)^2}{2m} - \dfrac{\delta'}{2} \end{pmatrix} \tag{1.2}$$

which can be rewritten in terms of the Pauli matrices as:

$$\hat{H}_R = \frac{(p\hat{\mathbb{1}} - \hbar k_R\hat{\sigma}_z)^2}{2m} + \frac{\delta'}{2}\hat{\sigma}_z + \frac{\Omega_R}{2}\hat{\sigma}_x. \tag{1.2}$$

This simple Hamiltonian features a uniform time-constant vector potential [63] along one direction $q\hat{A} = \hbar k_R\hat{\sigma}_z$ and provides the same non-trivial dispersion relation of a particle subjected to equal Rashba-Dresselhaus spin-orbit coupling and an external magnetic field [64, 65]. Recently, it has been implemented for both Bose-Einstein condensates [16] and degenerate Fermi gases [17, 66]. This simple scheme, with the addition of an external magnetic field gradient, led to the generation of an artificial magnetic field for neutral atoms [11], which is the main topic of this PhD thesis.

1.4 Interactions in ultracold quantum gases

Due to the low-density character of ultracold atoms samples, most of the scattering properties are related to two-body collisions [67–69]. The interatomic interaction is described by a central potential $V(r)$, which at large

distances takes the typical attractive form $-C_6/r^6$ and at short distances, on the order of a few Bohr radii a_0, can be treated as an hard-core repulsive potential. This is only an approximation because the exact inclusion of the interatomic potential in the description of the gas would be extremely difficult. However, the samples we are dealing with are ultracold and ultradilute, which implies that both the de Broglie wavelength λ_{dB} and the interparticle separation $n^{-1/3} \sim 5000 - 10000\, a_0$ are much larger than the range of the interatomic potential r_0, which is of the order of the van der Waals length $r_0 \sim (2\mu C_6/\hbar^2)^{1/4} \sim 150\, a_0$ for ^{173}Yb. As a result, scattering processes never explore the fine details of the short-range scattering potential and the entire collision process can be described by a single quantity, the *scattering length* a.

We start from the Schrödinger equation for two colliding atoms, written in the center of mass frame. The relative wavefunction satisfies:

$$(\nabla^2 + k^2)\Psi_k(\mathbf{r}) = v(r)\Psi_k(\mathbf{r}) \text{ with } k^2 = \frac{2\mu E}{\hbar^2} \text{ and } v(r) = \frac{2\mu \mathcal{V}(r)}{\hbar^2} \quad (1.2)$$

where $\mu = m/2$ is the reduced mass. At large distance from the scattering potential, the relative wavefunction is given by the sum of an incoming plane wave plus an outgoing scattered wave:

$$\Psi_k(\mathbf{r}) \sim e^{i\mathbf{k}\cdot\mathbf{r}} + f(\mathbf{k},\mathbf{k}')\frac{e^{ikr}}{r} \quad \text{for } r \to \infty \quad (1.2)$$

where $f(\mathbf{k},\mathbf{k}')$ is the scattering amplitude for scattering an incident plane wave with wave vector $\mathbf{k}$ into the direction $\mathbf{k}'$. Since we are considering elastic collisions, $|\mathbf{k}| = |\mathbf{k}'|$.

The potential we are dealing with has spherical symmetry so we can expand the scattered wavefunction into partial waves with angular momentum l [69]. In the limit of ultracold collisions, it is sufficient to consider the scattering processes at low momenta $k \ll 1/r_0$ and, in the absence of resonance phenomena (e.g. shape resonances [68] or a Feshbach Resonance [5]) for $l \neq 0$, s-wave scattering $l = 0$ dominates over all other partial waves (in case Pauli principle allows it):

$$f \simeq f_0 = \frac{1}{2ik}(e^{2i\delta_0} - 1) = \frac{1}{k\cot\delta_0 - ik} \quad (1.2)$$

where f_0 and δ_0 are the s-wave scattering amplitude and phase shift respectively. For low momenta, we may expand $k\cot\delta_0$ to order k^2:

$$k\cot\delta_0 \simeq -\frac{1}{a} + r_{\text{eff}}\frac{k^2}{2} \quad (1.2)$$

which defines the scattering length

$$-\lim_{k\to 0}\frac{\tan\delta_0}{k} = a, \quad (1.2)$$

and the effective range r_{eff} of the scattering potential, which, for van der Waals potentials, is of the order of r_0 [70]. We can thus rewrite the scattering amplitude f as [71]:

$$f(k) = \frac{1}{-\frac{1}{a} + r_{\text{eff}}\frac{k^2}{2} - ik}. \tag{1.2}$$

In the limit $k|a| \ll 1$ and $r_{\text{eff}} \lesssim 1/k$, f becomes momentum-independent and equals $-a$. For $k|a| \gg 1$ and $r_{\text{eff}} \ll 1/k$, the scattering amplitude is $f = i/k$ and the cross section for atom-atom collisions is $\sigma = 4\pi/k^2$. This is the so-called unitarity limit in which the details of the scattering process become completely irrelevant and the only length scale of importance is the interparticle distance $n^{-1/3}$.

At really low temperature the de Broglie wavelength of the colliding particles is much larger than the finite range r_0 of the potential and it is possible to introduce a much simpler description of the scattering event based upon the concept of a "pseudo-potential" [72]. The idea is to introduce an easy-to-treat artificial potential that still reproduces the correct s-wave scattering. It can be demonstrated that the right form for the pseudo-potential, in the limit $kr_{\text{eff}} \ll 1$ is:

$$\hat{\mathcal{V}}(\mathbf{r}) = g\,\delta(\mathbf{r})\frac{\partial}{\partial r}(r\cdot), \tag{1.2}$$

with the coupling constant $g = 4\pi\hbar^2 a/m$.

1.4.1 $SU(N)$-symmetric interactions

The importance of $SU(N)$ symmetry in fermionic system goes beyond the research on ultracold gases. For instance, in particle physics the theory of quantum chromodynamics (QCD) contains two kinds of $SU(3)$ groups [73]. In the field of nuclear physics, the $SU(6)$ group has also been considered as a candidate to unify the description of baryons and mesons into a single group [74]. The $SU(N)$ symmetry can also have remarkable consequences in condensed-matter physics, in particular in the context of quantum magnetism [34, 75].

In order to understand how the $SU(N)$ symmetry emerges at ultracold temperatures we have to generalize the pseudo-potential (1.4) to spin-F fermions where $\mathbf{F} = \mathbf{J} + \mathbf{I}$ is the sum of the electronic and nuclear total angular momenta which, in the case of ^{173}Yb in the $^1S_0$ state, equals to $F = 5/2$. The generalized form must be [76]:

$$\hat{\mathcal{V}}(\mathbf{r}) = \sum_{\text{even } F_{tot}=0}^{2F-1} \frac{4\pi\hbar^2 a_{F_{tot}}}{m}\delta(\mathbf{r})\frac{\partial}{\partial r}[r\cdot]\,\hat{\mathcal{P}}_{F_{tot}} \tag{1.2}$$

where $\hat{\mathcal{P}}_{F_{tot}}$ is the projector onto two-particle states with total spin equal to $F_{tot} = 0, 2, .., 2F-1$. Due to the symmetry of the relative wavefunction under the exchange of two fermionic particles, only the even F_{tot} values are possible in s-wave collisions. Hence it follows that $\lfloor F-1 \rfloor$ scattering lengths are needed to describe the interaction between spin-F fermions. Roughly speaking, the dependence of the s-wave scattering lengths $a_0, ..., a_{2F-1}$ on the total angular momentum F_{tot} comes from the possible arrangements the electronic shells of the colliding atoms can assume. Since in the case of ytterbium and of the other Alkaline-Earth and Alkaline-Earth-like atoms, the total electronic angular momentum is zero in the ground state, the influence of nuclear spins on the scattering process reduces simply to the Pauli exclusion principle, and all the scattering lengths $a_{F_{tot}}$ are equal. As a consequence, the interaction Hamiltonian will be invariant under transformations belonging to the $SU(N = 2F+1)$ group [73]. This means that the spin projection m_F of each fermion is individually conserved preventing any possible spin-relaxation mechanism. A remarkable experimental consequence is that all the prepared spin mixtures are stable against collisions. This will be important in Chapter 6 where a multi-component one-dimensional liquid of fermions is described.

2 | The Ytterbium Machine

This chapter illustrates the experimental apparatus and the procedures adopted to trap and cool atomic ytterbium down to quantum degeneracy. We will then focus on the optical techniques used to manipulate the nuclear spin components, giving the emphasis to the optical Stern Gerlach detection scheme and to the optical pumping procedures.

In section 2.1 we outline the principal chemical and physical properties of atomic ytterbium, in particular the electronic level structure with the experimentally relevant optical transitions and the scattering properties in the ultracold regime. In section 2.2.1 we describe the essential features of the vacuum apparatus, evidencing peculiarities such as the in-vacuum Fabry-Perot cavity and the high-optical-access glass cell. In section 2.3, the different laser setups will be briefly described, with reference to their role in the experimental procedure. Section 2.4 is devoted to the description of the overall experimental steps which lead to the realization of a degenerate Fermi gas. Finally, in section 2.5, we outline the nuclear spin detection and manipulation techniques used to initialize the atomic spin distribution.

2.1 Ytterbium: fundamental properties

Ytterbium is a rare earth metal, strongly diamagnetic and whose electronic configuration in its fundamental state is [Xe]$4f^{14}s^2$. Its atomic mass is 173.04 u. The melting and boiling points are 824 °C and 1196 °C respectively. Due to the high atomic number $Z = 70$ it possesses many stable isotopes [77], both bosonic and fermionic, as it is illustrated in Table 2.1.

Due to the presence of two electrons in the valence shell, the ytterbium electronic level structure reproduces the typical structure of alkaline-earth elements, which in turn partially resembles the one of Helium. This structure can be divided in terms of the total electronic spin, which can assume two values: $S = 0$ singlet states, or $S = 1$ triplet states. In Figure 2.1 we report the energy level scheme, with the optical transitions used in the experiment. The transition $6s^2\,{}^1S_0 \rightarrow 6s6p\,{}^1P_1$ is dipole allowed, has a linewidth of $\Gamma = 2\pi \cdot 29.1$ MHz corresponding to a lifetime of about 5.5 ns and a saturation intensity of $I_s = 60\,\mathrm{mW/cm^2}$ [78]. It is used in

Table 2.1: Ytterbium isotopes properties

Isotope	Relative abundance (%)	Nuclear spin	Statistics
^{168}Yb	0.13	0	bosonic
^{170}Yb	3.05	0	bosonic
^{171}Yb	14.3	1/2	fermionic
^{172}Yb	21.9	0	bosonic
^{173}Yb	16.12	5/2	fermionic
^{174}Yb	31.8	0	bosonic
^{176}Yb	12.7	0	bosonic

the Zeeman Slower cooling stage (see next Sections) and in the imaging stage. The transitions towards the triplet states $^3P_0$, $^3P_1$, $^3P_2$ are called intercombination transitions because they connect states with different spin multiplicity ($\Delta S \neq 0$) and they are forbidden in the pure $LS-$coupling picture. However, a significant mixing between the $^1P_1$ and the $^3P_1$ states is caused by the spin-orbit interaction, which is a direct manifestation of the high atomic number Z of ytterbium. The transition $6s^2\,^1S_0 \rightarrow 6s6p\,^3P_1$ has a linewidth $\Gamma = 2\pi \cdot 182.4$ kHz, corresponding to a lifetime of 850 ns and a saturation intensity of $I_s = 0.14\,\mathrm{mW/cm^2}$ [78]. It is perhaps the most important transition in the context of this thesis, since it is exploited for the MOT cooling stage, for the spin manipulation and detection schemes and for the engineering of the Raman coupling between the spin components. The transition $6s^2\,^1S_0 \rightarrow 6s6p\,^3P_0$ would be stricly forbidden ($J = 0 \rightarrow J' = 0$), but the hyperfine interaction for the fermionic isotopes between the ^3P states, originating from the non-zero nuclear magnetic moment, indirectly enables a decay from the $^3P_0$ to the ground state. This transition connects the ground state to the metastable state $^3P_0$ and has a calculated linewidth of about $\Gamma \simeq 2\pi \cdot 10$ mHz [79, 80], corresponding to a lifetime of 20 s. In order to address this transition, an ultra-narrow laser has been built [49, 81].

The $s-$wave scattering processes between ground state atoms have been deeply characterized in [82]. Thanks to two-colour photoassociation spectroscopy on the $^1S_0 \rightarrow {}^3P_1$ transition, the scattering lengths for all isotope combinations have been precisely determined. The measured $s-$wave scattering lengths are summarized in Table 2.2, in which the large variety of abundant isotopes and available interaction strengths highlights how ytterbium is particularly suitable also in the context of many-body physics with ultracold mixtures [83, 84].

In the next sections we will illustrate the experimental apparatus and the procedures adopted to trap and cool atomic ytterbium down to quan-

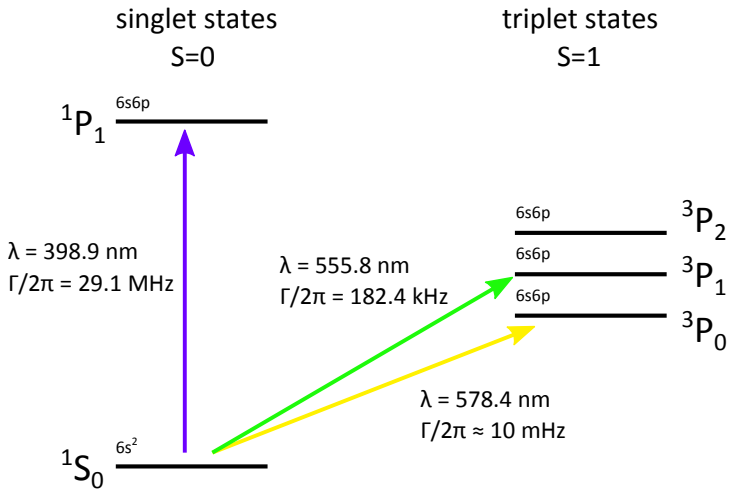

Figure 2.1: Yb energy level scheme with the relevant optical transitions.

tum degeneracy and to optically manipulate and detect the nuclear spin components.

Table 2.2: Ytterbium scattering lengths in a_0 units [82]

	^{168}Yb	^{170}Yb	^{171}Yb	^{172}Yb	^{173}Yb	^{174}Yb	^{176}Yb
^{168}Yb	**252**	117	89	65	39	2	-359
^{170}Yb		**64**	36	-2	-81	-518	209
^{171}Yb			**-3**	-84	-578	429	142
^{172}Yb				**-600**	418	200	106
^{173}Yb					**200**	139	80
^{174}Yb						**105**	54
^{176}Yb							**-24**

2.2 Experimental Setup

The experimental apparatus has been extensively described in [45, 85, 86]. With respect to the previous references, some modifications have been introduced, especially in the locking scheme for the green transition. Here we will briefly recap the main components of the system.

2.2.1 Vacuum system

The vacuum apparatus is shown in Fig. 2.2. A sample of Ytterbium chunks in natural isotopes composition is heated up in an oven at a mean temperature of 525°C (**1**). Its vapor pressure (about 10^{-2} Torr) generates an atomic beam which is collimated thanks to a square array of 100 small tubes, 1 cm long and with internal diameter of 0.2 mm. In this region, an ion pump 20 l/s Varian Starcell is present (**3**) which executes a first pumping stage. After this, a second ion pump 20 l/s Varian Starcell (**3**) performs a second pumping stage which contributes to the efficiency of differential pumping between the oven and the MOT region. The atoms pass through two small tubes (**6**) with lengths 8 and 10 cm, respectively, and with internal diameter 5 mm, placed before and after the second ion pump. Here a compressed-air shutter (**4**) to block the atomic beam and a VAT-48124 UHV gate valve (**7**) are present. This valve is necessary to separate the UHV region (10^{-11} Torr), implemented by the 55 l/s Varian Starcell (**14**), from the oven region ($10^{-7} - 10^{-10}$ Torr). The atoms then travel along the Zeeman Slower (**8**) where they are slowed down from thermal velocity ($\sim$ 340 m/s) to a few tens of m/s (see section 2.4.1) in order to be captured in a magneto-optical trap (MOT, see section 2.4.2). The compensation coil (**10**) extinguishes the residual magnetic field of the Zeeman slower in the MOT chamber.

The MOT is implemented with two, water-cooled, anti-Helmoltz coils (**12**) (for details see Ref. [86]) mounted on a AISI L316 stainless steel octagonal chamber (**9**). The chamber features seven CF40 flanges on the horizontal plane: one is used to attach the MOT chamber to the Zeeman slower; the four flanges at 45° degrees with respect to the atomic beam axis are used for the horizontal MOT beams; the two flanges orthogonal to the atomic beam axis are used respectively as input window for the optical transport beam and to connect to the glass cell (**11**). Finally, there is a CF63 flange on the atomic beam axis towards the cross connecting to the 55 l/s Varian Starcell ion pump (**14**). Moreover, the MOT chamber has two CF100 flanges on the vertical direction, both with a CF40 window in the center. The upper CF100 flange has two metallic supports to implement an in-vacuum optical cavity (see section 2.2.2) along the axis of two of the four CF16 windows in the horizontal plane of the MOT chamber (see Fig. 2.10). To further improve the vacuum a titanium sublimation pump (TSP) (**13**) is present too. The pressure is measured with an Ion Gauge UHV-24P Bayard-Alpert (**15**). The input window (**17**) of the Zeeman slower beam (**18**) is made of sapphire and it is kept at a temperature of about 250 °C to avoid atom deposition which could lower the transmissivity.

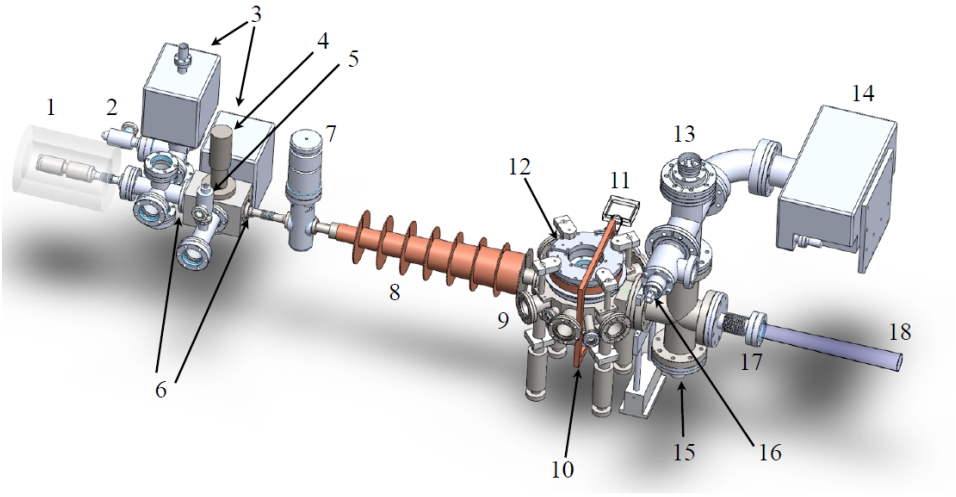

Figure 2.2: 1) Oven. 2) UHV valve. 3) Ion pumps for differential pumping (20 l/s each). 4) Compressed air shutter for atomic beam. 5) UHV valve. 6) Differential pumping tubes (not shown). 7) VAT UHV gate-valve. 8) Zeeman Slower. 9) MOT chamber. 10) Compensation coil. 11) Glass cell. 12) MOT coils. 13) Titanium sublimation pump (TSP). 14) Ion pump for MOT chamber (55 l/s). 15) UHV Gauge, mod. Bayard-Alpert, Varian UHV-24p. 16) UHV Valve. 17) Sapphire window with bellow. 18) Slowing beam at 399 nm.

2.2.2 In-vacuum optical cavity

Inside the MOT chamber we mounted an in-vacuum optical cavity [87] to trap and pre-cool the atoms before being transported in the glass cell (see section 2.2.3). The Fabry-Perot cavity is held by two metallic supports screwed down in the CF100 upper flange of the MOT. The supports hold two spherical mirrors with a radius of curvature $r_c = 2$ m, diameter $d = 6.35$ mm and thickness 2.3 mm. The outer side of the mirrors is AR coated while the inner side has a reflectivity $R = 99.8\%$, which results in a theoretical finesse of $\mathcal{F} \simeq 1570$. The fixed cavity length is $L = 9$ cm, leading to a free spectral range FSR= 1.67 GHz. The geometry chosen for the cavity results in a $w_0 = 300$ μm waist which, along with a measured finesse of $\mathcal{F} \simeq 1850$, leads to a trap depth of $V_0/k_B \simeq 800$ μK $\gtrsim 10\, T_{\mathrm{MOT}}$ with an incident power of $P_{\mathrm{in}} = 1.8$ W.

2.2.3 The glass cell

Another crucial feature of this experimental apparatus is the presence of a high-optical-access glass cell where the atoms are transported for a distance of 26 cm by means of an optical translation stage (see section 2.4.4). Our glass cell is manufactured by HELMA ANALYTICS. The external dimensions are $(60 \times 60 \times 18)$ mm (see Fig. 2.3). Each face is 5 mm thick

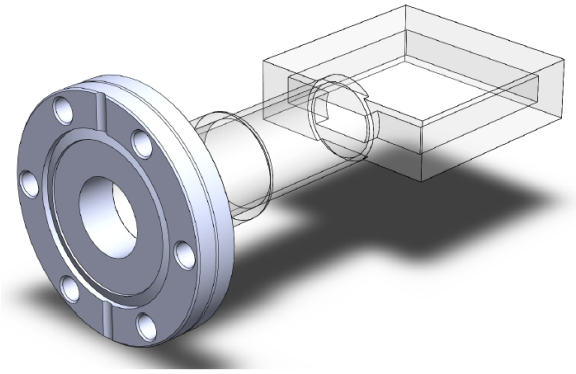

Figure 2.3: 3D model of the glass cell.

leading to internal dimensions of $(50 \times 50 \times 8)$ mm. The reduced thickness in the vertical direction (9 mm between the center and the outer face) comes from the future implementation of a high-numerical-aperture objective with a small working distance [88–91]. The glass cell features a glass-metal junction which leads to a CF40 flange that is attached to the MOT chamber.

2.3 Laser setup

All the relevant atomic transitions of Ytterbium are in the visible range (578 nm, 556 nm, 399 nm). Unfortunately, high-power, narrow-linewidth lasers directly emitting at these wavelengths are not commercially available, and a convenient way to produce such radiations is to use second harmonic generation (SHG) starting from commercial infrared high-power lasers (except for the 578 nm radiation for which a 1156 nm low-power quantum dot is used, [81]). The scheme adopted in our lab is to use bow-tie cavities to enhance the efficiency of the frequency-doubling process. In this section, we first outline the laser systems necessary to address resonantly atomic Ytterbium transitions at 399 nm and 556 nm[1]. Then we describe the implemented laser setups which generate the far-off resonant dipole traps at 1064 nm and the optical lattices at 759 nm.

2.3.1 Laser systems at 399 nm and 556 nm

Laser radiation at 399 nm is used both to slow down the atomic beam in the Zeeman slower and to perform absorption imaging (see [45, 85, 86])

[1]The laser system at 578 nm will be extensively described in the PhD thesis of my colleague, G. Cappellini [49, 81].

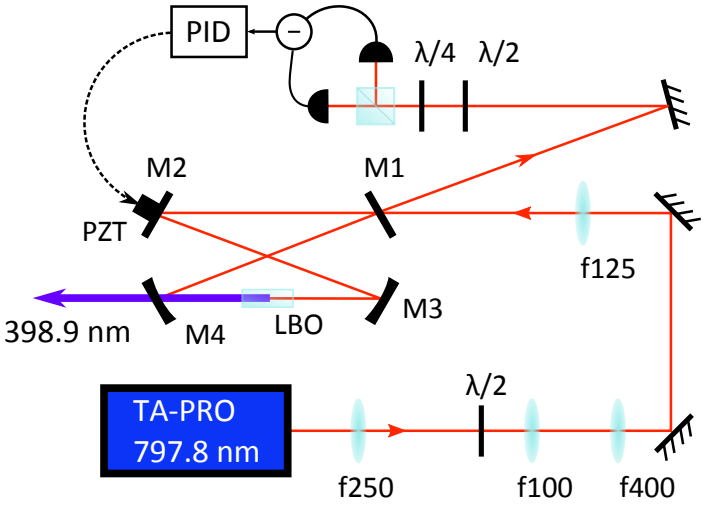

Figure 2.4: Laser setup for SHG from 798 nm to 399 nm. The input coupler (M1) reflectivity is $r_1 = 99\,\%$ at 798 nm. The other mirrors (M1, M2, M3) have 99.9 % reflectivity at 798 nm. The beam waist at the center of the crystal is $w_0 = 30\ \mu$m. Attached to M2, a piezo stack (PZT) changes the cavity length according to the Hansch-Couillaud error signal (PID).

addressing the ${}^1S_0 \rightarrow {}^1P_1$ Yb strongest transition. A fiber-coupled tapered-amplifier laser-diode system TOPTICA TA PRO delivers 1.1 W of 798 nm radiation, which is used to inject a Lithium-Triborate (LBO) non-linear crystal, 15 mm long, cut for type-I phase matching and stabilized at a temperature of 55 °C (see Fig. 2.4). The LBO is placed in a bow-tie cavity where the second-harmonic generation takes place. The cavity is formed by two plane mirrors M1 and M2 and two curved mirrors M3 and M4 with radii of curvature $r_c = 60$ mm and $r_c = 100$ mm respectively. The cavity has a free spectral range (FSR) FSR $= 749$ MHz and a finesse $\mathcal{F} \sim 100$. The cavity length is locked to resonance by means of the Hansch-Couillaud technique [92], acting on a piezoelectric stack (PZT) mounted behind one of the cavity mirrors (M2). We obtain a stable output of 550 mW of 399 nm radiation out of 1 W of 798 nm pumping light with a conversion efficiency of about 50 %.

The green light for the ${}^1S_0 \rightarrow {}^3P_1$ transition at 556 nm is generated exploiting the same techniques described above. This radiation is perhaps the most important one since it is used for many purposes: from magneto-optical trapping (section 2.4.2), to optical Stern-Gerlach and optical pumping schemes (section 2.5) and, last but not least, to Raman coupling of the different spin components (Chapter 3). In this case a fiber laser at 1112 nm (Menlo Systems mod. ORANGE ONE) pumps a bow-tie cavity in which the non-linear medium is a 10 mm long Lithium Tantalate ($LiTaO_3$) crystal. The crystal is periodically poled with a period of 9.12 μm to ensure

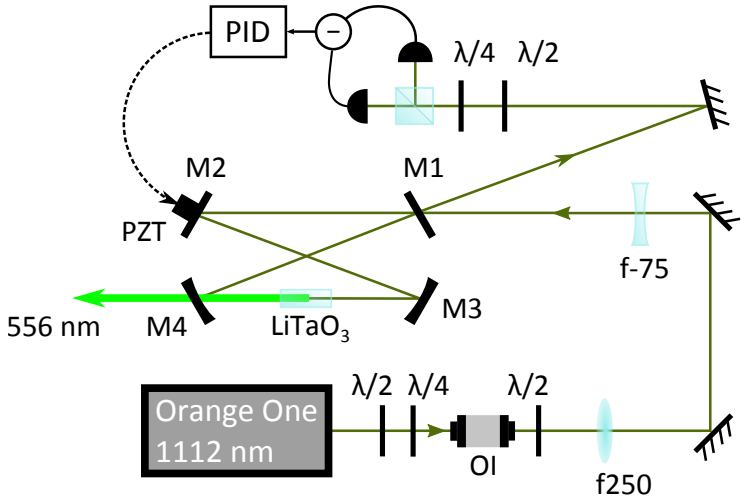

Figure 2.5: Laser setup for SHG from 1112 nm to 556 nm. At the infrared output an optical isolator (OI) is placed. The input coupler (M1) reflectivity is $r_1 = 95\,\%$ at 1112 nm. The other mirrors (M1, M2, M3) have 99.9 % reflectivity at 1112 nm. The radius of curvature of both spherical mirrors is $r_c = 100$ mm. The beam waist at the center of the crystal is $w_0 = 13$ μm. Attached to M2, a piezo stack (PZT) changes the cavity length according to the Hansch-Couillaud error signal (PID).

quasi phase-matching and is AR-coated for 1112 nm light. The cavity FSR is FSR $= 567$ MHz and the measured finesse is $\mathcal{F} = 67$. When locked using the Hansch-Couillaud method, the cavity produces 1.050 W of 556 nm light out of 2 W of 1112 nm infrared light. Both cavities are sealed inside aluminum boxes under vacuum in order to guarantee thermal and acoustic isolation and achieve a better lock stability.

2.3.2 Locking scheme on the intercombination transition

In order to lock the laser frequencies on the atomic transitions we use standard fluorescence spectroscopy techniques and electronic feedback on the lasers. Both spectroscopy setups rely on an independent atomic beam generated in an additional oven with the same characteristics as the one in the main setup (Fig. 2.2) at average temperature $T = 535$ °C. The atoms are interrogated with transverse spectroscopy in two crosses after the oven.

In the case of the strongest transition ${}^1S_0 \rightarrow {}^1P_1$ at 399 nm, it is sufficient to perform transverse spectroscopy since the linewidth $\Gamma = 2\pi \times 29$ MHz is larger than the transverse Doppler profile of the collimated atomic beam. On the other hand, the intercombination transition ${}^1S_0 \rightarrow {}^3P_1$ at 556 nm has a much narrower linewidth, ($\Gamma = 2\pi \times 182$ kHz) and Doppler-free saturation spectroscopy is needed. For further details on both spectroscopy setups and on the locking procedures we refer to Refs.

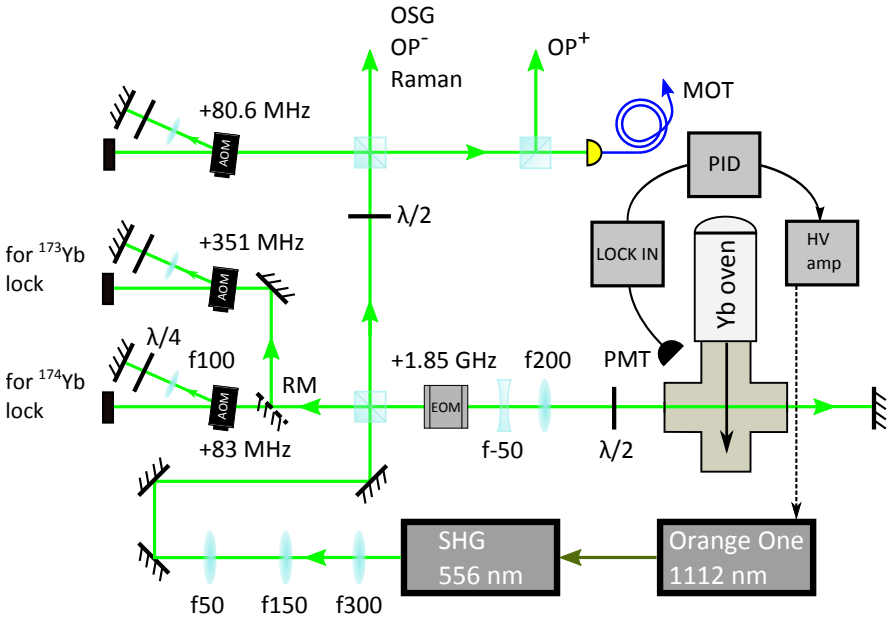

Figure 2.6: 556 nm optical setup for the production of MOT beams and locking on ${}^1S_0 \rightarrow {}^3P_1$ transition. RM is a removable mirror used to switch between the ^{173}Yb and the ^{174}Yb locking schemes. The fluorescence signal, detected by a photomultiplier (PMT), is sent to a Lock-In amplifier. The demodulated signal is processed by a PID, amplified again by a high voltage amplifier (HV) and sent to the laser piezo.

[85, 86].

With respect to [85], a few changes have been made in the green locking scheme for the fermionic isotope ^{173}Yb [45]. In particular, also in this case, the Doppler-free signal comes from the bosonic ^{174}Yb, which is the most abundant isotope. Indeed when the experiments are performed with ^{174}Yb, the high signal-to-noise ratio (SNR) allows a stable lock due to the absence of hyperfine structure ($I = 0$). We use π-polarized light which selects only the magnetic field insensitive $|J = 0, m_J = 0\rangle \rightarrow |J' = 1, m'_J = 0\rangle$ transition. After the double-passage in an acousto-optical modulator (AOM), the effective laser frequency is red-detuned by -166 MHz with respect to the ^{174}Yb atomic resonance (see Fig. 2.6). In the case of the closed $F = 5/2 \rightarrow F' = 7/2$ transition of ^{173}Yb, atomic fluorescence has a worse SNR because, in addition to a smaller natural abundance, the $I = 5/2$ nuclear spin gives rise to six π-transitions, which further reduces the spectroscopy signal. Moreover all six Doppler-free signals are sensitive to magnetic field fluctuations.

To overcome these difficulties, an alternative optical setup has been designed in which the locking signal comes from the bosonic ^{174}Yb isotope also when operating with fermionic ^{173}Yb. In this scheme (see Fig. 2.6), the

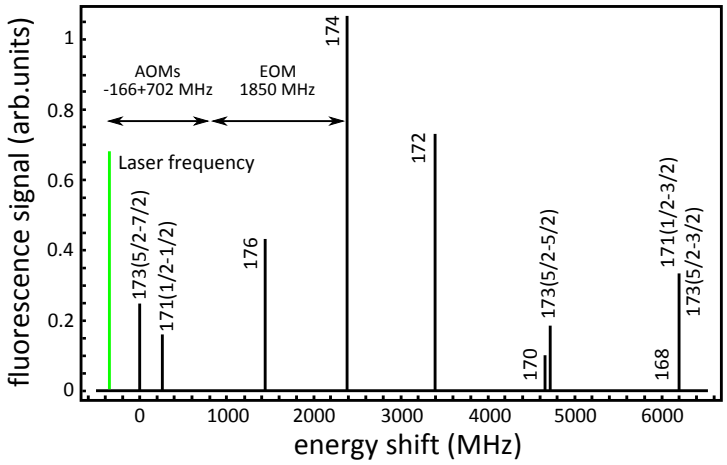

Figure 2.7: Isotope shifts for the intercombination transition ${}^1S_0 \rightarrow {}^3P_1$ [78]. In green we indicate the effective laser frequency when operating with the fermionic isotope ^{173}Yb. The isotope shift with respect to the boson ^{174}Yb is covered by AOMs and the EOM.

laser frequency in the spectroscopy branch is blue-detuned by +702 MHz using a double-passage AOM and then it passes through a Qubig electro-optical modulator (EOM) EO-T1850M3-VIS resonant at 1.85 GHz. In this way, the effective laser frequency is red-detuned by -2552 MHz (Δ_1) with respect to the blue sideband of the EOM-modulated spectroscopy beam. Since the isotope shift between the $F = 5/2 \rightarrow F' = 7/2$ transition of ^{173}Yb and the transition of ^{174}Yb is $\Delta_{174-173} = 2386$ MHz (see Fig. 2.7), when the spectroscopy beam is resonant with ^{174}Yb, the effective detuning between the laser and the ^{173}Yb resonance is $\Delta_1 - \Delta_{174-173} = -166$ MHz, as in the case of the bosonic ^{174}Yb locking scheme. In this way it is possible to use the same AOMs in the other branches (MOT, OSG, OP) for operation with both ^{174}Yb and ^{173}Yb.

It is possible to switch between the two locking schemes simply using a removable mirror (RM in Fig. 2.6) which selects the right spectroscopy path. It shall be noted that when we operate with the bosonic isotope ^{174}Yb, the EOM is switched off and the lock-in frequency modulation is executed by the AOM.

2.3.3 1064 nm Laser system

Laser radiation at 1064 nm is used both to inject the in-vacuum Fabry-Perot cavity where the atoms are trapped (section 2.4.3) and to perform optical transport from the MOT chamber to the glass cell (section 2.4.4). The source is a Nd:Yag MEPHISTO MOPA 25 (Innolight/Coherent) laser with linewidth below 100 kHz and maximum output power of 25 W. The frequency of the laser can be tuned using a piezo for fast corrections (about

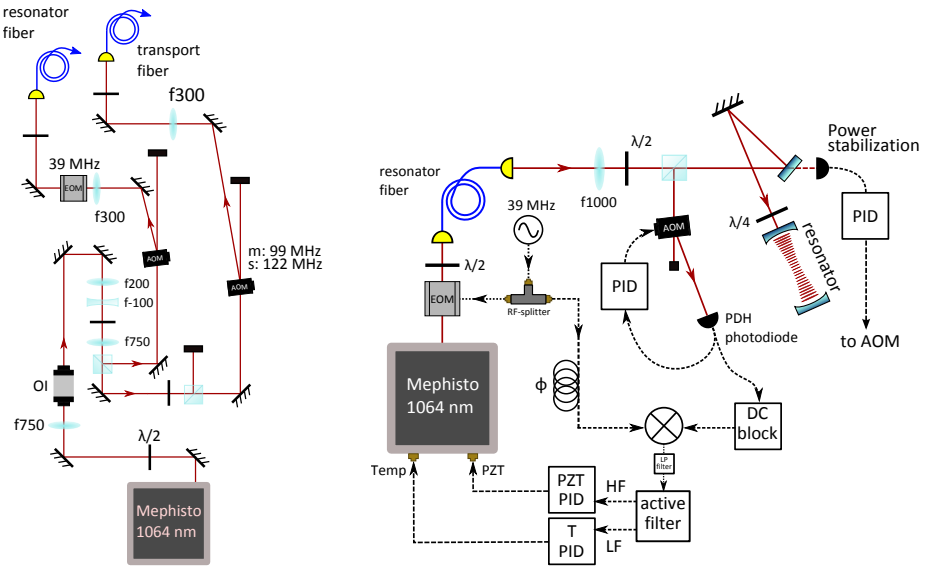

(a) Optical Setup **(b)** PDH lock setup

Figure 2.8: a) Optical setup for the 1064 Mephisto laser. **b)** PDH locking scheme to the resonator. See text for details.

100 kHz bandwidth) and using the laser seed temperature for slow and large range corrections (1 Hz bandwidth, 3 GHz/°C). In Fig. 2.8a, we show the 1064 nm optical scheme in which the radiation is split in two optical paths that bring the laser power to the resonator and to the optical transport setup. Due to the high optical powers involved, the AOMs are double-frequency driven [85, 93] in order not to damage the optical fibers by thermally-induced misalignments. The frequency lock to the in-vacuum optical cavity is performed by a standard Pound-Drever-Hall (PDH) scheme [94]. The laser frequency is modulated at 39 MHz with a Qubig EOM. The error signal is split in two by an active filter that separates the high-frequency components from the low-frequency components. The high-frequency parts go to the PID acting on the piezo controlling the seed laser of the Mephisto in order to perform fast corrections. The low-frequency parts (<3 Hz) are processed by a PID whose output feeds the temperature seed of the laser. We also actively stabilize the cavity-reflected power impinging on the PDH photodiode with an additional AOM (see Fig. 2.8b). More specifically, we use the AC part of the error signal for the PDH feedback loop and the DC signal of the PDH photodiode for the PDH power-lock. In this way we obtain an error signal independent on the in-cavity power and we avoid damages to the photodiode. The lock is very stable and it is characterized by a broad power range spanning four orders of magnitudes ($100\,\mu$W, 2 W).

2.3.4 759 nm Laser system

To produce the optical lattices we use laser radiation at 759 nm. This particular wavelength has been chosen because the light shift it induces is the same both for the $^1S_0$ state and for $^3P_0$ metastable excited state ("magic wavelength", see Chapter 7). The radiation is produced by a standard Titanium-Sapphire laser (Coherent MBR 110) pumped by a single-mode, 532 nm, Coherent VERDI 18. We get routinely 3.5 W of 759 nm light, which is split in three different optical paths, each featuring an AOM and an optical fiber to implement the optical lattices along three orthogonal directions. A small portion of the laser light is used to inject a confocal Fabry-Perot cavity to monitor single-mode emission of the MBR.

2.4 Overview of the experimental procedure

2.4.1 Zeeman Slower $(^1S_0 \rightarrow {}^1P_1)$

The experimental cycle begins by slowing down the atomic beam coming from the oven by means of a Zeeman Slower [95]. A counter-propagating laser beam, acting on the $^1S_0 \rightarrow {}^1P_1$ transition, exerts the necessary radiation pressure force, capable of slowing the atoms from an average velocity of about 340 m/s to a few 10 m/s in a distance of 50 cm [85, 86, 96]. The atoms are kept in resonance by an inhomogeneous magnetic field $B_{ZS}(z)$, whose profile Zeeman-shifts the atomic energy levels matching the Doppler condition [97]. We use 399 nm, σ^- polarized light [98], which is red-detuned by -983 MHz from the cycling $F = 5/2 \rightarrow F' = 7/2$ transition of the fermionic ^{173}Yb isotope. In this way, light is resonant with most of the atoms coming out from the oven and does not affect the slow ones arrived in the center of the MOT cell[2], where the Zeeman Slower residual magnetic field is compensated by a dedicated coil (see Fig. 2.2).

2.4.2 Magneto-optical trap $(^1S_0 \rightarrow {}^3P_1)$

The magneto-optical trap (MOT) is formed with the standard configuration of three pairs of orthogonal laser beams operating at 556 nm, on the $^1S_0 \rightarrow {}^3P_1$ intercombination transition. For fermionic ^{173}Yb we use the cycling transition $F = 5/2 \rightarrow F' = 7/2$ to avoid optical pumping towards dark states. Due to the narrowness of the transition ($\Gamma_{556} = 2\pi \times 182$ kHz),

[2] Actually in our setup, the radiation pressure on the slow fermionic atoms is not negligible since, for the atoms trapped in the MOT, the slowing beam is detuned only -216 MHz with respect to the $F = 5/2 \rightarrow F' = 5/2$ transition. On the one hand, this gives us the possibility to use the Zeeman slower light to perform a preliminary optical pumping stage inside the MOT chamber to produce a large spin-polarized Fermi gas in the $m_F = -5/2$ component. On the other hand this additional radiation pressure has to be taken into account in the fermionic MOT optimization process [45, 85].

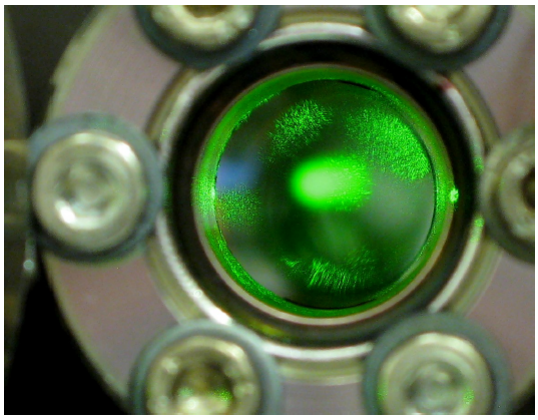

Figure 2.9: MOT of ^{174}Yb bosonic atoms.

we increase the capture velocity by putting frequency sidebands on the laser light [99]. The $N_{sb} = 18$ sidebands are all red-detuned with respect to the carrier frequency and are separated by 600 kHz. In this way, the uniformly "filled" spectral region explored with the frequency modulation is maximized in order to capture the highest possible number of velocity classes. With this method, we can routinely trap $N_{at} \simeq 1 \cdot 10^8$ ^{173}Yb atoms and $N_{at} \simeq 1 \cdot 10^9$ ^{174}Yb atoms. For further details see [45, 85, 86]. The multi-frequency MOT stage lasts for 20 s after which the modulation is switched off and the carrier frequency and intensity are optimized, in order to minimize the sample temperature.[3] The temperature we get is $T \simeq 25\ \mu$K for the fermionic isotope, which is low enough to reach an efficient transfer inside the Fabry-Perot optical dipole trap (see section 2.4.3).

2.4.3 Resonator stage

As explained in section 2.2.2, the infra-red radiation at 1064 nm is kept in resonance with the in-vacuum Fabry-Perot cavity by a Pound-Drever-Hall locking scheme [94]. For the injection power we use, the obtained maximum trap depth ($V_0/k_B \simeq 800\ \mu$K) combined with a beam waist $w_0 \simeq 300\,\mu$m, guarantees a transfer efficiency from the MOT of about 80%. Before the transfer, the MOT is compressed and gently moved in the center of the dipole trap by means of three orthogonal compensation coils that

[3] Indeed the Doppler temperature limit is:

$$T = \frac{\hbar\Gamma}{8k_B}\frac{\Gamma}{|\delta_L|}\left[1 + \frac{I}{I_s} + \left(\frac{2\delta_L}{\Gamma}\right)^2\right]$$

where δ_L is the detuning from resonance, I is the light intensity, I_s is the saturation intensity and Γ is the transition linewidth. We are not considering sub-doppler cooling effects, since the lowest temperature we reach is approximately 30 times higher than the Doppler temperature, probably due to light-assisted collision processes [45, 86].

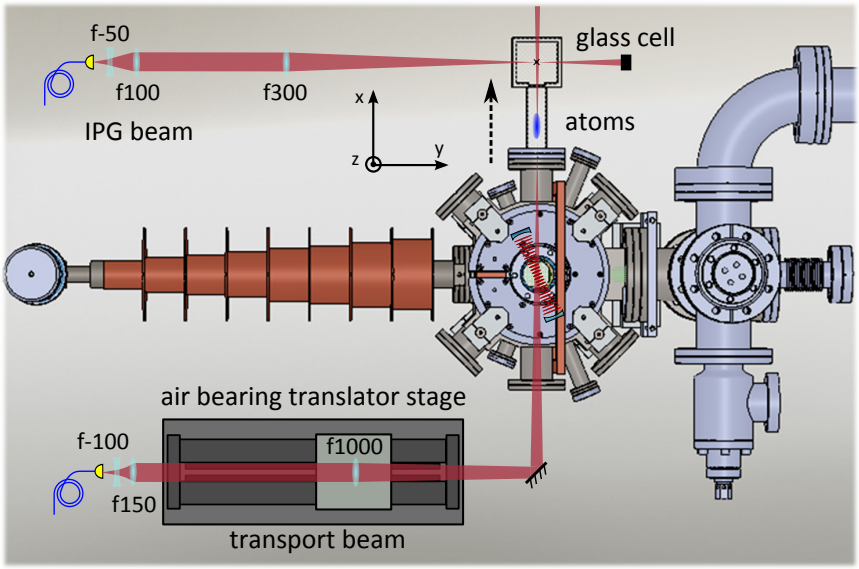

Figure 2.10: Sketch of the optical transport stage. By means of the air-bearing translator, the focus of the transport beam is moved along $\hat{x}$, towards the center of the glass cell. Along the orthogonal direction $\hat{y}$, the IPG beam is used to generate the crossed dipole trap.

shift the position of the zero of the quadrupole magnetic field [45, 85]. After having completed the transfer, the MOT beams and the magnetic fields are switched off and a first evaporation stage inside the optical cavity starts. We exponentially lower the trap depth to approximately $V_0/k_B \simeq 60\ \mu$K obtaining $N_{at} \sim 1 \cdot 10^7$ atoms at roughly $T \simeq 3\ \mu$K.

2.4.4 Optical Transport and Crossed Dipole Trap

In order to move the atomic sample from the MOT cell to the center of the glass cell we use an air-bearing translation stage AEROTECH ABL 1500b [100]. A laser beam at 1064 nm is tightly focused ($P = 3.5\,$W, $w_0 = 30\,\mu m$, $V_0/k_B \simeq 90\ \mu$K) onto the atoms by a lens mounted on the stage, thus providing a movable transport dipole trap. The Fabry-Perot injection power is adiabatically lowered to an idle value[4] and the atoms are transfered with 30 % efficiency to the transport dipole trap. The beam focus, initially coincident with the center of the optical resonator trap, is then moved in $T = 2.5$ s by a distance $\Delta x = 26.4$ cm towards the center of the glass cell [45, 101, 102], transporting approximately 66 % of the initial atomic population (see Fig. 2.10). Once arrived at the final position, an additional

[4] Which is approximately $100\,\mu$W. This power is low enough not to trap the atoms anymore, but high enough to keep the laser locked to the cavity for the next experimental cycle.

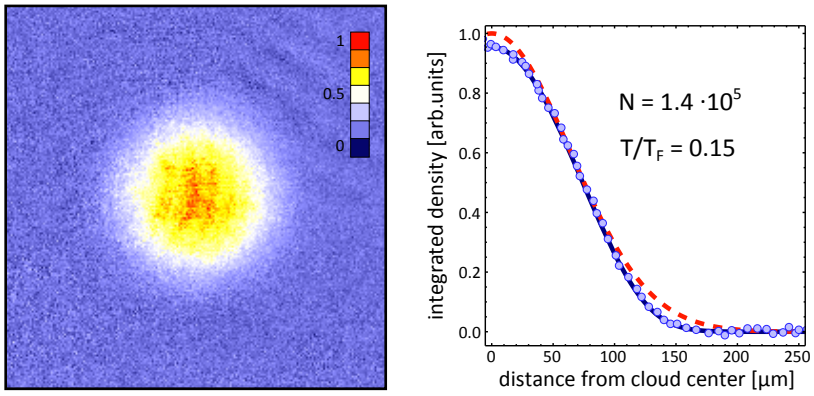

(a) **(b)**

Figure 2.11: Degenerate Fermi gas of ^{173}Yb with six spin components. **(a)** False color image of the momentum distribution detected after a 23 ms time of flight. **(b)** One dimensional integrated (along $\hat{y}$) density together with the result of a two-dimensional Fermi distribution and Gaussian fits to the data. N denotes the total atom number in the cloud. For such a low temperature $T = 0.15\,T_F$, the deviation of the data from the Gaussian profile is clearly visible.

beam ($w_0 = 60$ μm, $P = 3$ W) is focused onto the atoms, along a direction which is orthogonal with respect to the transport beam, see Fig. 2.10. The source is an IPG FIBERTECH multimode laser at 1070 nm, which is used to create a crossed dipole trap where the final evaporation towards quantum degeneracy takes place.

2.4.5 ^{173}Yb Degenerate Fermi Gas

Quantum degeneracy is reached by means of optical evaporation inside the crossed dipole trap. The optimal condition to obtain colder and larger samples of quantum degenerate Fermi gases is to use two different exponential ramps for the transport beam and for the IPG beam. The transport power is lowered with an exponential ramp of duration $T_{ramp} = 3.5$ s, and decay constant $\tau_{ramp} = 3$ s from the maximum power of 3.4 W to the final power of 35 mW, whereas the IPG power is lowered from the maximum power of 3.0 W to the final power of 1 W with an exponential ramp of duration $T_{ramp} = 6.1$ s, and decay constant $\tau_{ramp} = 2.95$ s [45]. At the end of the evaporation we routinely obtain Fermi gases with six spin-components with $N \simeq 1.4 \cdot 10^5$ atoms at a temperature $T \simeq 0.15\,T_F$ where T_F is of the order of 200 nK (see Fig. 2.11).

The final crossed dipole trap is characterized by the trap frequencies reported in Table 2.3.

Table 2.3: ODT trap frequencies after evaporation.

ν_x [Hz]	ν_y [Hz]	ν_z [Hz]	$\overline{\nu}$ [Hz]
(53.8 ± 0.5)	(99.5 ± 0.5)	(90.3 ± 0.6)	(78.4 ± 0.4)

2.4.6 Optical Lattices

All the experiments described in this thesis are performed by loading the atoms in an optical lattice potential. The laser setup is constituted by three orthogonal retroreflected beams, one along the vertical direction $\hat{z}$ (OL_3) and the other two in the horizontal plane $\hat{x} - \hat{y}$ (OL_1 and OL_2). The in-plane beams are rotated with respect to the $\hat{y}$ direction defined by the IPG beam by an angle $\theta = 55°$, as is shown in Fig. 2.12.

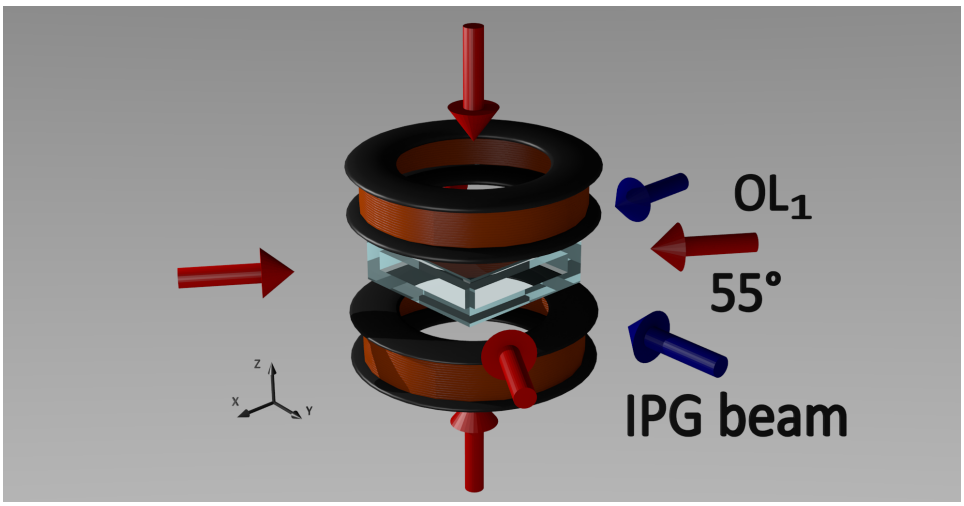

Figure 2.12: Optical lattice setup. Beam 1 (OL_1) is tilted by 55° with respect to the IPG-beam ($\hat{y}$ direction).

The optical lattice beam powers are actively stabilized by standard feedback loops and the estimated beam waists and residual harmonic trapping frequencies (along the orthogonal direction of the corresponding lattice beam) are reported in Table 2.4:

2.5 Nuclear spins detection and manipulation

In this Section we will present the experimental techniques for the detection and manipulation of the spin degree of freedom in an ultracold gas of fermionic ^{173}Yb. We start with a brief recap of the absorbtion imaging

Table 2.4: Lattice beam waists, and trap frequencies calibration. The frequencies are expressed in terms of the lattice depth in recoil units s. OL_1 and OL_2 are in the $\hat{x}-\hat{y}$ plane, whereas OL_3 is along the vertical $\hat{z}$ direction.

	OL_1	OL_2	OL_3
$w_0\,[\mu\text{m}]$	96.1	111.3	102.3
$\nu_r(s)\,[\text{Hz}]$	$7.1\sqrt{s}$	$6.2\sqrt{s}$	$6.8\sqrt{s}$

technique to then explain how the intercombination transition at 556 nm is used, in order to separate in time of flight the different spin components (optical Stern-Gerlach) and to prepare arbitrary spin-state mixtures through optical pumping.

2.5.1 Imaging

In order to detect the atomic sample we use standard absorption imaging techniques [103]. The principle of operation consists in recording on a CCD camera the shadow cast by an atomic sample due to the absorption of a resonant light probe. In order to reduce the interrogation time, a strong dipole-allowed transition is preferable. In our case we use a probe beam at $\lambda = 399$ nm acting on the cycling transition ${}^1S_0\,(F = 5/2) \rightarrow {}^1P_1\,(F' = 7/2)$. The column density of the cloud $n_c(x,y) = \int n(x,y,z)dz$ integrated along the imaging direction z is deduced from the transmitted intensity profile $I_t(x,y)$ of the imaging resonant beam:

$$I_t(x,y) = I_0(x,y)e^{-\sigma n_c(x,y)} \longrightarrow n_c(x,y) = -\frac{1}{\sigma}\log\left(\frac{I_t(x,y)}{I_0(x,y)}\right), \qquad (2.0)$$

where $I_0(x,y)$ is the intensity profile of the probe beam and $\sigma = 3\lambda^2/2\pi$ is the resonant scattering cross section in the low intensity limit. The discretized density on the CCD pixels is measured as:

$$n_c(i,j) = -\frac{S}{\sigma}\log\left(\frac{P_{ij} - B_{ij}}{F_{ij} - B_{ij}}\right), \qquad (2.0)$$

where S is the pixel area ($2.68\,\mu\text{m} \times 2.68\,\mu\text{m}$) including the magnification of the optical system (2.985x) and P_{ij}, F_{ij}, B_{ij} are the recorded counts at pixel position (i,j) corresponding respectively to the picture taken with atoms, without the atoms and with the probed beam switched off in order to remove the background [45].

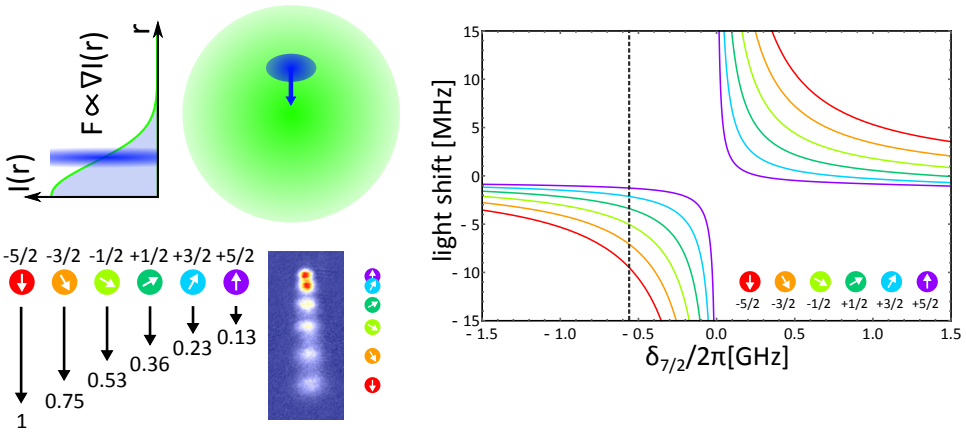

Figure 2.13: Principle of operation of OSG. Top left, alignment geometry: the force experienced by the atoms is proportional to the gradient of the optical intensity. Bottom left, line-strengths for our experimental parameters and a typical absorption image of the OSG experiment. Top right, spin-dependent OSG potential as a function of the detuning with respect to the $F = 5/2 \rightarrow F' = 7/2$ resonance for σ^- polarization. The dotted line at -566 MHz corresponds to the frequency of the OSG beam. The different colors indicate different nuclear spin components. The beam waist is $w_0 = 60\ \mu$m and the power is $P = 10$ mW.

2.5.2 Spin distribution detection

^{173}Yb is a strongly diamagnetic atom which possesses only a nuclear spin in its ground state. For this reason it is not possible to use standard magnetic Stern-Gerlach techniques to separate the different spin components. To circumvent this problem we use an optical technique that is called "optical Stern-Gerlach" [84, 104]. As was explained in Section 1.2.3, in the specific case of the transition $^1S_0 \rightarrow {}^3P_1$, the optical dipole force exerted on atoms in the ground state with spin component m_F is given by the contribution of the three excited states $F' = 7/2, 5/2, 3/2$ of the $^3P_1$ manifold:

$$U_{m_F}(\mathbf{r}, \omega, q) = \frac{3\pi c^2}{2\omega_0^3} 3\Gamma \left(\frac{|\mathcal{C}_{7/2,m_F}(q)|^2}{\delta_{7/2}} + \frac{|\mathcal{C}_{5/2,m_F}(q)|^2}{\delta_{5/2}} + \frac{|\mathcal{C}_{3/2,m_F}(q)|^2}{\delta_{3/2}} \right) I(\mathbf{r}), \tag{2.0}$$

where q refers to light polarization, $\delta_{F'} = \omega - \omega_{F'}$ are the detunings from the F'-states, $\Gamma = 2\pi \times 182\,$kHz is the decay rate of the $^3P_1$ state with the proper multiplicity factor and $\omega_0 = 2\pi c/\lambda$ with $\lambda = 556$ nm. In particular, a σ^--polarized laser beam with a detuning $\delta_{7/2} = -566$ MHz $\simeq -3100\,\Gamma$ and waist $w_0 = 60\,\mu$m is used to exert a spin-dependent potential on the atoms. In Fig. 2.13 we report the principle of operation of the optical Stern-Gerlach scheme. The beam waist center is slightly misaligned with respect to the atomic sample so that the atoms experience the maximum intensity gradient, which is proportional to the spin-dependent

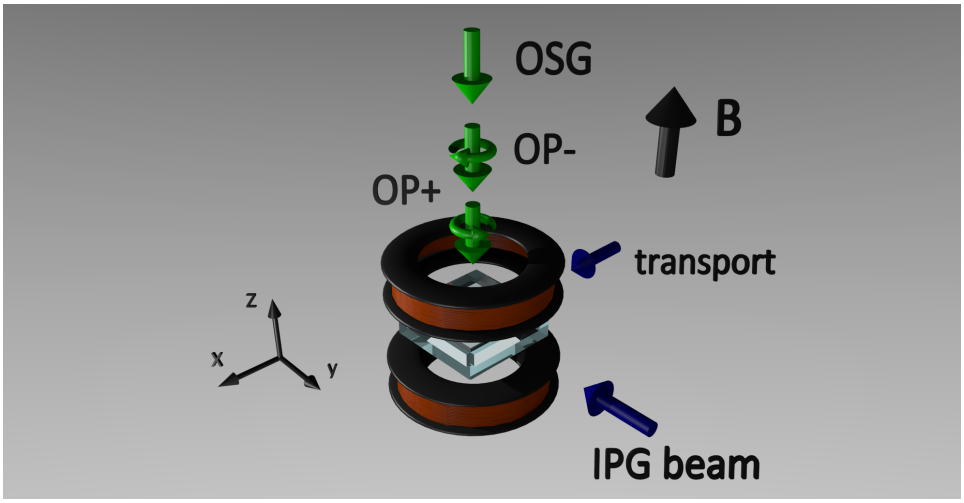

Figure 2.14: Optical scheme for OSG and OP beams. The OSG beam has σ polarization, the sign of which depends on the particular experimental configuration.

dipole force (Fig. (2.13), top left). For the frequency detuning and polarization chosen in our setup, the maximum force is felt by the $m_F = -5/2$ component[5] (Fig. (2.13), bottom left). To perform the nuclear spin population detection, we use a 1.25 ms square pulse with power $P = 10$ mW and, after suddenly switching off the ODT, we let the cloud expand for a $t_{TOF} = 4.5$ ms. To define the quantization axis, a bias magnetic field $B_{OSG} = 2.5$ Gauss is applied along the light propagation axis. A typical absorption image of the OSG experiment is shown in Fig. 2.13.

2.5.3 Spin distribution preparation

The ${}^1S_0\,(F = 5/2) \rightarrow {}^3P_1\,(F' = 7/2)$ is a narrow transition ($\Gamma = 2\pi \times$ 182 kHz) that allows us to develop optical pumping protocols capable of realizing mixtures with arbitrary number of spin components. Indeed it is sufficient to Zeeman-split the excited-state spin components (Zeeman splitting $\Delta_Z = 2\pi \times 595 \cdot B$ kHz/G between states with $\Delta m_F = 1$), in order to address selectively a particular transition, Fig. 2.15. The ${}^3P_1\,(F' = 7/2)$ Zeeman sublevels are separated by a homogeneous magnetic field of $B = 23$ Gauss, resulting in a Zeeman shift $\Delta_Z = 2\pi \times 13.7$ MHz $\simeq$ 75 Γ. The optical pumping protocol is then carried out by two independent circularly polarized beams OP^+ and OP^- (see Fig. 2.14) which address the transitions $m_F \rightarrow m_F \pm 1$. By shining two series of light pulses of 5 ms each at the right laser frequencies (green arrows in Fig. 2.15), it is possible

[5]Of course we can switch to σ^+ polarization so that the maximum force is felt by the $m_F = +5/2$ component.

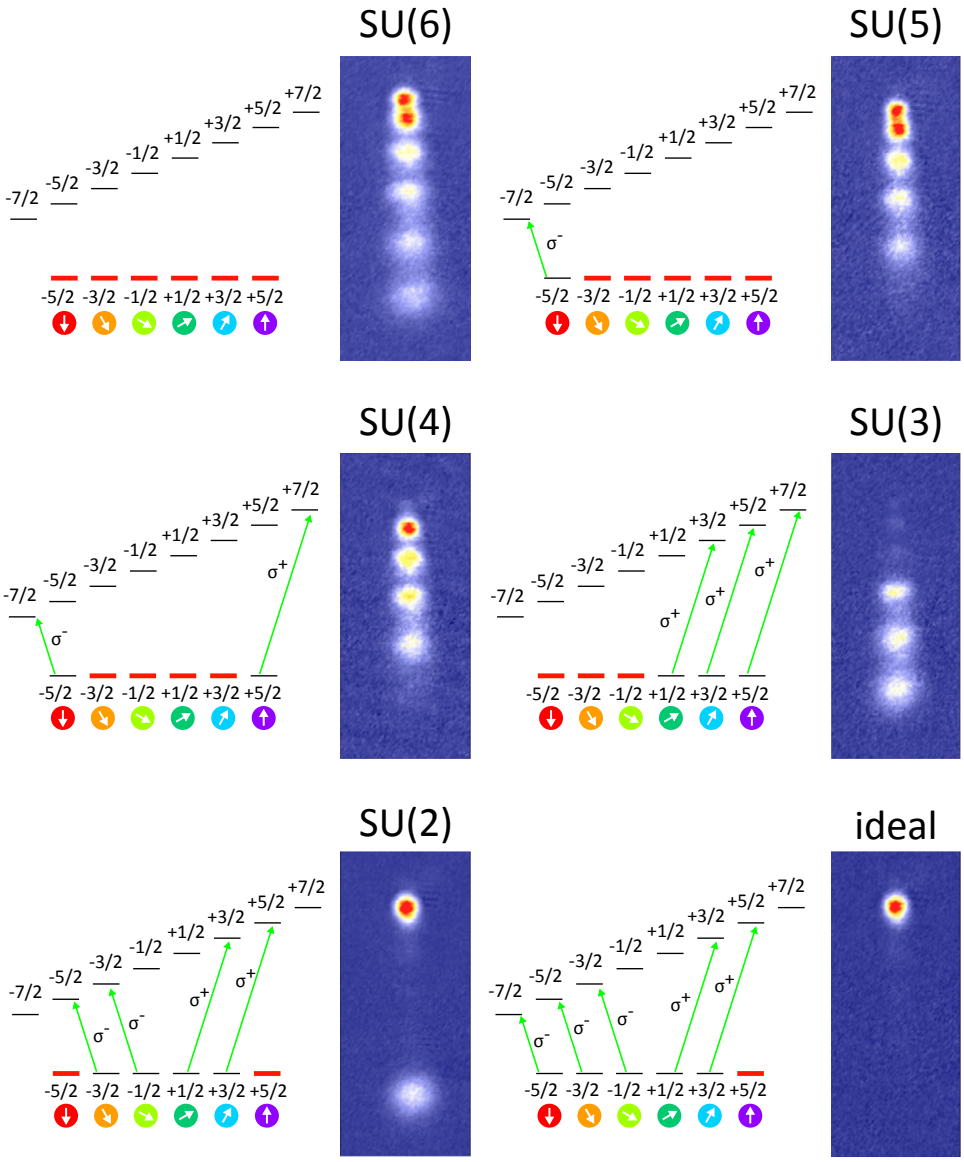

Figure 2.15: Protocols for spin initialization with optical pumping performed through σ^+ and σ^--polarized beams resonant on specific Zeeman components of the ${}^1S_0 \rightarrow {}^3P_1$ transition. Green arrows indicate the transitions used in the optical pumping procedure. Pulses from $|m_F| = 5/2$ to $|m_{F'}| = 7/2$ are "blast" pulses for which the atoms are expelled from the trap. In red, the spin components remained after the pumping/blasts procedure. The mixture with six components, SU(6), does not need any pumping pulse. For the sake of clarity, the spontaneous emission processes are not shown.

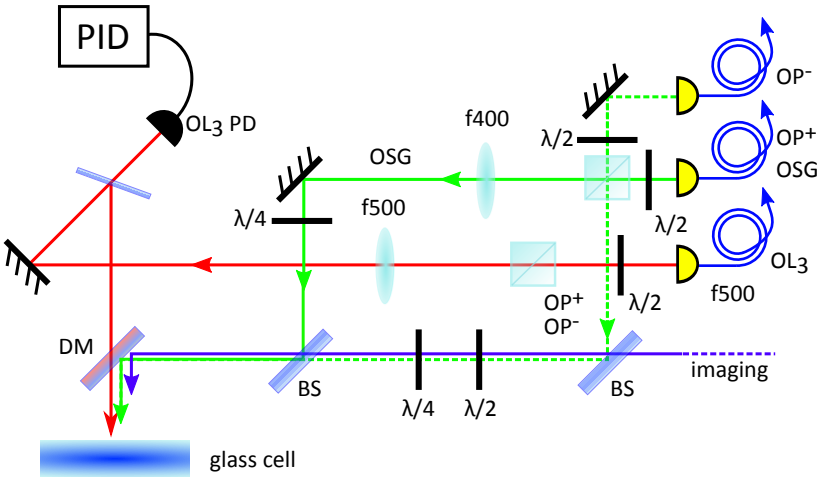

Figure 2.16: Optical scheme for vertical imaging, optical Stern-Gerlach (OSG, green solid line), optical pumping beams ($OP^{\pm}$, green dashed line) and vertical optical lattice (OL_3). DM: long-pass dichroic mirror. BS: beam splitter. PD: OL_3 power stabilization photodiode.

to selectively pump the atoms towards a specific nuclear spin state. The pumping procedure starts when the atoms are transported in the glass cell, before the evaporation ramps. In this way the trap depth is high enough to allow the atoms to scatter many photons without being kicked out off the trap. In order to produce a spin-polarized Fermi gas an additional "blast" pulse is needed at the end of the evaporation [45] (see Fig. 2.15) in order to kick out the unwanted populations from the trap. With these protocols we can prepare balanced[6] mixture with an arbitrary number of spin components.

Optical pumping and OSG setup

Two indipendent fibers mounted on a vertical breadboard deliver the optical pumping beams OP^+ and OP^- to the atoms, Fig. 2.16. The OP^+ beam is generated using the MOT AOM and injected in the same fiber of OSG with orthogonal polarization with respect to it (see Fig. 2.6). The OSG and OP^+ beams are then separated by a polarizing beam splitter (PBS) placed right after the fiber. The same PBS is also used to combine the two optical pumping beams having linear and orthogonal polarization. Two waveplates turn the horizontal and vertical polarization into σ^+ and σ^- respectively (see Fig. 2.16). In the OSG beam optical path there is a $f = 400$ mm lens mounted on a translation stage, used to adjust the waist in order to maximize the optical gradient on the atoms, and a $\lambda/4$ waveplate to de-

[6]The mixture are balanced at 5% tolerance and the apparent density differences in Fig. 2.15 come from the compression induced by the OSG dipole potential.

termine the polarization of the OSG light. The two optical pumping and OSG beams are then recombined by a 70:30 beam splitter and reflected by a long-pass dichroic mirror Thorlabs-DMLP567 through the glass cell, onto the atoms. The vertical lattice beam (OL_3) passes through the same dichroic mirror and the vertical imaging beam is superimposed on the OP path using another beam splitter (see Fig. 2.16).

2.5.4 Spin-selective imaging

For the experiments we will present in Chapter 5 it is important to selectively image the atoms occupying a particular spin state. In the experiments we will describe, the atomic sample is characterized by a spin population formed by the components $m_F = (-5/2, -1/2, +3/2)$ out of the $F = 5/2$ manifold in the $^1S_0$ ground state. We developed a simple procedure with which we image each spin component selectively. The experimental routine is based on a sequence of pumping and blast pulses, perfomed during the first 2.5 ms of time-of-flight expansion (when all the dipole traps are completely switched off) of the atomic cloud, at a magnetic field intensity $B = 15$ G. In Figs. 2.17a, b, c we show the results of the experimental routine, after which an OSG pulse is applied, in order to verify that the procedure was succesful[7]. All the pumping and blast pulses have a duration of 250 μs, and approximately 750 μs are needed to change the frequencies of the pumping beams $OP^{\pm}$. The sequences are as follows:

- imaging of the $m_F = +3/2$ spin component: atoms in the $m_F = -1/2$ spin state are pumped twice, first in the $m_F = -3/2$ spin component and then in the $m_F = -5/2$ spin component. After a final blast pulse, resonant with the transition $(^1S_0, F = 5/2, m_F = -5/2) \rightarrow (^3P_1, F' = 7/2, m_{F'} = -7/2)$, we are left with the atoms in the desired $m_F = +3/2$ spin state (see Fig. 2.17a);

- imaging of the $m_F = -1/2$ spin component: atoms in the $m_F = -5/2$ spin state are blasted away as in the previous sequence. Atoms in the $m_F = +3/2$ spin state are first pumped in the $m_F = +5/2$ spin component. After a final blast pulse, resonant with the transition $(^1S_0, F = 5/2, m_F = +5/2) \rightarrow (^3P_1, F' = 7/2, m_{F'} = +7/2)$, we are left with the atoms in the desired $m_F = -1/2$ spin state (see Fig. 2.17b);

- imaging of the $m_F = -5/2$ spin component: atoms in the $m_F = -1/2$ spin state are pumped three times, first in the $m_F = +1/2$ spin component, then in the $m_F = +3/2$ spin component and finally

[7] Once verified that we are left with the desired spin component, the OSG pulse is not needed anymore and the final detection is executed by standard time-of-flight imaging.

in the $m_F = +5/2$ spin component . After a final blast pulse, resonant with the transition $(^1S_0, F = 5/2, m_F = +5/2) \rightarrow (^3P_1, F' = 7/2, m_{F'} = +7/2)$, we are left with the atoms in the desired $m_F = -5/2$ spin state (see Fig. 2.17c);

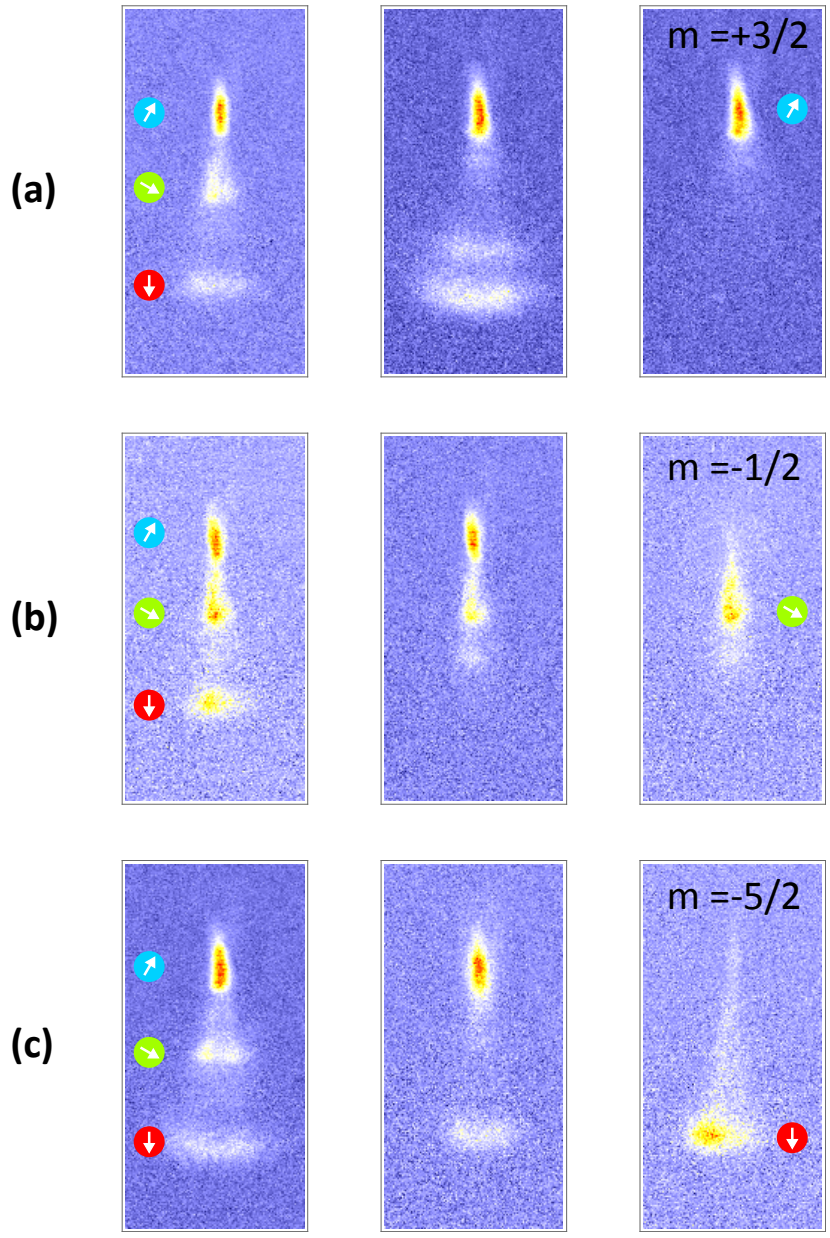

Figure 2.17: Spin selective imaging procedure. **(a)**, **(b)**, **(c)** refer to the sequence used to image the atoms in the $m_F = +3/2, -1/2, -5/2$ spin states respectively.

3 | Raman-induced coherent coupling in ^{173}Yb

The fundamental ingredient of this PhD thesis is the introduction of a coherent coupling among the different spin components. This is achieved by means of Raman transitions, whose basic principles have been introduced in Section 1.3. This chapter reports the experimental implementation of the ^{173}Yb Raman system, which is at the basis of the generation of spin-orbit coupling and synthetic dimensions. We will start by generalizing the Λ-configuration introduced in Section 1.3 to the more complex case of a multi-level atom such as ^{173}Yb. We will then illustrate the optical setup built within this PhD thesis used to generate and characterize the coherent coupling among the spin components.

3.1 Raman transitions in multi-level atoms

In this section we generalize the Raman process in a Λ-configuration, illustrated in section 1.3, to the more complex case of a multi-level atom such as ^{173}Yb. This fermionic isotope has purely nuclear spin in the $^1S_0$ ground state, so in order to induce a coherent coupling among the different spin components, the Raman detuning must be comparable to the hyperfine splitting of the excited state manifold, $\Delta \lesssim \Delta_{HFS}$. Indeed, we have to "talk" with the nuclear spin, passing through the electronic degree of freedom. Therefore, analogously to the light shift for a multi-level atom evaluated in Eq. (1.2.3), we consider two-photon processes relying on the hyperfine structure of the excited state $^3P_1$. The Raman amplitude coherently coupling two sublevels m_F, m_F' in the ground state can be calculated by summing over the excited state manifold, taking into account

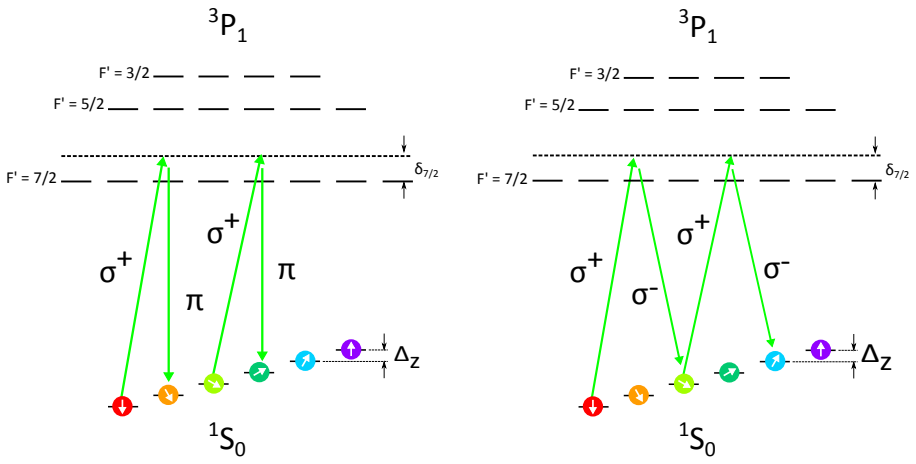

(a) $\Delta m_F = \pm 1$ **(b)** $\Delta m_F = \pm 2$

Figure 3.1: Scheme of Raman transitions in the case of $\sigma^+\pi$ **(a)** and $\sigma^+\sigma^-$ **(b)** polarizations. Typically, the Zeeman splitting is $\Delta_Z \sim 2\pi \times 10$ kHz. The excited state hyperfine energy width Δ_{HFS} (several GHz) is not to scale.

the detuning from a particular hyperfine level:

$$\begin{aligned}\Omega_R^{(qq')} &= \frac{\Omega_q \Omega_{q'}^*}{4}\left(\sum_{F'}\frac{\mathcal{C}_{F',m_F}(q)\mathcal{C}_{F',m_F'}(q')}{\delta_{F'}}\right) \\ &= \frac{3\pi c^2}{2\omega_0^3}3\Gamma\left(\sum_{F'}\frac{\mathcal{C}_{F',m_F}(q)\mathcal{C}_{F',m_F'}(q')}{\delta_{F'}}\right)\sqrt{I_q I_{q'}},\end{aligned} \tag{3.0}$$

where the polarizations of the two Raman beams satisfy $m_F' - m_F = q - q'$ and $\delta_{F'}$ are the frequency detunings of the Raman light with respect to the transitions $^1S_0\,(F = 5/2) \rightarrow {}^3P_1(F')$. In particular we consider $\delta_{7/2}$ to be the "reference" Raman detuning (Δ in Sec. 1.3). We note that, because of the Clebsch-Gordan coefficients in the Eq. (3.1), the Raman amplitudes depend also on the specific m_F state as can be seen in Figs. 3.3. Depending on the polarization of the Raman beams, the two-photon process can flip the spin by one unit of angular momentum ($\sigma - \pi$ polarizations) or by two units of angular momentum ($\sigma^+ - \sigma^-$ polarizations), as we sketch in Fig. 3.1. This feature opens the possibility to induce a coherent dynamics in a subset of the $^1S_0$ manifold through $\sigma^+\sigma^-$ processes just by tuning the polarization of the Raman beams. We decided to use the narrow-line inter-combination transition $^1S_0 \rightarrow {}^3P_1$ at 556 nm ($\Gamma = 2\pi \times 182$ kHz) instead of the dipole allowed $^1S_0 \rightarrow {}^1P_1$ transition at 399 nm ($\Gamma' = 2\pi \times 29$ MHz) in order to maximize the ratio between the coherent Raman coupling, that we generically indicate with Ω_R, and the inelastic scattering rate Γ_{sc}. Infact, for $\delta_{7/2} \sim \Delta_{HFS}$, the scaling relations $\Gamma_{sc} \sim \Gamma/\delta_{7/2}^2$ and $\Omega_R \sim \Delta_{HFS}/\delta_{7/2}^2$

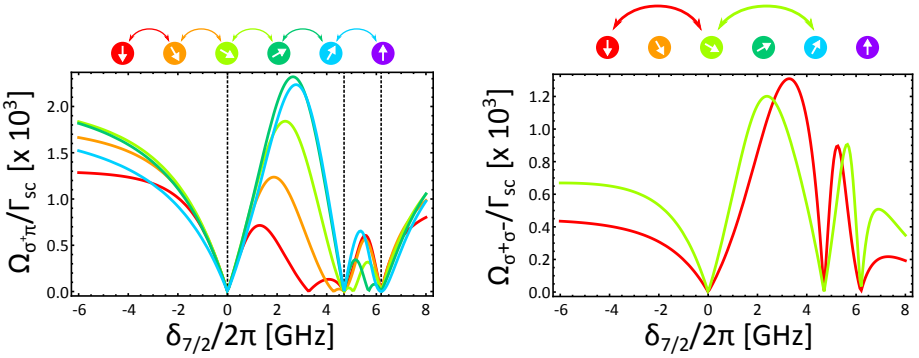

(a) $\Delta m_F = \pm 1$ **(b)** $\Delta m_F = \pm 2$

Figure 3.2: Ratio of the Raman coupling Ω_R (in absolute value) to the inelastic scattering rate Γ_{sc} for the $\sigma^+\pi$ **(a)** and $\sigma^+\sigma^-$ **(b)** processes as a function of detuning $\delta_{7/5}$ with respect to the $F' = 7/2$ resonance. The dashed-dotted lines indicate the hyperfine levels $F' = 7/2, 5/2, 3/2$.

yield the proportionality $\Omega_R/\Gamma_{sc} \sim \Delta_{HFS}/\Gamma$ [105], namely the ratio between the hyperfine separation and the decay rate of the excited state used to generate the Raman couplings. The combination of a longer lifetime for the $^3P_1$ excited state and a larger hyperfine splitting than the $^1P_1$, allows us to reach a large ratio $\Omega_R/\Gamma_{sc} \sim 10^3$ at $\delta_{7/2} \sim 2\pi \times 2$ GHz. We chose the value $\delta_{7/2} = 2\pi \times 1.876$ GHz for which we have a relatively high ratio both for the $\Delta m_F = 1$ and $\Delta m_F = 2$ transitions (see Fig. 3.2). In particular we will work with the simpler configuration $\Delta m_F = 2$, reducing the effective spin manifold to maximum three components. The cause for this resides in the complications brought by the Raman light in terms of spin-dependent light shifts. Indeed, without these light shifts, the only energy difference among the nuclear spins comes from the linear Zeeman effect ($\Delta_Z = 207 \cdot B\,\mathrm{Hz/Gauss}$) which can be easily compensated by adjusting the Raman beams frequencies, ensuring a resonant coupling among all different spins. Unfortunately, the Raman light spin-dependent light shifts, see Eqs. (1.2.3-1.3), breaks down the perfect linearity of the Zeeman splitting introducing energy offsets that complicate dramatically the dynamics, especially in the presence of more than three spins. In Fig. 3.4 we plot the state-dependent energy offsets normalized to the case of uniform polarization ($1/3\,\sigma^+ + 1/3\,\sigma^- + 1/3\,\pi$) for the detuning $\delta_{7/2} = 1.876\,\mathrm{GHz}$. Nevertheless, by tuning the polarization and the two-photon detuning, two and three spin components can be coherently coupled opening the way to the study of synthetic gauge fields in synthetic dimensions. In the next sections we will describe the Raman setup and the characterization of the Raman coupling based upon dynamical study of the spin populations.

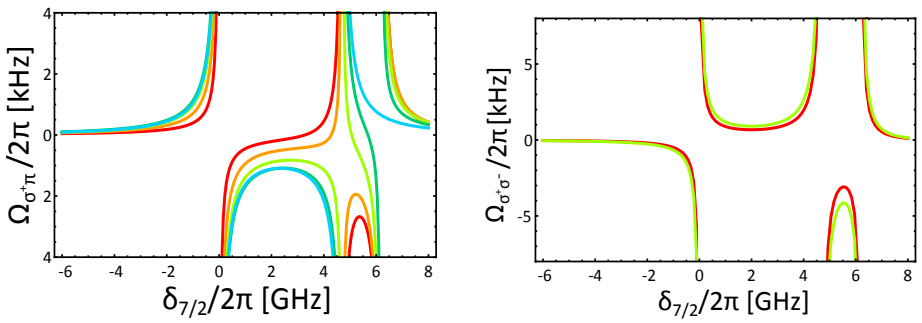

(a) $\Delta m_F = \pm 1$ **(b)** $\Delta m_F = \pm 2$

Figure 3.3: Typical Raman couplings Ω_R expressed in kHz for a total power of $P = 66\,\mu$W (left), $P = 100\,\mu$W (right) and beam waists $w_0 = 150\,\mu$m. **(a)** $\sigma^+\pi$ transitions and **(b)** $\sigma^+\sigma^-$ transitions as a function of the detuning from the $F' = 7/2$ resonance. Note that for large detuning $\delta_{7/2} \gg \Delta_{HFS}$ the coupling amplitudes go to zero.

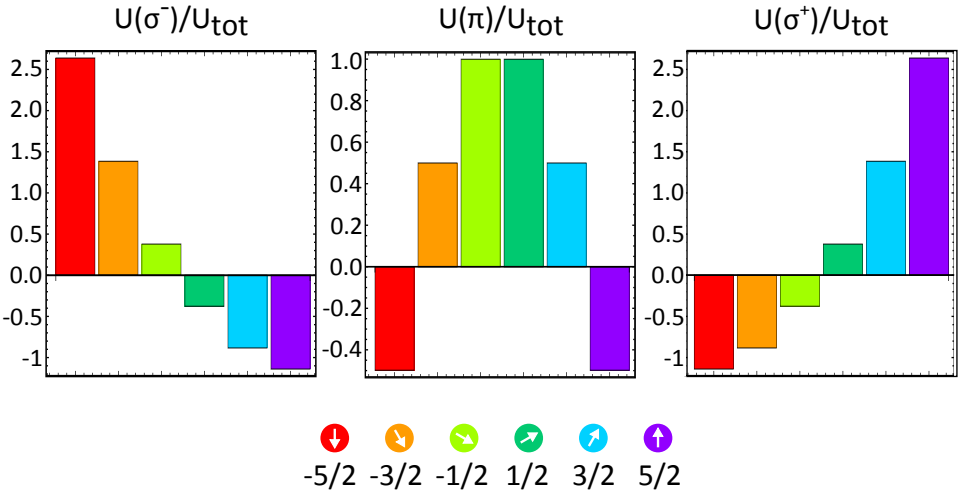

Figure 3.4: Spin-dependent light shift for polarization $q = \sigma^-, \pi, \sigma^+$ at detuning $\delta_{7/2} = 1.876$ GHz and $B = 0$. All values are normalized to the light shift U_{tot} induced by a "uniform" polarization $\hat{\varepsilon} = 1/\sqrt{3}(\hat{\varepsilon}_+ + \hat{\varepsilon}_- + \hat{\varepsilon}_\pi)$ which is independent from the specific spin state. Note that $U^{\sigma^+}_{m_F} = U^{\sigma^-}_{-m_F}$.

3.2 Raman setup

The Raman setup is constituted by two parts. The first one is formed by a series of AOMs used to reach the desired detuning of +1.876 GHz from the $F = 5/2 \rightarrow F' = 7/2$ transition. The light is then injected into an optical fiber and brought to the glass cell region where a custom-made breadboard is present over which all the Raman optics are mounted. In Fig. 3.5 the AOMs table is illustrated. The radio-frequency setup amounts

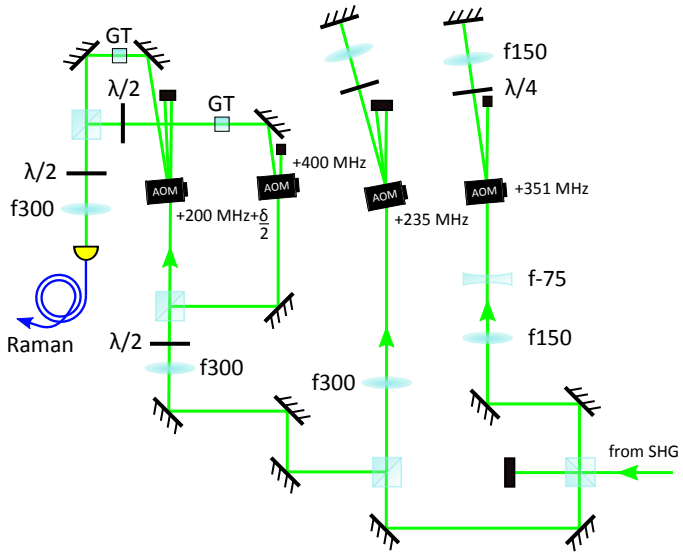

Figure 3.5: Raman AOMs setup used to generate a frequency detuning of $+1.876\,\text{GHz}$ with respect to the $F = 5/2 \rightarrow F' = 7/2$ transition. The last AOM at $200\,\text{MHz} + \delta/2$ is PLL-driven, in order to produce the desired two-photon Raman detuning. The 556 nm light enters the setup with a frequency detuning of $-166\,\text{MHz}$. Glenn-Taylor (GT) polarizer are put after the last two AOMs in order to have stable, linear polarization.

to

- a 351 MHz AOM in double passage at first order (+702 MHz)
- a 235 MHz AOM in double passage at second order (+940 MHz)
- a 400 MHz AOM in single passage at first order (+400 MHz) (first Raman beam).
- a PLL driven (200 MHz+$\delta/2$) AOM in single passage at second order (+400 MHz+δ) (second Raman beam), phase locked with the local oscillator driving the previous AOM.

The frequency difference δ between the two beams constitute the two-photon frequency detuning that must match the energy difference between two spin states that one wants to coherently couple. The total frequency shift results in 2.042 GHz that, taking into account the -166 MHz detuning of the laser with respect to the resonance ${}^1S_0 \rightarrow {}^3P_1(F' = 7/2)$ (see Fig. 2.7), leads to the desired +1.876 GHz. Before the last two AOMs, the Raman beam path is split in two in order to generate the two Raman beams. One passes through the 400 MHz AOM and it is injected into the fiber with vertical polarization. For the second beam, horizontally polarized, we use the 200 MHz AOM in single passage at second order, locked in

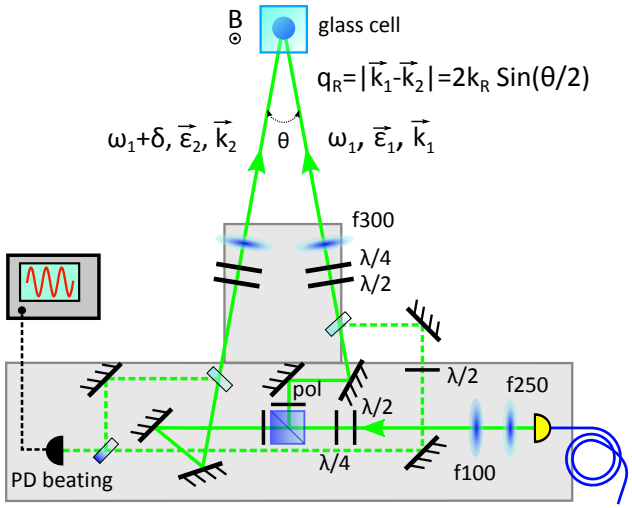

Figure 3.6: Raman optical setup. The two Raman beams come out from the fiber with orthogonal polarizations. They split at the polarizing beam splitter after which two linear film polarizers (LPVISB050-Thorlabs, "pol" in figure) are present. The beams are then focused onto the atoms at the center of the glass cell, to a beam waist of approximately $w_0 = 150\,\mu$m. The dotted lines indicate the pick-ups, taken to monitor the beating frequency δ. The angle $\theta \simeq 19°$ determines the momentum transfer q_R. The magnetic field comes out of the plane, along the $\hat{z}$ direction and defines the quantization axis.

phase with the local oscillator driving the 400 MHz AOM. The two beams coming from the two AOMs are then recombined into a polarizing beam splitter and injected into the same polarization-maintaining fiber in order to reduce relative phase fluctuations. Since they have also orthogonal polarizations, which are injected parallel to the fiber principal axes, they can be split at the end of the fiber by another polarizing beam splitter.

In order to induce a spin-flip, the two-photon detuning must match the energy difference between the spin components. The two beams must thus have frequencies that satisfy the condition $\hbar(\omega_1 - \omega_2) = \hbar\delta = E_{m_F} - E_{m'_F}$. For this reason, the frequency of one beam is controllable with an Agilent 3320 that drives the AOM in PLL-mode (AOM at 200 MHz in Fig. 3.5). The Agilent is phase locked with the local oscillator driving the 400 MHz AOM that shifts the frequency of the other Raman beam.

In Fig. 3.6 we show the second part of the Raman setup, that is the optical setup built to bring the light onto the atomic sample. The Raman beams come out from the fiber with orthogonal polarizations and are separated at the polarizing beam splitter (PBS). Right after the outputs of the PBS, two linear film polarizers (LPVISB050-Thorlabs) help to clean the polarization even further. The beams are then focused onto the atoms in the center of the glass cell where the beam waist is approximately

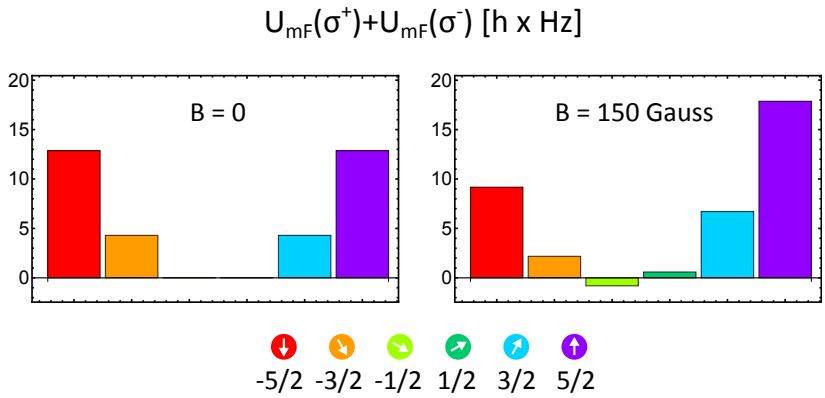

Figure 3.7: State-dependent light shifts induced by equal amounts of σ^+ and σ^- light. Note how the symmetry $U_{m_F} = U_{-mF}$ is broken by the presence of a magnetic field. The beam waist chosen for the calculation is $w_0 = 150\,\mu$m whereas the total power is $P = 1\,\mu$W.

$w_0 = 150\,\mu$m. Part of the light is picked up by two beam samplers and sent to a reference photodiode, where the beat note between the Raman beams is monitored. The optical path mismatch between the two beams is kept at minimum, since they travel along the same fiber. In this way we don't need to actively stabilize the beating note.

Since the Raman beams impinge onto the atoms from different directions, there is also a momentum kick in addition to the energy and angular momentum transfer. The absolute value of the momentum kick q_R depends on the angle between the Raman beams and is given by:

$$q_R = |\vec{k}_1 - \vec{k}_2| = 2k_R \sin\theta/2 \tag{3.0}$$

in which k_R is the linear momentum of the green radiation at 556 nm. We will see in Chapter 5 that this is the ingredient at the basis of the creation of an artificial gauge field in a synthetic 2D lattice.

3.3 Raman-induced spin oscillations

In order to characterize the Raman couplings, we perform spin-oscillations measurements from which we extract the Raman amplitudes given by Eq. (3.1). The system under study is characterized by a maximum number of spin components equal to three ($\Delta m_F = \pm 2$) and also the experiments described in Chapter 5 are performed under these conditions.
We load a fully polarized Fermi gas ($N_{at} \sim 3 \cdot 10^4$, $T/T_F \sim 0.2$, $m_F = \pm 5/2$) in a 3D optical lattice with periodicity $d = \lambda_L/2 = 380$ nm and lattice depths $s_x = s_y = s_z = 30$. In this way we can neglect[1] the ki-

[1]The atomic sample under study has a momentum spread that is given by the Fermi momentum k_F. Since the Raman coupling introduces also a momentum kick, not all

netic energy in Eq. (1.3), since the tunneling at such high lattice depths is completely suppressed. This restricts the dynamics to only the internal degrees of freedom and we can forget about the momentum kick given by the Raman process.

3.3.1 Two-level system

We start from the simplest configuration explored, the two-level case, in which only two spin components are made to participate to the dynamics. To select this configuration each Raman beam must have horizontal polarization[2] which, with respect to the quantization axis, is decomposed in equal amounts of σ^+ and σ^- polarizations. To separate the otherwise degenerate spin components, we put a magnetic field ranging from $B = 50\,\mathrm{G}$ to $B = 153\,\mathrm{G}$ giving a Zeeman splitting in the range $\Delta_Z = 2\pi \times 10 - 31\,\mathrm{kHz}$. This splitting is enough to suppress unwanted Raman transitions (arising from a possible power broadening) and also makes non resonant possible transitions to higher lattice bands [106, 107]. In Fig. 3.7 we plot the state-dependent light shifts induced by equal amounts of σ^+ and σ^- light. As a comparison we show also the $B = 0$ case, noticing that the presence of a magnetic field breaks the symmetry[3] $U_{m_F} = U_{-m_F}$. This is true also for the Raman amplitudes[4], as is shown in Fig. 3.8. The spin components entering the dynamics are $m_F = -5/2, -1/2, +3/2$. Let's suppose we start from the $m_F = -5/2$ component. By choosing a two-photon Raman detuning that matches both the Zeeman energy splitting and the differential light shifts $U_{-1/2} - U_{-5/2}$, the first two spin components can be put precisely on resonance whereas the last one acquires all the energy offset, as can be easily seen by the form of the Hamiltonian governing the spin dynamics (from which we subtracted the Zeeman en-

the atoms will be at resonance [17, 61, 66] with the Raman light, apart from the case in which the Raman coupling satisfies the power broadening condition $\hbar\Omega_R \gg E_F$. This is different with respect to a Bose-Einstein condensate for which the momentum spread can be neglected [16].

[2] That is, perpendicular to the magnetic field quantization axis, see Fig. 3.6.

[3] As we show in Appendix B, this is due to the behaviour of the excited state $^3P_1$ manifold energy levels in the presence of a magnetic field.

[4] Since the polarization of both beams is horizontal, the atomic sample sees both σ^+ and σ^- polarization components with a double frequency spectrum, giving rise to several possible processes. Nevertheless, in the frame rotating at $2\Delta_Z$, only one transition is resonant since the others are detuned at least by $2\Delta_Z$ (see Fig. 3.1). These processes are then negligible if the power broadening is lower than the level separation.

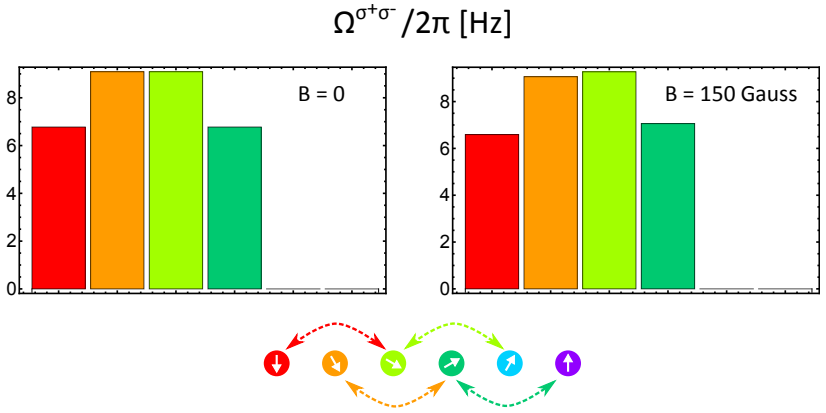

Figure 3.8: Raman couplings $\Omega_{m_F}^{\sigma^+\sigma^-}$ in case of complete horizontal polarization. Note how the symmetry $\Omega_{m_F}^{\sigma^+\sigma^-} = \Omega_{-m_F}^{\sigma^+\sigma^-}$ is broken by the presence of a magnetic field. The beam waist chosen for the calculation is $w_0 = 150\,\mu$m whereas the total power is $P = 1\,\mu$W

ergy):

$$H_R \simeq \begin{pmatrix} U_{-5/2} & \hbar\Omega_{R,1}/2 & 0 \\ \hbar\Omega_{R,1}/2 & U_{-1/2} - \hbar\delta_R & \hbar\Omega_{R,2}/2 \\ 0 & \hbar\Omega_{R,2}/2 & U_{+3/2} - 2\hbar\delta_R \end{pmatrix} \xrightarrow{\hbar\delta_R = U_{-1/2} - U_{-5/2}}$$

$$\begin{pmatrix} 0 & \hbar\Omega_{R,1}/2 & 0 \\ \hbar\Omega_{R,1}/2 & 0 & \hbar\Omega_{R,2}/2 \\ 0 & \hbar\Omega_{R,2}/2 & U_{+3/2} + U_{-5/2} - 2U_{-1/2} \end{pmatrix}$$

in which δ_R is the two-photon Raman detuning (already including the linear Zeeman splitting $2\Delta_Z$), U_{m_F} are the spin-dependent light shifts and $\Omega_{R,1}$, $\Omega_{R,2}$ are the Raman couplings $m_F = -5/2 \to m_F = -1/2$, $m_F = -1/2 \to m_F = +3/2$ respectively. Rewriting the various terms as a function of $\Omega_{R,1}$, we obtain:

$$\frac{H_R}{\hbar} \simeq \begin{pmatrix} 0 & \Omega_{R,1}/2 & 0 \\ \Omega_{R,1}/2 & 0 & \alpha_1 \cdot \Omega_{R,1}/2 \\ 0 & \alpha_1 \cdot \Omega_{R,1}/2 & \alpha_2 \cdot \Omega_{R,1} \end{pmatrix}$$

where the numerical coefficients[5] α_1, α_2 come from the proportionalities imposed by Eqs. (1.2.3) and (3.1), and weakly depend on the magnetic field B. For $B = 153\,G$, $\alpha_1 = 1.41$ and $\alpha_2 = 2.65$, from which wee see that the $m_F = +3/2$ component is out of resonance by an amount $2.65 \cdot \Omega_{R,1}$. This is sufficient to consider the dynamics effectively restricted to the

[5]The exact value of these coefficients depends on the magnetic field, which causes corrections of the order of 6%, see Appendix B.

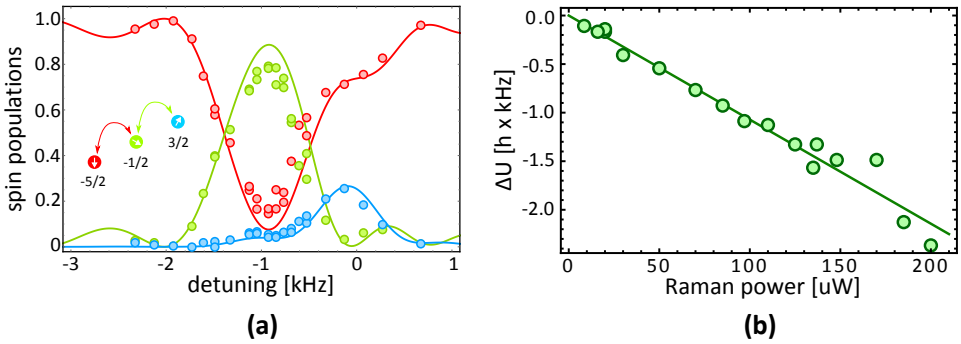

Figure 3.9: Light shift characterization for the 2-level case. **(a)** Typical two-photon resonance starting from $m_F = -5/2$: the parameters are $P = 85$ μW, $B = 153$ Gauss and $\tau = 800$ μs. Solid lines are the fit results (see text). The frequencies on the x-axis are rescaled in the rotating frame by subtracting $2\Delta_Z = 2\pi \times 63.3(2)$ kHz. **(b)** Differential light shift measured as a function of the Raman power.

$m_F = -5/2, -1/2$ components only. Of course we could arrive at similar conclusions by starting from the $m_F = +5/2$ components and obtain a dynamics restricted to $m_F = +5/2, +1/2$. In order to start a coherent oscillation it is necessary to find the resonance condition, i.e. the two-photon detuning that matches, in the rotating frame, the differential light shift $U_{-1/2} - U_{-5/2}$. We fix the total Raman power and we perfom Raman spectroscopy starting from the $m_F = -5/2$ spin component. By varying the two-photon frequency detuning, we record the spin-population distribution after a certain amount of time τ of Raman evolution. This time interval satisfies the condition $\Omega_{R,1}\tau < \pi$, i.e. the spin-population does not invert during the dynamics. This can be done for various Raman powers in order to compare the measured differential light shifts with the ones calculated starting from Eq. (1.2.3). In Fig. 3.9a we show a typical resonance measurement in which the solid lines are fitted curves based upon Eq. (3.3.1) in which $U_{-5/2}$ and $\Omega_{R,1}$ are used as fit parameters and $U_{-1/2}$, $U_{+3/2}$, $\Omega_{R,2}$ are fixed by the proportionality relations imposed by the Clebsch-Gordan coefficients. In Fig. 3.9b we report the measured differential light shift as a function of the Raman power.

Having found the resonances at a certain Raman power, we start the Rabi dynamics which, as is shown in Fig. 3.10a, is basically confined to only two spin components. In order to measure the system parameters, we fit the data to the Raman evolution governed by the Hamiltonian (3.3.1) using $\Omega_{R,1}$ as a free parameter[6] and taking the light shift $U_{-5/2}$ extracted from the resonance fit in Fig. 3.9. In particular, we simulate numeri-

[6]We discard the $\Omega_{R,1}$ resulting from the resonance fit, since it is much more precise to extract the Raman amplitude directly from the oscillation fit.

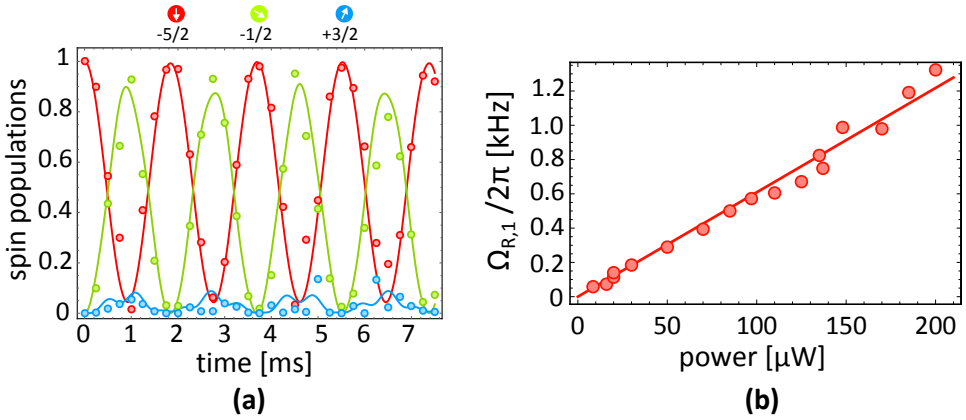

Figure 3.10: Raman evolution characterization. **(a)** Typical Raman evolution with pure horizontal polarizations starting from the $m_F = -5/2$ state. Solid lines are the fitted population evolutions with parameters $P = 85\,\mu$W, $U_{-5/2} = h \times 757$ Hz and $\Omega_{R,1} = 2\pi \times 547$ Hz. At $B = 153$ G the other parameters are determined by the relations $U_{+3/2} + U_{-5/2} - 2U_{-1/2} = 2.65 \cdot \hbar\Omega_{R,1}$ and $\Omega_{R,2} = 1.41 \cdot \Omega_{R,1}$. **(b)** Raman coupling $\Omega_{R,1}$ measured as a function of the Raman power.

cally the three-level evolution for a set of $\Omega_{R,1}$ and choose the one that minimizes the mean squared error with respect to the experimental data points. In Fig. 3.10b we show the experimentally measured Raman coupling $\Omega_{R,1}$ as a function of power. These data and the measured light shifts can be combined in order to extract the ratio $(U_{-1/2} - U_{-5/2})/\hbar\Omega_{R,1} = 1.53 \pm 0.03$, that is in very good agreement with the theoretical expectation $\Delta U/\hbar\Omega_{R,1} = 1.51$, see Fig. 3.11. Having studied the simple two-level case, we are ready to move to the more complex three-level system.

3.3.2 Three-level system

In order to couple resonantly also the third state, it is necessary that the spin-dependent energy offsets are equal. At zero magnetic field this is achieved by using a uniform polarization[7]:

$$\hat{\boldsymbol{\varepsilon}}_{tot} = \frac{1}{\sqrt{3}}(\hat{\boldsymbol{\varepsilon}}_+ + \hat{\boldsymbol{\varepsilon}}_- + \hat{\boldsymbol{\varepsilon}}_\pi). \tag{3.-2}$$

The Hamiltonian governing the system is the same as in Eq. (3.3.1), in which the uniform polarizations condition determines the new spin dependent light shifts U_{m_F}. By rewriting Eq. (3.3.1) in terms of $\Omega_{R,1}$ we

[7] This comes from a symmetry relation that the Clebsch-Gordan coefficients satisfy. In particuar we have that $\sum_q |\mathcal{C}_{mn}(q)|^2 = \left\{ \begin{matrix} J & J' & 1 \\ F' & F & I \end{matrix} \right\} (2F'+1)(2J+1)$, independent of the particular spin component m_F.

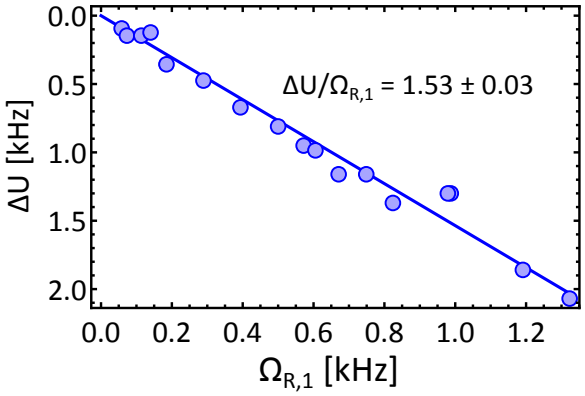

Figure 3.11: Measured differential light shift $\Delta U = (U_{-1/2} - U_{-5/2})$ as a function of the Raman coupling $\Omega_{R,1}$. The solid line is a linear fit giving the ratio $\Delta U/\hbar\Omega_{R,1} = 1.53 \pm 0.03$ in very good agreement with the theoretical expectation $\Delta U/\hbar\Omega_{R,1} = 1.51$.

obtain:

$$\frac{H_R}{\hbar} \simeq \begin{pmatrix} 0 & \Omega_{R,1}/2 & 0 \\ \Omega_{R,1}/2 & 0 & \alpha_1 \cdot \Omega_{R,1}/2 \\ 0 & \alpha_1 \cdot \Omega_{R,1}/2 & \beta_2 \cdot \Omega_{R,1} \end{pmatrix}$$

in which the new coefficient β_2 depends on the magnetic field and on the new polarization chosen. For $B = 153\,G$ we have $\alpha_1 \simeq 1.41$ and $\beta_2 \simeq 0.16$, from which we see that the third state is only slightly out of resonance and can still be coupled in an efficient way.

If, from one side, the uniform polarization allows us to resonantly couple all the three states, from the other, it sets an additional constraint to the validity of the three-level model (3.3.2). Indeed, given the presence of π polarization in the Raman beams, $\sigma^{\pm}\pi$ processes have a non-zero probability and are detuned only by Δ_Z. Therefore, the additional condition $\Omega^{\sigma^{\pm}\pi} \ll \Delta_Z$ must be fulfilled to prevent power broadening to excite these unwanted processes. For this reason, we decided to work only at magnetic field $B > 150$ Gauss in order to relax the constraint on the power broadening and limit the spurious $\sigma^{\pm}\pi$ processes by increasing the Zeeman splitting. The presence of such a large magnetic field breaks the light shifts symmetry and causes a linear dependence of the resonance on the Raman power. By performing Raman spectroscopy as in the two-level system, we can compare the measured resonance position with the one expected by the theoretical model of Eq. (3.3.2) in which $U_{-5/2}$ and $\Omega_{R,1}$ are used as fit parameters. In Fig. 3.13 (left) we show a typical resonance acquisition from which we extract the expected light shift $U_{-5/2}$. This measurement is performed as a function of the total Raman power, as is shown in Fig. 3.13 (right). The linear dependence of the light shift on the total Raman

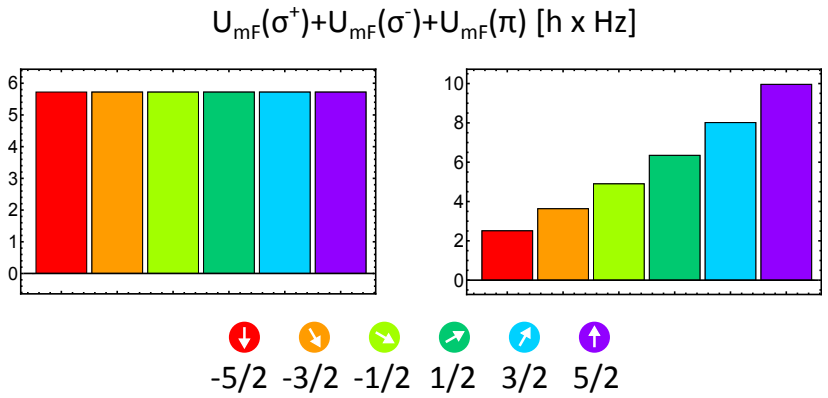

Figure 3.12: State-dependent light shifts induced by uniform polarization. $B = 0\,G$ (left) and $B = 153\,G$ (right). Note how the symmetry $U_{m_F} = U_{-mF}$ is broken by the presence of a magnetic field. The beam waist chosen for the calculation is $w_0 = 150\,\mu$m

power is an order of magnitude smaller than the pure horizontal polarization configuration (2.8 ± 0.13 Hz/μW) and it is in reasonable agreement with the expected slope of 2.52 Hz/μW.

Having found the optimal two-photon detuning, the Raman evolution is started, as is displayed in Fig. 3.14a. All three states are involved in the coherent dynamics and also in this case, the evolution is fitted by fixing $U_{-5/2}$ to the value measured with the resonance fit and letting $\Omega_{R,1}$ as a free parameter. Especially in the three-level evolution, we observe a small damping that we attribute to technical problems such as the inhomogeneity of the Raman beams profile and imperfections in the polarization. The first one causes the atoms to experience space-dependent Rabi frequencies and light shifts which lead to a dephasing in the global population evolution. This issue can be solved by using much bigger waists for the Raman beams. The polarization imperfections introduce unwanted energy offsets by modifying the spin-dependent light shifts. This causes the dynamics to be much more complicated as can be seen in the theoretical curves in Fig. 3.16 in which the polarization has been slightly modified with respect to the uniform condition (10% more of σ^+ and σ^- polarizations). In Fig. 3.14b we plot the extracted Raman coupling $\Omega_{R,1}$ as a function of the total Raman power. The measured slope[8], 4.2 ± 0.3 Hz/μW is quite consistent with the expected value 4.4 Hz/μW. We can combine the measured Raman couplings and light shifts $U_{-5/2}$ in a single plot that we show in Fig. 3.15. The measured ratio $U_{-5/2}/\hbar\Omega_{R,1} = 0.68 \pm 0.08$ is 16% higher than the expected $U_{-5/2}/\hbar\Omega_{R,1} = 0.57$ value. This discrepancy could come from the

[8]This slope is lower than the one in Fig. 3.8 by a factor of 2/3 because of the lower fraction of σ^+, σ^- light on the total power in the case of uniform polarization with respect to the case of pure horizontal polarization.

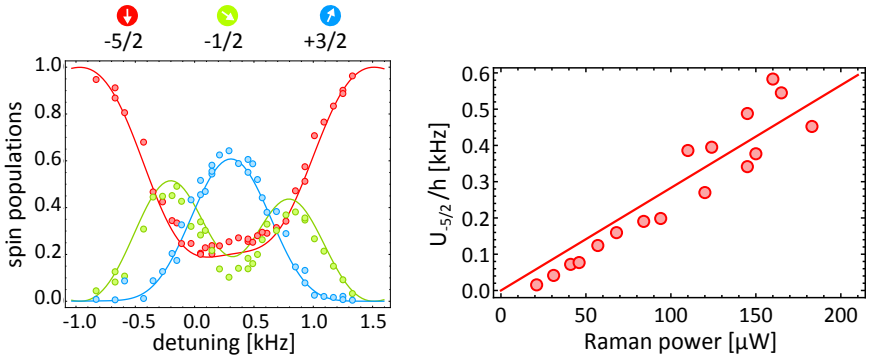

Figure 3.13: Light shift characterization for the 3-level case. Typical two-photon resonance (left) starting from $m_F = -5/2$: the parameters are $P = 145$ μW, $B = 153$ Gauss and $\tau = 800$ μs. Solid lines are the fit results (see text). The frequencies on the x-axis are rescaled in the rotating-frame by subtracting $2\Delta_Z = 2\pi \times 63.3(2)$ kHz. Light shift $U_{-5/2}$ extracted from the resonance fit versus the total Raman power (right).

imperfect polarization determining different energy offsets with respect to the one expected from uniform polarization.

All the characterizations presented in these sections have been made by loading a full polarized Fermi gas in a deep 3D optical lattice. For such a system, the kinetic energy is completely negligible on the time-scale of the experiment and we can forget about the momentum kick imparted to the atoms by the Raman beams. In Chapter 5 we will relax this condition and, in particular, we will lower one of the optical lattice depths in order to restore the tunneling between neighboring lattice sites. In this way there will be two dynamical processes: tunneling, which is governed by the kinetic energy of the atoms, and spin population evolution, governed by the Raman coupling. Both processes are coherent and mathematically describable with the same formalism, based on a tight-binding Hamiltonian [22]. Indeed, in both cases there is a particle hopping between neighboring sites, real 1D lattice sites and *spin-lattice sites*. In this sense we can talk about an effectively two-dimensional hybrid lattice in which one direction is formed by the real lattice wells of a 1D lattice and the other direction is formed by the spin components, coherently coupled by the Raman beams. Now that the kinetic energy of the atoms is not negligible anymore, the Raman-imparted momentum kick becomes fundamental in determining a new type of quantum behaviour, governed by the famous Harper-Hofstadter hamiltonian [108, 109], that has been recently engineered with ultracold bosonic samples [12, 13, 21, 23] and that describes the behaviour of electrons moving in a 2D lattice in the presence of a uniform magnetic field. This new type of physics is at the core of this PhD thesis and will be described in the next Chapters.

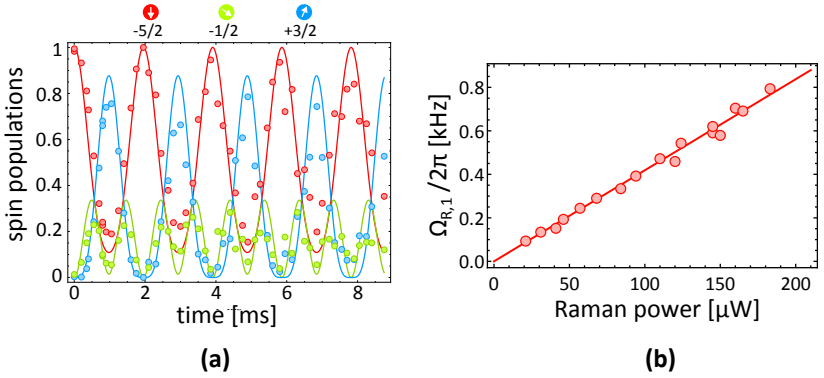

Figure 3.14: **(a)** Raman evolution with uniform polarization starting from the $m_F = -5/2$ state for $P = 145\,\mu$W. Solid lines are the fitted population evolutions with $U_{-5/2} = h \times 341.5$ Hz and $\Omega_{R,1} = 2\pi \times 590$ Hz. At $B = 153$ G the other parameters are determined by the relations $U_{+3/2} + U_{-5/2} - 2U_{-1/2} = 0.16 \cdot \Omega_{R,1}$ and $\Omega_{R,2} = 1.41 \cdot \Omega_{R,1}$. **(b)** Raman coupling $\Omega_{R,1}$ versus total Raman power.

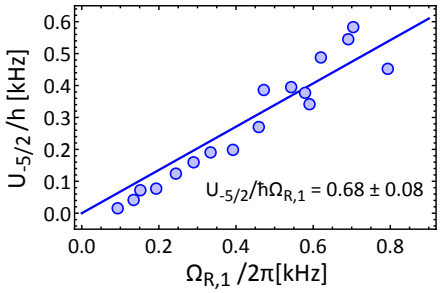

Figure 3.15: Measured light shift $U_{-5/2}$ as a function of the Raman coupling $\Omega_{R,1}$. The solid line is a linear fit giving the ratio $U_{-5/2}/\hbar\Omega_{R,1} = 0.68 \pm 0.08$ which is 16% higher then the expected value of $U_{-5/2}/\hbar\Omega_{R,1} = 0.57$.

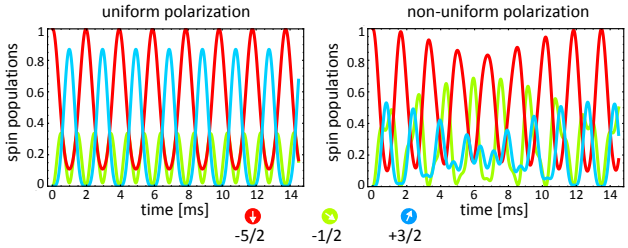

Figure 3.16: Theoretical evolution for the 3-level system in case of uniform polarization (left) or non-uniform polarization (right) in which the fraction of σ^+ and σ^- light is 10% higher than in the uniform case. Parameters: $P = 145\,\mu$W, $w_0 = 150\,\mu$m and $\delta_R = U_{-1/2}(\varepsilon_{tot}) - U_{-5/2}(\varepsilon_{tot})$ in both cases.

4 Quantum Hall physics on a lattice: an overview

A recurring theme in condensed matter physics has been the discovery and classification of distinctive phases of matter. Landau's approach characterizes states in terms of underlying symmetries that are spontaneously broken, bringing a system to display a particular order. For example in a crystal, ions are arranged periodically owing to their electrostatic interactions, thereby breaking the continuous symmetry of space under rotations and translations. In typical magnets, some of the rotational symmetry of spin space is broken, together with time-reversal symmetry [110, 111].

A completely different, topological [112, 113], type of order was discovered in the 1980s, when electrons confined to two dimensional structures were subjected to strong magnetic fields. When placed in a magnetic field large enough that Landau-level quantization becomes important, electrons exhibit a *quantized Hall effect*, in which the Hall conductance is an integer in units of the quantum of conductance, e^2/h and the transport becomes dissipationless along the edges of the system [114–116].

This Chapter gives a description of such phenomena from a lattice perspective introducing the notions that will be important for our synthetic two-dimensional system based upon neutral ultracold fermions.

4.1 Magnetic field on a square lattice

Electrons moving in a periodic structure are typically described by the Hubbard model, which represents a valuable approximation when the particles occupy only the lowest energy band [57]. The non-interacting Hamiltonian on a 2D square lattice can be written as:

$$\hat{H}_0 = -t \sum_{n,m} \left(\hat{c}^\dagger_{n+1,m} \hat{c}_{n,m} + \hat{c}^\dagger_{n,m+1} \hat{c}_{n,m} \right) + h.c. \tag{4.0}$$

where $\hat{c}^\dagger_{n,m}$, $\hat{c}_{n,m}$ are the creation and annihilation operators on site (n, m) respectively, n is the site along $\hat{x}$ direction, m is the site along $\hat{y}$ direction and t is the tunneling between nearest neighboring sites which, in the

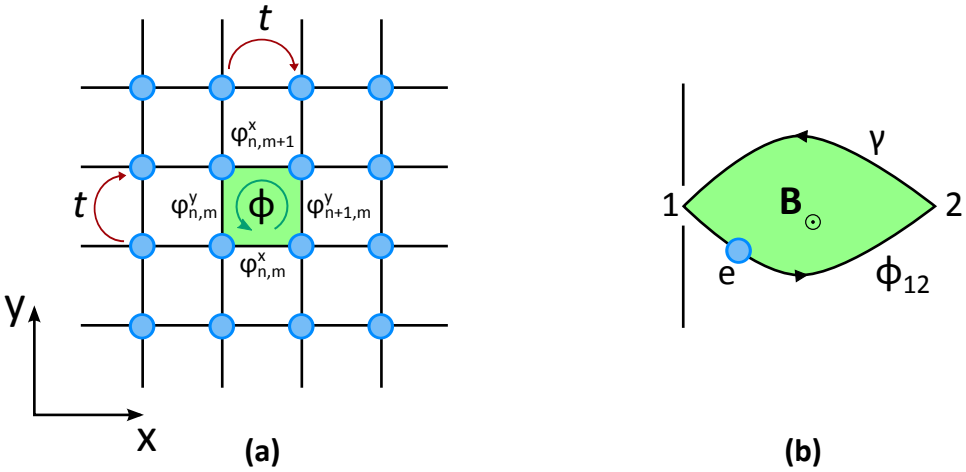

Figure 4.1: Equivalence between Peierls phase and Aharonov-Bohm phase. **(a)** Sketch of a 2D lattice in which the tunneling is complex. When an electron hops around a plaquette it acquires a phase $\Phi = \phi^x_{n,m} + \phi^y_{n+1,m} - \phi^x_{n,m+1} - \phi^y_{n,m}$ due to the presence of a vector potential $\mathbf{A}$. **(b)** Aharonov-Bohm effect in which an electron moving along a closed trajectory γ in an external magnetic field $\mathbf{B} = \nabla \times \mathbf{A}$, picks up a geometric phase Φ_{12}.

tight-binding approximation, are occupied by the ions. According to the Peierls substitution [115], when a transverse magnetic field is added to the system, the tunneling matrix elements become complex and hopping between sites acquires a phase $\phi^k_{n,m} = eA^k_{n,m}/\hbar$, $k = x, y$, which is known as *Peierls phase* (Fig. 4.1a), where e is the electron charge and $\mathbf{A}(\mathbf{r})$ is the external vector potential. Accordingly, the tight-binding Hamiltonian takes the form:

$$\hat{H} = -t \sum_{n,m} \left(e^{i\phi^x_{n,m}} \hat{c}^\dagger_{n+1,m} \hat{c}_{n,m} + e^{i\phi^y_{n,m}} \hat{c}^\dagger_{n,m+1} \hat{c}_{n,m} \right) + h.c. \tag{4.0}$$

The Peierls phases are directly related to the Aharonov-Bohm phase acquired by a charged particle when moving in a magnetic field (Fig. 4.1b):

$$\Phi_{12} = \frac{e}{\hbar} \oint_\gamma \mathbf{A} \cdot d\mathbf{r} = 2\pi \frac{\Phi_B}{\Phi_0} \tag{4.0}$$

where Φ_B is the magnetic flux penetrating the area enclosed by the contour γ and $\Phi_0 = h/e$ is the magnetic flux quantum [117]. We can also define the magnetic flux per plaquette in units of magnetic flux quantum as:

$$\alpha = \frac{\Phi}{2\pi} = \frac{1}{2\pi}(\phi^x_{n,m} + \phi^y_{n+1,m} - \phi^x_{n,m+1} - \phi^y_{n,m}). \tag{4.0}$$

The lattice hamiltonian (4.1) has a $U(1)$ gauge symmetry:

$$\hat{c}_i \to U_i \hat{c}_i, \qquad e^{i\phi_{i,j}} \to U_i e^{i\phi_{i,j}} U_j^{-1}, \qquad |U_i| = 1, \ \forall i \in (n, m) \tag{4.0}$$

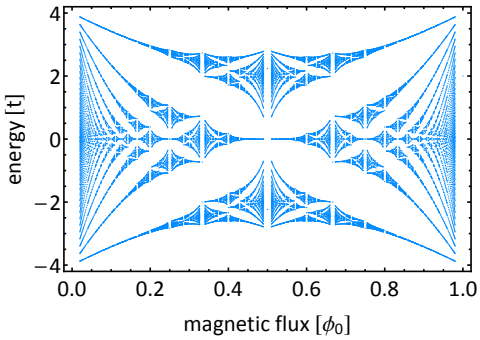

Figure 4.2: Single-particle energy spectrum of hamiltonian (4.1) with periodic boundary conditions known as Hofstadter's butterfly.

that is just a gauge transformation on $\mathbf{A}$. In particular, by choosing the Landau gauge $\mathbf{A} = (0, x\,\Phi, 0)$ we can rewrite the hamiltonian (4.1) as:

$$\hat{H} = -t \sum_{n,m} \left(\hat{c}^{\dagger}_{n+1,m} \hat{c}_{n,m} + e^{i\Phi n} \hat{c}^{\dagger}_{n,m+1} \hat{c}_{n,m} \right) + h.c. \tag{4.0}$$

in which only the tunneling along $\hat{y}-$direction is complex, whereas the tunneling along $\hat{x}$ is real. This Hamiltonian is known as the famous Harper-Hofstadter Hamiltonian [108, 109] and, in the case of periodic boundary conditions, its single-particle energy spectrum exhibits a fractal self-similar structure as a function of the flux α, known as Hofstadter's butterfly which is shown in Fig. 4.2. The fractal structure emerges from the fact that in presence of a rational flux per plaquette $\alpha = p/q$, the fundamental energy band splits into q subbands with dispersion relations $\varepsilon_{\eta}(\mathbf{k})$, $\eta = \{1, ..., q\}$ [115]. When the flux is an irrational number, the energy spectrum becomes even more complicated and splits into an infinite number of energy levels forming a Cantor set [109].

4.2 Diagonalization of the Harper-Hofstadter Hamiltonian

In order to extract the Hofstadter's butterfly we have to diagonalize Hamiltonian (4.1) and calculate the single-particle energy spectrum. We will start by performing a Fourier-transform:

$$\hat{c}_{n,m} = \frac{1}{(2\pi)^2} \int_{-\pi}^{\pi} dk_x \int_{-\pi}^{\pi} dk_y e^{ik_x n + ik_y m} \hat{c}_{k_x,k_y} \tag{4.0}$$

where $-\pi \leq k_x, k_y \leq \pi$, and require $\hat{c}_{k_x+2\pi i, k_y+2\pi j} = \hat{c}_{k_x,k_y}$. The presence of a magnetic field couples different $k-$sectors of the Fourier-transformed

Hamiltonian:

$$\hat{H} = -t \int_{-\pi}^{\pi} \frac{dk_x dk_y}{(2\pi)^2} \left[2\cos(k_x) \hat{c}^{\dagger}_{k_x,k_y} \hat{c}_{k_x,k_y} + \hat{c}^{\dagger}_{k_x+2\pi\alpha,k_y} \hat{c}_{k_x,k_y} e^{-ik_y} + h.c. \right] \quad (4.0)$$

where we wrote $\Phi = 2\pi\alpha$. The Fourier transform of the Hamiltonian mixes $(k_x, k_y) \rightarrow (k_x \pm 2\pi\alpha, k_y)$ and we need to find a momentum space where the mixing is absent. If the flux is a rational number $\alpha = p/q$, where p and q are coprimes, Eq. (4.2) splits in several sectors if the Brillouin zone is taken to be q times smaller than the initial one in the $\hat{x}-$direction:

$$\hat{H} = \frac{1}{(2\pi)^2} \int_{-\pi/q}^{\pi/q} dk_x \int_{-\pi}^{\pi} dk_y \hat{H}_{k_x,k_y} \quad (4.0)$$

where

$$\begin{aligned} \hat{H}_{k_x,k_y} = & -t \sum_{n=0}^{q-1} \Big[2\cos(k_x + 2\pi\alpha n) \hat{c}^{\dagger}_{k_x+2\pi\alpha n,k_y} \hat{c}_{k_x+2\pi\alpha n,k_y} + \\ & + \left(e^{-ik_y} \hat{c}^{\dagger}_{k_x+2\pi\alpha(n+1),k_y} \hat{c}_{k_x+2\pi\alpha n,k_y} + e^{ik_y} \hat{c}^{\dagger}_{k_x+2\pi\alpha(n-1),k_y} \hat{c}_{k_x+2\pi\alpha n,k_y} \right) \Big] \end{aligned}$$

in which $k_x \rightarrow k_x + 2\pi\alpha n$. This partition of the Brillouin zone (BZ) works only if p and q are relatively prime, only in this case is the covering $k_x + 2\pi\alpha n$ able to reproduce the whole initial $-\pi \leq k_x \leq \pi$ [115].

With this partition for the Hamiltonian, no k_{x1} mixes with another k_{x2} when both are in the $[-\pi/q, \pi/q]$ reduced BZ. The price paid is that the *magnetic unit cell* is made up of q plaquettes in the $\hat{x}-$direction and the *magnetic BZ* is q times smaller than the non magnetic one. The Schrodinger equation in a $q-$ sector,

$$\hat{H}_{k_x,k_y} |\psi\rangle = E_{k_x,k_y} |\psi\rangle, \quad (4.\text{-}1)$$

reduces to solving a 1D tight binding model on a 1D lattice chain in momentum space, $k_x + 2\pi\alpha n$, $n = 0, 1, 2..., q-1$. The single-particle energies are obtained by expanding into single-particle states at each momentum lattice point n,

$$\psi = \sum_{n=0}^{q-1} a_n \hat{c}^{\dagger}_{k_x+2\pi\alpha n,k_y} |0\rangle \quad (4.\text{-}1)$$

and diagonalizing. The eigenvalue equation is:

$$-t \left[2\cos(k_x + 2\pi\alpha n) a_n + e^{-ik_y} a_{n-1} + e^{ik_y} a_{n+1} \right] = E_{k_x,k_y} a_n \quad (4.\text{-}1)$$

which can be numerically solved with the boundary conditions $a_{n+q} = a_n$. This is called the Harper equation and its solutions give the famous Hofstadter's butterfly, Fig. 4.2.

4.3 Chern numbers

The Harper-Hofstadter Hamiltonian is characterized by topological invariants, i.e. integer numbers that classify equivalence classes of $\hat{H}$ that can be continuosly deformed into one another without closing energy gaps. It has been shown that the quantization of the Hall conductance is directly related to such topological invariants known as Chern numbers [112]. In a quantum Hall experiment, a DC current is fed into a sample and the transverse voltage, in the presence of a strong magnetic field, is measured. The Hall conductance σ_H can be extracted and, at sufficiently low temperatures, it is quantized according to:

$$\sigma_H = \frac{e^2}{h} \sum_q \nu_q \tag{4.-1}$$

where ν_q is the Chern number of the $q-$th band E_q and the sum has to be taken over all occupied energy bands below the Fermi energy E_F. The Chern number ν_q can be deduced from the equation:

$$\nu_q = \frac{1}{2\pi} \int_{FBZ} dk_x dk_y \Omega_q(\mathbf{k}) \tag{4.-1}$$

in which:

$$\Omega_q(\mathbf{k}) = i\langle \frac{\partial u_q(\mathbf{k})}{\partial k_x} | \frac{\partial u_q(\mathbf{k})}{\partial k_y} \rangle - \langle \frac{\partial u_q(\mathbf{k})}{\partial k_y} | \frac{\partial u_q(\mathbf{k})}{\partial k_x} \rangle \tag{4.-1}$$

is the Berry curvature of the $q-$th band [118], and the integral is carried out over the fundamental magnetic BZ. The functions $u_q(\mathbf{k})$ are the eigenstates determined from Eq. (4.2). The Chern number was derived by assuming an infinite 2D system without edges. In the presence of edges, it can be demonstrated [119] that, if there are q energy bands, each energy gap has one edge state, i.e. there are $q-1$ edge states. The energies of such edge states are given by the zero points of the Bloch function on some Riemann surface and the Hall conductance σ_H is given by the winding number of the edge states around the holes of this Riemann surface [119]. There is thus a *bulk-edge correspondance* that relates the topological properties of the edge modes to the ones of the bulk.

Fortunately, a simple analytical relation exists which determines the value of the Chern number. Indeed, consider a generic insulator and suppose that we place the Fermi level in a band gap. Then, given a rational flux $\alpha = p/q$, there exist two integers s_r and t_r determined by the Diophantine equation [115, 121]:

$$r = qs_r + pt_r, \qquad |t_r| \leq \frac{q}{2}, \qquad s_r, t_r \in \mathbb{Z} \tag{4.-1}$$

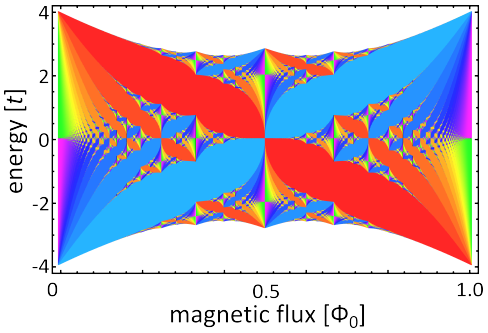

Figure 4.3: Color coded Hofstadter's butterfly. Warm colors represent positive values of Hall conductance and cold colors represent negative values. Zero Hall conductance is left blank. Adapted from [120].

where r denotes the $r-$th energy gap of the single particle energy spectrum. The solutions of Eq. (4.3) are uniquely defined and in particular, the integer t_r is directly related to the Hall conductivity according to:

$$\sigma_H = -\frac{e^2}{h} t_r. \tag{4.-1}$$

In Fig. 4.3 we plot the Hofstadter's butterfly, in which the band gaps have been color coded [120] according to the Hall conductance (Chern numbers): warm colors represent positive values of Hall conductance and cold colors represent negative values. Zero Hall conductance is left blank.

4.4 Edge states

A fundamental consequence of the topological classification of gapped band structures is the existence of gapless conducting states at interfaces where the topological invariant changes [110]. Indeed, bring two insulators[1], each with different values of the Hall conductance, close to each other, so that they share a boundary. Because we know that the Hall conductance is an integer which characterizes the phase of the system, and we know that it cannot be changed unless a bulk band gap closes and reopens again, the conclusion is that the boundary region linking both the insulators must have a gap-closing-and-reopening point somewhere on it, i.e. it must have an *edge mode* crossing the Fermi level. For a quantum Hall state, such edge mode may be understood in terms of cyclotron orbits that are naturally truncated at the boundary of the system (skipping orbits). Importantly, the states responsible for this motion are *chiral* in the sense that they propagate in one direction only along the edge. Also, they are

[1] One of the insulator can also be the vacuum.

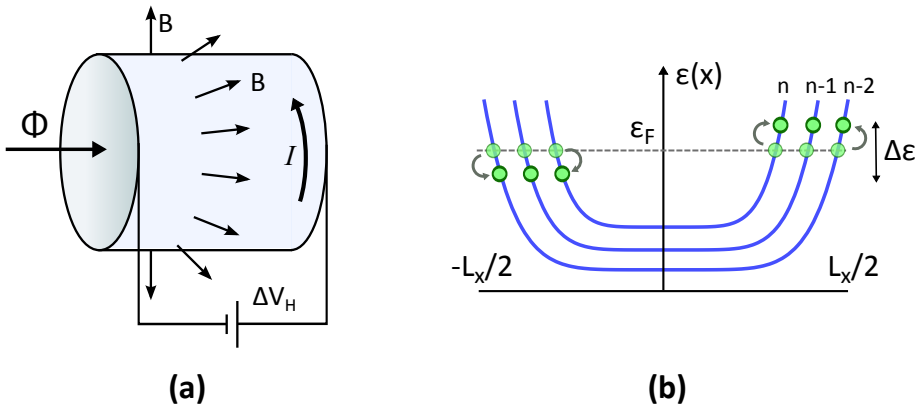

Figure 4.4: Laughlin argument. **(a)** Schematic drawing of the Laughlin cylinder. **(b)** One particle per energy level jumps from one edge to the other, when a magnetic flux quantum is injected through the cylinder, causing an energy drop $\Delta E = ne\Delta V_H$ which defines the Hall voltage.

insensitive to disorder because there are no states available for backscattering, a fact that is at the basis of the perfect quantization of the Hall conductance. The original argument for the presence of edge states in the quantum Hall effect is due to Laughlin [122] in the early 1980s. We will now review his seminal paper.

4.4.1 Laughlin's argument

In [122], Laughlin argued that the presence of edge modes is an inescapable consequence of transverse quantized transport in an insulator. We consider a two-dimensional material (no lattice is present) with a magnetic field perpendicular to it. We choose periodic boundary conditions along the longitudinal direction $\hat{y}$ but place edges on the sample along the transversal direction $\hat{x}$. Such a geometry is equivalent to the one of a cylinder, whose axis is along $\hat{x}$ and in which the magnetic field points along the radial direction (see Fig. 4.4a). We know that, [71], the single-particle eigenfunctions of the problem in the Landau gauge are given by the product of a plane wave along $\hat{y}$ and a harmonic oscillator wavefunction along $\hat{x}$. The harmonic oscillator wavefunction is centered around x_0, which in turn depends linearly on k_y, so that the electrons centered in the proximity of the left/right edge of the cylinder, have specific wavenumbers along $\hat{y}$.

Through the cylinder, parallel to the $\hat{x}-$axis, insert a flux Φ. This flux is different from the flux generated by the magnetic field, which is normal to the surface of the cylinder. We wish to relate the total current I carried around the cylinder to the voltage drop ΔV_H from one edge to the other. This current is equal to the adiabatic derivative of the total energy E of the

system with respect to the magnetic flux Φ through the cylinder:

$$I = \frac{\partial E}{\partial \Phi} = \frac{1}{L}\frac{\partial E}{\partial A_\theta} \tag{4.-1}$$

in which $\vec{A}$ is the vector potential pointing around the cylinder, that can be written as:

$$\vec{A} = (A_r,\, A_\theta,\, A_z) = \frac{\Phi}{L}\hat{\theta} \tag{4.-1}$$

where L is the circumference of the cylinder. If the injected flux is precisely one flux quantum $\Phi_0 = h/e$, the momentum[2] along the cylinder k_y of all the occupied states changes by $2\pi/L$, which is the momentum level spacing in the $\hat{y}$ direction.

Very close to the edge, where the open boundary conditions force the energy bands to bend upwards (see Fig. 4.4b), every single band that raises above the Fermi energy now has one occupied momentum state above the Fermi level on, e.g., the right edge and one unoccupied momentum state below the Fermi level on the left edge of the sample [115, 123]. If n energy levels are occupied, this increase in energy ΔE corresponds to having transferred one particle per energy level, from the left edge to the right edge, causing a potential drop $\Delta V_H = \Delta E/ne$, see Fig. 4.4b. The current can thus be written as:

$$I = \frac{\Delta E}{\Delta \Phi} = n\frac{e^2}{h}\Delta V_H \tag{4.-1}$$

which highlights the quantization of the Hall conductance $\sigma_H = ne^2/h$.

4.4.2 Full open boundary conditions: numerics

In order to have a better insight on the meaning of the edge states we diagonalize the Harper Hamiltonian in real space (4.1) by imposing full open boundary conditions. The calculation is performed for a 2D lattice of 30×30 sites. The flux is $2\pi\alpha = 2\pi \times p/q = 2\pi \times 1/5$ in units of flux quantum and the tunneling is set to one along both directions. In Fig. 4.5 we plot the single particle energy spectrum as a function of the quantum state index. We compare the energy spectrum calculated with (Fig. 4.5a) and without (Fig. 4.5b) periodic boundary conditions. The edge states appear in the gaps of the energy spectrum. It is instructive to consider also the density distribution associated to each eigenstate. Indeed an edge state appears to be localized across the boundary of the system. In Fig. 4.6 we plot the density distributions related to **(a)** the first edge state, **(b)** the single particle ground state and **(c)** a Fermi sea of 160 non-interacting particles, almost filling completely the lowest magnetic sub-level.

[2] In presence of a vector potential, the $\hat{y}-$momentum transforms according to $\hat{p}_y \rightarrow \hat{p}_y + e\hat{A} = \hbar(\hat{k}_y + 2\pi\frac{e}{h}\hat{A})$.

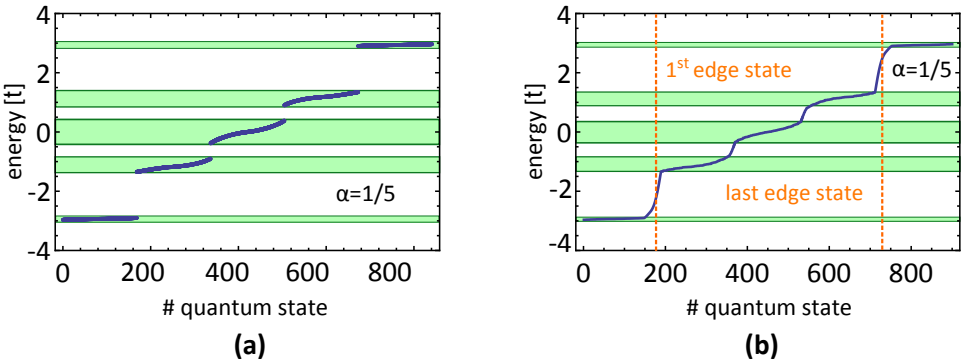

Figure 4.5: Single particle energy spectrum of hamiltonian Eq. (4.1). **(a)** Periodic boundary conditions. **(b)** Open boundary conditions. The gaps close and edge states appear. The calculation is performed for $2\pi\alpha = 2\pi \times p/q = 2\pi \times 1/5$ on a 2D lattice of 30×30 sites.

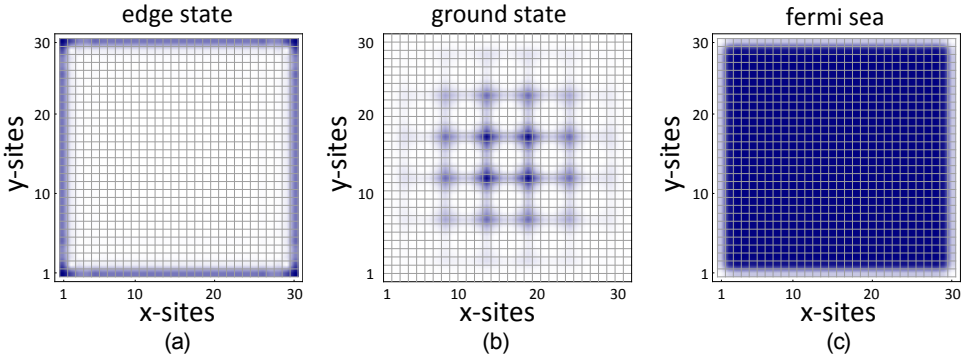

Figure 4.6: Density distribution associated to the eigenstates of Hamiltonian (4.1). **(a)** The first edge state, **(b)** single particle ground state and **(c)** a Fermi sea of 160 non-interacting particles.

As a last step we numerically calculate the current associated to the edge states in order to highlight their chiral nature. In Fig. 4.7 we plot the vector fields $\mathbf{j} = (j_x, j_y)$ corresponding to the first edge state (Fig. 4.7a), to the last edge state (Fig. 4.7b) and to the single particle ground state (Fig. 4.7c) which is a bulk state. For the edge states, the current circulates only in one sense and the verse depends on which edge state is considered and on the sign of the magnetic flux. This type of behaviour is pictorially described in terms of skipping orbits, cyclotron orbits that are naturally truncated at the edges of the sample, as is depicted in Fig. 4.8. On the other hand, by populating many bulk states such as the single particle ground state depicted in Fig. 4.6b, the sample acquires an insulating character in its bulk region, giving rise to a zero current circulation. In this sense, the system we are discussing is an example of a *topological insulator* [110], a material that has a bulk band gap like an ordinary insulator, but has

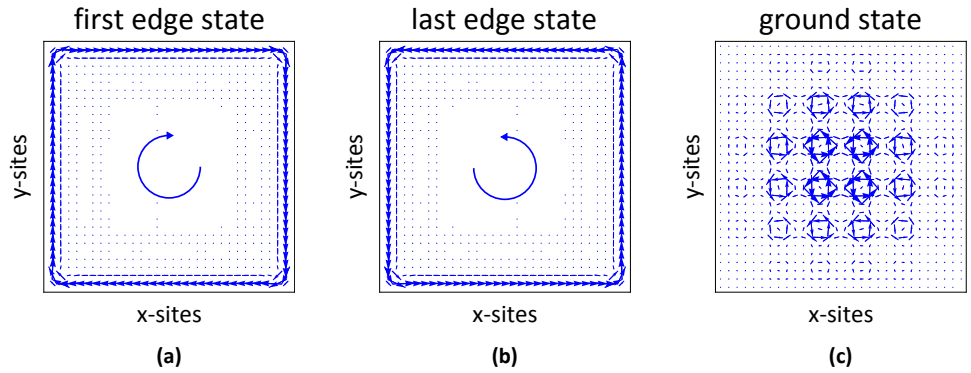

Figure 4.7: Vector plot of the current for: **(a)** the first edge state, **(b)** the last edge state, **(c)** the single particle ground state, of Hamiltonian (4.1). Each edge state is *chiral* and the sign of the chirality depends on the magnetic field and on which edge state is considered. The single particle ground state displays the typical cyclotron orbits. The magnetic flux is $\alpha = 1/5$ in units of flux quantum.

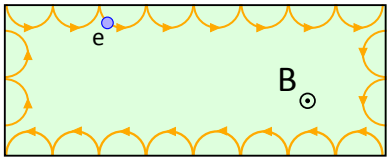

Figure 4.8: Skipping type cyclotron orbit. The circular motion of the electron is naturally truncated at the boundary of the system

protected conducting states on its edge.

Everything we described in this chapter refers to two-dimensional lattice systems. The only ingredients are coherent couplings along the sites of both directions and a magnetic field flux. Nothing prevents one of the directions from being the internal degree of freedom of the atoms. It is sufficient that the sites, i.e. the spin components, are coherently coupled. In the previous Chapter we described how to engineer this coupling, in the next one, we will show how this coupling gives rise to an effective magnetic field, if the atoms are loaded in a shallow, real, one-dimensional lattice. We will thus have all the necessary ingredients to study mechanisms typical of quantum Hall physics within our neutral, atomic system.

5 | Chiral edge states in synthetic dimensions

In Chapter 3 we discussed in detail how it is possible to coherently couple two or three spin components by using Raman transitions. The characterization relied upon loading a fully polarized Fermi gas in a deep 3D lattice so to freeze the kinetic energy and study only the dynamics in the internal spin space. In this Chapter we relax this constraint by lowering one of the optical lattice to $s \in (4, 8)$ in order to restore the tunneling along one spatial direction. We will see in Section 5.2 how this condition leads the Raman coupling to be equivalent to an effective magnetic flux, piercing the hybrid 2D lattice formed by the real one-dimensional lattice and the "orthogonal" internal degree of freedom. This novel geometry, based upon the concept of synthetic dimensions, allowed us, for the first time, to directly observe chiral edge states in ultracold neutral matter. We will describe our main results [24] in Section 5.4 and Section 5.5. Section 5.6 presents the first observation of skipping-type orbits, which are a hallmark of quantum Hall physics. Finally, Section 5.8 describes some preliminary results regarding the observation of a synthetic Hall drift in our hybrid 2D geometry.

We start with Section 5.1 in which a brief review of the available techniques for realizing artificial gauge fields with ultracold atoms in optical lattices, is presented. We emphasize how our novel scheme, based upon the concept of synthetic dimensions, opens up a simple and straightforward way to the study of quantum Hall physics with ultracold atoms.

5.1 Artificial gauge fields for ultracold atoms in optical lattices

Up to now there are essentialy three techniques to engineer a synthetic gauge field in a system of ultracold atoms loaded in an optical lattice. The first one, exploited by the group of Immanuel Bloch in Munich [12, 13, 19, 124] and by the group of Wolfgang Ketterle at MIT, Boston [21, 125], is based upon the principle of laser-assisted tunneling in optical lattices

[126–128]. The second one, used by the group of Klaus Sengstock [14, 55] in Hamburg and by the group of Tillmann Esslinger [18] in Zurich, relies upon the principle of lattice shaking. The last one, exploited by our group in Florence and by the group of Ian Spielman at JQI, Maryland, introduces a novel approach, based upon che concept of synthetic dimensions.

5.1.1 Gauge fields by means of laser-assisted tunneling

In Bloch's and Ketterle's groups, a Bose-Einstein condensate is loaded in a two-dimensional optical lattice. Along one of the directions a magnetic field gradient[1], B', is applied to generate a linear potential $\Delta \cdot n$ (n is the lattice site index and Δ is the energy offset between two consecutive sites), which suppresses tunneling along the corresponding direction for $\Delta \gg t_x$ (where t_x is the tunneling energy, and we took the gradient to be along the $\hat{x}-$direction). Resonant tunneling is then restored using a pair of far-detuned running-wave beams having a frequency difference that matches precisely the energy offset Δ. The two beams come from orthogonal directions, so that they also imprint a spatial phase pattern to the atoms moving around the lattice. Using Floquet analysis it can be demonstrated [129] that such a geometric configuration yields an effective Hamiltonian that coincides with the Harper-Hofstadter Hamiltonian.

This technique has two main limitations:

- the Harper-Hofstadter Hamiltonian appears only after (Floquet formalism) a time-averaging over a driving period $T \sim 1/\Delta$ of the complete, time-dependent Hamiltonian. This has the disadvantage that information about the evolution within one driving period is lost. This is the so-called micro-motion, whose impact on physical observables (such as the atomic momentum distribution) strongly depends on the specific implemented scheme, suggesting that the physical description in terms of an effective Hamiltonian is in general not sufficient to capture the full time-evolution of the system [130]. In addition, in these experiments a substantial heating has been observed, which is likely to be ascribed to the combination of micro-motion and interactions;

- it is definitely not trivial to adiabatically load the lowest energy band of the effective Harper-Hofstadter Hamiltonian [19, 129].

5.1.2 Gauge fields by means of lattice shaking

A quite different strategy consists in using time-dependent optical lattices [65]. The Hamburg and Zurich groups exploit lattice shaking, which relies

[1] The Munich group has also implemented a closely related all-optical technique, which is based on superlattice potentials to produce a uniform magnetic field.

upon an off-resonant modulated potential that perturbs the tight-binding Hamiltonian in such a way as to engineer complex hoppings between the lattice sites. Also in this case, Floquet theory is necessary to derive an effective, time-averaged Hamiltonian which displays the desired complex tunnelings.

This technique has two main disadvantages:

- technical difficulties related to the piezoelectric stacks mounted on the lattice beam mirrors. Also, in order to generate a complex hopping, a non-trivial modulation is needed;
- the periodic force driving induces heating in the atomic sample.

5.1.3 Gauge fields in synthetic dimensions

Our group in Florence and the group of Ian Spielman in Maryland exploit the novel concept of synthetic dimensions [22, 23] in which a hybrid 2D geometry is realized by using a real one-dimensional lattice combined to the atomic spin components coherently coupled by means of Raman transitions.

With this techniques there are some main advantages:

- no Floquet theory is needed;
- a synthetic gauge field is easily realized without potential gradients, complex super-lattice structures or periodic driving of the lattice sites position;
- thanks to spin-selective imaging, synthetic single-site resolution is effectively realized;
- it is quite easy to adiabatically load the lowest energy band of the engineered Hamiltonian;
- due to the finite number of sites along the synthetic direction, edge physics can be studied;
- one could think of possible ways to engineer periodic boundary conditions along the synthetic direction, thus investigating bulk physics too;
- heating effects are completely negligible;

and of course a few limitations

- the synthetic dimension is limited to the maximum number of available spin components ($dim(\mathcal{M}) = 6$, for ^{173}Yb)

- since the Raman beams couple different spin components on the same real lattice site, interactions have effectively an infinite range along the synthetic direction[2].

This technique is of course the topic of this Chapter and it will be described in detail in the next sections.

5.2 Raman coupling as a synthetic gauge field

Let's consider ^{173}Yb atoms moving in a 1D lattice, for which a Raman coupling among the spin components exists. We can write the Raman coupling Hamiltonian in terms of fermionic ladders operators:

$$\hat{H}_R = -\frac{\hbar}{2}\sum_{n,m_F}\Omega_{R,m_F}e^{i\mathbf{q}_R\cdot\mathbf{r}_n}\hat{c}^\dagger_{n,m_F+2}\hat{c}_{n,m_F} + h.c. \tag{5.0}$$

where $\hat{c}^\dagger_{n,m_F+2}\hat{c}_{n,m_F}$ destroys a particle at site n with spin component m_F and recreates it at the same site n but with spin component m_F+2, Ω_{R,m_F} is the Raman amplitude for the transition $m_F \to m_F+2$ and $e^{i\mathbf{q}_R\cdot\mathbf{r}_n}$ is the phase term of the Raman electric field, calculated at the atom position $\mathbf{r}_n$ and containing the Raman wavevector $\mathbf{q}_R$. We have omitted, for now, the Raman-induced spin-dependent light shifts. Since we are considering a one-dimensional lattice, we can rewrite the position of an atom in terms of the lattice site index n, $\mathbf{r}_n = nd_L$ in which $d_L = \lambda_L/2$ is the lattice spacing. The Raman phase now becomes:

$$\mathbf{q}_R\cdot\mathbf{r}_n = q_{R,x}d_L n = q_{R,x}\frac{\lambda_L}{2}n = \frac{q_{R,x}}{2k_L}2\pi n = \Phi n \tag{5.0}$$

where we supposed the lattice to be oriented along the $\hat{x}$-direction, k_L is the lattice wavevector and we defined the new parameter Φ:

$$\Phi = 2\pi\times\frac{q_{R,x}}{2k_L} \tag{5.0}$$

which is the ratio between the Raman momentum kick along the lattice direction $q_{R,x}$ and the one-dimensional lattice momentum kick $2k_L$. Now consider also the Hamiltonian describing the motion of the atoms along the one dimensional lattice:

$$\hat{H}_L = -t\sum_{n,m_F}\hat{c}^\dagger_{n+1,m_F}\hat{c}_{n,m_F} + h.c. \tag{5.0}$$

[2]This is not necessarily a disadvantage, it could also become the source of new exciting studies.

where t is the tunneling energy and $\hat{c}^{\dagger}_{n+1,m_F}\hat{c}_{n,m_F}$ describes the particle hopping between neighboring sites without changing the spin. The complete, non-interacting, Hamiltonian $\hat{H} = \hat{H}_L + \hat{H}_R$ becomes:

$$\hat{H} = -\sum_{n,m}\left(t\,\hat{c}^{\dagger}_{n+1,m}\hat{c}_{n,m} + \frac{\hbar}{2}\Omega_{R,m}e^{i\Phi n}\,\hat{c}^{\dagger}_{n,m+1}\hat{c}_{n,m}\right) + h.c. \tag{5.0}$$

where we omitted the label F from the spin component and we introduced the subset $\hat{m} = (-5/2, -1/2, +3/2)$. This is precisely the Harper-Hofstadter Hamiltonian (4.1) that we wrote in the previous Chapter. Indeed we can demonstrate that the parameter Φ acts as a magnetic flux, when considering a particle hopping around a plaquette of the hybrid lattice, as it is sketched in Fig. 5.1.

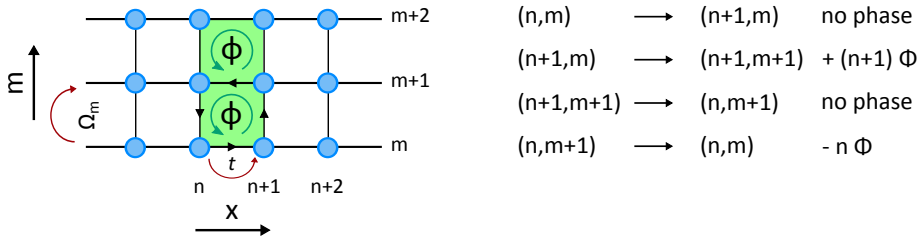

Figure 5.1: Hybrid 2D lattice scheme. The $\hat{x}-$direction is defined by the real one-dimensional lattice and the $\hat{m}-$direction is defined by the atomic spin components. When a particle hops around a plaquette it acquires a phase Φ.

We note also that the we can change the sign of the artificial magnetic field simply by inverting the Raman momentum kick: $\mathbf{q}_R \to -\mathbf{q}_R$. This can be done by swapping the frequencies of the two Raman beams (see Fig. 3.6).

Because of the low number of sites along the synthetic direction $\hat{m}$, we call this hybrid 2D geometry, a *Hall ribbon*. The ribbon is made by two *legs*, in the case of only two spin components, thus constituting a *two-leg ladder*, or by three legs, forming a *three-leg ladder*. We note that, even in this latter small system, chiral currents circulating along the edges are predicted to exist, as can be seen from the numerical simulations (see Fig. 5.2) made for a hybrid 2D lattice of 30×3 lattice sites and a magnetic field flux $\alpha = 1/5$. With such a low number of sites along $\hat{m}$ is more difficult to identify properly the magnetic sub-bands and in particular the corresponding edge state. Nevertheless, also in this simple case, populating many bulk states brings the system to display an insulating character in the bulk region, which is constituted by only a single leg. This simple geometry can thus be exploited as a toy-model in order to study fundamental phenomena typical of larger quantum Hall systems. Since experimentally we have access to the momentum distribution and to the spin composition of the atomic sample, it is useful to consider the spatial Fourier-transform of

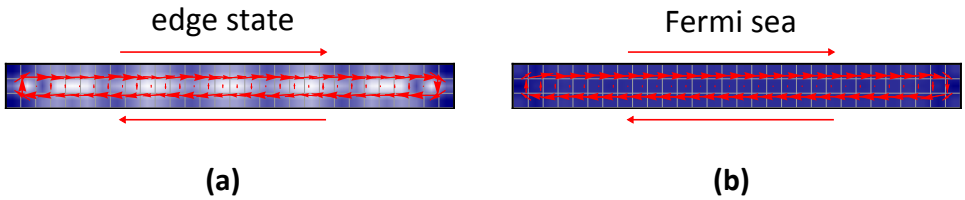

Figure 5.2: Three-leg case vector plots. **(a)** Density distribution and current vector plots corresponding to the first edge state of Hamiltonian 4.1. **(b)** Density distribution and current vector plots corresponding to a Fermi sea, filling completely the "first" magnetic sub-band. In both situation the system displays current circulating only along the edges.

Hamiltonian (5.2). Considering a total of L sites along $\hat{x}$ and introducing the operators:

$$\hat{b}^{\dagger}_{q,m} = \frac{1}{\sqrt{L}} \sum_{n=1}^{n=L} \hat{c}^{\dagger}_{n,m} e^{-i(q+\Phi m)n}, \tag{5.0}$$

the Hamiltonian can be written as a sum over momentum states $\hat{H} = \sum_q \hat{H}_q$,

$$\hat{H}_q = \sum_m \varepsilon_{q+m\Phi} \hat{b}^{\dagger}_{q,m} \hat{b}_{q,m} - \frac{\hbar}{2} \Omega_{R,m} \left(\hat{b}^{\dagger}_{q,m+1} \hat{b}_{q,m} + \hat{b}^{\dagger}_{q,m} \hat{b}_{q,m+1} \right) + U_m \hat{b}^{\dagger}_{q,m} \hat{b}_{q,m} \tag{5.0}$$

where $\varepsilon_k = -2t\cos(k)$, $q \equiv 2\pi j/L$ with $j = 1, 2, ..., L$, [23] and we considered also the spin-dependent light shifts U_m acting as additional energy offsets along the diagonal of the Hamiltonian. Fig. 5.3 shows the resulting band structure for the two and three-level system in the case of a one-dimensional lattice of depth $s = 6.5$ ($t \simeq h \times 90\,\mathrm{Hz}$) and a magnetic flux $\Phi = 0.37\pi$, corresponding to our experimental parameters. Fig. 5.3a, Fig. 5.3b are the band structure calculations for the two-level case whereas Fig. 5.3c, Fig. 5.3d refer to the three-level case. The energy bands are color-coded according to the spin population compositions. In both situations, away from the avoided crossings, the lowest band describes the propagation of currents along the legs corresponding to $m = (-5/2, -1/2)$ (two-level system[3]) and $m = (-5/2, +3/2)$ (three-level system): these currents propagate along $\hat{x}$ in opposite directions. In the physical system, these give rise to a spin current $j_s(x) = j_\uparrow - j_\downarrow$. When the number of participating spin states increases, $dim(M) \gg 1$ this behaviour becomes analogous to the one in quantum Hall systems described in the previous chapter. We note that, with respect to Fig. 4.6 we are effectively making horizontal cuts of the 2D lattice in order to study the current carried by each row separately. In Fig. 5.4 we plot the calculated spin composition of the lowest energy band of Hamiltonian (5.2) as a function of the couplings ratio

[3] We are considering the case $\hbar\Omega_{R,1} > t$ for which the two level-approximation is valid.

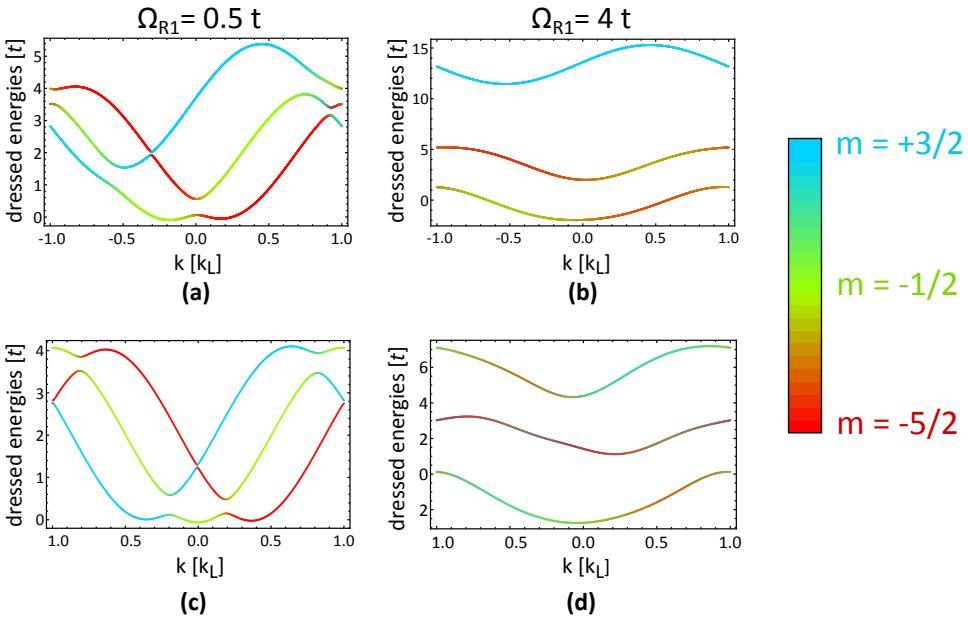

Figure 5.3: Band-structure calculation of Hamiltonian (5.2). Colors specify the spin state. The magnetic flux chosen is $\Phi = 0.37\pi$. **(a), (b)** Two-level case. **(c), (d)** Three-level case.

$\Omega_{R,1}/t$, both for the two-leg case and for the three-leg case. The populations have been averaged over the lattice Brillouin zone $[-k_L, k_L]$, in order to consider the fermionic statistics of our sample having a fermi wavevector of the order $k_F \sim k_L$.

Our next step will be to load the atoms in the lowest energy band of Hamiltonian (5.2) in order to directly observe the chiral nature of the current, carried by each spin state.

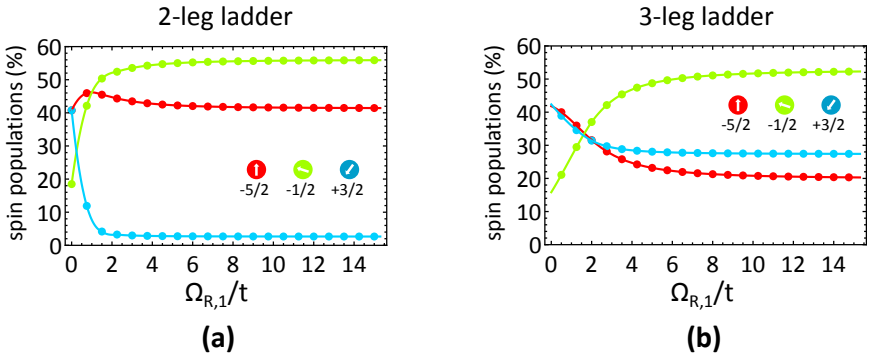

Figure 5.4: Calculated spin composition of the lowest dressed band. **(a)** Two-leg case. **(b)** Three-leg case. The populations have been averaged over the lattice Brillouin zone $[-k_L, k_L]$.

5.3 Experimental realization of a synthetic magnetic field in synthetic dimensions

We can now proceed in describing how we experimentally realize an artificial magnetic field within our system. In Fig. 5.5 we show the geometrical configuration of the Raman beams with respect to the optical lattice beams. The second optical lattice (OL_2) is lowered at $s \lesssim 6.5$ while the

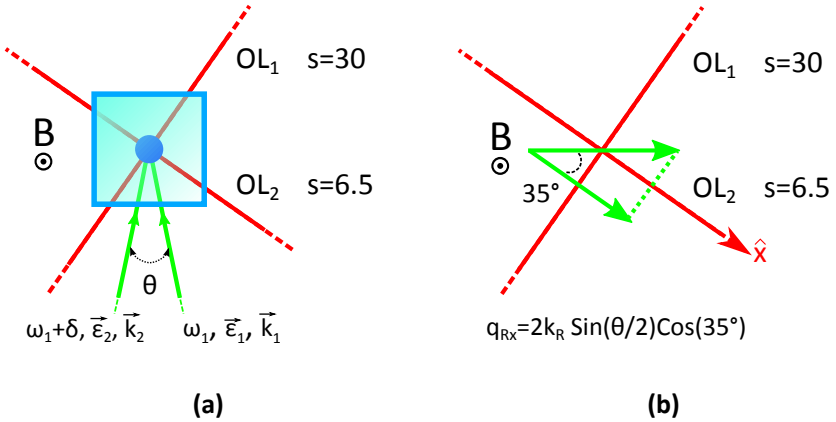

Figure 5.5: Raman beams geometric configuration. The Raman momentum kick makes an angle of 35° with the optical lattice OL_2, whose direction is taken as $\hat{x}-$axis. The lattices OL_1 and OL_3 (vertical direction, out of the page) are kept at $s = 30$ so that the atomic kinetic energy along these directions is frozen.

others (OL_1, OL_3) are kept at a lattice depth of $s = 30$. We can thus consider the atomic kinetic energy to be frozen along directions $\hat{1}$ and $\hat{3}$ and keep only the projection of the Raman momentum kick along the direction of OL_2, taken to be the $\hat{x}-$axis. Considering the angle $\theta \simeq 19°$ between the Raman beams, the transfered momentum becomes:

$$q_{R,x} = 2k_R \sin\left(\frac{\theta}{2}\right) \cos(35°) = 3.06 \cdot 10^6 \, \mu\text{m}^{-1} \tag{5.0}$$

corresponding to a magnetic flux per plaquette

$$\Phi = 2\pi \times \frac{q_{R,x}}{2k_L} \simeq 0.37\pi. \tag{5.0}$$

We have to note that the chosen arrangement for the optical lattice, effectively realizes many independent one-dimensional tubes (~ 1000), along which the shallow OL_2 is superimposed. Therefore, the system under study is composed by many independent 2D hybrid lattices contributing on their own to the measured signals. By considering also the Raman-induced state-dependent light shifts and the residual harmonic confinement along OL_2 due to the presence of OL_1 and OL_3, the Hamiltonian

describing a single hybrid lattice becomes:

$$\hat{H} = -\sum_{n,m}\left(t\,\hat{c}^{\dagger}_{n+1,m}\hat{c}_{n,m} + \mu_n \hat{n}_{n,m} + \frac{\hbar}{2}\Omega_{R,m} e^{i\Phi n}\,\hat{c}^{\dagger}_{n,m+1}\hat{c}_{n,m} + U_m \hat{n}_{n,m}\right) + h.c. \tag{5.0}$$

in which $t \simeq h \times 90\,\mathrm{Hz}$, $\mu_n = 1/2\, M\,\omega_x^2 d_L^2\, n^2$ is the residual harmonic trapping potential, $\omega_x = 2\pi \times 55$ Hz[4] and U_m are the state-dependent light shifts that depend on the particular polarization chosen for the Raman beams as discussed in Chapter 3. Exploiting the state-dependent light shifts it is possibile to choose between two configurations: a two-leg ladder, in which only two spin states are coherently coupled and a three-leg ladder, in which three spin states participate to the dynamics.

In the next sections we will study both the configurations, presenting the experimental results and comparing them with the theoretical predictions made by our collaborators in Innsbruck, Marie Rider, Marcello Dalmonte and Peter Zoller [24].

5.4 Two-leg ladder: equilibrium properties

The first thing we need to do, which is valid also in the case of the three-leg ladder, is to adiabatically load the lowest energy band of Hamiltonian (5.2). We first consider the case of a two-leg ladder (see Sec. 3.3.1) constituted by the nuclear spin states $m = -5/2$ and $m = -1/2$. A quantum degenerate ^{173}Yb Fermi gas with $1.6 \cdot 10^4$ atoms and an initial temperature $T \simeq 0.2\, T_F$ is first spin-polarized in $m = -5/2$. By slowly turning on ($T_{ramp} = 150\,\mathrm{ms}$) the intensity of the optical lattice OL_2 along $\hat{x}$ (and of the additional strong lattices OL_1 and OL_3), we prepare a system of ladders in which all atoms occupy the $m = -5/2$ leg with less than one atom per site (maximum filling fraction $\eta \simeq 0.8$). During the lattice ramp we switch off the optical dipole trap in 40 ms in order to decompress the atomic cloud and reduce the overall harmonic confinement to $\omega_x/2\pi \simeq 55$ Hz. After 5 ms, we turn on the Raman beams with an initial two-photon detuning $\delta_{R,in} \simeq -25\,\Omega_{R,1}$(we have subtracted the Zeeman energy splitting $2\Delta_Z$) and perform an exponential frequency sweep of the form:

$$\delta_R(t) = \delta_{R,in} + (\delta_{R,f} - \delta_{R,in})\left(\frac{1 - e^{-t/\tau}}{1 - e^{-T_{adiab}/\tau}}\right) \tag{5.0}$$

where $\delta_{R,f} = U_{-5/2} - U_{-1/2}$ (see Hamiltonian (3.3.1)). The ramp duration T_{adiab} ranges from 20 to 80 ms depending on the particular Raman

[4] In order to take into account repulsive interactions at the mean-field level, we considered, in the numerical simulations, a slightly less harmonic frequency $\omega_x/2\pi \simeq 40$ Hz.

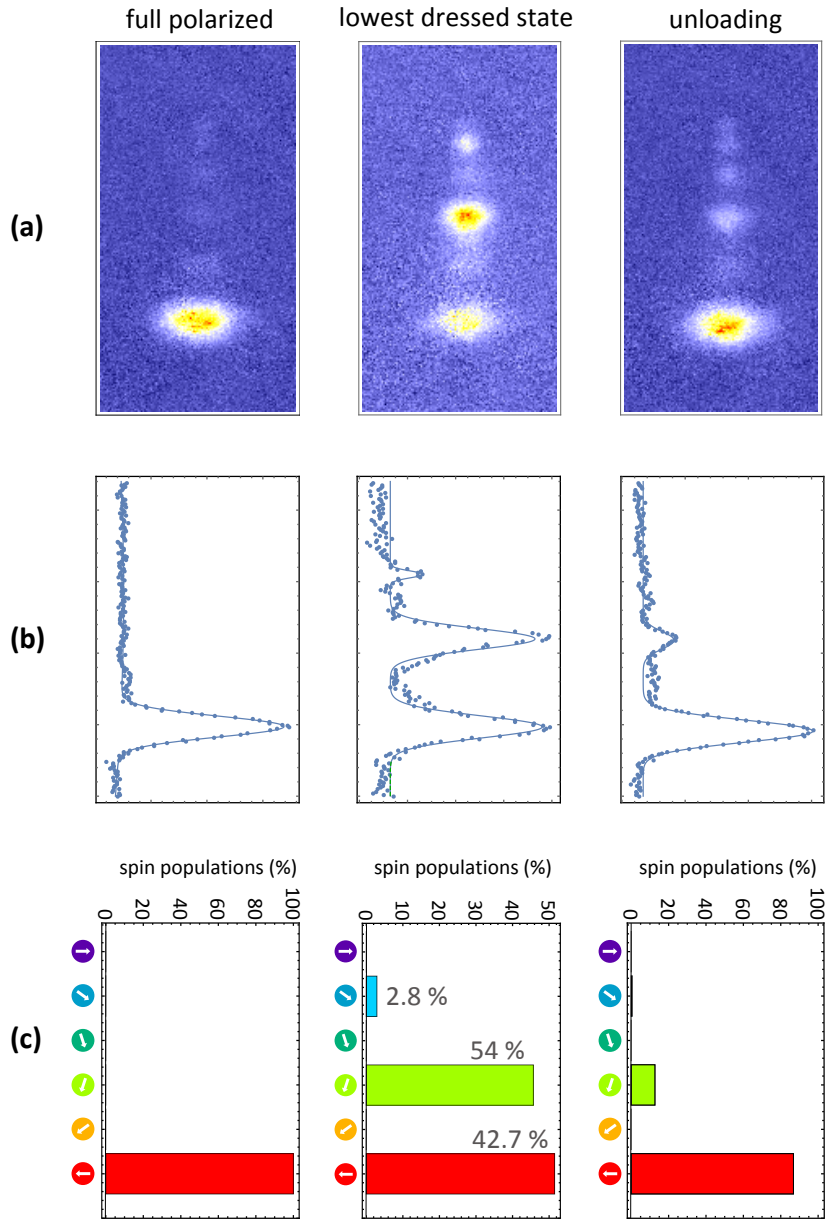

Figure 5.6: Typical adiabatic loading of the two-leg ladder lowest-energy band. **(a)** OSG detection of the spin population during the loading and unloading procedure. **(b)** Gaussian fits of the integrated density profiles, for extracting the spin relative populations. **(c)** Barcharts showing the experimental spin populations. The uncertainty in the spin populations is around 3%. The grey percentages are the theoretical expectations obtained by diagonalizing Hamiltonian (5.2) and averaging over the range $[-k_L, k_L]$. Experimental parameters: $\hbar\Omega_{R,1}/t \simeq 4$, $B = 153\,G$, $N_{at} \simeq 2.5 \cdot 10^4$.

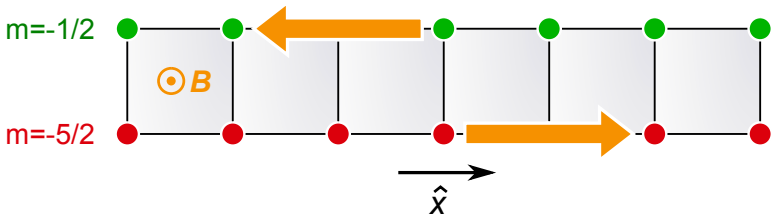

Figure 5.7: Sketch of the two-leg ladder configuration. The arrows are a pictorial representation of the chiral currents.

coupling[5] $\Omega_{R,1}$, with τ ranging from 5 to 25 ms accordingly. The adiabaticity of the whole process is verified experimentally by reversing the whole procedure to recover approximately[6] a spin-polarized Fermi gas, as can be seen in Fig. 5.6.

Despite the absence of a real bulk region, this two-leg configuration is expected to support chiral currents with atoms flowing in opposite directions along the legs (Fig. 5.7), as investigated recently in bosonic systems [124]. To observe this, we measured the relative motion of the atoms in the two legs by spin-selective imaging of the lattice momentum distribution, obtained by switching off the synthetic coupling and releasing the atoms from the lattice through a band mapping procedure (see 1.2.1). The single-site imaging along the synthetic direction is perfomed by using a sequence of spin-selective laser pulses, in resonance with different components of the narrow intercombination transition ${}^1S_0 \rightarrow {}^3P_1(F' = 7/2)$, to remove atoms in all spin states but one (see Sec. 2.5.4). The sequence is carried out during the first 2.5 ms of ballistic expansion. At this time the (real) magnetic field is $B_{blast} = 15\,\mathrm{G}$, leading to a Zeeman shift $\Delta_Z \simeq 50\Gamma$ between adjacent spin components in the ${}^3P_1$ manifold. After ballistic expansion, absorption imaging is perfomed on the dipole-allowed 399 nm transition. In Fig. 5.8 (upper panel), we show two time-of-flight images corresponding to the $m = -5/2$ and $m = -1/2$ legs for $\Omega_{R,1} = 2\pi \times 489\,\mathrm{Hz}$ and $t = h \times 134\,\mathrm{Hz}$ ($\hbar\Omega_{R,1}/t = 3.65$). Here we are interested only in direction $\hat{x}$, which reflects the distribution of the lattice momenta k along the legs (in units of the real-lattice wave vector k_L). The lattice momentum distri-

[5] In choosing the ramp profile we must be adiabatic with respect to the band gap between the lowest and the first excited energy band in order to avoid Landau-Zener tunneling processes. As a general rule we try to satisfy $\frac{d\delta_R}{dt} < \frac{\Omega_{R,1}^2}{2}$.

[6] The imperfect adiabaticity is more pronounced at low lattice depth ($s < 10$) of the real one-dimensional lattice probably because of the higher mobility of the atoms. Indeed, even if we start from a non-interacting fully polarized Fermi gas, when we turn on the momentum-dependent Raman coupling, atoms in different spin states become effectively distinguishable, opening the way to possible interactions that could introduce decoherence mechanisms. Also, a possible relative phase noise, between the Raman electric field an the optical lattice electric field, could lead to fluctuations in the synthetic magnetic field, introducing heating effects.

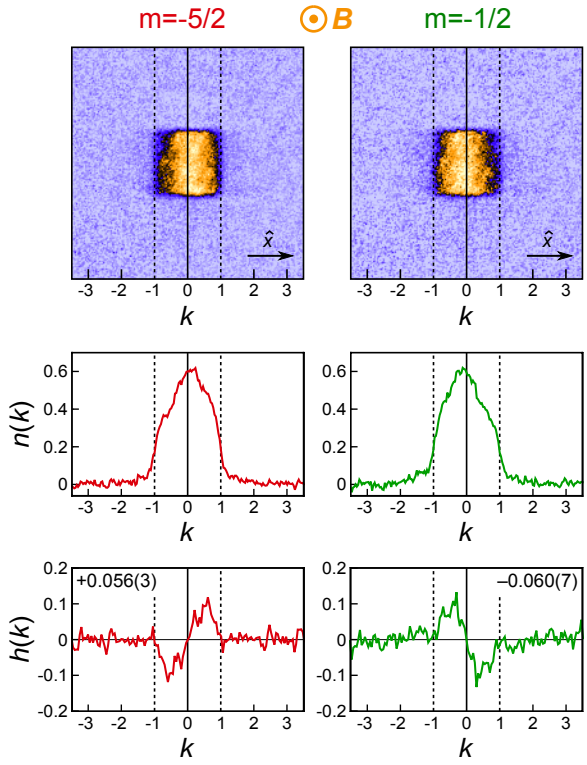

Figure 5.8: Chiral dynamics in two-leg ladders. (Top) False-color time-of-flight images of the atoms in the $m = -5/2$ and $m = -1/2$ legs. (Middle) Integrated lattice momentum distribution $n(k)$. (Bottom) $h(k) = n(k) - n(-k)$. Experimental parameters: $\Omega_{R,1} = 2\pi \times 489\,\mathrm{Hz}$, $t = h \times 134\,\mathrm{Hz}$, $\hbar\Omega_{R,1}/t = 3.65$, and $\Phi = 0.37\pi$. In this figure we have taken $k_L = 1$.

bution along the orthogonal spatial direction $\hat{y}$ is a uniform square due to the presence of the strong optical lattice along the transverse (frozen) directions. We take at least 30 images for each spin state and in order to remove residual gradients or fringes due to imperfections in the imaging setup, also background images are acquired, averaged and subtracted from those with atoms.

The central panel of Fig. 5.8 shows the lattice momentum distribution $n(k)$ after integration of the images along $\hat{y}$ (orthogonal direction with respect to $\hat{x}$ in the figure) and normalization according to $\int n(k)dk = 1$. We observe a clear asymmetry in $n(k)$, similar to what was reported in experiments with spin-orbit coupling in harmonically trapped gases [17, 66]. We characterize the asymmetry by defining the function

$$h(k) = n(k) - n(-k) \tag{5.0}$$

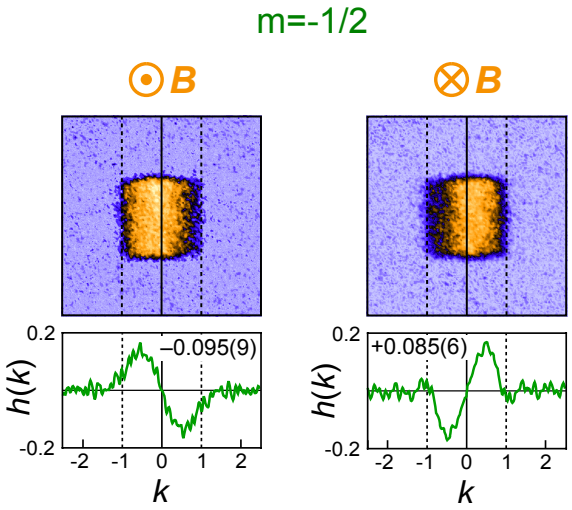

Figure 5.9: Time-of-flight images and $h(k)$ of the $m = -1/2$ leg for opposite directions of the effective magnetic field. Experimental parameters: $\Omega_{R,1} = 2\pi \times 394\,\mathrm{Hz}$, $t = h \times 87\,\mathrm{Hz}$, $\hbar\Omega_{R,1}/t = 4.53$, and $\Phi = \pm 0.37\pi$.

which is plotted in the lower panel of Fig. 5.8. The expression

$$J = \int_0^1 h(k)dk \tag{5.0}$$

provides a measurement of the lattice momentum unbalance and quantifies the strength of the chiral motion of the particles along the two legs. The values $J = +0.056(3)$ for $m = -5/2$ and $J = -0.060(7)$ for $m = -1/2$ are approximately equal in intensity and opposite in sign, providing direct evidence for the presence of chirality in the system. The small value of J is attributable to the fact that, in addition to states exhibiting chiral currents, fermions occupy other states at the bottom of the band, which do not display chiral features (see Fig. 4.6). We also perfomed the same experiment with reversed direction of the synthetic magnetic field **B** (Fig. 5.9, observing a change of sign in J, corresponding to currents circulating in the opposite direction. This behavior confirms the interpretation of our data in terms of chiral currents induced by a synthetic magnetic field in a sythetic 2D lattice.

The stability of chiral edge states in fermionic systems is of key importance, for example, for quantum information applications [131]. In our system, the appearence of a chiral behavior is governed by several key parameters, including the ratio $\hbar\Omega_{R,1}/t$, the Fermi energy E_F, and the flux Φ. These parameters are easy to adjust, so they can be used to investigate the rise and fall of the edge currents as a function of the Hamiltonian parameters [124], as well as to identify which regimes exhibit stronger chiral features. By varying the tunneling rates along $\hat{x}$ and $\hat{m}$, we observe a

crossover between a chiral behavior and a nonchiral regime. The lattice momentum distribution is measured as a function of $\hbar\Omega_{R,1}/t$ without affecting other relevant parameters, such as E_F and T. Fig. 5.10 illustrates the measurement of $|J|$ as a function of $\hbar\Omega_{R,1}/t$ (circles). As expected, no chirality is observed for vanishing $\Omega_{R,1}$, when the legs are decoupled. Chirality is also suppressed for large inter-edge coupling $\Omega_{R,1} \gg t$. In the latter regime, the largest energy scale in the system is the effective kinetic energy along the synthetic direction: this contribution is minimized when the fermions occupy the lowest energy state on each rung, which does not exhibit any chiral behavior. The measured values of $|J|$ compare well with the results of a numerical simulation[7] that includes thermal fluctuations. (shaded area in Fig. 5.10).

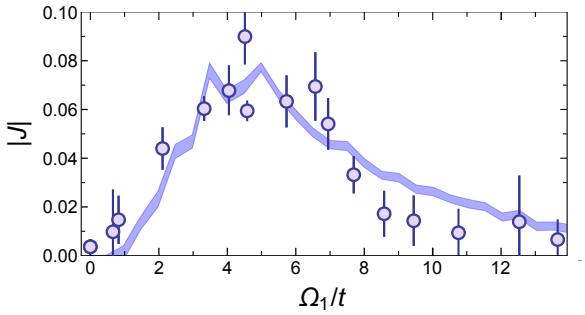

Figure 5.10: Chiral current vs Hamiltonian couplings. Circles show experimental values of $|J|$ for the $m = -1/2$ leg as a function of $\hbar\Omega_{R,1}/t$ (averages of data sets taken for $\Phi = \pm 0.37\pi$). The error bars are obtained with a bootstrapping method [132] applied on ~ 30 different measurements. The shaded area depicts the result of a numerical simulation that includes thermal fluctuations, see Sec. 5.7.

5.5 Three-leg ladder: equilibrium properties

We next consider a three-leg ladder (see Sec. 3.3.2), which is the minimal configuration for which chiral currents at the edges can be sharply distinguished from the behavior of the bulk, Fig. 5.12. The adiabatic loading procedure of the lowest energy band is similar to the one previously described for the two-leg case. In Fig. 5.11 we show the loading and unloading of the lowest dressed state for typical experimental parameters, $\hbar\Omega_{R,1}/t \simeq 4$, $B = 153\,G$, $N_{at} \simeq 2.8 \cdot 10^4$.

Fig. 5.13 shows the measured $n(k)$ and $h(k)$ for each of the three legs for $\Omega_{R,1} = 2\pi \times 620\,\text{Hz}$ and $t = h \times 94\,\text{Hz}$ ($\hbar\Omega_{R,1}/t = 6.6$). We observe strong chiral currents in the upper and lower-edge chains, showing values of J with opposite sign, similar to the two-leg case ($J = +0.079(6)$ for

[7] See Sec. 5.7.

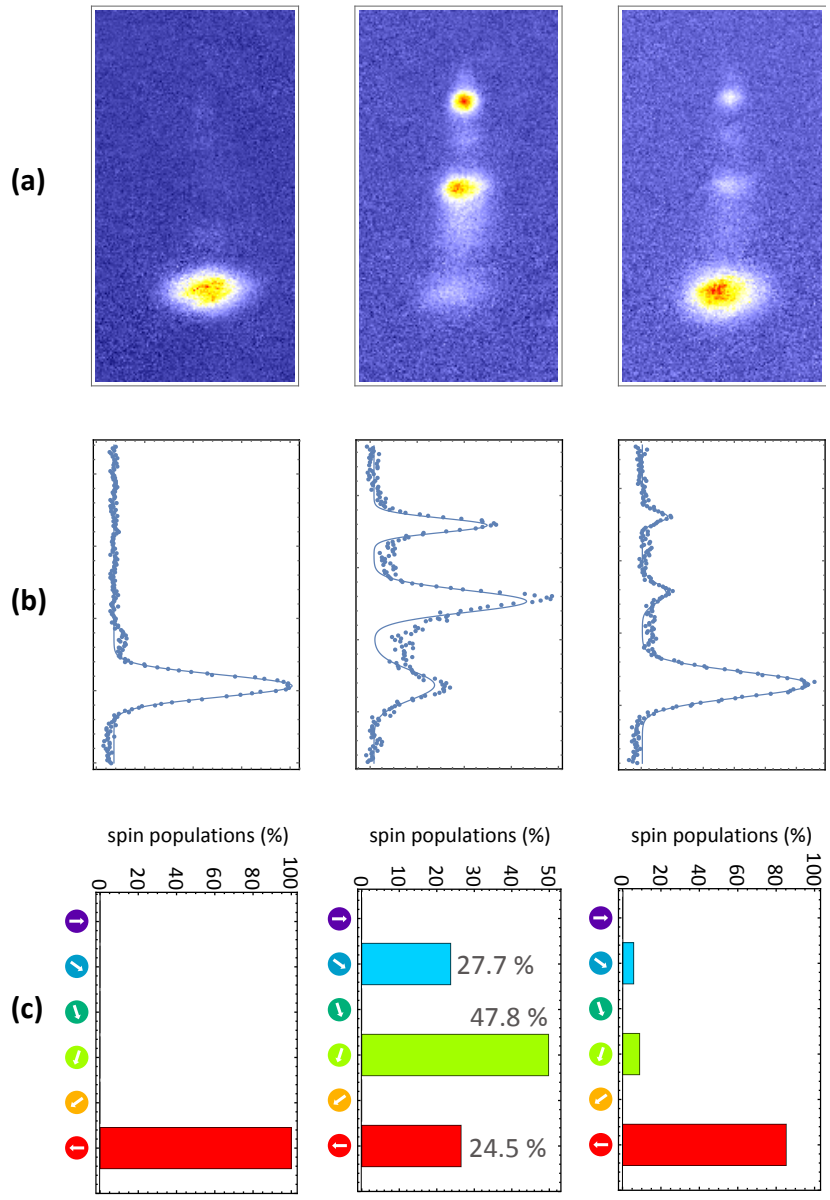

Figure 5.11: Typical adiabatic loading of the three-leg ladder lowest energy state. **(a)** OSG detection of the spin population during the loading and unloading procedure. **(b)** Gaussian fits of the integrated density distributions for extracting the spin relative populations. **(c)** Barcharts showing the experimental spin populations. The uncertainty in the spin populations is around 3%. The grey percentages are the theoretical expectations obtained by diagonalizing Hamiltonian 5.2 and averaging over the range $[-k_L, k_L]$. Experimental parameters: $\hbar\Omega_{R,1}/t \simeq 4$, $B = 153\,G$, $N_{at} \simeq 2.8 \cdot 10^4$.

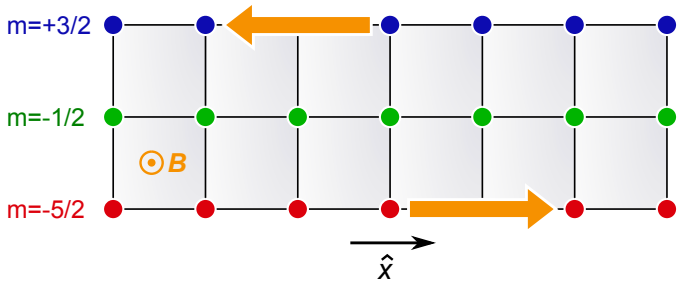

Figure 5.12: Sketch of the three-leg ladder configuration.

$m = -5/2$ and $J = -0.062(4)$ for $m = +3/2$). In contrast, the central leg shows a much reduced asymmetry in $n(k)$ ($J = +0.018(5)$), signaling a suppressed net current in the bulk. This is a direct evidence of the ex-

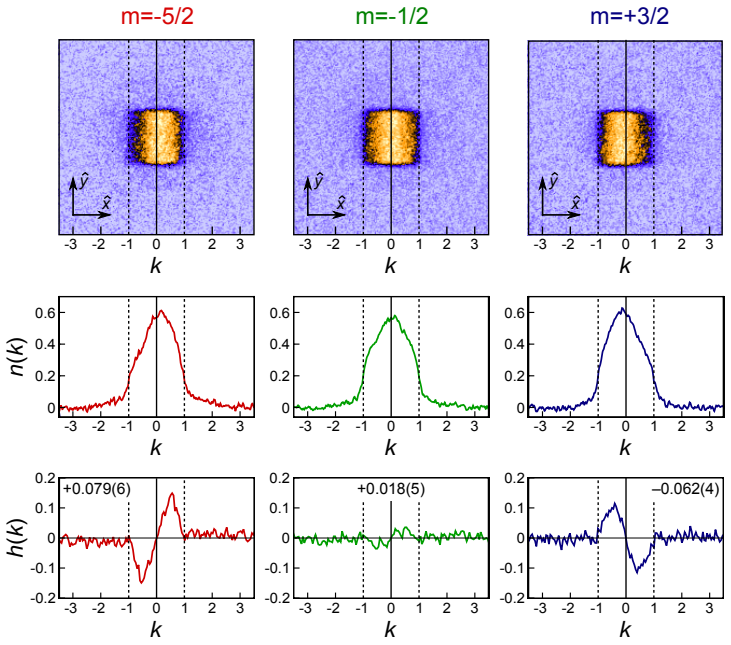

Figure 5.13: Chiral edge currents in a three-leg ladder. Experimental time-of-flight images (top). $n(k)$ (center), and $h(k) = n(k) - n(-k)$ (bottom) for each of the three legs $m = -5/2$, $m = -1/2$, $m = +3/2$ constituting the ladder, respectively. Experimental parameters: $\Omega_{R,1} = 2\pi \times 620\,\mathrm{Hz}$, $t = h \times 94\,\mathrm{Hz}$, $\hbar\Omega_{R,1}/t = 6.6$, and $\Phi = 0.37\pi$. In this figure we have taken $k_L = 1$.

istence of chiral states propagating along the edges of the system, which leave the bulk mostly decoupled from the edges (Fig. 5.14). This behavior is akin to what is expected for a fermionic system in a Harper-Hofstadter Hamiltonian (see Sec. 4.4). Bulk states exhibit only local circulation of current, which averages to zero when all of the different states enclosed by

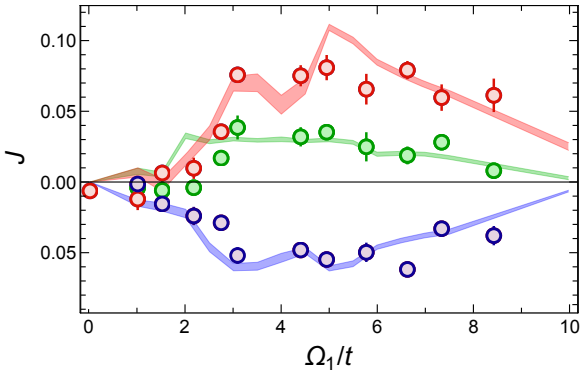

Figure 5.14: Chiral currents vs Hamiltonian couplings. Circles show experimental values of the net momentum unbalance J for each leg as a function of $\hbar\Omega_{R,1}/t$. The error bars are obtained with a bootstrapping method applied on $\sim$ 30 different measurements. The shaded area depicts the result of a numerical simulation taking into account temperature fluctuations (see Sec. 5.7). For both experimental and simulation data, red, green and blue correspond to $m = -5/2$, $m = -1/2$, $m = +3/2$, respectively.

the Fermi surface are considered. Only the edges of the system experience a nonzero current, because there the chiral nature of the states prevents this cancellation effect from occurring. In the ribbon geometry of the experiment, the bulk reduces to just a single central line. Nevertheless, the behavior discussed above is clearly present and detectable in the experimental signal. The small width of the ribbon favors the observations of edge states, given the large boundary-to-surface ratio of the system, which is reflected in a substantial population of states with edge character. Fig. 5.14 shows the values of J as a function of $\hbar\Omega_{R,1}/t$ for the three different legs of the ladder. The results illustrate the role of the bulk-edge coupling: similar to the two-leg case, chirality is very weak for small coupling and increases as $\hbar\Omega_{R,1}/t$ approaches $\sim$ 3. The theoretical curves show that further increasing $\hbar\Omega_{R,1}/t$ eventually leads to attenuation of the signal because of the effective coupling between edges, which smoothens the chiral features of the system. We observe a substantial agreement between experiment and theory for the range of $\hbar\Omega_{R,1}/t$ that can be explored in our experimental setup[8]. The nonzero current in the bulk ($J < 0.035$) can be ascribed to the different couplings $\Omega_{R,1}$, $\Omega_{R,2}$, as well as to a residual light shift that breaks the symmetry between the two edges (see Sec. 3.3.2).

[8]For $\hbar\Omega_{R,1}/t \gg 1$ the adiabatic loading procedure of the lowest dressed state is spoiled by the presence of $\sigma^+\pi$ Raman transitions that populate unwanted spin states when the two-photon frequency sweep starts from nearby a $m_F \to m_F + 1$ resonance. This problem is not present in the two-leg case because there the polarization is purely $\sigma^+/sigma^-$.

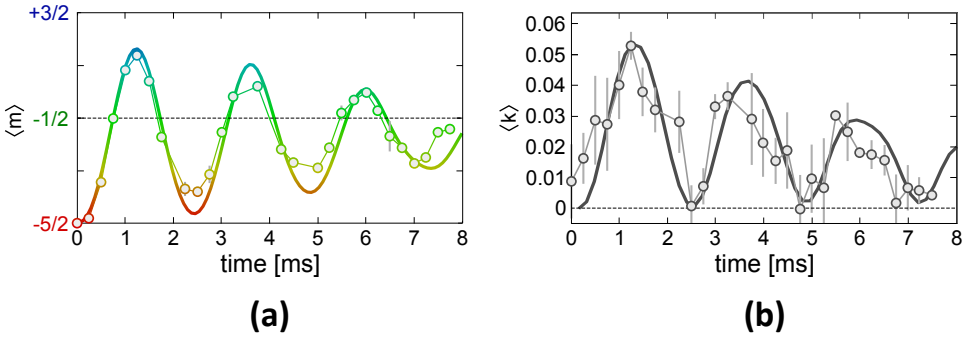

Figure 5.15: Quench dynamics. **(a)** Time dependence of the average position in the synthetic direction $\langle m \rangle$ after a quench of the synthetic tunneling. **(b)** Time dependence of the average lattice momentum $\langle k \rangle$ along the $\hat{x}$ direction. In both the figures the circles represent experimental data, the thin lines connect the points, and the thick lines illustrate the theoretical predictions. Experimental parameters $\Omega_{R,1} = 2\pi \times 490\,\mathrm{Hz}$ and $t = h \times 94\,\mathrm{Hz}$.

5.6 Three-leg ladder: skipping orbits

In the previous sections we discussed equilibrium properties of the experimentally realized hybrid 2D lattice. Now we want to discuss another experiment performed on the three-leg ladder configuration regarding the study of quench dynamics, that provides direct evidence of chiral transport properties along the edges. We prepared a system of lattice fermions in an initial state with zero average momentum on the lower $m = -5/2$ leg of the three-leg ladder. We then perfomed a quench by suddenly activating the complex tunneling in the synthetic direction. Fig. 5.15a shows the time dependence of the average position in the synthetic direction $\langle m \rangle$, measured by optical Stern Gerlach detection. Fig. 5.15b shows the time dependence of the average lattice momentum $\langle k \rangle$ along $\hat{x}$, measured by time-of-flight imaging of the whole cloud. We observe clear in-phase oscillations demonstrating the spin-momentum locking of the atom dynamics.

The data can be combined in order to study the average orbits in the $\hat{x} - \hat{m}$ plane. We first determined the average position $\langle x \rangle$ of the atomic cloud assuming the validity of the semiclassical equation of motion along the real lattice [57]. In this framework, considering the lowest band dispersion as $\varepsilon(k) = 2t\,[1 - \cos(kd)]$, the velocity of the $k-$component of the Fermi sea is:

$$v_k = \frac{1}{\hbar}\frac{\partial \varepsilon(k)}{\partial k} = \frac{2td}{\hbar}\sin(kd). \tag{5.0}$$

Then, knowing the tunneling t, we can measure the average velocity of the whole cloud at a given time τ from the experimental lattice momentum

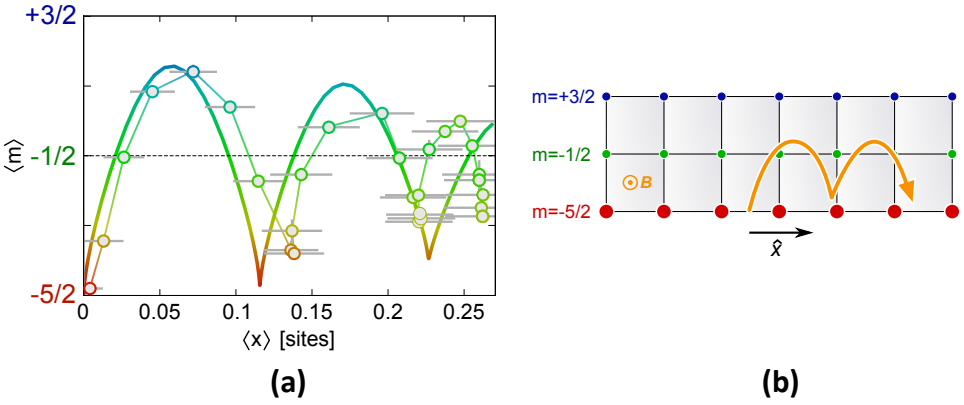

Figure 5.16: Edge-cyclotron orbits. **(a)** Average position in $\hat{m} - \hat{x}$ space. The circles represent experimental data, the thin lines connect the points, and the thick lines illustrate the theoretical prediction. Experimental parameters $\Omega_{R,1} = 2\pi \times 490\,\text{Hz}$ and $t = h \times 94\,\text{Hz}$. **(b)** Schematics of the edge-cyclotron orbit commonly called skipping-orbit.

distribution $n(k, \tau)$:

$$\langle v(\tau) \rangle = \frac{2td}{\hbar} \int n(k, \tau) \sin(kd) dk. \tag{5.0}$$

Finally, to obtain the average position at a given time τ, we integrate the interpolated average velocity over time:

$$\langle x(\tau) \rangle = \int_0^\tau \langle v(\tau') \rangle \, d\tau'. \tag{5.0}$$

In order to estimate the error bars of the edge-cyclotron orbits we perform a bootstrap analysis [132] over a set of different $\langle x(\tau) \rangle$ reconstructed from a random sampling of the experimental images. As can be seen in Fig. 5.16a, the error bars increases during the time evolution. This is due to the accumulated error coming from the numerical integration in Eq. (5.6). Fig. 5.16b shows an experimental reconstruction of the average orbit on the ribbon surface as a plot of $\langle m \rangle$ versus the average position in real space $\langle x \rangle$. The dynamics displays a strong chiral character, demonstrated by the in-phase oscillations in Fig. 5.15a, and b and the orbits in Fig. 5.16b. Under the effect of the synthetic magnetic field, the fermions move according to cyclotron-type dynamics, which is naturally truncated by the synthetic edge, giving rise to a skipping-type orbit, as expected for a quantum Hall system [110, 133]. Furthermore, the experimental data are in reasonable agreement with the theoretical predictions (see Sec. 5.7), represented by the thick lines in Fig. 5.15a, b and Fig. 5.16b. The theoretical simulations have been perfomed by solving numerically the time-evolution of systems at different densities. Indeed, it turned out that assuming a single value

for the density is usually not sufficient to capture the full time-dependent dynamics at the edge. As a matter of fact, in the different ladders of the system, each with a different density, there is a very different fraction of particles participating in the edge dynamics. Whilst not affecting drastically the behavior of J, this inhomogeneity has strong effects on the single edge-dynamics probed by a quench. In order to take into account the inhomogeneity effect, we have simulated systems at various sizes up to $L = 55$ lattice rungs and different densities. For the data shown in Fig. 5.16b, we considered a system of $L = 35$ rungs and averaged over a set of different densities $\overline{n} = (0.2, 0.4, 0.6, 0.8)$ equally weighted. We notice that, when taken singularly, none of these density realizations captures the system dynamics correctly, while the average gives a good quantitative agreement with the experimental results.

These dynamics are effectively damped, even in the idealized case described by theory, as a result of averaging over many different fermionic trajectories, which also causes a reduction of the average orbit radius to less than one real lattice site, Fig. 5.16b. This is markedly different from the behavior of a non-interacting Bose gas, which would occupy a single condensed wave packet undergoing undamped oscillations [25].

5.7 Temperature effects

5.7.1 Thermal fluctuations

In order to include finite temperature effects in the calculation of the chiral currents J plotted in Figs. 5.10, 5.14, two methods can be used. The first one relies upon considering the partition function of the system and calculating the thermal average of the quantity of interest, such as the momentum distribution:

$$\langle n(k) \rangle_T = \sum_j \frac{\langle j|n(k)|j\rangle}{e^{\beta(\varepsilon_j - \mu)} + 1} \tag{5.0}$$

in which $\beta = 1/k_B T$, $|j\rangle$ are the eigenstates of the Hamiltonian (5.3) with energies ε_j and μ is the chemical potential, fixed by the total number of particles.

The second method, which is computationally more efficient, relies upon adding "by hand" a fraction of random thermal excitations. The procedure is as follows:

- one calculates the full spectrum of the Hamiltonian (5.3);
- given a certain number of particles N, one populates the lowest N states up to the Fermi energy E_F and extracts the zero-temperature momentum distribution $n(k)$;

- one introduces particle-hole excitations by hand. Formally, we evaluate a set of momentum distributions, where a certain random fraction $x/|\mu|$ of excited states is populated (and the corresponding $x/|\mu|$ holes are left behind). In each of this realizations f, one considers M states with energy $\varepsilon < E_F$ and $N - M$ states with energy $\varepsilon > E_F$, so that

$$n_f(k) = \sum_{m=1}^{M} n_m(k) + \sum_{l=1}^{N-M} n_l(k) \tag{5.0}$$

  where the index m, l is a state index;

- finally, one sums up all the realizations f, for example F realizations, and obtains the result:

$$n(k, T) = \sum_{f=1}^{F} n_f(k). \tag{5.0}$$

We note that this procedure does not produce an exact thermal average, but rather a very good approximation of a thermal state. The calculations in Figs. 5.10, 5.14 are performed by simulating a system [9] with an average $x/|\mu|$ of 20% thermal excitations above the Fermi sea (both the 2-leg and 3-leg case) and performed averages over up to $F = 200$ configurations. These results are approximately recovered by investigating a finite-temperature partition function with temperature $k_B T \sim 0.4\, t$. The width of the theoretical curves, representing the effect of thermal excitations, has been evaluated as the 68.27% percentile interval centered around the mean value of the statistical distribution obtained with a bootstrapping analysis of 100 realizations of the simulation.

5.8 Synthetic Hall drift

In this Section we describe some preliminary results regarding the observation of Hall-drift like dynamics in the synthetic dimension. By superimposing a linear potential to the real one-dimensional lattice, a Bloch oscillation is induced, corresponding to an AC-current [134, 135]. Due to the presence of the synthetic magnetic field, this current translates in a motion along the "orthogonal" synthetic direction, similar to what happens in a Hall bar.

[9] We considered a single ribbon of 25 sites along the real dimension, and 2 or 3 sites along the synthetic dimensions. The number of particles is taken to correspond to an average filling $\overline{n} \sim 0.8$ with respect to the real one-dimensional lattice.

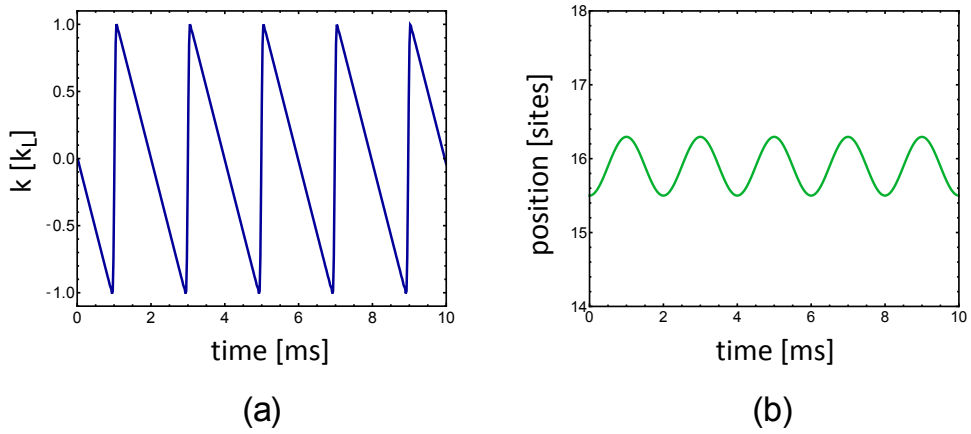

Figure 5.17: Calculated Bloch oscillations in a 1D optical lattice. **(a)** Quasi-momentum evolution. **(b)** Spatial position evolution. Numerical parameters: $\nu_B = 500\,\mathrm{Hz}$, $t = h \times 100\,\mathrm{Hz}$ $L = 30$.

5.8.1 Bloch oscillations in ultracold Fermi gases

We consider a fully polarized Fermi gas loaded in an homogeneous 1D optical lattice. By applying a linear gradient, the single particle Hamiltonian describing the system becomes:

$$\hat{H} = \frac{\hat{p}^2}{2m} + sE_R \sin^2(k_L x) - F_0 x \tag{5.0}$$

where F_0 is a constant force, applied to the atoms along the direction of the lattice. In the limit of weak perturbation (single-band approximation), the semiclassical equation of motion [57] are given by:

$$\frac{dx(t)}{dt} = \frac{1}{\hbar}\frac{\partial \varepsilon(k)}{\partial k}$$
$$\frac{dk(t)}{dt} = \frac{F_0}{\hbar}$$

from which we see that the quasi-momentum k sweeps across the first-Brillouin zone at a frequency:

$$\nu_B = \frac{Fd}{2\pi\hbar} \tag{5.0}$$

where $d = \lambda_L/2$ is the lattice spacing. In Fig. 5.17 we plot the calculated single-particle dynamics for a one-dimensional lattice of 30 sites, Bloch frequency $\nu_B = 500\,\mathrm{Hz}$ and tunneling energy $t = h \times 100\,\mathrm{Hz}$. Note that the maximum excursion along the $\hat{x}$ direction is given by $A_{max} = 4t/h\nu_B$. If we consider a one-dimensional Fermi sea of width $k_F \leq k_L$ along the $\hat{x}$ direction, we have to average over all the momentum states, obtaining a

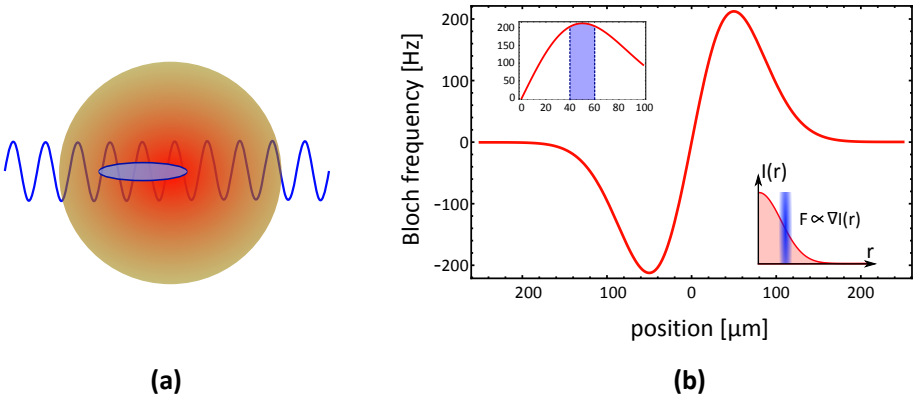

Figure 5.18: Experimental configuration for the optical gradient generation. **(a)** A 1064 nm laser beam is focused onto the atoms, slightly dislocated from the atomic cloud center. **(b)** Calculated Bloch frequency as a function of the distance from the beam spot center. The inset shows a zoom around the maximum Bloch frequency achievable. The beam waist assumed is $w_0 = 100\,\mu$m whereas the laser power is $P = 1\,$W.

zero-amplitude Bloch oscillation in case the Brillouin zone is completely filled. It is thus preferable to work with a low number of atoms ($\lesssim 1.5 \cdot 10^4$) in order to keep the average filling $0.5 \leq \overline{n} \leq 0.8$.

In order to experimentally perform Bloch oscillations with our ^{173}Yb fully polarized Fermi gas, we exploit an optical gradient, generated with a laser beam at 1064 nm slightly misaligned with respect to the atomic cloud (see Fig. 5.18a) center, as in the optical Stern-Gerlach configuration (see Sec. 2.5.2). The laser beam is shone onto the atoms along an orthogonal direction with respect to the real 1D optical lattice (along OL_1 direction of Fig. 5.5). If the laser beam waist is sufficiently large, the optical gradient can be considered approximately linear in the region of the atomic sample. In Fig. 5.18b we show the calculated Bloch frequency for a measured beam waist $w_0 \simeq 100\,\mu$m as a function of the distance from the beam spot center. By choosing $w_0 \gtrsim 10R_F$ (where $R_F \simeq 10\,\mu$m is the typical Fermi radius) the Bloch frequency is approximately constant all over the sample (3.5% of variation around the maximum).

Another important aspect that we need to consider, in order to see long-lived Bloch oscillations, is the effect of a residual harmonic trapping potential along the gradient direction. Indeed, if the Bloch frequency is comparable to the harmonic trapping frequency, dephasing caused by the atomic motion will completely wash out the Bloch oscillations. We thus decided to keep the optical lattice depth along direction OL_1 and OL_3 at a lower level in order to reduce the harmonic trapping potential. Unfortunately, the lattice depth is not a high-range turning knob, since the residual trapping frequency scale as $\sqrt{s}$. In Fig. 5.19 we show a measurement of

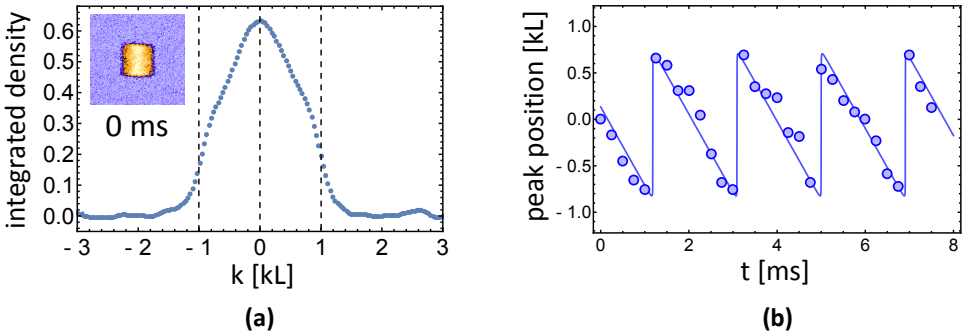

Figure 5.19: Bloch oscillation with a fully polarized Fermi gas. **(a)** Quasimomentum distribution used to extract the peak position. **(b)** Bloch oscillations in an optical gradient. The points are the experimentally determined maximum peak position and the solid line is a fit to the data with a sawtooth-like function. Experimental parameters: $s_1 = s_3 \simeq 22$, $s_2 \simeq 5$, $t \simeq 130\,\mathrm{Hz}$, $P_{grad} \simeq 2.9\,\mathrm{Watt}$, $N_{at} \simeq 1.5 \cdot 10^4$.

the Bloch oscillation for a spin polarized Fermi gas loaded in an optical lattice, with parameters $s_1 = s_3 \simeq 22$, $s_2 \simeq 5$, $t \simeq 130\,\mathrm{Hz}$, giving a residual trapping frequency along OL_2 direction of $\nu_x \simeq 46\,\mathrm{Hz}$. The atoms are adiabatically loaded in the optical lattice, and after 10 ms, the optical gradient beam is suddenly turned on in less then 10 μs. After a variable holding time in the force field, we perform the band mapping procedure in order to map the quasimomentum distribution within the lattice to the free particle momentum states. The cloud is then imaged after a time-of-flight of 23 ms. We fit the evolution of the lattice momentum distribution peak with a sawtooth-like function, and extract the Bloch period. The measured Bloch frequency is $\nu_B = 523\,\mathrm{Hz}$ for a beam power $P_{grad} \simeq 2.9\,\mathrm{Watt}$, 10% less then the expected value, probably due to an imperfect alignment of the optical gradient beam. We note that, due to fermionic statistics, the amplitude of the oscillation is less than k_L. Unfortunately, the alignment of the optical gradient beam is very critical, and it has to be checked on a daily basis. Also, due to the residual harmonic confinement, we are not able to see any complete Bloch oscillation below approximately 200 Hz. This is a limitation since we are interested in the regime $t \sim \Omega_R/2 \sim \nu_B$ and in particular, we would like to avoid the Bragg reflection at the boundary of the Brillouin zone in order to have a current along the real dimension $\hat{x}$ always in the same direction (first half-period of the Bloch oscillation). This would be more similar to what happens in real quatum Hall solid state devices, in which a DC-current is applied to the sample (and not an AC-current).

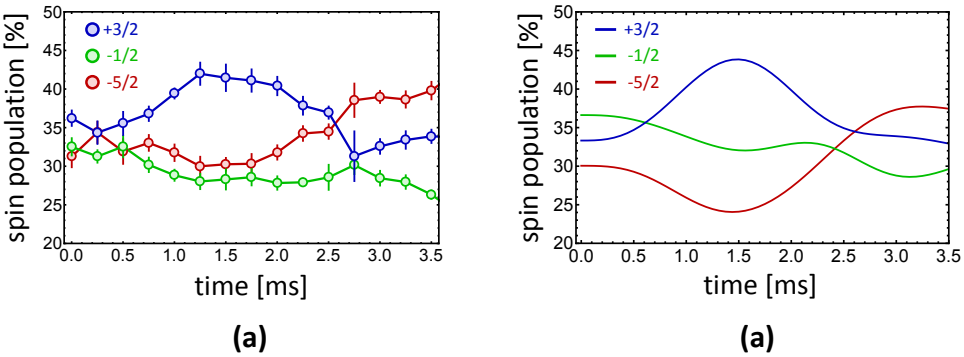

Figure 5.20: Synthetic Hall drift. **(a)** Spin population evolution caused by the optical gradient applied along the real direction $\hat{x}$. The red, green and blue points refer to the $m = -5/2 - 1/2 + 3/2$ spin populations respectively. **(b)** Numerical simulation perfomed over a single hybrid 2D lattice of 30×3 sites. A filling of $\overline{n} = 0.7$ (with respect to the one-dimensional lattice sites, i.e. 30) and a temperature of $T = 0.3\, T_F$ have been considered.

5.8.2 Hall dynamics in the synthetic dimension

In this section we perform the Bloch oscillation experiment in the presence of a Raman coupling in the three-leg ladder configuration (see Sec. 5.5). We thus study the dynamics in the synthetic dimension in the presence of an applied current along the real direction. We prepare the system in the lowest equilibrium state as in the previous sections, we suddenly turn on the optical gradient beam and we monitor the spin population distribution by OSG detection after a variable holding time. In Fig. 5.20a we report a synthetic Hall drift measurement for the following parameters: $s_1 = s_3 = 23$, $s_2 = 4$, $t \simeq 172\,\mathrm{Hz}$, $\nu_B \simeq 207\,\mathrm{Hz}$, $N_{at} \sim 1.2 \cdot 10^4$. The agreement with the numerical simulation, 5.20b, is rather good. There, we considered a single hybrid 2D lattice of 30×3 sites and a filling $\overline{n} = 0.7$ with respect to the one-dimensional lattice available sites, i.e. 30. Within the first quarter of the Bloch period ($\sim 1.25\,\mathrm{ms}$), the population of the $-5/2$ ($+3/2$) edge decreases (increases), giving rise to a positive "Hall voltage drop" $\Delta V_H = \mathrm{Pop}(+3/2) - \mathrm{Pop}(-5/2)$, (see Fig. 5.21). The voltage drop then decreases and changes sign, mainly due to the low number of sites along the synthetic direction and to the AC-character of the Bloch oscillation.

Discrepancies between theory and experiment can be ascribed to the imperfect initial preparation of the lowest dressed band, and also to the possible inhomogeneities in the optical gradient. From the theoretical point of view, we are considering only a single tube (out of approximately 1000 thousands tubes generated by the optical lattice potential), and an average over many different filling factors should be included. We postpone further investigation both experimentally and theoretically, to future

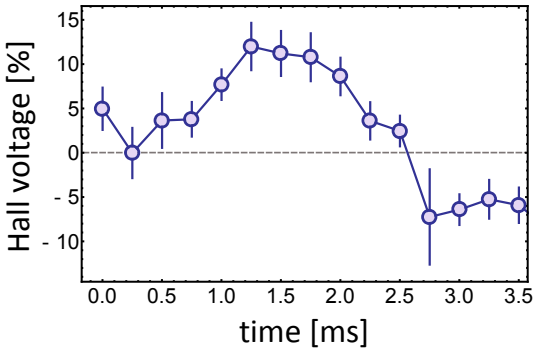

Figure 5.21: Measured "synthetic Hall voltage" defined as $\Delta V_H = \mathrm{Pop}(+3/2) - \mathrm{Pop}(-5/2)$.

studies. Nevertheless, these preliminary data are very promising and it would be very interesting to perform experiments with a larger system, for example by coupling all the six spin states.

5.9 Conclusions and perspectives

In this chapter we reported the first observation of chiral edge states in a system of neutral fermions subjected to a synthetic magnetic field and some very preliminary results regarding the visualization of a synthetic Hall drift with measurement of a Hall voltage in an atomic system with edges. We exploited the high level of control in our system to investigate the emergence of chirality as a function of the Hamiltonian couplings. These results have been enabled by a completely innovative approach, proposed in [22, 23], where an internal degree of freedom of the atoms is used to encode a lattice structure lying in an extra-dimension, providing direct access to edge physics. Our approach can be extended to wide ladder systems with as many as $2I + 1$ legs (up to a maximum of 6 in ^{173}Yb, see Fig. 5.22a), providing a setting for the investigation of both edge and bulk 2D topological matter, complementary to recent works on Chern insulators [18]. This would allow a controlled study of the combined effect of interactions and synthetic gauge fields, crucial for the realization of fractional quantum Hall physics, potentially leading to exotic states of matter in ladder systems. Indeed, in Ref. [43], analytical and numerical studies have predicted the existence of a full hierarchy of gapped and gapless phases with unusual properties. The simultaneuous presence of interactions and gauge potentials, leads the system to displays different behaviours ranging from magnetic crystals to helical phases.

Moreover, the flexibility offered by the present scheme allows the engineering of arbitrary lattice patterns, including disorder and constriction, in ladder systems. Indeed, it would be very interesting to study the ro-

bustness of the observed chiral currents, in presence of localized impurities. Also, the possibility to engineer periodic boundary conditions (Fig. 5.22b) along the synthetic dimension [136], opens the door to the study of the topological properties of bulk physics, focusing on the observation of the fractal structure of the Hofstadter spectrum, see Fig. (Fig. 5.23), for example by exploiting the ultranarrow clock transition of Ytterbium (see Chapter 7), to perform precise spectroscopy of the magnetic subbands. Last but not least, thanks to the periodic boundary conditions, it would be possible to realize the famous topological Laughlin pump [122], measure the quantization of the Hall conductivity and extract the corresponding Chern number. Combining periodic boundary conditions and interactions [43], allows the system to reach the thin torus limit [137, 138], in which the fractional quantum Hall states are density waves, with features that respect the conditions for observing the Laughling series in the quantum Hall effect.

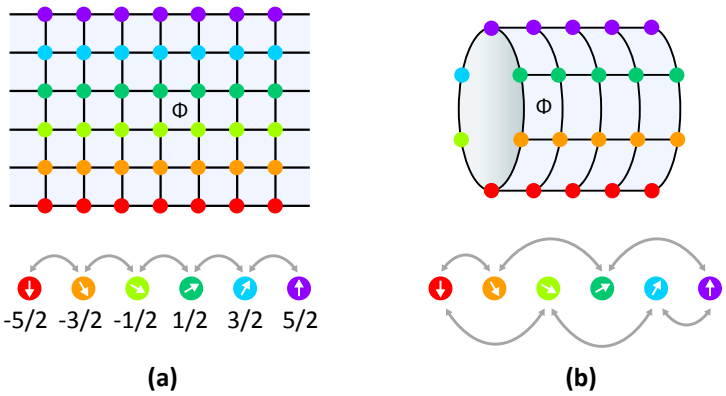

Figure 5.22: Designing the synthetic dimension. By using laser light producing state-dependent light shifts and selective Raman couplings with appropriate polarization/frequencies, it is possible to engineer different connectivities in the synthetic direction. From ladders with up to six legs **(a)** (with sharp synthetic edges) to a cylinder geometry with periodic boundary conditions **(b)**.

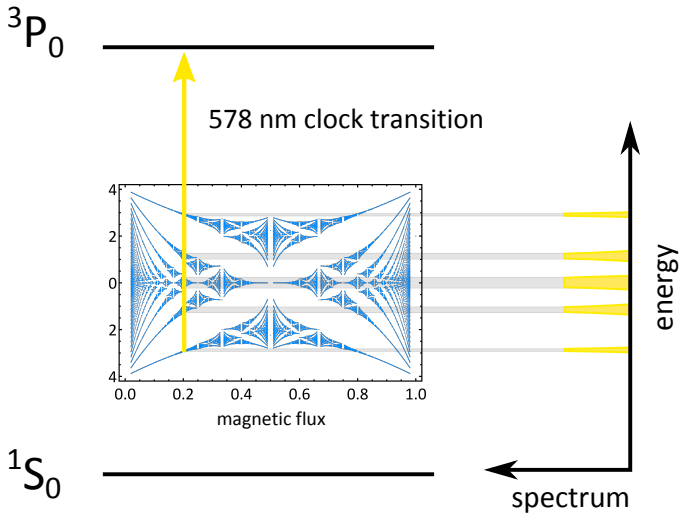

Figure 5.23: Detecting the Hofstadter's butterfly. The ultranarrow Yb 578 nm $^1S_0 \rightarrow {}^3P_0$ clock transition could be used, in combination with state-dependent potentials, to perform a spectroscopic measurement of the Harper-Hofstadter spectrum, exhibiting the fractal butterfly structure.

6 A multicomponent 1D liquid of fermions

Correlations in systems with spin degree of freedom are at the heart of fundamental phenomena, ranging from magnetism to superconductivity. The effects of correlations depend strongly on dimensionality, a striking example being one-dimensional electronic systems, extensively studied theoretically over the past fifty years [139–142]. However, the experimental investigation of the role of spin multiplicity in 1D fermions, and especially for more than two spin components, was lacking. In this Chapter, we report the first realization and experimental study of 1D, strongly correlated liquids of ultracold fermions interacting repulsively within $SU(N)$ symmetry, with a tunable number N of spin components.

We will proceed as follows. Section 6.1 introduces some basic aspects of the Tomonaga-Luttinger model [139], a successful theoretical framework for the description of fermions confined to one-dimensional geometries. Section 6.2 describes the experiments performed in order to investigate a one-dimensional liquid of fermions with a tunable number of spin components. In particular we will focus on the behavior of the momentum distribution of the atomic sample as a function of the spin multiplicity, on the measurement of the low energy excitations with Bragg spectroscopy techniques and finally, on the role of the number of spin components in determining the frequencies of the lowest collective mode of excitation.

6.1 Basic principles of 1D liquid of fermions

One-dimensional quantum systems show specific, sometimes counterintuitive behaviours that are absent in the 3D world. These behaviours, predicted by many-body models of interacting bosons [143] and fermions [140, 141], include the "fermionization" of bosons [144] and the separation of spin and density (most commonly referred to as "charge") branches in the excitation spectrum of interacting fermions. The last phenomenon is predicted within the celebrated Luttinger liquid model [139], which describes the low-energy excitations of interacting spin-1/2 fermions.

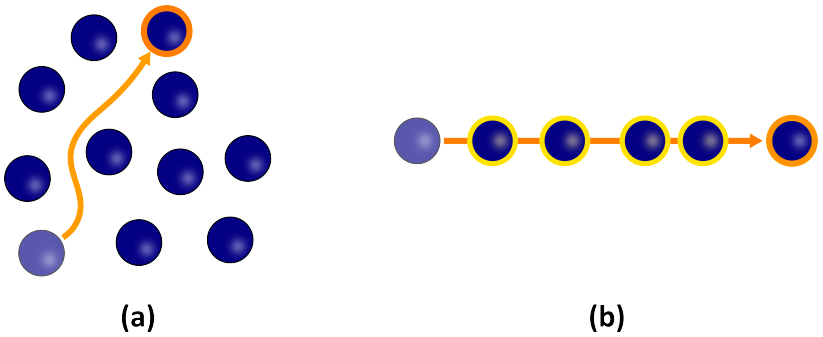

Figure 6.1: Pictorial representation of the failure of the Fermi liquid model. **(a)** In high dimensions, nearly free quasi-particle excitations exist. **(b)** In a one-dimensional interacting system, only collective excitations can exist.

In this Section we will give a brief review of that model with emphasis on its application to a system of ultracold atoms.

6.1.1 Failure of the Fermi liquid paradigm

At $T = 0$ all states up to the Fermi energy are occupied in a 3D gas of free fermions. The excitations of the system, relative to the ground state, have a particle-hole character, having a well defined momentum $\mathbf{q}$ and energy $\varepsilon(\mathbf{q})$. To characterize these excitations one can introduce the probability fo find a state with frequency ω and momentum $\mathbf{q}$, which is described by the spectral function $A(\mathbf{q}, \omega)$ [139]. The remarkable result of the Landau's approach to the Fermi liquid theory is that turning on the interactions doesn't change much, in the sense that the properties of the system remain essentially similar to those of free fermionic particles. The elementary particles are now fermionic quasi-particles, fermions dressed by the density fluctuations around them. These new characters behave as they were essentially free, apart from a few changes in the effective mass m^* or in some quantities like susceptibilities [145].

In one dimension, instead, interactions have drastic effects compared to higher dimension, where nearly free quasiparticle excitations exist. Let us consider the case of repulsive interactions. Naively, in one dimension, a fermion that tries to propagate has to push the other particles because of the repulsive interactions, see Fig. 6.1. Any single-particle excitation now becomes a collective one. This characteristic clearly makes any attempt to describe the situation within the Fermi liquid framework, unsuccesful. For fermions with spin things get even worse[1], because a single fermionic excitation has to split into a collective mode carrying charge and a collective mode carrying spin. This is the famous phenomenon of spin-charge separation, because in general the two excitations have different velocities.

[1] Or more exciting.

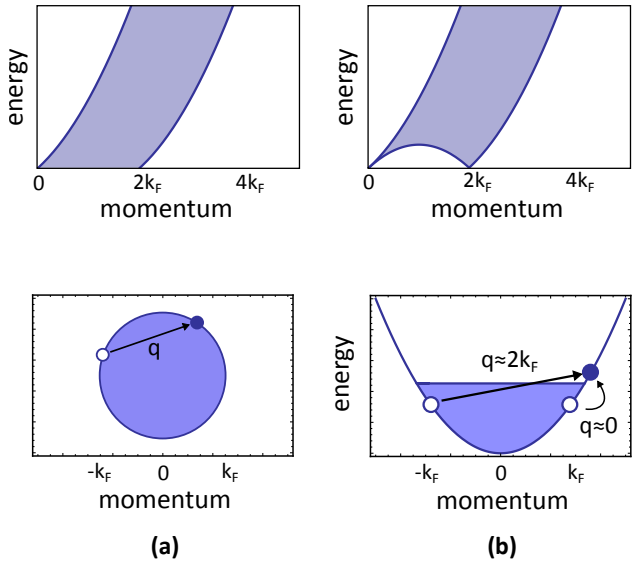

Figure 6.2: Particle-hole excitation spectrum in high dimensions **(a)** and one dimension **(b)**. The energy gap between $q = 0$ and $q = 2k_F$ is a peculiarity of the one-dimensional geometry.

Another difference between one and higher dimensions is the particle-hole continuum, namely the region of the $(\hbar\mathbf{q}, \hbar\omega)$ plane (with $\hbar\mathbf{q}$ and $\hbar\omega(\mathbf{q})$ being the momentum and excitation energy respectively) where it is possible to create a number-conserving particle-hole excitation. In high dimensions, for $|\mathbf{q}| < 2k_F$ it is possible to create an excitation of arbitrarily low-energy by annihilating a particle just below the Fermi surface and recreating it just above. In one dimension the situation is different because the Fermi surface is constituted by just two points at $\pm k_F$ and therefore the excitations of vanishing energy are only possible at $q = 0, 2k_F$ as is depicted in Fig. 6.2. All these properties, quite different from the ones of a Fermi liquid, are the essence of the Tomonaga-Luttinger liquid, that we will now briefly describe in the context of ultracold Fermi gases.

6.1.2 Luttinger liquid approach to 1D Fermi gases

Following Refs. [146, 147], we briefly discuss the properties of one-dimensional fermionic atoms using the Luttinger liquid theory. One dimensional, harmonically trapped, Fermi gases can be efficiently described by the following Hamiltonian:

$$\hat{H} = \sum_{\sigma} \int dx\, \hat{\Psi}^{\dagger}_{\sigma}(x) \left[-\frac{\hbar^2}{2m}\partial_x^2 + V_{ext}(x) \right] \hat{\Psi}_{\sigma}(x) + g_{1D} \int dx\, \hat{\Psi}^{\dagger}_{\uparrow}(x)\hat{\Psi}^{\dagger}_{\downarrow}(x)\hat{\Psi}_{\downarrow}(x)\hat{\Psi}_{\uparrow}(x)$$

where $V_{ext}(x)$ is the external harmonic potential, $\hat{\Psi}^{\dagger}_{\sigma}(x)$ and $\hat{\Psi}_{\sigma}(x)$ are fermionic creation and annihilation operators in real space and the quantity g_{1D} represents the strength of the repulsive zero-range interaction given by the formula [148]:

$$g_{1D} = -\frac{2\hbar^2}{ma_{1D}} = \frac{2\hbar^2 a_{3D}}{ma_{\perp}^2}\frac{1}{1-1.033a_{3D}/a_{\perp}} \tag{6.-1}$$

in which a_{3D} is the 3D scattering length and $a_{\perp}$ is the harmonic oscillator length associated to the confinement in the transverse (frozen) directions. We can introduce a dimensionless parameter γ, [149]

$$\gamma = \frac{mg_{1D}}{\hbar^2 n_{1D}} = -\frac{2}{n_{1D}a_{1D}} \tag{6.-1}$$

giving the (approximate) ratio between the interaction energy $g_{1D}n_{1D}$ and the kinetic energy of an ideal homogeneous Fermi gas $\varepsilon = \hbar^2\pi^2 n_{1D}^2/8m$. From Eq. (6.1.2) we observe that, counterintuitively, the role of interactions increases by decreasing the density of the sample.

In the homogeneous case ($V_{ext} = 0$), the Hamiltonian can be written in momentum space as:

$$\hat{H} = \sum \varepsilon_k \hat{c}^{\dagger}_{k,\sigma}\hat{c}_{k,\sigma} + \frac{g_{1D}}{L}\sum_{kk'q}\hat{c}^{\dagger}_{k+q,\uparrow}\hat{c}^{\dagger}_{k'-q\downarrow}\hat{c}_{k'\downarrow}\hat{c}_{k\uparrow} \tag{6.-1}$$

where $\varepsilon_k = (\hbar^2k^2/2m - \mu)$ and $\hat{c}^{\dagger}_{k,\sigma}$, $\hat{c}_{k,\sigma}$ are creation and destruction fermionic operators at momentum k and spin state σ. Eq. (6.1.2) can be further manipulated by introducing left-moving (around $-k_F$) and right-moving (around k_F) fermionic annihilation (creation) operators $\hat{c}^{\dagger}_{r,\sigma}(k)$, where $r = R, L$, and the respective densities fluctuations operators $\hat{\rho}_{r,\sigma}(q) = \sum_k \hat{c}^{\dagger}_{r,\sigma}(k+q)\hat{c}_{r,\sigma}(k)$. In the model, the four particle species ($R\uparrow$, $R\downarrow$, $L\uparrow$, $L\downarrow$) have unbounded free dispersion relation $\varepsilon_r(q) = a_r\hbar v_F q$, where v_F is the Fermi velocity and $a_{R(L)} = +(-)$. All states up to the Fermi energy are occupied and one has two branches of particles with boundless energy and momentum, and the densities obey Bose-type commutation relations [146]. One can then introduce four new boson fields $\hat{\phi}_{\nu}$, $\hat{\Pi}_{\nu}$, with $\nu = c, s$, related to the fluctuations of the total density $\hat{\rho}_c = \partial_x\hat{\phi}_c/\sqrt{\pi}$, of the spin-density $\hat{\rho}_s = \partial_x\hat{\phi}_s/\sqrt{\pi}$, of the current density $j_c = -\hat{\Pi}_c/\sqrt{\pi}$ and of the spin current density $j_s = -\hat{\Pi}_s/\sqrt{\pi}$. With these new fields, we can write the Luttinger Hamiltonian in the bosonized form [146]:

$$\hat{H} = \sum_{\nu=c,s}\frac{u_{\nu}}{2}\int dx\left[K_{\nu}\hat{\Pi}_{\nu}^2 + \frac{1}{K_{\nu}}(\partial_x\hat{\phi})^2\right] \tag{6.-1}$$

which represents two independent elastic strings with the eigenmodes corresponding to the collective density and spin-density fluctuation of the

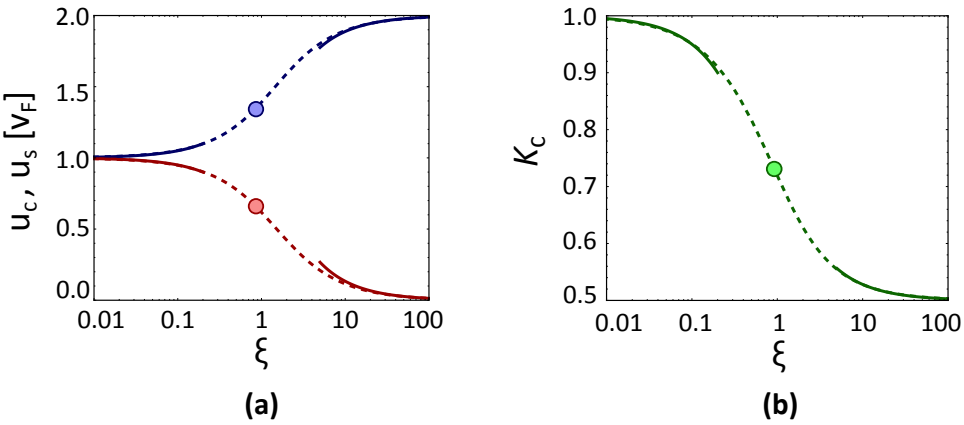

Figure 6.3: **(a)** Charge (blue) and spin (red) velocities in unit of the Fermi velocity v_F as a function of the interaction parameter ξ. The solid lines are u_c, u_s in the strong and weak coupling regime. The dashed lines are an interpolation between the two limits. The points correspond to the value of ξ obtained for our experimental parameters. **(b)** Luttinger parameter as a function of ξ. The point correspond to the value $K \simeq 0.7$ obtained for our experimental parameters.

fermion liquid respectively. The parameters u_ν are the "sound" velocities, while K_ν are called Luttinger parameters and completely characterize the low energy physics. In a spin rotationally invariant Fermi gas the quantity $K_s = 1$ so that the only independent parameters are K_c and u_ν. The sound velocities can be expressed as a function of the interaction parameter in the weak coupling limit as:

$$u_c = v_F\sqrt{1+\tilde{\xi}},$$
$$u_s = v_F\sqrt{1-\tilde{\xi}}$$

in which $\tilde{\xi} = 2\gamma/\pi^2$, and in the strong coupling limit as [140]:

$$u_s = \frac{2\pi\hbar n_{1D}}{3m\xi},$$
$$u_c = \frac{\pi\hbar n_{1D}}{m}(1 - 8\ln(2)/\pi^2\xi),$$

In Fig. 6.3a, we plot the interpolated velocities as a function of the interaction parameter $\xi = 2\gamma/\pi^2$. The behavior of the velocities in the strong coupling regime $\xi \to \infty$ confirms the physical intuition that when the atoms repel each other so strongly, some properties of the gas are similar to those of an ideal full-polarized gas of indistinguishable particles. This phenomenon is called "fermionization" [139], because the infinite repulsion mimics the effects of a Pauli repulsion between distinguishable particles. In this limit, the spin velocity becomes $u_s = 0$ and the charge

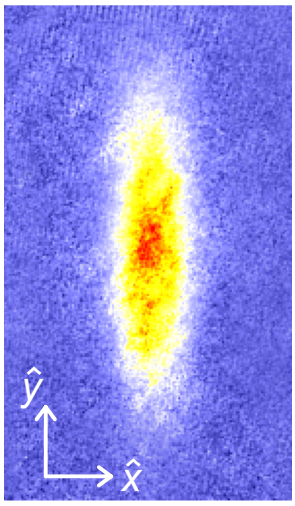

Figure 6.4: Typical false color, averaged absorption image (the $\hat{x}$ axis denotes the direction of the wires) of the released one-dimensional tubes.

velocity becomes $u_c = 2v_F$, that is the Fermi velocity of a non-interacting Fermi gas with twice the number of atoms.

The regime explored in the experiment is that of intermediate coupling with $\xi \simeq 1$, as shown by the points in Fig. 6.3a. Analogously, the Luttinger parameter in our system is $K_c \simeq 0.7$, an intermediate value between the non-interacting case $K_c = 1$ and the case of infinite repulsion $K_c = 0.5$ (see Fig. 6.3b). In order to estimate the Luttinger parameters of the experimental system, the inhomogeneity due to the harmonic trapping potential has been taken into account by performing a local density approximation (LDA) [45].

6.2 Experimental realization of a 1D liquid of fermions with tunable spin

In this Section we report the experiments performed during the beginning of my PhD, which are the main topics of my colleague's G. Pagano PhD thesis [44, 45]. In particular, we investigated the properties of a multi-component one dimensional liquid of fermions realized by loading ^{173}Yb atoms in a two-dimensional optical lattice. Such a geometry creates an array of approximately 1000 thousands independent tubes of which we studied the average properties.

First of all, we characterized the role of correlations in the one-dimensional fermionic tubes by studying the interactions-induced broadening of the momentum distribution with increasing number of spin components. Secondly, the technique of Bragg spectroscopy has been exploited in order

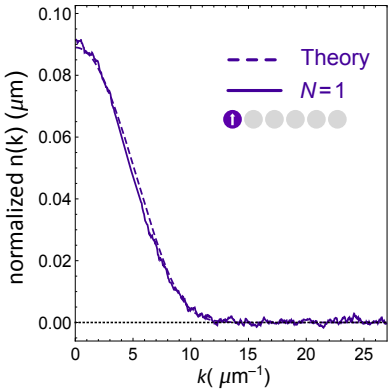

Figure 6.5: Momentum distribution $n(k)$ measured after time-of-flight for polarized fermions loaded in 1D tubes. The dashed line is the theoretical curve calculated taking $\omega_x = 2\pi \times 103$ Hz, $T/T_F = 0.3$, $s = 40$, $N_{at} = 6500$. The experimental curve is obtained as an average over 35 images.

to investigate the low momentum density-excitation spectrum ($q \ll k_F$) as a function of the number of spin components. From these data, the "charge" velocity for a two-component Fermi gas can be extracted. Finally, we characterized the system by measuring the lowest collective mode frequency (breathing mode) as a function of the spin multiplicity. For the first time, we confirmed the large-spin bosonization prediction of Ref. [39], for which a one-dimensional liquid of fermions with a high number of spin components, exhibits properties of an interacting, bosonic, spinless liquid.

6.2.1 Momentum distribution

The system consists in a ^{173}Yb degenerate Fermi gas trapped in a harmonic potential at $T < 0.3T_F$ and with $N_{at} \simeq 6500$ atoms per spin component. The spin population distribution is initialized thanks to the optical pumping techniques described in Sec. 2.5.3. After loading the Fermi gas in a two-dimensional optical lattice at $s = 40$, we wait 10 ms and then suddenly switch off the trap in less then 10 μs. After a ballistic expansion of $t_{TOF} = 23$ ms, the sample is detected by means of absorbtion imaging, as done in previous works to measure the momentum distribution $n(k)$ of a Tonks-Girardeu gas [150]. In Fig. 6.4, we report a typical false-color image of the atomic cloud, in which the direction of the tubes is $\hat{x}$. Due to the tighter confinement induced by the optical lattices, the cloud is elongated along the orthogonal direction $\hat{y}$. To obtain the curves plotted in Fig. 6.5 and 6.6, we integrate over $\hat{y}$ and normalize the resulting $n(k)$ in such a way as to have $\int n(k)\, dk = 1$, being k the momentum along $\hat{x}$. Increasing the number of spin components N, we observe a clear monotonic broad-

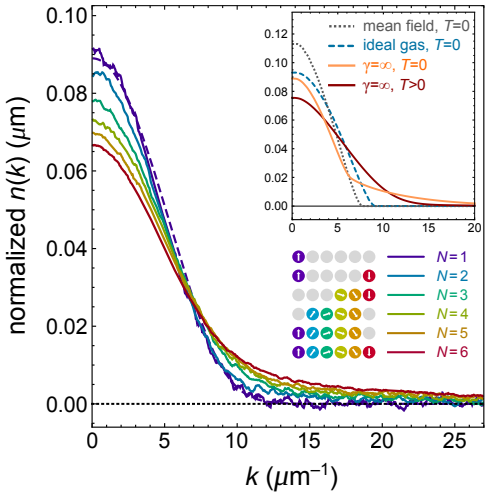

Figure 6.6: Momentum distribution $n(k)$ measured with time-of-flight absorption imaging for different N and the same atom number N_{at} per spin component. Each curve results from the average of 30-50 experimental images. The inset represents the theoretical $n(k)$ for the $N = 2$ system derived from different models: ideal Fermi gas at $T = 0$ (dashed), mean-field treatment of finite interactions at $T = 0$ (dotted), full many-body problem for infinite interactions both for $T = 0$ (light solid from ref. [151]) and $T_s \ll T \ll T_F$ (dark solid from ref. [152]). Only the many-body curves account for the observed broadening.

ening of $n(k)$, with a reduction of the weight at low k and a slower decay of the large-k tails (see Fig. 6.6). We rule out a possible explanation of the observed changes in $n(k)$ in terms of different temperatures for different N. Indeed, we have verified that, after slowly ramping down the lattices to recover a 3D Fermi gas, the temperature measured for the different spin mixtures has the same value $T = 0.3\,T_F$ for all N within the experimental uncertainties. In this 3D regime the effects of interactions are very weak. As a matter of fact, for 3D Fermi gases we have not detected any significative change in $n(k)$ as a function of N. This observation both makes the temperature measurement in 3D reliable and demonstrates that the observed increase in width comes from the increased correlations in the interacting 1D systems[2].

We start by analysing the non interacting case $N = 1$, for which a theoretical prediction can be easily formulated. Indeed, the momentum

[2]Since the number of atoms per spin components is kept constant for all the spin mixtures, if interactions were absent, the width of $n(k)$ would be the same for all curves. Indeed the Fermi momentum would be equal for all spin mixtures.

distribution of a trapped 1D Fermi gas is:

$$n_{1D}(k) = -\sqrt{\frac{k_B T}{2\pi m\hbar^2\omega_x^2}}\mathrm{Li}_{1/2}\left(-ze^{-\frac{\hbar^2k^2}{2mk_BT}}\right), \tag{6.-3}$$

in which $\omega_x = 2\pi \times 103(1)$ Hz is the measured trapping frequency along the tubes axis $\hat{x}$, z is the fugacity and $\mathrm{Li}_{1/2}$ is the Polylogarithmic function of order $1/2$. Since many independent tubes are present, we have to take into account the contribution of each one to the total signal. Infact, the number of atoms per tube decreases from a maximum of 20 (per spin component) in the central tube, to a vanishing occupation of the more peripheral tubes [44]. The number of fermions in the tube ij is calculated in the ideal case by minimizing the total energy of the system imposing Fermi statistics (for $T = 0$) and the constraint on the total number of atom $N_{at} = \sum_{ij} N_{ij}$. The expression to be minimized is:

$$E\left[\{N_{ij}\}\right] = \sum_{ij} N_{ij}\left(\frac{1}{2}m\omega_y^2 d^2 i^2 + \frac{1}{2}m\omega_z^2 d^2 j^2\right) + \sum_{n_x=0}^{N_{ij}-1}\hbar\omega_x\left(n_x + \frac{1}{2}\right) \tag{6.-3}$$

in which $\omega_{y,z} = (2\pi \times 93\,\mathrm{Hz}, 2\pi \times 96\,\mathrm{Hz})$ are the angular frequencies of the slowly varying harmonic trapping potentials in the direction orthogonal to the tubes, and $d = \lambda_L/2$ is the lattice spacing. Through the relation $k_B T_F(i,j) = N_{ij}\hbar\omega_x$, the local Fermi temperature is calculated, which is then used for extracting the local fugacity z_{ij}:

$$\mathrm{Li}_1(-z_{ij}) - \frac{T_F(ij)}{T}. \tag{6.-3}$$

Using Eq. (6.2.1) it is possible to calculate the momentum distribution for each tube and then to take the weighted avarage over all tubes:

$$n(k) = \frac{1}{N_{at}}\sum_{ij} N_{ij} n_{ij}(k). \tag{6.-3}$$

This procedure works very well as can be seen by the agreement between the experimental data and the calculated momentum distribution in Fig. 6.5.

The observed $n(k)$ broadening in Fig. 6.6 arises from a pure many-body effect not accounted for by standard mean-field physics [44]. To our knowledge, no theoretical calculations have been performed for finite interaction strength and finite temperature, neither for the $N = 2$ case nor for $N > 2$. Nevertheless we can give a qualitative explanation for the detected broadening in the $N = 2$ case and observe that, for $N > 2$, the effect is amplified. Indeed, if we consider a mixture of spin-1/2 fermions in the limit of infinite repulsive interaction, the density-density correlation

function $G_{\uparrow\downarrow)}(d) = \langle \hat{n}_\uparrow(x+d)\hat{n}_\downarrow(x)\rangle$ (where $\hat{n}_\uparrow(x)$ and $\hat{n}_\downarrow(x)$ are the density operators for the two spin components) falls to zero for $d \to \infty$ as $G_{\uparrow\uparrow}(d)$ does in the case of a spin polarized gas, thus mimicking the effects of Pauli repulsion between distinguishable particles. This fermionization, restricting the effective space which is available to the particles, causes them to populate states with larger momentum [151, 152]. We note that an opposite behaviour would be predicted by a mean-field treatment of interactions: the effectively weaker confinement along $\hat{x}$ induced by the atom-atom repulsion would lead to more extended single-particle wavefunctions, hence to a decreased width of $n(k)$. For $N = 2$ the interaction regime of our 1D samples is described by the parameters $\gamma \simeq 4.8$ and $K_c \simeq 0.73$.

The details of $n(k)$ depend nontrivially on the temperature, owing to the thermal population of spin excitations. Infact, one can define a spin temperature [153] $T_s = (8\log 2)T_F/3\gamma$, which corresponds to the maximum energy difference between different spin configurations. This energy scale separates two different regimes: at $T \ll T_s$ we have the pure Luttinger liquid model (see inset of Fig. 6.6) whereas at $T > T_s$ we have an intermediate regime where the spin degree of freedom is strongly disordered. The latter regime is generally called "spin-incoherent Luttinger liquid" [142]. For our experimental parameters we obtain $T_s \simeq 0.4T_F$, so that $T \lesssim T_s$, in the crossover between the spin-ordered regime and that of a spin-incoherent Luttinger liquid. In the inset of Fig. 6.6 we show the theoretical $n(k)$ for $N = 2$ and infinite repulsion in the limiting regimes $T = 0$ and $T \gg T_s$. Although both curves show an evident $n(k)$ broadening, in accordance with our observations, their shape is different and, in the finite temperature case, can be explained in terms of a modified effective Fermi momentum [154].

6.2.2 Probing Excitations

A distinctive feature of 1D fermions is the existence of a well-resolved excitation spectrum at low momenta $q \ll k_F$. Number conserving excitations in the ideal 1D Fermi gas correspond to particle-hole pairs with energy $\hbar\omega = v_F\hbar q$, where v_F is the Fermi velocity. According to the Luttinger theory, interactions make excitations acquire a purely collective character. The spectrum of phononic excitations is still described by a linear dispersion $\omega = cq$, where $c = v_F/K_c$ is a renormalized sound velocity which, in a two-component mixture, depends on the Luttinger liquid parameter K_c. Since $0.5 < K_c < 1$, the sound velocity is larger than the Fermi velocity (see Sec. 6.1).

We characterized the excitation spectrum of the fermionic tubes by performing Bragg spectroscopy with 759 nm light. This technique, relying on inelastic light scattering, allows the selective excitation of density

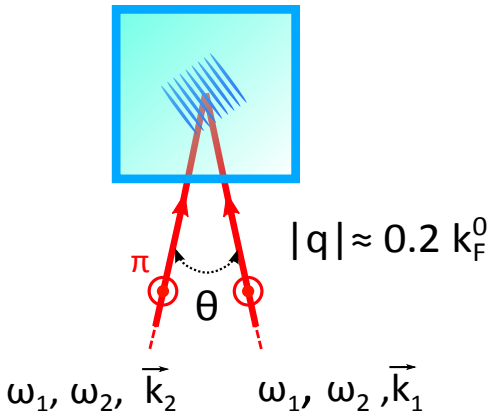

Figure 6.7: Sketch of the experimental configuration for probing the excitation spectrum. The Bragg spectroscopy technique that we have implemented, relies on the inelastic scattering of light at 759 nm. The momentum transferred to the atoms depend on the angle θ between the Bragg beams and the energy is given by $\hbar(\omega_2 - \omega_1)$ [45].

waves with energy $\hbar\omega$ and momentum $\hbar q$ [44, 155]. Note that, since the light used is far-detuned with respect to any atomic transition, the Bragg excitation acts equally on each spin components, i.e. we are only exciting charge modes. In Fig. 6.7 we sketch the experimental setup used to impart momentum and energy to the 1D tubes[3]. The angle between the Bragg beams is small enough to guarantee that the transferred momentum is much lower than the Fermi momentum, $q \ll k_F$, so that we can study the phononic part of the excitation spectrum. Also, Bragg pulse length and intensity are chosen in such a way to result in a combined interaction-time and power broadening < 100 Hz, much less than the width of the measured spectra. In order to both minimize the effect of laser phase fluctuations and increase the signal, the spectrum of each of the two Bragg beams contains both the frequencies ω_1 and ω_2, resulting in both left-moving and right-moving excitations. The transferred momentum to the cloud, measured by time-of-flight imaging, is directly proportional to the imaginary part of the response function $\chi(q,\omega)$ [156], which is directly related to the dynamic structure factor $S(q,\omega)$ by the relation:

$$Im[\chi(q,\omega)] = -\frac{\pi}{\hbar}\left[S(q,\omega) - S(-q,\omega)\right] \tag{6.-3}$$

Fig. 6.8 shows the measured increase of the atomic momentum for $N = 1$ at low momentum transfer $q \simeq 0.2k_F^0$ (with k_F^0 being the peak Fermi wave

[3]The setup is very similar to the one exploited in the previous Chapter, with the difference that the polarizations of both beams are vertical with respect to the quantization axis (π polarizations). Also, the light used is far-detuned so that spin-flip mechanisms are not possible.

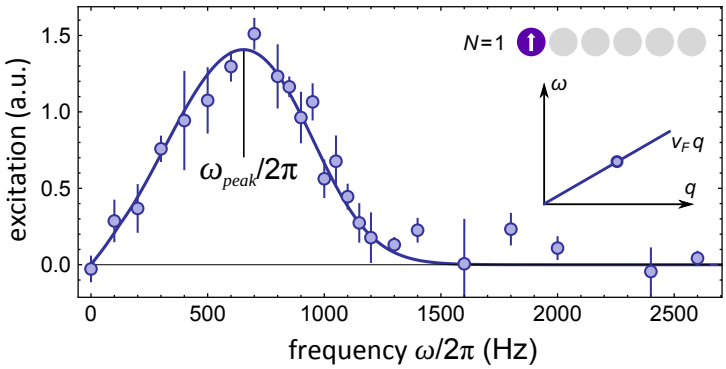

Figure 6.8: Excitation spectrum of 1D non-interacting fermions. The points show the measured increase in atomic momentum after a Bragg excitation with energy $\hbar\omega$ and momentum $q \simeq 0.2k_F^0$ for $N = 1$. The solid line is the calculated response function for the ideal Fermi gas.

vector in the central tube). A clear resonance is observed, in excellent agreement with the calculated response for ideal fermions (solid line, with no free parameters). For $N = 2$ the resonance is clearly shifted towards higher frequencies (Fig. 6.9a), as expected from the Luttinger theory. The measured shift $(+15 \pm 4)\%$ agrees with the expected $(+10 \pm 2)\%$ shift in the sound velocity predicted on the basis of the Luttinger theory for a trapped system [149]. For $N = 6$ the spectrum shows a much larger shift $(+33 \pm 4)\%$ (Fig. 6.9b), which disagrees with the predictions for $N = 2$, signalling an increased effect of interactions, in qualitative accordance with the $n(k)$ broadening. We also plot the calculated spectra for trapped fermions with infinite interactions (Fig. 6.9a,b dotted lines), which show how the measured spectra lie between the response of the ideal Fermi gas (solid lines) and that of a fermionized system.

6.2.3 Collective mode frequencies

More insight into the physics of multicomponent 1D fermions can be gained by studying the low-energy breathing oscillations in which the cloud radius oscillates in time. We measure the frequency of this collective mode by suddenly changing the trap frequency and measuring the time evolution of the radius. In Fig. 6.10a, we plot the measured squared ratio $\beta = (\omega_B/\omega_x)^2$ of the breathing frequency ω_B to the trap frequency ω_x as a function of N (squares). For $N = 1$ the measured value is in good agreement with the expected value $\beta = 4$ for ideal fermions (upper horizontal line). With increasing N our data clearly show a monotonic decrease of β, induced by the repulsive interactions in the spin mixture. The dependence of β on the interaction strength is remarkably non trivial already for $N = 2$, as first predicted in [149]. Indeed, $\beta = 4$ in both the limiting cases

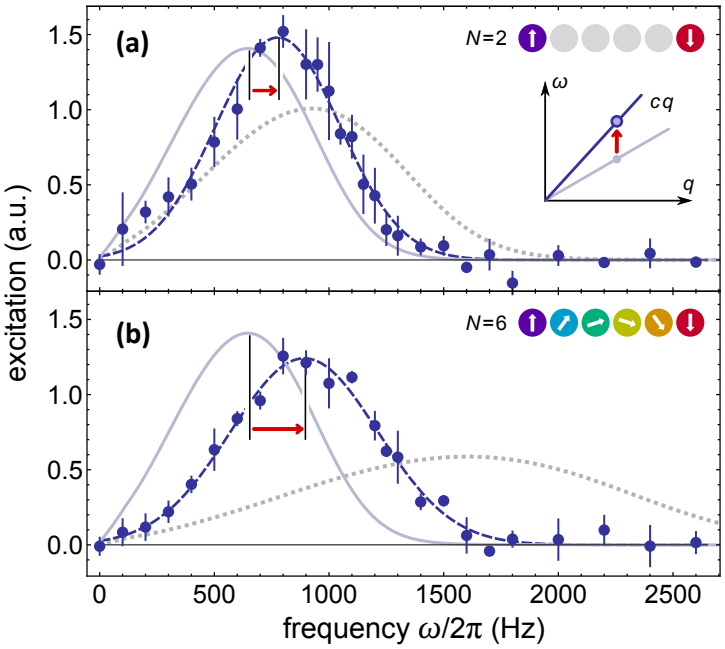

Figure 6.9: Excitation spectra of 1D interacting spinful fermions. **(a)** $N = 2$ and **(b)** $N = 6$. The dashed lines are Gaussian fits to the experimental points to extract the peak excitation frequency. The dotted lines show the calculation in the limit of infinite repulsion. Both experimental and theoretical spectra have been normalized to unit area. The graph in the inset show a sketch of the excitation spectrum at low q for the two-component Luttinger liquid with repulsive interactions. The red arrows indicate the shift in the excitation resonance with respect to the peak of the non-interacting case (grey solid lines).

of an ideal gas ($\gamma = 0$) and a fermionized ($\gamma = \infty$) system, whereas for finite repulsion it is expected to exhibit a nonmonotonic behaviour, with a minimum at finite interaction strength. The theoretical curves in Fig. 6.10b show the expected dependence of β on the interaction parameter $\eta = N_{at}^1(a_{1D}/a_x)^2$ in which N_{at}^1 is the number of atoms per tube, a_{1D} is the 1D scattering length and a_x is the trap oscillator length. These results have been derived by our collaborators at the Swinburne University, H. Hu and X.-J. Liu, by combining a Bethe Ansatz approach with the exact solution of the hydrodynamic equations describing a 1D fermionic liquid with N components [45, 157]. As N is increased, the curves exhibit an increasingly larger redshift of β, and for $N \to \infty$ they asymptotically approach the curve for $1D$ spinless bosons. The circles indicate the theoretical values for the average $\eta = 0.44$ in our experiment. The agreement between experiment and theory is excellent, as shown in Fig. 6.10a. The experimental data, accompanied by the theoretical curve, clearly show that changing N causes markedly different effects from those induced by simply changing

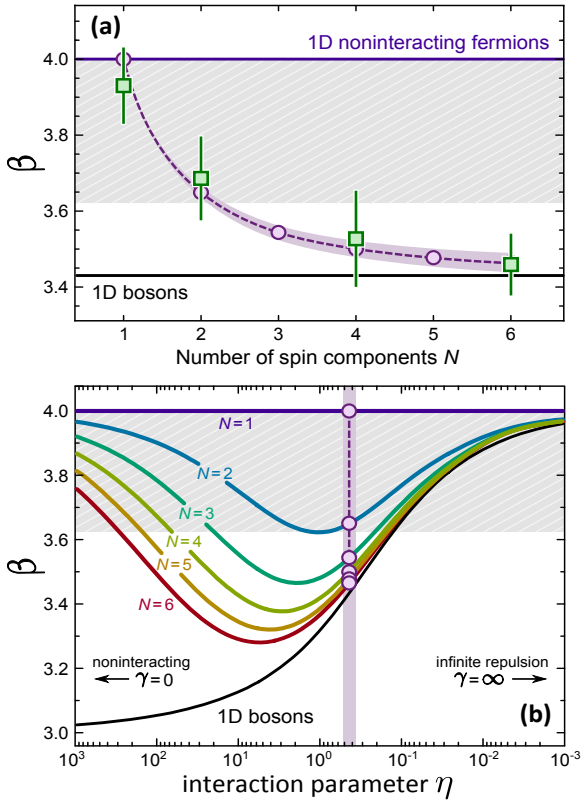

Figure 6.10: Breathing oscillations. The quantity that is plotted in the graph is $\beta = (\omega_B/\omega_x)^2$. **(a)** The squares show the experimental data, as a function of N, obtained as the weighted mean over sets of up to nine repeated measurements. The circles show the theoretical predictions for the average interaction parameter $\eta = 0.44$ for our experiment. The dashed line is a guide to the eye, while the height of the violet shaded area indicates the uncertainty on the theoretical values resulting from the experimental uncertainty $\Delta\eta = 0.08$ coming from the measured atom number and trapping frequencies. The upper horizontal line shows the theoretical value for the non-interacting Fermi gas while the lower line shows the result for 1D spinless bosons. **(b)** The lines show the theoretical dependence of β on the interaction parameter η. The circles show the predicted values for our average interaction parameter (also shown in **(a)**). In both panels the height of the grey region shows the range of β for $N = 2$ and any possible value of the repulsion strength.

the interaction strength in an $N = 2$ mixture. In fact, by increasing N, the constraints of the Pauli principle become less stringent and the number of binary-collisional partners increases, causing the system to acquire a more "bosonic" character. Our experimental value at $N = 6$ clearly falls out of the range of β expected for an $N = 2$ liquid (grey regions in Fig. 6.10), and already approaches the value expected for 1D spinless bosons. This bosonic limit for $N \to \infty$ is called "high spin bosonization" and is a re-

markable property of multi-component 1D fermions that has been pointed out theoretically only very recently by C.N. Yang [39].

6.3 Conclusions and perspectives

In this set of experiments we provided the first experimental characterization of multi-component Luttinger liquids with tunable $SU(N)$ symmetry. The possibility of tuning the number of spin components allows us to study different regimes of interplay between Fermi statistics and degree of distinguishability in this novel 1D tunable system. In a quantum simulation perspective, the controlled realization of 1D multi-component fermions represents a powerful test bench for large-spin models and opens to the investigation of fundamental effects, such as spin-charge separation, first predicted for a $N = 2$ fermionic system. Indeed, the work carried out so far concerns exclusively charge (density) collective modes, since the excitations studied are all spin-independent. In particular we observed a blue shift in the resonance of the charge dynamical structure factor in the case of two-component Fermi gas. Differently, given two spin species $|\uparrow\rangle$ and $|\downarrow\rangle$, a spin-selective Bragg excitation [158, 159] should in principle allow the comparison between charge and spin velocity through the measurement of the charge and spin dynamical structure factors, defined as:

$$S_{c,s}(\mathbf{q},\omega) = 2\left[S_{\uparrow\uparrow}(\mathbf{q},\omega) \pm S_{\uparrow\downarrow}(\mathbf{q},\omega)\right], \tag{6.-3}$$

where plus and minus signs refer respectively to charge and spin subscripts. Alternatively, a redshift of the spin dipole frequency is predicted to be observed [146] as a consequence of a spin-selective excitation. In Section 1.2.3 it is explained in detail how to generate the spin-dependent light shifts necessary to access collective spin excitations.

7 | Two-orbital physics with fermionic ^{173}Yb

As already mentioned in the Introduction, another important property of Ytterbium, common to all alkaline-earth and alkaline-earth-like atoms, is the existence of a metastable excited state which is connected to the ground state through an ultranarrow clock transition [28, 30, 160]. In this Chapter we report experiments performed exciting the clock transition $^1S_0 \rightarrow {}^3P_0$ in ^{173}Yb. The atoms are loaded in a dipole potential generated by light at 759 nm. The light shift experienced at this "magic wavelength" is the same both for the $^1S_0$ state and for the $^3P_0$, so that the clock transition frequency is indipendent from the dipole potential depth [79, 161]. The realization of mixtures of $^1S_0$ and $^3P_0$ atoms allows the investigation of novel experimental implementations of multi-orbital Hubbard models, where each atom is characterized by both spin and orbital (electronic) degree of freedom. Indeed the main focus of this Chapter is to study two-body collisions between atoms in two different orbitals in a three-dimensional optical lattice. We evidenced the effects of a strong spin-exchange interaction between atoms in the two different states, proving for the first time fast, coherent, orbital magnetization oscillations. Also, we present some very recent results [50] regarding the first observation of an *orbital* Feshbach resonance, first predicted in [36]. In this case, two-body collisions between atoms in two different orbitals are studied in a typical dipole trap, generated by laser beams at 759 nm. We evidenced the effects of strong interactions, tunable by means of a magnetic field, by studying the anistropic expansion of a two-orbital mixture of atoms in differents spin components.

This Chapter is organized as follows. Section 7.1 describes briefly the laser system built my coworker G. Cappellini [49, 81] to address the ultra-narrow optical transition towards the metastable state. Section 7.2 introduces the theoretical model developed to quantitatively describe the strongly-repulsive interaction between two atoms in a lattice site. Section 7.3 describes spectroscopic measurements performed on a two-spin mixture, loaded in a deep 3D optical lattice. We will illustrate how the an-

tisymmetric character of the two-particle wavefunction, imposed by the Fermi statistics, affects inter-orbital binary collisions. Section 7.4 concerns the direct observation of inter-orbital spin-exchange oscillations that allowed us to extract some important properties such as the scattering lengths characterizing binary collisions between $^1S_0$ and $^3P_0$ atoms. Finally, Section 7.5 presents briefly some very recent results concerning the first observation of a novel kind of Feshbach resonance called orbital Feshbach resonance, appearing between atoms occupying different electronic orbitals.

7.1 The $^1S_0 \rightarrow {}^3P_0$ ultra-narrow clock transition

In the last years, alkaline-earth-like atoms such as Yb [27, 28] or Sr [29–31] have become the main characters in the field of frequency metrology thanks to the realization of optical lattice clocks that could improve the current frequency standards. Indeed, these two-electron atoms exhibit an ultranarrow transition $^1S_0 \nrightarrow {}^3P_0$, which would be stricly forbidden by the selection rule $J = 0 \nrightarrow J' = 0$. In the case of fermionic Ytterbium, the hyperfine interaction between the ^3P states originating from the non-zero nuclear magnetic moment, indirectly enables a decay from the $^3P_0$ to the ground state. This transition has a calculated linewidth of about $\Gamma \simeq 2\pi \cdot 10$ mHz [79, 80] corresponding to a lifetime of 20 s. The exact excitation frequency for the ^{173}Yb isotope 518 294 576 847.6 $\pm$ 4.4 kHz, corresponding to $\lambda_C = 578.4$ nm, has been measured in Ref. [27].

In order to optically reach the $^3P_0$ state, we developed an ultra-stable laser source starting from the 1156 nm light emitted by a quantum dot laser in a 15-cm long external-cavity configuration with an intra-cavity electro-optical modulator (Qubig GmbH, DC-coupled, broadband, Brewster-cut facets) for high-bandwidth frequency stabilization. The laser radiation at 578 nm is then produced by second-harmonic generation in a bow-tie cavity, similarly to the laser systems for 399 and 556 nm wavelengths, described in Section 2.3.1. We obtain up to 50 mW of 578 nm light, a small part of which is coupled to a 10 cm long ULE (Ultra-Low Expansion) glass cavity to which the laser frequency is locked. The feedback is performed by both the piezo moving the grating of the external cavity and the EOM inside the external cavity. The former is used to correct in the low-frequency range up to 200 Hz, whereas the latter is used in the high-frequency domain obtaining an overall bandwidth of 500 kHz. The ULE cavity, surrounded by a thermally-stabilized copper shield, is located in a 10^{-7} mbar vacuum chamber to greatly reduce its mechanical and thermal sensitivity. The whole system is placed on an anti-vibration platform to further reduce seismic noise, and is enclosed in an isolation box to decouple the system from the lab environment. The long-term drift of the

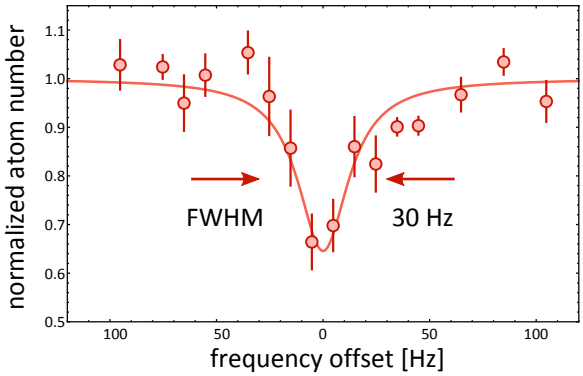

Figure 7.1: Narrow resonance showing the linewidth of our laser on the time scale of 5 minutes. The main limitation is the mid-term drift of the ULE cavity.

cavity has been characterized to be 3.5 Hz/s and is corrected using a digital feed-forward loop. However, erratic fluctuations of some Hz/s, that we ascribe to an imperfect thermal stabilization of the ULE cavity, limit the mid-term stability of our laser. More details about the laser system and the characterization of the ULE drift can be found in Ref. [81] and in the PhD thesis of my colleague Giacomo Cappellini [49]. In order to address coherently atoms in the metastable state, it is important to trap them in an optical potential that generates a light shift which is the same both for the $^1S_0$ state and for the $^3P_0$ state. In this way all the atoms experience the same clock transition frequency since the broadening due to the inhomogeneity of the harmonc confinement is avoided. There are several optical magic wavelengths [161], but the most convenient experimentally is $\lambda_L = 759.35$ nm [32], which is used in this experiment (see Fig. 1.2).

Beside being subjected to the same light shift in the ground and excited states, to observe narrow lines, it is crucial to "eliminate" the Doppler broadening induced by the atomic motion. Atoms are thus loaded in a deep 3D optical lattice so that the "Lamb-Dicke" regime is well reached. We define the Lamb-Dicke parameter as:

$$\eta = \frac{k_C a_{ho}}{\sqrt{2}} = \frac{\lambda_L}{\lambda_C} \frac{1}{s^{1/4}\sqrt{2}} \tag{7.0}$$

in which k_C is the clock laser wavenumber, a_{ho} is the harmonic oscillator length along the direction of excitation and s is the optical lattice trap depth in recoil units. The Lamb-Dicke regime is reached when $\eta < 1$, meaning that the atomic wave-packet is smaller than the wavelength of the interrogation beam. For our experimental parameters, $s \in (30, 40)$, the Lamb-Dicke parameter varies in the range $(0.37, 0.4)$.

In order to observe the transition $^1S_0 \rightarrow {}^3P_0$ we load a fully polarized Fermi gas in a 3D optical lattice at $s = 30$. During the lattice loading, the

1064 nm dipole trap is switched off adiabatically in 50 ms in order to avoid spurious differential light shifts between $^1S_0$ and $^3P_0$ states that would affect the resonance frequency. Then, after 10 ms, we shine a 100 ms 578 nm laser pulse and we switch off the lattice beams. After ballistic expansion, we detect the atoms remained in the ground state by absorption imaging on the $^1S_0 \rightarrow {}^1P_1$ transition. This detection method is reliable as the lifetime of the excited state is much longer than the typical time of flight. Since the saturation intensity is extremely low ($I_s = 0.26$ nW/cm^2), the transition is always saturated by the laser light and by tuning the intensity we can decide at will the resonance power-broadened width. The narrowest resonance we managed to observe, compatibly with the mid-term drift of the ULE cavity, has a linewidth of 30 Hz, as shown in Fig. 7.1.

7.2 Two cold atoms in a lattice site

Before describing in Sec. 7.3 the more complicated spectrum of a two-spin mixture in a 3D optical lattice, here we discuss the interaction energy shift for two strongly interacting trapped particles.

Following Ref. [60, 162] we developed a simple model describing two interacting particles confined in a lattice well of a 3D optical lattice. At large interaction strength (and we will see in the next Section, that this is indeed the case), the two-particle wavefunction cannot be expressed in terms of lowest-band Wannier functions since, in the limit of infinite repulsion, the phenomenon of "fermionization" intervenes, causing the probability of finding two particles at the same position to drop to zero. For a system of two particles in a harmonic potential it has been shown that, for a scattering length a_s significantly larger than the harmonic oscillator length a_{ho}, the interaction energy saturates at the energy of the first excited harmonic oscillator state [60]. We want to improve the model in [60] in order to take into account the anharmonicities caused by the real lattice potential. The Hamiltonian describing two atoms interacting in a lattice potential well is

$$\hat{H} = \frac{\hat{p}_1^2}{2m} + \frac{\hat{p}_2^2}{2m} + \hat{\mathcal{V}}_{lat}(\mathbf{r}_1) + \hat{\mathcal{V}}_{lat}(\mathbf{r}_2) + \hat{\mathcal{V}}_{int}(\mathbf{r}_1 - \mathbf{r}_2), \tag{7.0}$$

in which $\hat{\mathcal{V}}_{lat}(\mathbf{r}) = \mathcal{V}_0 \sum_{i=x,y,z} \sin^2(k_L r_i)$ is the 3D lattice potential experienced by each atom and $\hat{\mathcal{V}}_{int}(\mathbf{r}) = \frac{4\pi\hbar^2}{m} a_s \, \delta(\mathbf{r}) \frac{\partial}{\partial r} r \cdot$ is the interaction potential, already introduced in Sec. 1.4. In order to take into account the anharmonic corrections induced by the lattice potential, we expand $\hat{\mathcal{V}}_{lat}(\mathbf{r})$ up to the 10$^{\text{th}}$ order, isolating the harmonic terms from the non-harmonic ones:

$$\hat{\mathcal{V}}_{lat}(\mathbf{r}) = \mathcal{V}_0 \sum_{i=x,y,z} (k^2 r_i^2 - \frac{1}{3} k^4 r_i^4 + \frac{2}{45} k^6 r_i^6 + ...). \tag{7.0}$$

This order of expansion is sufficiently high to describe well the shape of each lattice site. In order to take into accounts also the effects of tunneling, which are important only at low lattice depth, the potential should be expanded to a higher order, at least to the 20$^{\text{th}}$, making the problem much more computationally expensive. Recalling that $\omega_{ho} = 2E_R/\hbar\sqrt{s}$ and $s = \mathcal{V}_0/E_R$ (Eq. 1.2.1) we can rewrite the Hamiltonian as:

$$\hat{H} = \frac{\hat{p}_1^2}{2m} + \frac{\hat{p}_2^2}{2m} + \frac{1}{2}m\omega_{ho}^2 r_1^2 + \frac{1}{2}m\omega_{ho}^2 r_2^2 + \hat{\mathcal{V}}_{int}(\mathbf{r}_1 - \mathbf{r}_2) + \hat{\mathcal{V}}_{anh}(\mathbf{r}_1, \mathbf{r}_2), \quad (7.0)$$

where $\hat{\mathcal{V}}_{anh}(\mathbf{r}_1, \mathbf{r}_2)$ contains only the anharmonic terms coming from the expansion of the lattice potential. By making the substitution[1] $\mathbf{R} = \frac{\mathbf{r}_1+\mathbf{r}_2}{\sqrt{2}}$ and $\mathbf{r} = \frac{\mathbf{r}_1-\mathbf{r}_2}{\sqrt{2}}$, we can write the Hamiltonian in terms of "center-of-mass" $\{\mathbf{R}, \mathbf{P}\}$ and "relative" $\{\mathbf{r}, \mathbf{p}\}$ coordinates:

$$\hat{H} = \underbrace{\frac{\hat{P}^2}{2m} + \frac{1}{2}m\omega_{ho}^2 R^2}_{\hat{H}_{CM}} + \underbrace{\frac{\hat{p}^2}{2m} + \frac{1}{2}m\omega_{ho}^2 r^2 + \hat{\mathcal{V}}_{int}(\mathbf{r})}_{\hat{H}_{\text{Busch}}} + \hat{\mathcal{V}}_{anh}(\mathbf{R}, \mathbf{r}). \quad (7.0)$$

where the first part refers to the center-of-mass motion, while the second part refers to the relative motion + interaction potential, a problem which has already been solved analytically by T. Busch et al. in Ref. [60] finding the following eigenfunctions:

$$\psi_{\text{B}}(\mathbf{r}) = A \exp\left(-\frac{r^2}{2a_\perp^2}\right) \Gamma\left(-\frac{E}{2\hbar\omega_{ho}} + \frac{3}{4}\right) \mathcal{U}\left(-\frac{E}{2\hbar\omega_{ho}} + \frac{3}{4}, \frac{3}{2}, \frac{r^2}{a_\perp^2}\right), \quad (7.0)$$

where Γ is the Euler function, $\mathcal{U}(n, m, x)$ are the confluent hypergeometric functions, A is a normalization factor, $a_\perp = \sqrt{\hbar/m\omega_\perp}$ is the harmonic oscillator length and E is the total energy of the relative coordinate, given by the solution of the equation:

$$\sqrt{2}\frac{\Gamma\left(-\frac{E}{2\hbar\omega_{ho}} + \frac{3}{4}\right)}{\Gamma\left(-\frac{E}{2\hbar\omega_{ho}} + \frac{1}{4}\right)} = \frac{a_\perp}{a_s}. \quad (7.0)$$

However, the anharmonic terms $\hat{\mathcal{V}}_{anh}(\mathbf{R}, \mathbf{r})$ couple the relative and center-of-mass motion, making the problem solvable only with numerical methods. We thus diagonalize numerically the full Hamiltonian in Eq. (7.2) written on the basis of the eigenfunctions of $\hat{H}_{CM} + \hat{H}_{\text{Busch}}$, namely

$$\Phi_{\alpha,\beta}(\mathbf{r}, \mathbf{R}) = \Psi_\alpha(\mathbf{R})\, \psi_\beta(\mathbf{r}), \quad (7.0)$$

[1] This unusual change of variables is used to write the center-of-mass and the relative motion contribution with the atomic mass instead of the total and reduced mass, respectively.

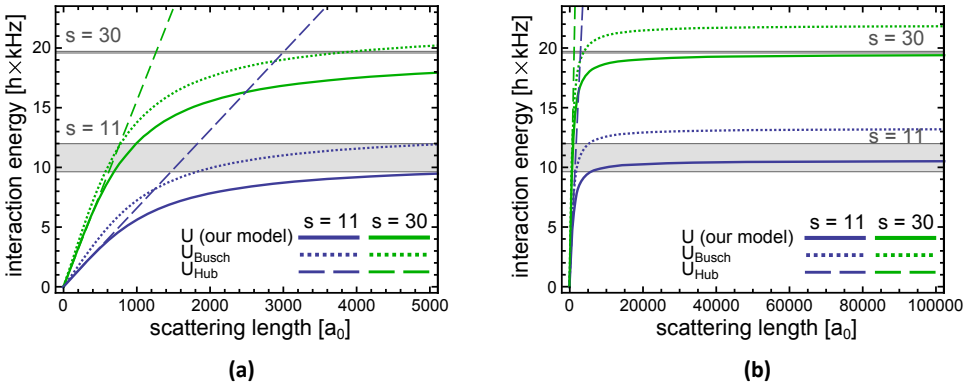

Figure 7.2: (a) Interaction energies for two particles in a lattice site, calculated for two lattice depths $s = 11$ and $s = 30$ according to three different models (see text). The interaction energy $\mathcal{U}$ calculated using our model is well approximated by the usual Hubbard relation $\mathcal{U}_{\mathrm{Hub}}$ at small scattering length. **(b)** The same results are plotted up to larger values of a_s. For large a_s the interaction energy $\mathcal{U}$ saturates at the energy difference between the ground and the first-excited lattice band, here represented by the grey regions (the width of these regions reflects the finite width of the energy bands caused by tunnelling).

where $\alpha = \{N, L, M\}$ and $\beta = \{n, \ell, m\}$ represent sets of quantum numbers of the 3D isotropic harmonic oscillator in spherical coordinates for the center-of-mass and the relative motion respectively. $\Psi_\alpha(\mathbf{R})$ are the center-of-mass 3D harmonic oscillator eigenfunctions, while $\psi_\beta(\mathbf{r})$ are the eigenfunctions for the relative motion which: for $\ell \neq 0$, correspond to the non-interacting harmonic oscillator eigenfunctions $\phi_{n,\ell,m}(\mathbf{r})$, that are not affected by the δ-like interaction potential, having a node in the origin, whereas for $\ell = 0$, correspond to the Busch eigenfunctions defined in Eq. (7.2), which are linear combinations of harmonic oscillators wavefunctions with $\ell = 0$.

By evaluating the matrix elements of the anharmonic terms on this complete basis and by numerical diagonalization of the total Hamiltonian, we derive the dependence of the interaction energy in the motional ground state $\mathcal{U}(s, a_s) = E(s, a_s) - E(s, 0)$ as a function of the scattering length a_s and of the lattice depth s. We found that taking $N_{max} = n_{max} = 4$ (corresponding to 196 states forming the basis) is sufficient to ensure convergence in the calculation of the ground-state energy. In Fig. 7.2 we plot the results for the interaction energy (defined as the total energy of the relative motion minus the total energy in the non interacting case) as a function of the scattering length a_s for two values of the lattice depth $s = 11$ and $s = 30$. The curves are based on three different models: 1) our model, containing anharmonic terms and the coupling between relative and center-of-mass motion ($\mathcal{U}$, solid lines); 2) the model containing

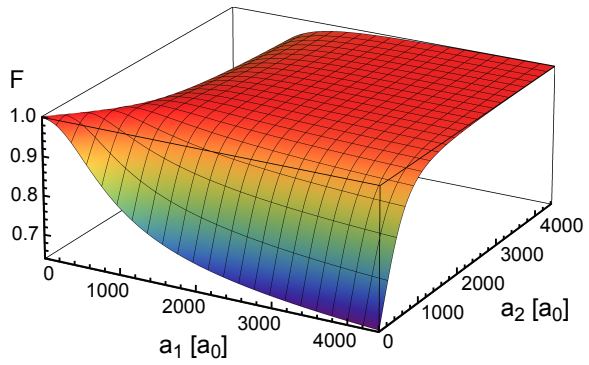

Figure 7.3: Franck-Condon factor $\langle\psi(a_{s1})|\psi(a_{s2})\rangle$ describing the overlap of the ground-state wavefunctions for two different scattering lengths a_{s1} and a_{s2} at $s = 30$.

only the harmonic part of the potential [60] ($\mathcal{U}_{\rm Busch}$, dotted lines); 3) the usual expression for the interaction energy in the Hubbard model [8] (see Sec. 1.2.2), which takes into account the full lattice potential and depends linearly on a_s ($\mathcal{U}_{\rm Hub}$, dashed lines). In addition, the first band gaps for $s = 11$ and for $s = 30$ are shown. The interaction energy derived from our model saturates at the first excited band of the lattice for large values of the scattering length, as expected, and, for low a_s, it is well approximated by the usual Hubbard expression $\mathcal{U}_{\rm Hub}$. Instead, the $\mathcal{U}_{\rm Busch}$ curves saturate at a higher energy, coincident with $\hbar\omega_{ho} = 2\sqrt{s}E_R$.

By numerical diagonalization we obtain also the eigenfunctions of the expanded Hamiltonian (7.2). It is thus possible to calculate the overlap between two eigenfunctions corresponding to different scattering lengths. This is the so called Franck-Condon factor $\mathcal{F}$:

$$\mathcal{F} = \int\int d\mathbf{r}_1 d\mathbf{r}_2 \psi^*_{a_{s1}}(\mathbf{r}_1, \mathbf{r}_2)\psi_{a_{s2}}(\mathbf{r}_1, \mathbf{r}_2) \tag{7.0}$$

and it is depicted in Fig. 7.3. As expected, $\mathcal{F} = 1$ along the diagonal (where $a_{s1} = a_{s2}$), since the two states coincide, while goes to ~ 0.6 for the maximal difference in scattering lengths.

7.3 Clock spectroscopy of a two-component Fermi gas

This section describes the spectroscopy performed over a two-component Fermi gas in a deep three-dimensional optical lattice. We will focus on the role played by the Fermi statistics and by the interaction shifts in determining the shape of the spectrum [163]. First of all we give a simple theoretical recipe that takes into account collisional channels associated to different electronic states, the interaction with the spectroscopy laser and the effect of magnetic fields on the atomic system. Secondly we focus on

the experimental spectrum at finite magnetic field, identifying the different peaks with the help of the introduced model.

7.3.1 Direct and exchange interactions

We consider two atoms in different nuclear spin states $|\uparrow\rangle$ and $|\downarrow\rangle$, where the arrows are placeholders for two arbitrary nuclear spin states, occupying the same lattice site and interacting via a delta-like repulsive potential [60]. Let us assume that the clock laser light is π-polarized so that the optical excitation does not flip the nuclear spin, and that the two particles occupy the same motional state. Due to the Fermi statistics, the complete Hilbert space consists in the following anti-symmetrized states:

$$\left\{ |gg\rangle \otimes |s\rangle,\ \frac{|eg\rangle + |ge\rangle}{\sqrt{2}} \otimes |s\rangle,\ \frac{|eg\rangle - |ge\rangle}{\sqrt{2}} \otimes |t\rangle,\ |ee\rangle \otimes |s\rangle \right\}, \tag{7.0}$$

where we defined $|g\rangle \equiv |^1S_0\rangle$, $|e\rangle \equiv |^3P_0\rangle$ and $|t\rangle$ and $|s\rangle$ stand for the symmetric (triplet) and antisymmetric (singlet) two-particle nuclear spin states:

$$|s\rangle = \frac{|\uparrow\downarrow\rangle - |\downarrow\uparrow\rangle}{\sqrt{2}},$$
$$|t\rangle = \frac{|\uparrow\downarrow\rangle + |\downarrow\uparrow\rangle}{\sqrt{2}}.$$

The collisional channel through which the two atoms interact, is determined by the orbital part of the wavefunction. In particular we focus on the two-particle collisions in which the atoms occupy different electronic states namely:

$$|eg^+\rangle \equiv |s\rangle \frac{|eg\rangle + |ge\rangle}{\sqrt{2}} = \frac{1}{\sqrt{2}}\left[|g\uparrow, e\downarrow\rangle - |g\downarrow, e\uparrow\rangle\right],$$
$$|eg^-\rangle \equiv |t\rangle \frac{|eg\rangle - |ge\rangle}{\sqrt{2}} = \frac{1}{\sqrt{2}}\left[|g\uparrow, e\downarrow\rangle + |g\downarrow, e\uparrow\rangle\right].$$

in which the antisymmetrization of the states $|g\uparrow, e\downarrow\rangle$ and $|g\downarrow, e\uparrow\rangle$ is implied. We can use these last expressions to derive the form of the two-body interaction potential in the center-of-mass reference frame, see Eq. (1.4.1):

$$\hat{\mathcal{V}}(\mathbf{r}) = \left(g_{gg}\hat{\mathcal{P}}_{gg} + g_{eg}^{+}\hat{\mathcal{P}}_{eg^+} + g_{eg}^{-}\hat{\mathcal{P}}_{eg^-} + g_{ee}\hat{\mathcal{P}}_{ee}\right)\delta(\mathbf{r})\frac{\partial}{\partial r}[r\cdot] \tag{7.-2}$$

with $(g_{gg}, g_{eg}^{\pm}, g_{ee}) = 4\pi\hbar^2(a_{gg}, a_{eg}^{\pm}, a_{ee})/m$ and $\hat{\mathcal{P}}_{nm}$ are the projector operators onto the state $|n\,m\rangle$. In particular, by decomposing the projection

operators $\hat{\mathcal{P}}_{eg^{\pm}}$ on the states defined in Eq. (7.3.1), we obtain:

$$\hat{\mathcal{P}}_{eg^{\pm}} = \frac{1}{2}\Big[\Big(|g\downarrow, e\uparrow\rangle\langle e\uparrow, g\downarrow| + |g\uparrow, e\downarrow\rangle\langle e\downarrow, g\uparrow|\Big) \pm \Big(|g\downarrow, e\uparrow\rangle\langle e\downarrow, g\uparrow| + |g\uparrow, e\downarrow\rangle\langle e\uparrow, g\downarrow|\Big)\Big]$$

where the first term represents the *direct* interaction operator $\hat{\mathcal{V}}_{dir}$, which takes into account those processes that conserve the individual nuclear spin, whereas the second term represents the *exchange* interaction operator $\hat{\mathcal{V}}_{ex}$, which describes collisions involving a nuclear spin-flip. We can thus rewrite the interaction Hamiltonian corresponding to atoms in different electronic states as:

$$\hat{\mathcal{V}}_{eg}(\mathbf{r}) = \left[\left(\frac{g_{eg^+} + g_{eg^-}}{2}\right)\hat{\mathcal{V}}_{dir} + \left(\frac{g_{eg^+} - g_{eg^-}}{2}\right)\hat{\mathcal{V}}_{ex}\right]\delta(\mathbf{r})\frac{\partial}{\partial r}[r\cdot]. \quad (7.\text{-}3)$$

The exchange energy term is effectively an on-site magnetic interaction between nuclear spins in different electronic orbitals: the difference in the symmetric and antisymmetric inter-orbital interaction energies $\mathcal{U}_{eg^+}$ and $\mathcal{U}_{eg^-}$, owing to fermionic statistics, lifts the degeneracy between singlet and triplet spin states. This energy lifting is directly proportional to the difference in the scattering length $a_{eg^+} - a_{eg^-}$ and is responsible for the inter-orbital spin-exchange oscillations that we will describe in Section 7.4.

7.3.2 Laser excitation of two-particle states

Following Ref. [164, 165], the interaction Hamiltonian of a pair of atoms with coherent laser light can be written as the sum of two operators acting on each atom individually:

$$\hat{H}_L = \hat{H}_{L,1} + \hat{H}_{L,2}, \quad (7.\text{-}3)$$

where $\hat{H}_{L,1(2)}$ describes the interaction between atom $1(2)$ and the laser field. We assume the atoms to occupy the same position and we consider two spin states $(\uparrow,\downarrow)$ that could be whatever spin projection states out of an arbitrarily large spin manifold. Since the phase of the electric field is the same for the two atoms we can write:

$$\hat{H}_{L,i} = |e_i\rangle\langle g_i| \otimes \frac{\hbar}{2}(\Omega_\uparrow P_{i\uparrow} + \Omega_\downarrow P_{i\downarrow}) + h.c., \quad (7.\text{-}3)$$

where $\hat{P}_{i\sigma} = |\sigma\rangle_i\langle\sigma|_i$ is the projection operator on the σ spin projection state of the i atom and Ω_σ is the Rabi frequency taking into account the appropriate Clebsch-Gordan coefficient. We note that, because of the dependence on the Clebsch-Gordan coefficients[2], the interaction Hamiltonian does operate on the spin sector via the projection operators in Eq.

[2] In the case of the transition ${}^1S_0 \rightarrow {}^3P_0$, the ${}^3P_0$ inherits the ${}^3P_1$ Clebsch-Gordan coefficients due to the mixing.

(7.3.2). As a matter of fact, by introducing the identity operator $\hat{\mathbb{1}}$ and the Pauli matrix $\hat{\sigma}_z$ acting on the spin component of the wavefunction, Eq. (7.3.2) can be recast as:

$$\hat{H}_{L,i} = |e_i\rangle\langle g_i| \otimes \frac{\hbar}{2}(\Omega^+ \mathbb{1}_i + \Omega^- \hat{\sigma}_{z,i}) + h.c.\,, \tag{7.-3}$$

with $\Omega^{\pm} = (\Omega_\uparrow \pm \Omega_\downarrow)/2$. In the case $\Omega_\uparrow = \Omega_\downarrow$ the Hamiltonian does not operate on the spin sector, while in all the other cases, it does. This formulation is convenient to highlight the optical transitions between the states defined in Eq. (7.3.1). In particular, starting from the lowest energy state $|gg\rangle|s\rangle$ we have:

$$H_L|gg\rangle|s\rangle = \frac{\hbar}{2}\left[\sqrt{2}\Omega^+|eg^+\rangle + \sqrt{2}\Omega^-|eg^-\rangle\right] \tag{7.-3}$$

In the special case $\Omega_\uparrow = -\Omega_\downarrow$, which only occurs in the spin-symmetric mixtures $m = \pm 5/2, \pm 3/2, \pm 1/2$ (see Appendix A), only the transition to the $|eg^-\rangle$ state is allowed and, counterintuitively, the symmetry of the nuclear spin wavefunction is changed from a singlet to a triplet by an optical excitation. In all the remaining spin mixtures there is a finite probability of exciting both the $|eg^+\rangle$ and the $|eg^-\rangle$ states. Moreover, starting from the states $|eg^{\pm}\rangle$, there is a finite probability of populating the state $|ee\rangle|s\rangle$, proportional to the following matrix elements:

$$\langle s|\langle ee|H_L|eg^+\rangle = \frac{\hbar}{2}\sqrt{2}\Omega^+,$$
$$\langle s|\langle ee|H_L|eg^-\rangle = \frac{\hbar}{2}\sqrt{2}\Omega^-.$$

It shall be noted that the Hilbert space basis (7.3.1) is made of eigenstates of the two-body interaction Hamiltonian, as they are all defined by the collisional channels. We will see in the next section how a magnetic field mixes these states defining a new eigenstate basis.

7.3.3 Magnetic field mixing

In a similar fashion, we can model the interaction with a magnetic field with the Hamiltonian:

$$\hat{H}_Z = \hat{H}_{Z,1} + \hat{H}_{Z,2} \tag{7.-4}$$

in which:

$$\hat{H}_{Z,i} = g_\alpha \mu_B \frac{\hat{F}_{zi}}{\hbar} B \tag{7.-4}$$

where g_α is the Landè g-factor of the state $\alpha = (g, e)$, μ_B is the Bohr magneton, $\hat{F}_{z,i}$ denotes the projection along the quantization axis of the total angular momentum of atom $i = 1, 2$ and $\mathbf{B} = B\,\hat{z}$. It shall be noted that

the hyperfine mixing with higher $^{2S+1}P_1$ states causes the $^3P_0$ state to have a different Landè g-factor with respect to the $^1S_0$ state, giving rise to a differential Zeeman splitting $\delta g \mu_B/\hbar = 113$ Hz/G. As for the case of laser fields, the Hamiltonian $\hat{H}_{Z,i}$ acts only on the atom i with orbital state α and magnetic momentum projection m as $\hat{H}_{Z,i}|\alpha, m\rangle_i = g_\alpha \mu_B m B\,|\alpha, m\rangle_i$. By using the former simple relation, we can calculate the matrix elements of $\hat{H}_Z$ on the interaction eigenstates introduced in Eq. (7.3.1):

$$\begin{aligned}
\langle gg|\hat{H}_Z|gg\rangle &= g_g(m+m')\frac{\mu_B}{\hbar}B,\\
\langle ee|\hat{H}_Z|ee\rangle &= g_e(m+m')\frac{\mu_B}{\hbar}B,\\
\langle eg^{\pm}|\hat{H}_Z|eg^{\mp}\rangle &= \frac{1}{2}(m-m')\delta g\,\frac{\mu_B}{\hbar}B\cdot\mathcal{F},\\
\langle eg^{\pm}|\hat{H}_Z|eg^{\pm}\rangle &= \frac{1}{2}(m+m')(g_e+g_g)\,\frac{\mu_B}{\hbar}B.
\end{aligned}$$

In these equations we have also considered the Franck-Condon factor $\mathcal{F}$, describing the overlap integral between the spatial wave functions[3] $\psi_{eg^\pm}$ of the two atoms interacting in the two different channels (see Sec. 7.4). Interestingly, the magnetic field mixes the two interaction eigenstates $|eg^\pm\rangle$. Therefore, considering only the sub-space $\{|eg^-\rangle, |eg^+\rangle\}$ and combining the Zeeman Hamiltonian $\hat{H}_Z$ and the onsite interaction Hamiltonian:

$$\hat{H}_0 = \begin{pmatrix} \mathcal{U}_{eg}^+ & 0 \\ 0 & \mathcal{U}_{eg}^- \end{pmatrix}, \tag{7.-7}$$

we can write the global Hamiltonian of the two-particle system $\hat{H}_{eg} = \hat{H}_0 + \hat{H}_Z$ as:

$$\hat{H}_{eg} = \begin{pmatrix} \mathcal{U}_{eg}^+ + \overline{g}\,(m+m')\frac{\mu_B}{\hbar}B & \frac{1}{2}(m-m')\delta g\,\frac{\mu_B}{\hbar}B\cdot\mathcal{F} \\ \frac{1}{2}(m-m')\delta g\,\frac{\mu_B}{\hbar}B\cdot\mathcal{F} & \mathcal{U}_{eg}^- + \overline{g}\,(m+m')\frac{\mu_B}{\hbar}B \end{pmatrix}, \tag{7.-7}$$

in which we defined $\overline{g} = (g_g + g_e)/2$ and where the interaction energy $\mathcal{U}_{gg}$ is taken as the zero-point energy, which is more closely related to the spectroscopic measurements. Therefore, the presence of the external magnetic field generates two energy branches:

$$\mathcal{U}_{eg}^{H,L}(B) = (m+m')\overline{g}\,\mu_B B + \mathcal{V} \pm \sqrt{\mathcal{V}_{ex}^2 + \left(\frac{1}{2}(m-m')\delta g\,\mu_B B\cdot\mathcal{F}\right)^2} \tag{7.-7}$$

[3] That is, we are considering the states $|eg^\pm\rangle = \frac{1}{\sqrt{2}}\left[|g\uparrow, e\downarrow\rangle \mp |g\downarrow, e\uparrow\rangle\right] \otimes |\psi_{eg^\pm}\rangle$. The two wavefunctions $\psi_{eg^\pm}$ may differ in the presence of different scattering lengths a_{eg^+}, a_{eg^-}, because of the mechanisms discussed in Sec. 7.2.

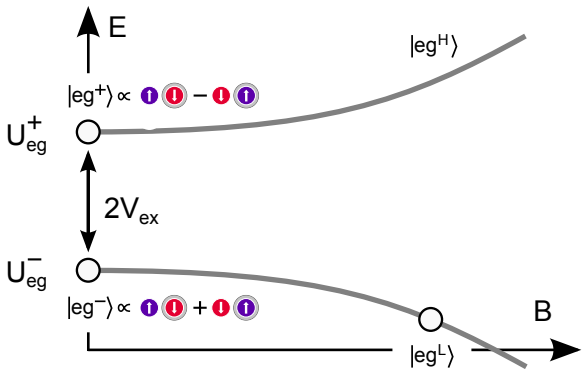

Figure 7.4: Eigenenergies of $\hat{H}_{eg}$ as a function of the magnetic field B in the case of a symmetric mixture $m = -m' = 5/2$.

where H, L correspond to the high and low-energy branches (see Fig. 7.4). As shown by spectroscopic studies [81, 163], the exchange energy $\mathcal{V}_{ex}$ is measured to be positive and therefore the high-(low-) energy branches are adiabatically connected to the $a^+_{eg}(a^-_{eg})$ collisional channels (see also Eq. (7.3.1)). In general, the two eigenstates as a function of magnetic field are:

$$|eg^L\rangle = \gamma(B)|eg^-\rangle + \delta(B)|eg^+\rangle$$
$$|eg^H\rangle = -\delta(B)|eg^-\rangle + \gamma(B)|eg^+\rangle$$

where the coefficients $\gamma(B)$ and $\delta(B)$ depend on the magnetic field and satisfy $\gamma^2(B) + \delta^2(B) = 1$ and $\gamma(0) = 1$, $\delta(0) = 0$. The qualitative dependence of the energy on the magnetic field is shown in Fig. 7.4 in the particular case of the symmetric mixture $(-5/2, +5/2)$. We are now ready to investigate the spectrum of such a system and identify the different spectroscopic peaks.

7.3.4 Spectroscopic measurements

Spectroscopy is perfomed by loading a balanced mixture of $(-5/2, +5/2)$ atoms at an initial temperature $T \simeq 0.15\, T_F$ into a 3D optical lattice at $s = 30$. In our experimental conditions [81], the site occupancy in the center of the trap is $n \simeq 1$ for each spin state. A typical spectrum for long excitation time ($T_{exc} = 100$ ms) is reported in Fig. 7.5. The external peaks correspond to the single particle excitations and are indeed separated by the Zeeman energy. Since the differential magnetic factor is positive $\delta g = 113.4$ Hz/G, we can assign the lowest energy peak to $m = -5/2$. The spectrum features other three additional peaks which refer to doubly occupied lattice sites. In Ref. [163] the identification of each peak has been determined by studying their dependence on the magnetic field. The one we are interested in is the central peak, which can be identified as the transition from $|gg\rangle \rightarrow$

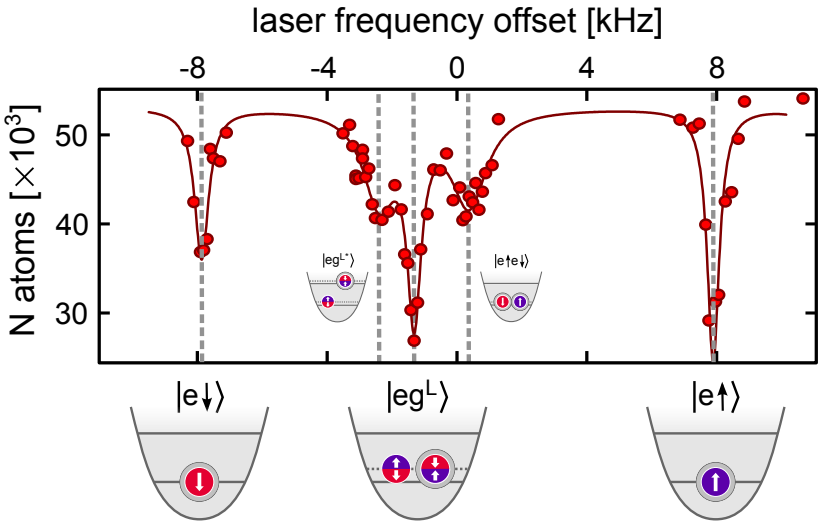

Figure 7.5: Spectroscopic measurement for a two-spin mixture. Atoms in $m = \pm 5/2$ are trapped in a $s = 30$ 3D lattice at $B = 28$ G. The vertical axis shows the number of residual $|g\rangle$ atoms after the excitation, while the horizontal axis shows the offset with respect to the clock transition frequency. The labels below the plot identify the different features of the spectrum. The dependence of the peak centers on the magnetic field B allows us to attribute them to the excitation of one atom in either singly-occupied sites ($|e\downarrow\rangle$ and $|e\uparrow\rangle$) or in doubly-occupied sites ($|eg^L\rangle, |ee\rangle$, and $|eg^{L*}\rangle$) [163]. The peak $|eg^{L*}\rangle$ corresponds to having one of the two particles in the first excited lattice band.

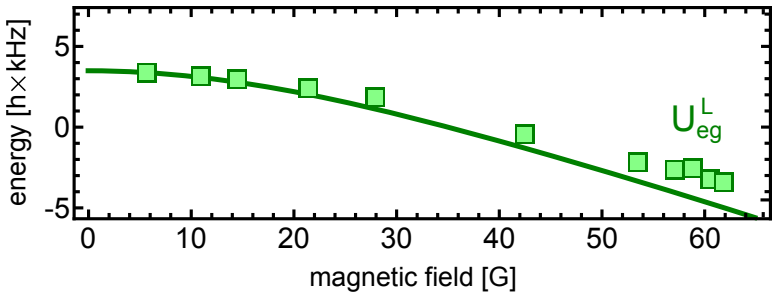

Figure 7.6: Magnetic field dependence of the energy of the $|eg^L\rangle$ state deduced from spectroscopic measurements. The solid line is a fit to the data based upon Hamiltonian 7.3.3

$|eg^L\rangle$. Its dependence on the magnetic field is illustrated in Fig. 7.6 from which we can infer that the sign of $\mathcal{V}_{ex}$ is positive. Indeed, this state is adiabatically connected with $|eg^-\rangle$ at $B = 0$ (see Sec. 7.3.2) and its energy decreases by increasing the magnetic field: from this behavior, we can infer that the $|eg^-\rangle$ state has a lower energy than the $|eg^+\rangle$ state and therefore the sign of $\mathcal{V}_{ex} = (\mathcal{U}^+_{eg} - \mathcal{U}^-_{eg})/2$ is positive. In the next Section

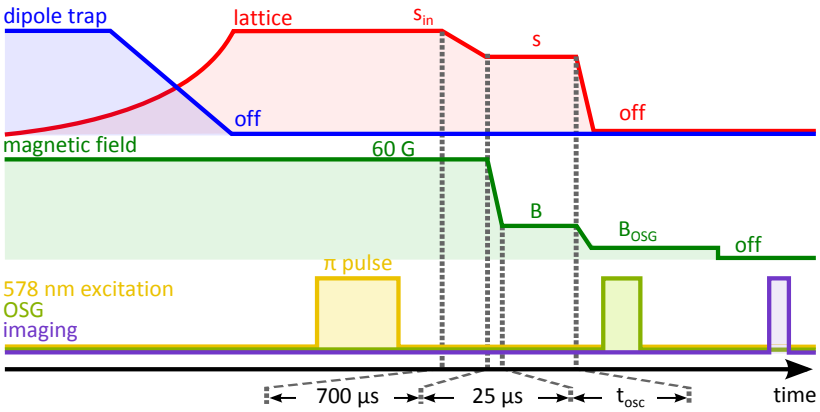

Figure 7.7: Experimental sequence used to induce inter-orbital spin-exchange oscillation dynamics.

we will see that these data can be combined with the measurement of the spin-exchange oscillation frequencies in order to extract the values of the scattering length a_{eg^+}, a_{eg^-}.

7.4 Inter-orbital spin-exchange oscillations

In this Section we report the first observation of spin-exchange oscillations between atoms in different orbitals, which is a direct demonstration of the coherent nature of the interaction between atoms in different electronic energy levels. Indeed, the spin-exchange [166–170] dynamics arises because of the different interaction energies $\mathcal{U}_{eg}^{+}$, $\mathcal{U}_{eg}^{-}$ in the two possible collisional channels $|eg^+\rangle$, $|eg^-\rangle$. Preparing the two atoms in the initial state $|\psi_0\rangle = 1/\sqrt{2}\,(|eg^+\rangle + |eg^-\rangle)$ results in a spin-exchange dynamics in which the spins of the $|g\rangle$ and $|e\rangle$ atoms are periodically flipped at a frequency $2\mathcal{V}_{ex}/h$, with the probability of finding a ground-state atom in the $|g\uparrow\rangle$ state being given by:

$$P(|g\uparrow\rangle)(t) = \frac{1}{2}\left[1 + \cos\left(\frac{2\mathcal{V}_{\mathrm{ex}}}{\hbar}t\right)\right]. \tag{7.-8}$$

In order to prepare a superposition state of both $|eg^+\rangle$ and $|eg^-\rangle$ we proceed as follows (see Fig. 7.7): we load a balanced mixture of atoms in the $m = \pm 5/2$ spin components ($N_{at} \simeq 2\cdot 10^4$/spin, $T/T_F \simeq 0.15$) in a 3D optical lattice at $s = 30$. While loading the lattice, the dipole trap is adiabatically turned off in 50 ms. For these experimental parameters the number of atoms in the excited bands of the lattice are minimized and the average filling is $0.5 \leq \overline{n} \leq 1$ atoms per lattice site and per spin component. We then apply a resonant 578 nm π-pulse exciting the $|gg\rangle \rightarrow |eg^L\rangle$

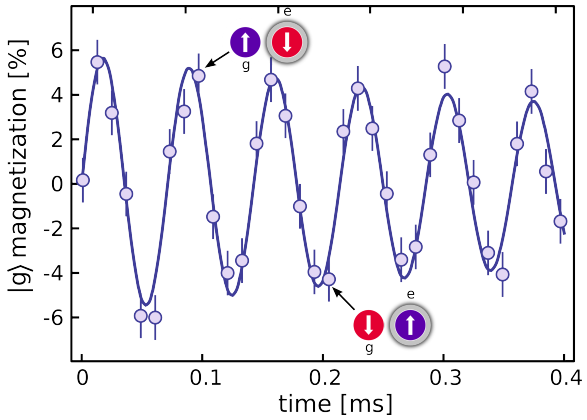

Figure 7.8: Time-resolved detection of two-orbital spin-exchange oscillations at a lattice depth $s = 30.8$ after quenching the magnetic field from 60 G to a bias field of 3.5 G. The points show the difference in fractional population between $|g\uparrow\rangle$ and $|g\downarrow\rangle$ atoms. The points are averages over 5 repeated measurements and the line is the result of a fit using a damped sinusoidal function (a global error bar based on the fit residuals has been assigned to the points).

transition at a magnetic field of 60 G, in order to have a sufficient superposition of spin-singlet and spin-triplet states into $|eg^L\rangle$ ($|\gamma|^2 \simeq 0.75$, $|\delta|^2 \simeq 0.25$). The lattice depth is then quickly lowered in 700 μs to the desired value s and right afterwards the magnetic field is quenched to a low bias field of 3.5 G in $t_{\mathrm{ramp}} = 25$ μs. This time interval is sufficiently fast to induce a population in the $|eg^+\rangle$ state via Landau-Zener tunneling. The formation of a superposition of $|eg^-\rangle$ and $|eg^+\rangle$ states allows us to start the spin-exchange dynamics, which is monitored via OSG detection, by counting the relative number of atoms in the different spin components $\pm 5/2$ of the $^1S_0$ ground state. Figure 7.8 shows clear oscillations of the ground-state magnetization $[N(g\uparrow) - N(g\downarrow)] / [N(g\uparrow) + N(g\downarrow)]$, which are driven by the spin-exchange process. The experimental points have been offset by a constant value ($\simeq 5\%$) to take into account a slight unbalance of the spin mixture resulting from an imperfect preparation of the initial state. These oscillations are a direct evidence of the coherent nature of this inter-orbital spin-exchange interaction. The measurement of their frequency provides a straightforward, model-independent determination of the interaction strength, which is $2V_{\mathrm{ex}} = h \times (13.87 \pm 0.17)$ kHz for the data in Fig. 7.8. The finite bias magnetic field $B \simeq 3.5$ G used for the measurement yields a slightly faster oscillation frequency than $2V_{\mathrm{ex}}/h$ (by ~ 100 Hz). In order to show the zero-field oscillation frequency the datapoints in Fig. 7.8 have been corrected by using the finite-B model described in section 7.3.3. The measured value for the spin-exchange fre-

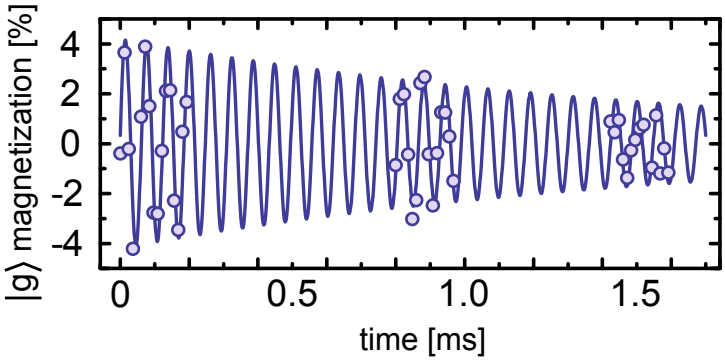

Figure 7.9: Spin exchange oscillations taken at $s = 35$ with longer hold times to evaluate the damping (see text for details).

quency highlights the strongly interacting character of the two-body system, being much higher than the typical energy scales such as the Fermi energy E_F and the thermal energy $k_B T$.

We note that the amplitude of the oscillation in Fig. 7.8 is relatively small. This can be ascribed to three different causes:

- at 60 G the fraction of $|eg^+\rangle$ into $|eg^L\rangle$ is only of $|\gamma(B)|^2 = 25\%$ leading to the more general time-dependent probability amplitude:

$$P(|g\uparrow\rangle)(t) = \frac{1}{2}\left[1 + 2\gamma\sqrt{1-|\gamma|^2}\cos\left(\frac{2V_{\mathrm{ex}}}{\hbar}t\right)\right]; \qquad (7.\text{-}8)$$

- the magnetic field is quenched to low values in 25 μs, which makes the projection onto the new eigenstates only partially diabatic;
- atoms in singly-occupied lattice sites do not participate to the dynamics but still contribute to the background signal.

We also have checked that these spin oscillations disappear if no laser excitation pulse is performed: collisions between $|g\rangle$ atoms can only take place in the spin-singlet channel, and the $SU(N)$ interaction symmetry prevents spin-relaxation mechanisms. It shall be noted that there is a residual damping, Fig. 7.9, on the spin-exchange oscillations on the order of $\tau \sim 2$ ms. We ascribed this finite lifetime of the oscillations to an imperfect quenching of the magnetic field that is slighlty different from run to run. This causes the dynamics to begin at each experimental cycle with slightly different initial conditions causing a dephasing of the overall oscillation data [81].

7.4.1 Lattice depth dependence

We measured the dependence of the spin-exchange oscillation frequency as a function of the lattice depth s. The optical excitation is perfomed at a

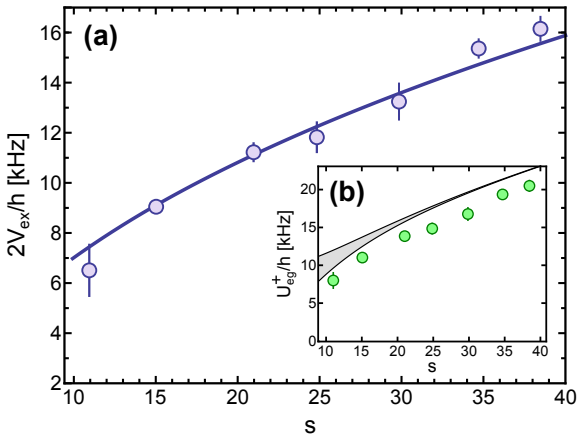

Figure 7.10: a) The points show the measured spin-exchange frequency as a function of the lattice depth s. The data have been corrected for the small bias magnetic field $B = 3.5$ G in order to show the zero-field spin-exchange frequency. Each point is the average of at least 3 different measurements and the error bar shows the statistical error. The line is a fit based on the model described in the main text. b) The points show the interaction energy of the $|eg^+\rangle$ state, calculated as the sum of the experimentally measured $2\mathcal{V}_{\rm ex}$ and $\mathcal{U}_{eg}^-$ calculated by using $a_{eg}^- = 219.5\,a_0$ [163]. The shaded area shows the energy difference between ground and first excited lattice band.

lattice depth $s_{in} \geq 30$ and subsequently the lattice is ramped to the desired s in $\sim 700\,\mu$s. The magnetic field is then quenched in $25\,\mu$s to initiate the spin dynamics (see Fig. 7.7). The measured values of $2\mathcal{V}_{\rm ex}$ are ≈ 5 times larger than the Hubbard interaction energy of two ground-state atoms trapped in the lattice sites, and approach from below the energy separation between the ground and first excited band of the three-dimensional lattice, as expected from the model we developed in Sec. 7.2 for strong interactions. We fit the experimental data of Fig. 7.10a with the expected energy difference $\left[\mathcal{U}(a_{eg}^+, s) - \mathcal{U}(a_{eg}^-, s)\right]/h$ (solid line) assuming the value $a_{eg}^- = 219.5\,a_0$ for the spin-triplet scattering length measured in Ref. [163]. The fit results in a spin-singlet scattering length $a_{eg}^+ = (3300 \pm 300)\,a_0$. This scattering length is remarkably large and, as shown in the inset of Fig. 7.10, causes the energy of the $|eg^+\rangle$ state to almost saturate to the energy gap between the first two lattice bands (grey curve of Fig. 7.10b).

7.4.2 Magnetic field dependence

At a finite magnetic field, the spin-exchange oscillation shows a faster frequency, as the Zeeman energy increasingly contributes to the energy difference between $|eg^L\rangle$ and $|eg^H\rangle$ (see Fig. 7.4). From the model of

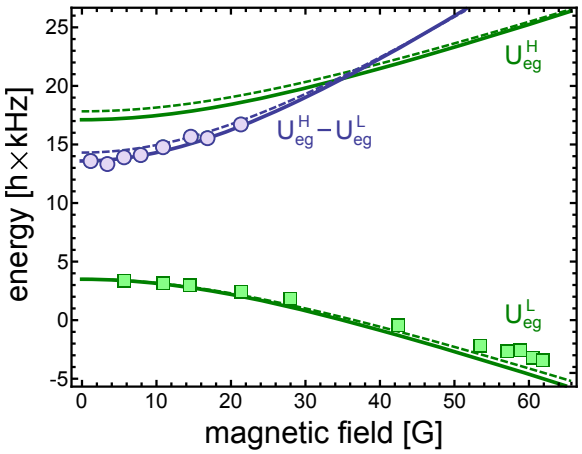

Figure 7.11: Circles: measured spin-exchange frequency $(\mathcal{U}_{eg}^{H}-\mathcal{U}_{eg}^{L})/h$ at $s=30$ as a function of the magnetic field. Squares: measured energy of the $|eg^{L}\rangle$ state derived from the spectroscopic measurements (Fig. 7.6). The solid lines show the predicted values according to Eq. (7.3.3) in which $\mathcal{F}=0.77$ derived from the fit of Fig. 7.10. The dashed lines show a fit of the points to the same model leaving a_{eg}^{-} as free parameter (see main text for more details).

Sec. 7.3.3 we know that the energy difference between the two interaction channels depends on the magnetic field as:

$$\mathcal{U}_{eg}^{H}(B)-\mathcal{U}_{eg}^{L}(B)=2\sqrt{\mathcal{V}_{ex}^{2}+(\mathcal{F}\Delta B)^{2}}. \tag{7.-8}$$

where $\Delta B=\frac{5}{2}\delta g\,\mu_B B$ and the Frank-Condon factor is $\mathcal{F}=0.77$ for the scattering lengths deduced in the previous section. We thus measure the spin-exchange oscillation frequency as a function of the final bias magnetic field (see Fig. 7.7). The circles in Fig. 7.11 show the measured spin-oscillation frequency $(\mathcal{U}_{eg}^{H}-\mathcal{U}_{eg}^{L})/h$ at lattice depth $s=30$ as a function of B, while the squares indicate the energy of the $|eg^{L}\rangle$ state determined by fitting the position of the peaks in the spectroscopic measurements (Fig. 7.6). The solid lines in Fig. 7.11 show the predictions of this model by using $a_{eg}^{-}=219.5\,a_0$, $a_{eg}^{+}=3300\,a_0$ (from the fit in Fig. 7.10) and the Franck-Condon factor $F=0.77$ calculated by using the interacting wavefunctions obtained previously. The agreement with the experimental data is quite good, showing the substantial validity of the model in Eq. (7.3.3) as long as the overlap factor F between the interacting wavefunctions is considered. Alternatively, we have performed a simultaneous fit of the two datasets in Fig. 7.11 using the fitting function (7.4.2) and taking $\mathcal{U}_{eg}^{+}$ and F as functions of the free parameter a_{eg}^{+} while considering $a_{eg}^{-}=219.5\,a_0$. The result (dashed lines) is $a_{eg}^{+}=(4400\pm600)\,a_0$, which is $\sim 2\sigma$ away from the more precise determination coming from the fit of the data shown in Fig. 7.10. We note that a precise determination of a_{eg}^{+} is complicated by the fact that,

in this regime of strong interactions, the dependence of $\mathcal{U}_{eg}^{+}$ on a_{eg}^{+} is extremely weak and small effects coming e.g. from calibration uncertainties or from higher-order contributions in the theory could yield significant changes. We also note that, in the presence of a tight trapping, the interpretation of the results in terms of an effective scattering length should be considered [171]. However, we stress that, differently from a_{eg}^{+}, our determination of $\mathcal{V}_{\mathrm{ex}}$ is free from any assumption or modeling and represents an accurate measurement of the spin-exchange coherent coupling in an actual experimental configuration.

7.5 Observation of an orbital Feshbach resonance

In this Section we present some very recent results [50] regarding the observation of a novel kind of Feshbach resonance, called *orbital* Feshbach resonance, affecting the scattering between ^{173}Yb atoms in different electronic states. We observe a hydrodynamic expansion of the Fermi gas in the strongly interacting regime and use it to identify the resonance position.

The determination, shown in the previous Section, of such a high scattering length a_{eg^+} in the triplet channel, has triggered a recent theoretical work [36] in which the orbital Feshbach resonance has been predicted. Indeed, the orbital-symmetric potential features a shallow bound state with $|E_c|$ in the tens of kHz range, which corresponds to a large background scattering length a_{eg^+}. The physical idea behind an orbital Feshbach resonance is that the orbital degree of freedom plays the same role as the spin degree of freedom in the typical magnetic Feshbach resonance. A coupling between an "open"-channel ($|o\rangle = |e\downarrow, g\uparrow\rangle$) and the bound state of a "closed"-channel ($|c\rangle = |g\downarrow, e\uparrow\rangle$) induces a resonance in the scattering process. These two states are nothing else then the $|eq^L\rangle$, $|eq^H\rangle$ states introduced before for $B \gg \mathcal{V}_{ex}$ (see Eq. 7.3.3). Due to the presence of a differential Landè factor δg, the energy separation between the two channels, $\Delta\mu B = \delta g \mu_B \Delta m B$, can be tuned, as in a typical magnetic Feshbach resonance. As the interatomic distance decreases, the appropriate basis for the description of the scattering is given by the orbital symmetric $|eg^+\rangle = (|c\rangle - |o\rangle)/\sqrt{2}$ and antisymmetric states $|eg^-\rangle = (|c\rangle + |o\rangle)/\sqrt{2}$, which are associated to two distinct molecular potentials. The difference between them determines an effective coupling between open and closed channels, which becomes resonant when the differential Zeeman energy $\Delta\mu B$ equals the binding energy $|E_c|$ of the least bound state in the closed channel (see Fig. 7.12).

Since in the 3D optical lattice we have measured a really high $\mathcal{V}_{ex} \sim 10\,\mathrm{kHz}$, magnetic fields above 1000 G would be necessary, to well define the collision channels. For this reason we perform the experiments in a

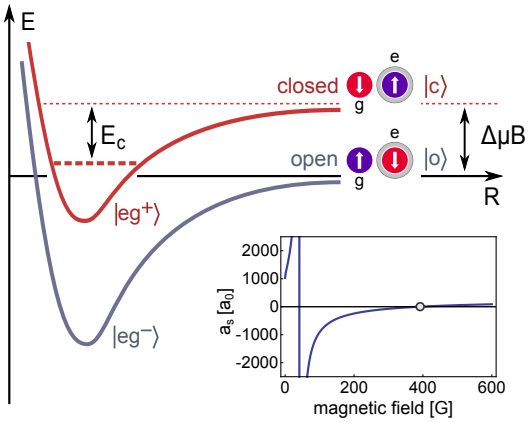

Figure 7.12: Scheme of the ^{173}Yb orbital Feshbach resonance affecting the scattering between one $|g\rangle = ^1S_0$ atom and one $|e\rangle = ^3P_0$ atom in two different spin states (see text for details). The inset shows the behavior of the scattering length for $\Delta m = 5$ as modeled in Ref. [36], with the center of the resonance adjusted to match our experimental observations in Fig. 7.13b (the circle identifies the predicted position of the zero crossing).

typical dipole trap, constituted by a 759 nm gaussian laser beam (along the same direction as OL_1, see Fig. 2.12) with beam waist $w_0 \simeq 30\,\mu$m and the orthogonal, vertical lattice beam in which the retroreflection has been blocked. With this trapping potential, $\mathcal{V}_{ex}$ is estimated to be at least one order of magnitude lower (~ 100 Hz) thus giving us the possibility to use more feasibile magnetic fields values, $B \sim 100\,$G.

The experiment starts by loading an atomic spin mixture $(-5/2, +5/2)$ in the $|g\rangle = {}^1S_0$ state in the "magic" dipole trap and promoting all the $m = -5/2$ atoms to the metastable $^3P_0$ state thus preparing the open-channel state. The excitation is perfomed with a $\pi-$pulse of duration $T_{pulse} = 400\,\mu$s at a magnetic field $B \sim 150\,G$ so that the collision channels $|o\rangle$, $|c\rangle$ are well defined. Then, we change the magnetic field intensity to the desired value B in about 2 ms. The trap is suddenly switched off and, after a time of flight t_{TOF} , the atoms remaining in the ground state $|g\rangle$ are imaged with typical absorption imaging. During the first 5 ms of the expansion the magnetic field is kept at the B value, thus allowing the atoms to release their interaction energy into kinetic energy. Fig. 7.13a shows the evolution of the aspect ratio of the Fermi gas after the release from the trap as a function of the time of flight. The aspect ratio is defined as the ratio R_y/R_x of the expanded atomic cloud size along $\hat{y}$ to the size along $\hat{x}$. In the case of a noninteracting Fermi gas (long-dashed lines) the expansion is ballistic, eventually resulting in a spherical shape and in an aspect ratio value of 1 for sufficiently long expansion times (much larger than the inverse trap frequencies). The experimental circles, showing the

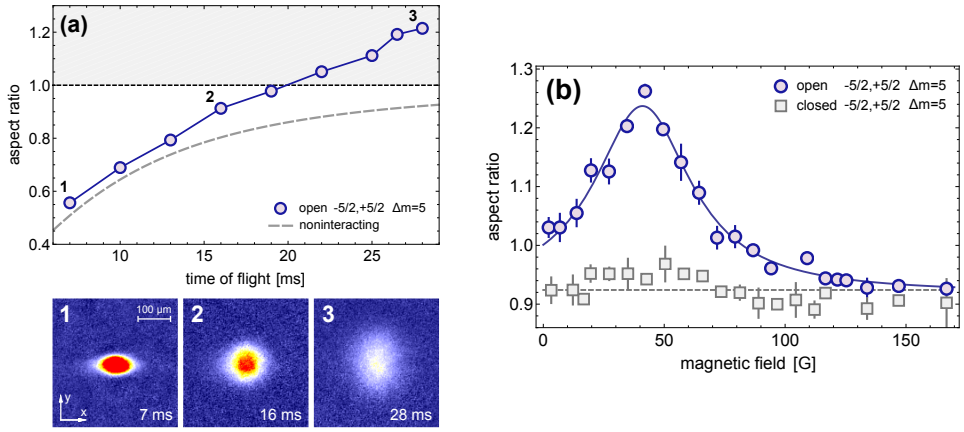

Figure 7.13: Observation of an orbital Feshbach resonance. **(a)** Aspect ratio of the atomic cloud after a time of flight $t_{TOF} = 28$ ms as a function of the magnetic field. The maximum determines the position of the orbital Feshbach resonance. **(b)** Anisotropic expansion of a strongly interacting ^{173}Yb Fermi gas, initially prepared in the open channel of a spin mixture of $m = \pm 5/2$, at a magnetic field B = 41 G. (Top) The circles show the aspect ratio of the expanded $|g\rangle$ atomic cloud as a function of the time of flight. The long-dashed grey line shows the behavior expected for an ideal Fermi gas. The short-dashed black line indicates the unit limit above which the experimental aspect ratio gets inverted because of hydrodynamic expansion. **(1)-(3)**. False-color absorption images of the $|g\rangle$ component of the atomic cloud after excitation in the open channel for increasing time of flight (**(1)** 7 ms **(2)** 16 ms **(3)** 28 ms).

behavior of the interacting spin mixture at a magnetic field $B = 41$ G, clearly show an inversion of the cloud shape from prolate to oblate, with an aspect ratio exceeding 1 after a $t_{TOF} \simeq 18$ ms. Figs. 7.13a(1,2,3) show false-color absorption images of the atomic cloud for different times of flight, as specified in Fig. 7.13a. The observation of the aspect ratio inversion is a hallmark of hydrodynamic expansion of the Fermi gas, which occurs in the regime of strong interactions, as observed for alkali fermionic gases close to magnetic Feshbach resonances [37, 38].

In Fig. 7.13b we show the difference in the aspect ratio between the open channel and the closed channel as a function of the magnetic field at $t_{TOF} = 28$ ms. In the open channel a clear resonant behavior is observed, with a maximum that is located at a magnetic field $B = (41 \pm 1)$ G, signalling the enhancement of the elastic collisional rate at the Feshbach resonance.

We have repeated the measurements for smaller $\Delta m = m' - m$, evidencing similar resonances at significantly larger magnetic fields. The data are plotted in Fig. 7.14 versus a rescaled magnetic field $\overline{B} = B\Delta m/5$. The different datasets clearly show a very similar dependence on $\overline{B}$, which

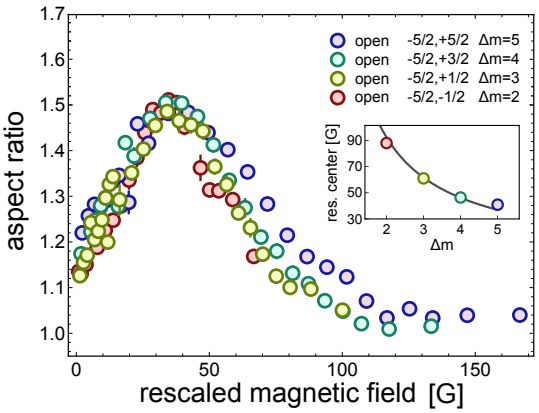

Figure 7.14: Comparison between open-channel mixtures with different $\Delta m = m - m'$, plotted as a fuction of a rescaled magnetic field $\overline{B} = B\Delta m/5$. Different colors refer to different spin states, as explained in the legend. The collapse of the different datasets onto the same curve is a verifcation of the orbital feshbach resonance scaling law, which is in turn a direct consequence of the $SU(N)$ symmetry of two-electron atoms.

is a distinctive feature of the orbital Feshbach resonance mechanism. As a matter of fact, the magnetic field at which the resonance is located is expected to scale as Δm^{-1} [36]. This scaling law directly follows from the $SU(N)$ invariance of scattering in ^{173}Yb, which determines $|E_c|$ to be independent of Δm. The collapse of the experimental data onto the same curve is, therefore, a verification of the orbital Feshbach scaling law, which is in turn a strong evidence for the $SU(N)$ symmetry of two-electron atoms.

7.6 Conclusions and perspectives

To conclude, in this Chapter we have described experiments perfomed by exploiting the ultranarrow clock transition of ^{173}Yb. In the first part of the Chapter we presented the first observation of fast, long-lived inter-orbital spin-exchange oscillations in a system of ^{173}Yb atoms trapped in a 3D optical lattice. We were able to measure directly the exchange interaction strength, which turns out to be much larger than the other energy scales in the system such as the Fermi energy E_F and the thermal energy $k_B T$. This is different with respect to other atomic systems, in which the spin dynamics arises from a small difference between the scattering lengths [166, 169, 170]. The direct measurement of $\mathcal{V}_{\rm ex}$ has also allowed us to extract important collisional parameters such as the scattering length a_{eg}^{+} in the spin-singlet channel, which exceeds the spin-triplet a_{eg}^{-} one by ~ 10 times. We note that such a measurement would be more challenging with Strontium because the scattering lengths have been determined to be very

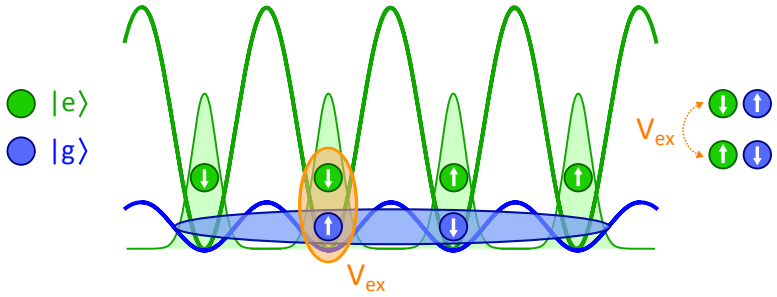

Figure 7.15: Illustration of the Kondo lattice model (KLM) implementation with Ytterbium atoms in a state-dependent optical lattice. The onsite exchange interaction $\mathcal{V}_{ex}$ between mobile particles and localised spins competes with the tunnelling t of mobile atoms.

similar [172].

These findings make ^{173}Yb a perfect candidate for the observation of quantum magnetism in a two-orbital system with $SU(N)$ interaction symmetry [34]. Furthermore, by exploiting a state dependent lattice [173] (for example at 655 nm) it would be possible to tightly trap the fermions in the metastable state while keeping the $^1S_0$ atoms in a metallic state. With this arrangement we could investigate basic properties of the Kondo lattice model in which localized, magnetic impurities ($^3P_0$ atoms) interact via spin-exchange with a bath of conductive electrons ($^1S_0$ atoms) [33, 34], inducing the formation of a strongly correlated state, Fig. 7.15.

The discovery of a Feshbach resonance between $^1S_0$ and $^3P_0$ state may open new exciting possibilities, such as the investigation of the two-order parameters BEC-BCS crossover [36], or the study of topological superfluidity [174–176]. Regarding the latter, we could engineer spin-orbit coupling in a mixture of $^1S_0$ and $^3P_0$ states simply by noticing that when an atom absorbs a 578 nm photon, it also acquires a momentum kick, thus creating a link between orbital excitation and momentum transfer. Furthermore, if spin-orbit coupling is induced in a mixture of of $^1S_0$ and $^3P_0$ states with different nuclear spin components, one could exploit the orbital Feshbach resonance and tune the interactions with a magnetic field, exploring the superfluid regime in presence of spin-orbit coupling [174, 177, 178], Fig. 7.16.

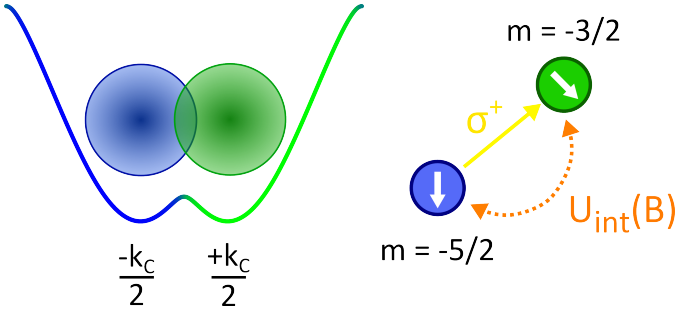

Figure 7.16: Schematic illustration of a strongly interacting mixture of $^1S_0$ and $^3P_0$ atoms in presence of spin-orbit coupling. If the scattering length is tuned across the orbital Feshbach resonance, one could in principle explore the topological superfluid regime.

Appendices

A | Clebsch-Gordan coefficients of ^{173}Yb

Table A.1: Clebsch-Gordan coefficient for $(^1S_0 \rightarrow {}^{2S+1}P_1)$ π transition

m_F	-5/2	-3/2	-1/2	+1/2	+3/2	+5/2
$F' = \frac{7}{2}$	$-\sqrt{\frac{2}{21}}$	$-\frac{1}{3}\sqrt{\frac{10}{7}}$	$-\sqrt{\frac{2}{21}}$	$-\sqrt{\frac{2}{21}}$	$-\frac{1}{3}\sqrt{\frac{10}{7}}$	$-\sqrt{\frac{2}{21}}$
$F' = \frac{5}{2}$	$\sqrt{\frac{5}{21}}$	$\sqrt{\frac{3}{35}}$	$\sqrt{\frac{1}{105}}$	$-\sqrt{\frac{1}{105}}$	$-\sqrt{\frac{3}{35}}$	$-\sqrt{\frac{5}{21}}$
$F' = \frac{3}{2}$	0	$\frac{2}{3\sqrt{5}}$	$\sqrt{\frac{2}{15}}$	$\sqrt{\frac{2}{15}}$	$\frac{2}{3\sqrt{5}}$	0

Table A.2: Clebsch-Gordan coefficient for $(^1S_0 \rightarrow {}^{2S+1}P_1)$ σ^+ transition

m_F	-5/2	-3/2	-1/2	+1/2	+3/2	+5/2
$F' = \frac{7}{2}$	$\frac{1}{3\sqrt{7}}$	$\frac{1}{\sqrt{21}}$	$\sqrt{\frac{2}{21}}$	$\frac{1}{3}\sqrt{\frac{10}{7}}$	$\sqrt{\frac{5}{21}}$	$\frac{1}{\sqrt{3}}$
$F' = \frac{5}{2}$	$-\sqrt{\frac{2}{21}}$	$-\frac{4}{\sqrt{105}}$	$-\sqrt{\frac{6}{35}}$	$-\frac{4}{\sqrt{105}}$	$-\sqrt{\frac{2}{21}}$	0
$F' = \frac{3}{2}$	$\frac{\sqrt{2}}{3}$	$\sqrt{\frac{2}{15}}$	$\sqrt{\frac{1}{15}}$	$\frac{1}{3\sqrt{5}}$	0	0

B State dependent potentials: magnetic field dependence

Due to the non-zero angular momentum J, the $^3P_1$ state has a magnetic field dependence which is depicted in Fig. B.3. This dependence must be included in the Eqs. (2.5.2,3.1) describing the light shifts and Raman amplitudes respectively. In particular, each Zeeman sublevel $m_{F'}$ belonging to the $^3P_1$ manifold with $F' = 7/2, 5/2, 3/2$ acquires an energy shift, depending on the value of the magnetic field. In Fig. B.1 we show the calculated magnetic field dependence of the state dependent light shift in the two-leg case (left) and in the three-leg case (right), assuming the $+1.876$ GHz as the frequency detuning with respect to the $F = 5/2 \rightarrow F' = 7/2$ transition. Especially in the case of uniform polarization, the magnetic field increases the degree of complexity of the system, since it becomes more difficult to coherently couple more than two spin states. In Fig. B.2 we plot the magnetic field dependence of the Raman couplings in case of $m_F \rightarrow m_F + 2$ transitions, that are fortunately, only weakly perturbed.

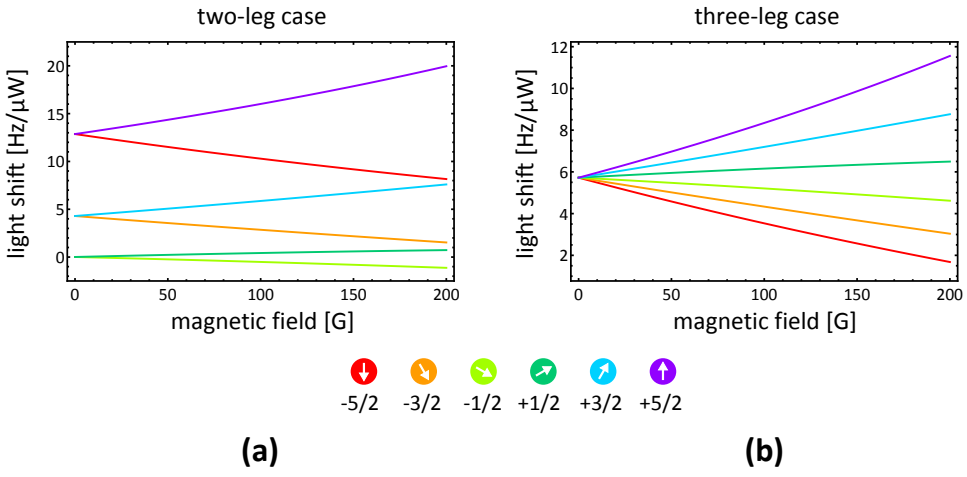

Figure B.1: Magnetic field dependence of the state dependent light shifts. **(a)** Two-leg case, H polarization. **(b)** Three-leg case, uniform polarization.

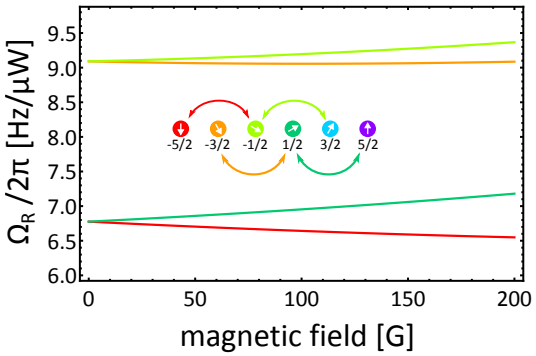

Figure B.2: Magnetic field dependence of the state $m_F \rightarrow m_F + 2$ Raman couplings.

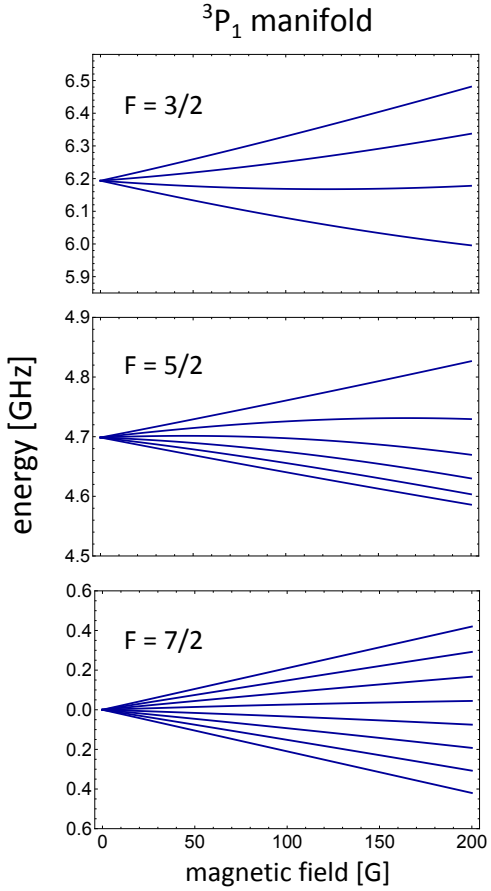

Figure B.3: Magnetic field dependence of the $^3P_1$ manifold energy levels.

Bibliography

[1] M. H. Anderson, J. R. Ensher, M. R. Matthews, C. E. Wieman, and E. A. Cornell. *Observation of Bose-Einstein Condensation in a Dilute Atomic Vapor*. Science **269**, 198–201 (1995).

[2] K. B. Davis, M. O. Mewes, M. R. Andrews, N. J. van Druten, D. S. Durfee, D. M. Kurn, and W. Ketterle. *Bose-Einstein Condensation in a Gas of Sodium Atoms*. Phys. Rev. Lett. **75**, 3969–3973 (1995).

[3] B. DeMarco and D. S. Jin. *Onset of Fermi Degeneracy in a Trapped Atomic Gas*. Science **285**, 1703–1706 (1999).

[4] R. P. Feynman. *Simulating physics with computers*. International Journal of Theoretical Physics **21**, 467–488 (1982). ISSN 0020-7748.

[5] C. Chin, P. Julienne, and E. Tiesinga. *Feshbach resonances in ultracold gases*. Rev. Mod. Phys. **82**, 1225–1286 (2010). ISSN 0034-6861.

[6] M. Greiner, O. Mandel, T. Esslinger, T. Hänsch, and I. Bloch. *Quantum phase transition from a superfluid to a Mott insulator in a gas of ultracold atoms.* Nature **415**, 39–44 (2002). ISSN 0028-0836.

[7] R. Grimm, M. Weidemuller, and Y. B. Ovchinnikov. *Optical Dipole Traps for Neutral Atoms*. Advances In Atomic, Molecular, and Optical Physics **42**, 95 – 170 (2000). ISSN 1049-250X.

[8] D. Jaksch, C. Bruder, J. Cirac, C. Gardiner, and P. Zoller. *Cold Bosonic Atoms in Optical Lattices*. Phys. Rev. Lett. **81**, 3108–3111 (1998). ISSN 0031-9007.

[9] I. Bloch, J. Dalibard, and W. Zwerger. *Many-body physics with ultracold gases*. Rev. Mod. Phys. **80**, 885–964 (2008). ISSN 0034-6861.

[10] I. Bloch, J. Dalibard, and S. Nascimbène. *Quantum simulations with ultracold quantum gases*. Nature Physics **8**, 267–276 (2012). ISSN 1745-2473.

[11] Y.-J. Lin, R. L. Compton, K. Jiménez-García, J. V. Porto, and I. B. Spielman. *Synthetic magnetic fields for ultracold neutral atoms.* Nature **462**, 628–632 (2009). ISSN 1476-4687.

[12] M. Aidelsburger, M. Atala, S. Nascimbène, S. Trotzky, Y.-a. Chen, and I. Bloch. *Experimental Realization of Strong Effective Magnetic Fields in an Optical Lattice*. Phys. Rev. Lett. **107**, 255301 (2011). ISSN 0031-9007.

[13] M. Aidelsburger, M. Atala, M. Lohse, J. T. Barreiro, B. Paredes, and I. Bloch. *Realization of the Hofstadter hamiltonian with ultracold atoms in optical lattices*. Phys. Rev. Lett. **111**, 185301 (2013). ISSN 00319007.

[14] J. Struck, C. Ölschläger, M. Weinberg, P. Hauke, J. Simonet, a. Eckardt, M. Lewenstein, K. Sengstock, and P. Windpassinger. *Tunable Gauge Potential for Neutral and Spinless Particles in Driven Optical Lattices*. Phys. Rev. Lett. **108**, 1–5 (2012). ISSN 0031-9007.

[15] K. Jiménez-García, L. LeBlanc, R. Williams, M. Beeler, a. Perry, and I. Spielman. *Peierls Substitution in an Engineered Lattice Potential*. Phys. Rev. Lett. **108**, 225303 (2012). ISSN 0031-9007.

[16] Y.-J. Lin, K. Jiménez-García, and I. B. Spielman. *Spin-orbit-coupled Bose-Einstein condensates.* Nature **471**, 83–86 (2011). ISSN 1476-4687.

[17] P. Wang, Z. Q. Yu, Z. Fu, J. Miao, L. Huang, S. Chai, H. Zhai, and J. Zhang. *Spin-orbit coupled degenerate Fermi gases*. Phys. Rev. Lett. **109**, 095301 (2012). ISSN 00319007.

[18] G. Jotzu, M. Messer, R. Desbuquois, M. Lebrat, T. Uehlinger, D. Greif, and T. Esslinger. *Experimental realisation of the topological Haldane model*. Nature **515**, 14 (2014). ISSN 0028-0836.

[19] M. Aidelsburger, M. Lohse, C. Schweizer, M. Atala, J. T. Barreiro, S. Nascimbene, N. R. Cooper, I. Bloch, and N. Goldman. *Measuring the Chern number of Hofstadter bands with ultracold bosonic atoms*. Nature Physics **11**, 162–166 (2015).

[20] L. Duca, T. Li, M. Reitter, I. Bloch, M. Schleier-Smith, and U. Schneider. *An Aharonov-Bohm interferometer for determining Bloch band topology*. Science **347**, 288–292 (2015).

[21] H. Miyake, G. A. Siviloglou, C. J. Kennedy, W. C. Burton, and W. Ketterle. *Realizing the Harper Hamiltonian with Laser-Assisted Tunneling in Optical Lattices*. Phys. Rev. Lett. **111**, 185302 (2013).

[22] O. Boada, a. Celi, J. Latorre, and M. Lewenstein. *Quantum Simulation of an Extra Dimension*. Phys. Rev. Lett. **108**, 133001 (2012). ISSN 0031-9007.

[23] A. Celi, P. Massignan, J. Ruseckas, N. Goldman, I. B. Spielman, G. Juzeliunas, and M. Lewenstein. *Synthetic Gauge Fields in Synthetic Dimensions*. Phys. Rev. Lett. **112**, 043001 (2014). ISSN 0031-9007.

[24] M. Mancini, G. Pagano, G. Cappellini, L. Livi, M. Rider, J. Catani, C. Sias, P. Zoller, M. Inguscio, M. Dalmonte, and L. Fallani. *Observation of chiral edge states with neutral fermions in synthetic Hall ribbons*. Science **349**, 1510–1513 (2015).

[25] B. K. Stuhl, H.-I. Lu, L. M. Aycock, D. Genkina, and I. B. Spielman. *Visualizing edge states with an atomic Bose gas in the quantum Hall regime*. Science **349**, 1514–1518 (2015).

[26] T. Fukuhara, Y. Takasu, M. Kumakura, and Y. Takahashi. *Degenerate Fermi Gases of Ytterbium*. Phys. Rev. Lett. **98**, 030401 (2007). ISSN 0031-9007.

[27] C. W. Hoyt, Z. W. Barber, C. W. Oates, T. M. Fortier, S. a. Diddams, and L. Hollberg. *Observation and absolute frequency measurements of the* $^1S_0$-$^3P_0$ *optical clock transition in neutral ytterbium*. Phys. Rev. Lett. **95**, 083003 (2005). ISSN 00319007.

[28] N. Hinkley, J. A. Sherman, N. B. Phillips, M. Schioppo, N. D. Lemke, M. Pizzocaro, C. W. Oates, and A. D. Ludlow. *An Atomic Clock with* 10^{-18} *Instability*. Science **341**, 1215–1218 (2013).

[29] M. Boyd, T. Zelevinsky, A. Ludlow, S. Blatt, T. Zanon-Willette, S. Foreman, and J. Ye. *Nuclear spin effects in optical lattice clocks*. Phys. Rev. A **76**, 022510 (2007). ISSN 1050-2947.

[30] B. J. Bloom, T. L. Nicholson, J. R. Williams, S. L. Campbell, M. Bishof, X. Zhang, W. Zhang, S. L. Bromley, and J. Ye. *An optical lattice clock with accuracy and stability at the* 10^{-18} *level*. Nature **506**, 71–75 (2014). ISSN 1476-4687.

[31] A. Derevianko and H. Katori. *Colloquium: Physics of optical lattice clocks*. Rev. Mod. Phys. **83**, 331–347 (2011).

[32] Z. Barber, J. Stalnaker, N. Lemke, N. Poli, C. Oates, T. Fortier, S. Diddams, L. Hollberg, C. Hoyt, a. Taichenachev, and V. Yudin. *Optical Lattice Induced Light Shifts in an Yb Atomic Clock*. Phys. Rev. Lett. **100**, 103002 (2008). ISSN 0031-9007.

[33] M. Foss-Feig, M. Hermele, and A. M. Rey. *Probing the Kondo lattice model with alkaline-earth-metal atoms*. Phys. Rev. A **81**, 051603 (2010). ISSN 1050-2947.

[34] A. V. Gorshkov, M. Hermele, V. Gurarie, C. Xu, P. S. Julienne, J. Ye, P. Zoller, E. Demler, M. D. Lukin, and a. M. Rey. *Two-orbital SU(N) magnetism with ultracold alkaline-earth atoms*. Nature Physics **6**, 289–295 (2010). ISSN 1745-2473.

[35] M. A. Cazalilla, A. F. Ho, and M. Ueda. *Ultracold gases of ytterbium: ferromagnetism and Mott states in an SU(6) Fermi system*. New Journal of Physics **11**, 103033 (2009). ISSN 1367-2630.

[36] R. Zhang, Y. Cheng, H. Zhai, and P. Zhang. *Orbital Feshbach Resonance in Alkali-Earth Atoms*. Phys. Rev. Lett. **115**, 135301 (2015).

[37] A. Trenkwalder, C. Kohstall, M. Zaccanti, D. Naik, A. I. Sidorov, F. Schreck, and R. Grimm. *Hydrodynamic Expansion of a Strongly Interacting Fermi-Fermi Mixture*. Phys. Rev. Lett. **106**, 115304 (2011).

[38] C. A. Regal and D. S. Jin. *Measurement of Positive and Negative Scattering Lengths in a Fermi Gas of Atoms*. Phys. Rev. Lett. **90**, 230404 (2003).

[39] C. N. Yang and Y.-Z. You. *One-Dimensional w -Component Fermions and Bosons with Repulsive Delta Function Interaction*. Chinese Physics Letters **28**, 020503 (2011). ISSN 0256-307X.

[40] D. C. Tsui, H. L. Stormer, and A. C. Gossard. *Two-Dimensional Magnetotransport in the Extreme Quantum Limit*. Phys. Rev. Lett. **48**, 1559–1562 (1982).

[41] R. B. Laughlin. *Anomalous Quantum Hall Effect: An Incompressible Quantum Fluid with Fractionally Charged Excitations*. Phys. Rev. Lett. **50**, 1395–1398 (1983).

[42] H. L. Stormer. *Nobel Lecture: The fractional quantum Hall effect*. Rev. Mod. Phys. **71**, 875–889 (1999).

[43] S. Barbarino, L. Taddia, D. Rossini, L. Mazza, and R. Fazio. *Magnetic crystals and helical liquids in alkaline-earth fermionic gases*. Nat Commun **6**, – (2015).

[44] G. Pagano, M. Mancini, G. Cappellini, P. Lombardi, F. Schäfer, H. Hu, X.-J. Liu, J. Catani, C. Sias, M. Inguscio, and L. Fallani. *A one-dimensional liquid of fermions with tunable spin*. Nature Physics **10**, 198–201 (2014).

[45] G. Pagano. *Many-body Physics with Ytterbium Fermi gases: from one-dimensional systems to orbital magnetism*. PhD thesis, Scuola Normale Superiore di Pisa (2015).

[46] J. M. Luttinger. *An Exactly Soluble Model of a Many-Fermion System*. Journal of Mathematical Physics **4**, 1154 (1963). ISSN 00222488.

[47] F. D. M. Haldane. *"Luttinger liquid theory" of one-dimensional quantum fluids. I. Properties of the Luttinger model and their extension to the general 1D interacting spinless Fermi gas*. Journal of Physics C: Solid State Physics **14**, 2585 (1981).

[48] G. Cappellini, M. Mancini, G. Pagano, P. Lombardi, L. Livi, M. Siciliani de Cumis, P. Cancio, M. Pizzocaro, D. Calonico, F. Levi, C. Sias, J. Catani, M. Inguscio, and L. Fallani. *Direct Observation of Coherent Interorbital Spin-Exchange Dynamics*. Phys. Rev. Lett. **113**, 120402 (2014). ISSN 0031-9007.

[49] G. Cappellini. PhD thesis, European Laboratory for Non-linear Spectroscopy (LENS) (in preparation).

[50] G. Pagano, M. Mancini, G. Cappellini, L. Livi, C. Sias, J. Catani, M. Inguscio, and L. Fallani. *Strongly Interacting Gas of Two-Electron Fermions at an Orbital Feshbach Resonance*. Phys. Rev. Lett. **115**, 265301 (2015).

[51] S. Giorgini, L. Pitaevskii, and S. Stringari. *Theory of ultracold atomic Fermi gases*. Rev. Mod. Phys. **80**, 1215–1274 (2008). ISSN 0034-6861.

[52] D. A. Butts and D. S. Rokhsar. *Trapped Fermi gases*. Phys. Rev. A **55**, 4346–4350 (1997).

[53] C. Cohen-Tannoudji and G. Grynberg. *Atom-photon interactions: basic processes and applications*, Volume 1. Wiley (1998).

[54] M. Greiner, I. Bloch, O. Mandel, T. Hänsch, and T. Esslinger. *Exploring Phase Coherence in a 2D Lattice of Bose-Einstein Condensates*. Phys. Rev. Lett. **87**, 160405 (2001). ISSN 0031-9007.

[55] J. Struck, M. Weinberg, C. Olschlager, P. Windpassinger, J. Simonet, K. Sengstock, R. Hoppner, P. Hauke, A. Eckardt, M. Lewenstein, and L. Mathey. *Engineering Ising-XY spin-models in a triangular lattice using tunable artificial gauge fields*. Nat Phys **9**, 738–743 (2013). ISSN 1745-2473.

[56] L. Tarruell, D. Greif, T. Uehlinger, G. Jotzu, and T. Esslinger. *Creating, moving and merging Dirac points with a Fermi gas in a tunable honeycomb lattice*. Nature **483**, 302–305 (2012). ISSN 0028-0836.

[57] N. W. Ashcroft and D. N. Mermin. *Solid State Physics*. Saunders College Publishing, Fort Worth, TX (1976).

[58] M. Köhl, H. Moritz, T. Stöferle, K. Günter, and T. Esslinger. *Fermionic Atoms in a Three Dimensional Optical Lattice: Observing Fermi Surfaces, Dynamics, and Interactions*. Phys. Rev. Lett. **94**, 080403 (2005). ISSN 0031-9007.

[59] N. Marzari, A. A. Mostofi, J. R. Yates, I. Souza, and D. Vanderbilt. *Maximally localized Wannier functions: Theory and applications*. Rev. Mod. Phys. **84**, 1419–1475 (2012).

[60] T. Busch, B. G. Englert, K. Rzazewski, and M. Wilkens. *Two cold atoms in a harmonic trap*. Foundations of Physics **28**, 549–559 (1998). ISSN 0015-9018.

[61] D. A. Steck. *Quantum and Atom Optics*. (2007).

[62] J. Bateman, A. Xuereb, and T. Freegarde. *Stimulated Raman transitions via multiple atomic levels*. Phys. Rev. A **81**, 043808 (2010).

[63] Y.-J. Lin, R. Compton, a. Perry, W. Phillips, J. Porto, and I. Spielman. *Bose-Einstein Condensate in a Uniform Light-Induced Vector Potential*. Phys. Rev. Lett. **102**, 130401 (2009). ISSN 0031-9007.

[64] V. Galitski and I. B. Spielman. *Spin-orbit coupling in quantum gases*. Nature **494**, 49–54 (2013). ISSN 1476-4687.

[65] N. Goldman, G. Juzeliunas, P. Ohberg, and I. B. Spielman. *Light-induced gauge fields for ultracold atoms*. Reports on Progress in Physics **77**, 126401 (2014).

[66] L. W. Cheuk, A. T. Sommer, Z. Hadzibabic, T. Yefsah, W. S. Bakr, and M. W. Zwierlein. *Spin-Injection Spectroscopy of a Spin-Orbit Coupled Fermi Gas*. Phys. Rev. Lett. **109**, 095302 (2012).

[67] W. Ketterle and M. W. Zwierlein. *Making, probing and understanding ultracold Fermi gases*. In M. Inguscio, W. Ketterle, and C. Salomon, editors, *Proceedings of the International School of Physics "Enrico Fermi", Course CLXIV, Varenna, 20 - 30 June 2006*, number June 2006, pages 20–30. IOS Press, Amsterdam (2006).

[68] J. Dalibard. *Collisional dynamics of ultra-cold atomic gases*. Proceedings of the International School of Physics "Enirco Fermi", Course CLXI pages 1–29 (1999).

[69] J. Walraven. *Quantum Gases - Collisions and Statistics*. Lecture course at master level, University of Vienna (2013).

[70] V. V. Flambaum, G. F. Gribakin, and C. Harabati. *Analytical calculation of cold-atom scattering*. Phys. Rev. A **59**, 1998–2005 (1999).

[71] L. Landau and E. Lifshitz. *Quantum Mechanics: Non-Relativistic Theory*. Pergamon Press, New York (1987).

[72] K. Huang. *Statistical Mechanics*. John Wiley and sons, Inc., New York (1987).

[73] M. A. Cazalilla and A. M. Rey. *Ultracold Fermi gases with emergent $SU(N)$ symmetry*. Reports on Progress in Physics **77**, 124401 (2014).

[74] F. Gursey, A. Pais, and L. A. Radicati. *Spin and Unitary Spin Independence of Strong Interactions*. Phys. Rev. Lett. **13**, 299–301 (1964).

[75] M. Hermele, V. Gurarie, and A. Rey. *Mott Insulators of Ultracold Fermionic Alkaline Earth Atoms: Underconstrained Magnetism and Chiral Spin Liquid*. Phys. Rev. Lett. **103**, 135301 (2009). ISSN 0031-9007.

[76] S.-K. Yip and T.-L. Ho. *Zero sound modes of dilute Fermi gases with arbitrary spin*. Phys. Rev. A **59**, 4653–4656 (1999).

[77] M. Berglund and M. Wieser. *Isotopic compositions of the elements 2009 (IUPAC Technical Report)*. Pure and Applied Chemistry **83** (2011).

[78] A. Yamaguchi. *Metastable State of Ultracold and Quantum Degenerate Ytterbium Atoms*. PhD thesis, Kyoto University (2008).

[79] S. Porsev, A. Derevianko, and E. Fortson. *Possibility of an optical clock using the $6^1S_0 \rightarrow 6^3P_0$ transition in $^{171,173}Yb$ atoms held in an optical lattice*. Phys. Rev. A **69**, 021403 (2004). ISSN 1050-2947.

[80] S. G. Porsev and A. Derevianko. *Hyperfine quenching of the metastable 3P0,2 states in divalent atoms*. Phys. Rev. A **69**, 042506–1 (2004). ISSN 10502947.

[81] G. Cappellini, P. Lombardi, M. Mancini, G. Pagano, M. Pizzocaro, L. Fallani, and J. Catani. *A compact ultranarrow high-power laser system for experiments with 578 nm ytterbium clock transition*. Review of Scientific Instruments **86**, 073111 (2015).

[82] M. Kitagawa, K. Enomoto, K. Kasa, Y. Takahashi, R. Ciuryo, P. Naidon, and P. Julienne. *Two-color photoassociation spectroscopy of ytterbium atoms and the precise determinations of s-wave scattering lengths*. Phys. Rev. A **77**, 012719 (2008). ISSN 1050-2947.

[83] T. Fukuhara, S. Sugawa, Y. Takasu, and Y. Takahashi. *All-optical formation of quantum degenerate mixtures*. Phys. Rev. A **79**, 021601 (2009).

[84] S. Taie, Y. Takasu, S. Sugawa, R. Yamazaki, T. Tsujimoto, R. Murakami, and Y. Takahashi. *Realization of a SU(2) × SU(6) System of Fermions in a Cold Atomic Gas*. Phys. Rev. Lett. **105**, 190401 (2010). ISSN 0031-9007.

[85] M. Mancini. *Realizzazione sperimentale di un gas quantistico degenere di atomi di Itterbio*. Master's thesis, Università degli Studi di Milano (2012).

[86] G. Pagano. *Raffreddamento e Intrappolamento di atomi di Itterbio*. Master's thesis, Università La Sapienza (2011).

[87] B. Zimmermann, T. Müller, J. Meineke, T. Esslinger, and H. Moritz. *High-resolution imaging of ultracold fermions in microscopically tailored optical potentials*. New Journal of Physics **13**, 043007 (2011). ISSN 1367-2630.

[88] W. S. Bakr, J. I. Gillen, A. Peng, S. Fölling, and M. Greiner. *A quantum gas microscope for detecting single atoms in a Hubbard-regime optical lattice.* Nature **462**, 74–7 (2009). ISSN 1476-4687.

[89] J. F. Sherson, C. Weitenberg, M. Endres, M. Cheneau, I. Bloch, and S. Kuhr. *Single-atom-resolved fluorescence imaging of an atomic Mott insulator.* Nature **467**, 68–72 (2010). ISSN 1476-4687.

[90] L. W. Cheuk, M. A. Nichols, M. Okan, T. Gersdorf, V. V. Ramasesh, W. S. Bakr, T. Lompe, and M. W. Zwierlein. *Quantum-Gas Microscope for Fermionic Atoms*. Phys. Rev. Lett. **114**, 193001 (2015).

[91] E. Haller, J. Hudson, A. Kelly, D. A. Cotta, B. Peaudecerf, G. D. Bruce, and S. Kuhr. *Single-atom imaging of fermions in a quantum-gas microscope*. Nature Physics **advance online publication** (2015).

[92] T. Hansch and B. Couillaud. *Laser frequency stabilization by polarization spectroscopy of a reflecting reference cavity*. Optics Communications **35**, 441–444 (1980). ISSN 0030-4018.

[93] B. Fröhlich, T. Lahaye, B. Kaltenhäuser, H. Kübler, S. Müller, T. Koch, M. Fattori, and T. Pfau. *Two-frequency acousto-optic modulator driver to improve the beam pointing stability during intensity ramps.* The Review of scientific instruments **78**, 043101 (2007). ISSN 0034-6748.

[94] E. Black. *An introduction to Pound–Drever–Hall laser frequency stabilization*. American Journal of Physics **69**, 79 (2001). ISSN 00029505.

[95] H. Metcalf and P. Van Der Straten. *Laser Cooling and Trapping*. Springer (1999).

[96] G. Insero. *Realizzazione di un Apparato Sperimentale per il rallentamento di un fascio atomico di Itterbio* (2010).

[97] W. Phillips and H. Metcalf. *Laser Deceleration of an Atomic Beam*. Phys. Rev. Lett. **48**, 596–599 (1982). ISSN 0031-9007.

[98] T. E. Barrett, S. W. Dapore-Schwartz, M. D. Ray, and G. P. Lafyatis. *Slowing atoms with σ^- polarized light*. Phys. Rev. Lett. **67**, 3483–3486 (1991).

[99] T. Kuwamoto, K. Honda, Y. Takahashi, and T. Yabuzaki. *Magneto-optical trapping of Yb atoms using an intercombination transition*. Phys. Rev. A **60**, R745–R748 (1999). ISSN 1050-2947.

[100] L. F. Livi. *Trasporto ottico di atomi freddi a lunga distanza* (2012).

[101] T. L. Gustavson, a. P. Chikkatur, a. E. Leanhardt, a. Görlitz, S. Gupta, D. E. Pritchard, and W. Ketterle. *Transport of Bose-Einstein condensates with optical tweezers*. Phys. Rev. Lett. **88**, 020601 (2002). ISSN 00319007.

[102] S. Schmid, G. Thalhammer, K. Winkler, F. Lang, and J. H. Denschlag. *Long distance transport of ultracold atoms using a 1D optical lattice*. New Journal of Physics **8**, 159–159 (2006). ISSN 1367-2630.

[103] W. Ketterle, D. Durfee, and D. Stamper-Kurn. *Making, probing and understanding Bose-Einstein condensate*. In M. Inguscio, S. Stringari, and C. Wieman, editors, *Proceedings of the International School of Physics "Enrico Fermi", Course CXL, Varenna, 7 - 17 July 1998*, number July 1998. IOS Press, Amsterdam (1998).

[104] S. Stellmer, R. Grimm, and F. Schreck. *Production of quantum-degenerate strontium gases*. Phys. Rev. A **87**, 013611 (2013). ISSN 10502947.

[105] R. Wei and E. J. Mueller. *Magnetic-field dependence of Raman coupling in alkali-metal atoms*. Phys. Rev. A **87**, 042514 (2013). ISSN 1050-2947.

[106] T. Mueller. *Exploring excited Bloch bands in optical lattices via stimulated Raman transitions*. Master's thesis, Institut fur Physik der Johannes Gutenberg-Universitat Mainz (2006).

[107] T. Müller, S. Fölling, A. Widera, and I. Bloch. *State Preparation and Dynamics of Ultracold Atoms in Higher Lattice Orbitals*. Phys. Rev. Lett. **99**, 200405 (2007).

[108] P. G. Harper. *Single Band Motion of Conduction Electrons in a Uniform Magnetic Field*. Proceedings of the Physical Society. Section A **68**, 874 (1955).

[109] D. R. Hofstadter. *Energy levels and wave functions of Bloch electrons in rational and irrational magnetic fields*. Phys. Rev. B **14**, 2239–2249 (1976).

[110] M. Z. Hasan and C. L. Kane. *Colloquium : Topological insulators*. Rev. Mod. Phys. **82**, 3045–3067 (2010).

[111] J. E. Moore. *The birth of topological insulators*. Nature **464**, 194–198 (2010). ISSN 0028-0836.

[112] D. J. Thouless, M. Kohmoto, M. P. Nightingale, and M. den Nijs. *Quantized Hall Conductance in a Two-Dimensional Periodic Potential*. Phys. Rev. Lett. **49**, 405–408 (1982).

[113] X.-G. Wen. *Topological orders and edge excitations in fractional quantum Hall states*. Advances in Physics **44**, 405–473 (1995).

[114] K. v. Klitzing, G. Dorda, and M. Pepper. *New Method for High-Accuracy Determination of the Fine-Structure Constant Based on Quantized Hall Resistance*. Phys. Rev. Lett. **45**, 494–497 (1980).

[115] T. L. H. B. Andrei Bernevig. *Topological Insulators and Topological Superconductors*. Princeton University Press (2013).

[116] B. I. Halperin. *Quantized Hall conductance, current-carrying edge states, and the existence of extended states in a two-dimensional disordered potential*. Phys. Rev. B **25**, 2185–2190 (1982).

[117] Y. Aharonov and D. Bohm. *Significance of Electromagnetic Potentials in the Quantum Theory*. Phys. Rev. **115**, 485–491 (1959).

[118] M. V. Berry. *Quantal Phase Factors Accompanying Adiabatic Changes*. Proceedings of the Royal Society A: Mathematical, Physical and Engineering Sciences **392**, 45–57 (1984). ISSN 1364-5021.

[119] Y. Hatsugai. *Chern number and edge states in the integer quantum Hall effect*. Phys. Rev. Lett. **71**, 3697–3700 (1993).

[120] D. Osadchy and J. E. Avron. *Hofstadter butterfly as quantum phase diagram*. Journal of Mathematical Physics **42**, 5665–5671 (2001).

[121] I. Dana, Y. Avron, and J. Zak. *Quantised Hall conductance in a perfect crystal*. Journal of Physics C: Solid State Physics **18**, L679 (1985).

[122] R. B. Laughlin. *Quantized Hall conductivity in two dimensions*. Phys. Rev. B **23**, 5632–5633 (1981).

[123] G. Giuliani and G. Vignale. *Quantum theory of the electron liquid*. Cambridge University Press (2005).

[124] M. Atala, M. Aidelsburger, M. Lohse, J. T. Barreiro, B. Paredes, and I. Bloch. *Observation of chiral currents with ultracold atoms in bosonic ladders*. Nature Physics **10**, 13–15 (2014). ISSN 1745-2473.

[125] C. J. Kennedy, W. C. Burton, W. C. Chung, and W. Ketterle. *Observation of Bose-Einstein condensation in a strong synthetic magnetic field*. Nat Phys **11**, 859–864 (2015). ISSN 1745-2473.

[126] D. Jaksch and P. Zoller. *Creation of effective magnetic fields in optical lattices: the Hofstadter butterfly for cold neutral atoms*. New Journal of Physics **5**, 56 (2003).

[127] C. Sias, H. Lignier, Y. P. Singh, A. Zenesini, D. Ciampini, O. Morsch, and E. Arimondo. *Observation of Photon-Assisted Tunneling in Optical Lattices*. Phys. Rev. Lett. **100**, 040404 (2008).

[128] F. Gerbier and J. Dalibard. *Gauge fields for ultracold atoms in optical superlattices*. New Journal of Physics **12**, 033007 (2010). ISSN 1367-2630.

[129] M. Aidelsburger. *Artificial gauge fields with ultracold atoms in optical lattices*. PhD thesis, Fakultät für Physik der Ludwig-Maximilians-Universität München (2015).

[130] N. Goldman, J. Dalibard, M. Aidelsburger, and N. R. Cooper. *Periodically driven quantum matter: The case of resonant modulations*. Phys. Rev. A **91**, 033632 (2015).

[131] N. Yao, C. Laumann, A. Gorshkov, H. Weimer, L. Jiang, J. Cirac, P. Zoller, and M. Lukin. *Topologically protected quantum state transfer in a chiral spin liquid*. Nat Commun **4**, 1585– (2013).

[132] B. Efron and R. J. Tibshirani. *An Introduction to the Bootstrap*. FL: CRC Press (1994).

[133] S. G. R.E. Prange and. *The Quantum Hall Effect*. Springer, New York (1990).

[134] M. Ben Dahan, E. Peik, J. Reichel, Y. Castin, and C. Salomon. *Bloch Oscillations of Atoms in an Optical Potential*. Phys. Rev. Lett. **76**, 4508–4511 (1996).

[135] G. Roati, E. de Mirandes, F. Ferlaino, H. Ott, G. Modugno, and M. Inguscio. *Atom Interferometry with Trapped Fermi Gases*. Phys. Rev. Lett. **92**, 230402 (2004).

[136] O. Boada, A. Celi, J. Rodriguez-Laguna, J. Latorre, and M. Lewenstein. *Quantum simulation of non-trivial topology*. New Journal of Physics **17**, 045007 (2015).

[137] E. J. Bergholtz and A. Karlhede. *Quantum Hall system in Tao-Thouless limit*. Phys. Rev. B **77**, 155308 (2008).

[138] F. Grusdt and M. Höning. *Realization of fractional Chern insulators in the thin-torus limit with ultracold bosons*. Phys. Rev. A **90**, 053623 (2014).

[139] T. Giamarchi. *Quantum Physics in One Dimension*. (2004).

[140] C. N. Yang. *Some Exact Results for the Many-Body Problem in one Dimension with Repulsive Delta-Function Interaction*. Phys. Rev. Lett. **19**, 1312–1315 (1967).

[141] B. Sutherland. *Further results for the many-body problem in one dimension*. Phys. Rev. Lett. **20**, 98–100 (1968). ISSN 00319007.

[142] G. a. Fiete. *Colloquium: The spin-incoherent Luttinger liquid*. Rev. Mod. Phys. **79**, 801–820 (2007). ISSN 00346861.

[143] E. H. Lieb and W. Liniger. *Exact analysis of an interacting Bose gas. 1. The General solution and the ground state*. Phys.Rev. **130**, 1605–1616 (1963).

[144] M. D. Girardeau. *Permutation Symmetry of Many-Particle Wave Functions*. Phys. Rev. **139**, B500–B508 (1965).

[145] P. Nozières and D. Pines. *The theory of quantum liquids*. Westview Press (1994) (1999).

[146] A. Recati, P. Fedichev, W. Zwerger, and P. Zoller. *Spin-Charge Separation in Ultracold Quantum Gases*. Phys. Rev. Lett. **90**, 020401 (2003). ISSN 0031-9007.

[147] A. Recati, P. O. Fedichev, W. Zwerger, and P. Zoller. *Fermi one-dimensional quantum gas: Luttinger liquid approach and spin-charge separation*. Journal of Optics B: Quantum and Semiclassical Optics **5**, S55 (2003).

[148] M. Olshanii. *Atomic Scattering in the Presence of an External Confinement and a Gas of Impenetrable Bosons*. Phys. Rev. Lett. **81**, 938–941 (1998). ISSN 0031-9007.

[149] G. Astrakharchik, D. Blume, S. Giorgini, and L. Pitaevskii. *Interacting Fermions in Highly Elongated Harmonic Traps*. Phys. Rev. Lett. **93**, 050402 (2004). ISSN 0031-9007.

[150] B. Paredes, A. Widera, V. Murg, O. Mandel, S. Folling, I. Cirac, G. V. Shlyapnikov, T. W. Hansch, and I. Bloch. *Tonks-Girardeau gas of ultracold atoms in an optical lattice*. Nature **429**, 277–281 (2004).

[151] M. Ogata and H. Shiba. *Bethe-ansatz wave function, momentum distribution, and spin correlation in the one-dimensional strongly correlated Hubbard model*. Phys. Rev. B **41**, 2326–2338 (1990).

[152] V. Cheianov, H. Smith, and M. Zvonarev. *Low-temperature crossover in the momentum distribution of cold atomic gases in one dimension*. Phys. Rev. A **71**, 033610 (2005). ISSN 1050-2947.

[153] V. Cheianov and M. Zvonarev. *Nonunitary Spin-Charge Separation in a One-Dimensional Fermion Gas*. Phys. Rev. Lett. **92**, 176401 (2004). ISSN 0031-9007.

[154] A. E. Feiguin and G. A. Fiete. *Spectral properties of a spin-incoherent Luttinger liquid*. Phys. Rev. B **81**, 075108 (2010).

[155] J. Stenger, S. Inouye, A. P. Chikkatur, D. M. Stamper-Kurn, D. E. Pritchard, and W. Ketterle. *Bragg Spectroscopy of a Bose-Einstein Condensate*. Phys. Rev. Lett. **82**, 4569–4573 (1999).

[156] A. Brunello, F. Dalfovo, L. Pitaevskii, S. Stringari, and F. Zambelli. *Momentum transferred to a trapped Bose-Einstein condensate by stimulated light scattering*. Phys. Rev. A **64**, 063614 (2001). ISSN 1050-2947.

[157] X.-J. Liu and H. Hu. *Collective mode evidence of high-spin bosonization in a trapped one-dimensional atomic Fermi gas with tunable spin*. Annals of Physics **350**, 84–94 (2014). ISSN 00034916.

[158] I. Carusotto. *Bragg scattering and the spin structure factor of two-component atomic gases*. Journal of Physics B: Atomic, Molecular and Optical Physics **39**, S211 (2006).

[159] S. Hoinka, M. Lingham, M. Delehaye, and C. J. Vale. *Dynamic Spin Response of a Strongly Interacting Fermi Gas*. Phys. Rev. Lett **109**, 050403 (2012).

[160] M. Petersen, R. Chicireanu, S. T. Dawkins, D. V. Magalhães, C. Mandache, Y. Le Coq, A. Clairon, and S. Bize. *Doppler-Free Spectroscopy of the $^1S_0$-$^3P_0$ Optical Clock Transition in Laser-Cooled Fermionic Isotopes of Neutral Mercury*. Phys. Rev. Lett. **101**, 183004 (2008).

[161] V. A. Dzuba and A. Derevianko. *Dynamic polarizabilities and related properties of clock states of ytterbium atom*. J. Phys. B: At. Mol. Opt. Phys **43**, 11 (2009). ISSN 0953-4075.

[162] F. Deuretzbacher, K. Plassmeier, D. Pfannkuche, F. Werner, C. Ospelkaus, S. Ospelkaus, K. Sengstock, and K. Bongs. *Heteronuclear molecules in an optical lattice: Theory and experiment*. Phys. Rev. A **77**, 032726 (2008). ISSN 1050-2947.

[163] F. Scazza, C. Hofrichter, M. Höfer, P. C. De Groot, I. Bloch, and S. Fölling. *Observation of two-orbital spin-exchange interactions with ultracold SU(N)-symmetric fermions*. Nature Physics **10**, 779–784 (2014). ISSN 17452473.

[164] R. H. Dicke. *Coherence in Spontaneous Radiation Processes*. Phys. Rev. **93**, 99–110 (1954).

[165] B. H. Bransden and C. J. Joachain. *Physics of Atoms and Molecules; 2nd ed.* Prentice-Hall, Harlow (2003).

[166] A. Widera, F. Gerbier, S. Fölling, T. Gericke, O. Mandel, and I. Bloch. *Coherent collisional spin dynamics in optical lattices*. Phys. Rev. Lett. **95**, 190405 (2005). ISSN 00319007.

[167] A. Widera, F. Gerbier, S. Folling, T. Gericke, O. Mandel, and I. Bloch. *Precision measurement of spin-dependent interaction strengths for spin-1 and spin-2 ^{87}Rb atoms*. New Journal of Physics **8**, 152 (2006).

[168] M. Anderlini, P. J. Lee, B. L. Brown, J. Sebby-Strabley, W. D. Phillips, and J. V. Porto. *Controlled exchange interaction between pairs of neutral atoms in an optical lattice.* Nature **448**, 452–6 (2007). ISSN 1476-4687.

[169] J. S. Krauser, J. Heinze, N. Fläschner, S. Götze, O. Jürgensen, D.-S. Lühmann, C. Becker, and K. Sengstock. *Coherent multi-flavour spin dynamics in a fermionic quantum gas*. Nature Physics **8**, 813–818 (2012). ISSN 1745-2473.

[170] J. S. Krauser, U. Ebling, N. Fläschner, J. Heinze, K. Sengstock, M. Lewenstein, a. Eckardt, and C. Becker. *Giant spin oscillations in an ultracold Fermi sea.* Science **343**, 157–60 (2014). ISSN 1095-9203.

[171] E. L. Bolda, E. Tiesinga, and P. S. Julienne. *Effective-scattering-length model of ultracold atomic collisions and Feshbach resonances in tight harmonic traps*. Phys. Rev. A **66**, 013403 (2002).

[172] X. Zhang, M. Bishof, S. L. Bromley, C. V. Kraus, M. S. Safronova, P. Zoller, A. M. Rey, and J. Ye. *Spectroscopic observation of SU(N)-symmetric interactions in Sr orbital magnetism*. Science **345**, 1467–1473 (2014).

[173] F. Scazza. *Probing SU(N)-symmetric orbital interactions with ytterbium Fermi gases in optical lattices*. PhD thesis, Ludwig-Maximilians-Universität München (2015).

[174] M. Sato, Y. Takahashi, and S. Fujimoto. *Non-Abelian Topological Order in s-Wave Superfluids of Ultracold Fermionic Atoms*. Phys. Rev. Lett. **103**, 020401 (2009). ISSN 0031-9007.

[175] M. Sato, Y. Takahashi, and S. Fujimoto. *Non-Abelian topological orders and Majorana fermions in spin-singlet superconductors*. Phys. Rev. B **82,** 134521 (2010). ISSN 1098-0121.

[176] E. M. Stoudenmire, J. Alicea, O. A. Starykh, and M. P. Fisher. *Interaction effects in topological superconducting wires supporting Majorana fermions*. Phys. Rev. B **84**, 014503 (2011).

[177] Z.-Q. Yu and H. Zhai. *Spin-Orbit Coupled Fermi Gases across a Feshbach Resonance*. Phys. Rev. Lett. **107**, 195305 (2011).

[178] M. Gong, S. Tewari, and C. Zhang. *BCS-BEC Crossover and Topological Phase Transition in 3D Spin-Orbit Coupled Degenerate Fermi Gases*. Phys. Rev. Lett. **107**, 195303 (2011).